Plasma Physics Reports, Vol. 26, No. 7, 2000, pp. 539–549. Translated from Fizika Plazmy, Vol. 26, No. 7, 2000, pp. 579–589.

TOKAMAKS

Simulation of START Shots with the Canonical Profile Transport Model

Yu. N. Dnestrovskij*, M. P. Gryaznevich, A. Yu. Dnestrovskij*, J. W. Connor**, S. E. Lysenko*, K. N. Tarasyan*, S. V. Cherkasov*, and M. J. Walsh*****

**Institute of Nuclear Fusion, Russian Research Centre Kurchatov Institute, Moscow, 123182 Russia*

***Euratom, UKAEA Fusion, Culham Science Centre, Abingdon, Oxon, OX14 3DB, UK*

****Walsh Scientific Ltd., Abingdon, Oxon, OX14 3EB, UK*

Received September 23, 1999; in final form, November 25, 1999

Abstract—The canonical profile transport model, which has been benchmarked previously for tokamaks with a conventional aspect ratio, is applied to simulations of the spherical tokamak START. A set of Ohmic shots is used to modify the model so that it is appropriate for the specific conditions of the spherical tokamak plasma. The application of the model as a tool to analyze neutral beam–heated START shots allows the estimation of the neutral beam-injection power absorbed by the plasma, P_{NB}^{abs}, which is experimentally uncertain. The modeling shows that both P_{NB}^{abs} and the energy confinement time increase with increasing the average density. Finally, the modified model is used to simulate the performance of the new megaampere spherical tokamak MAST at Culham. © *2000 MAIK "Nauka/Interperiodica".*

1. INTRODUCTION

In recent years, successful experiments on the START device (a spherical tokamak with a tight aspect ratio $A = R/a \approx 1.3$, $R = 0.2$–0.25 m, $a = 0.2$–0.25 m, current $I_p = 0.15$–0.3 MA, and magnetic field $B = 0.2$–0.3 T) have been performed [1–4]. The use of neutral beam injection (NBI) allows one to increase the ion temperature from $T_i \sim 0.15$ keV to $T_i \sim T_e \sim 0.3$ keV. Record values of the total beta β_t and normalized current I_p/aB have been achieved. Improvements in diagnostics [multichannel Thomson scattering (up to 30 chords) and multichannel charge-exchange recombination spectroscopy (20 chords)] permit one to obtain T_e and T_i profiles. All these achievements allow a detailed study of the plasma energy balance.

In this paper, we invoke the canonical profile transport model (CPTM) [5–6] for the analysis of the plasma energy balance in START. The parameters of this semiempirical transport model have been chosen by a comparison with the experimental data from a range of conventional aspect ratio tokamaks. A wide database of Ohmic (OH) discharges is used to extend the CPTM to tight aspect ratio tokamaks. Thus, the transport model is first validated for OH discharges and then is used to analyze NBI discharges. Here, the simulation provides the solution of the inverse problem of the determination of the absorbed NBI power P_{NB}^{abs}.

Our calculations show that, at low plasma currents ($I_p < 0.18$ MA) and low densities $\bar{n} < 2 \times 10^{19}$ m^{-3}, only a small fraction of the beam power P_{NB} is absorbed in the plasma. Apparently, in this case, the main part of the trapped hot-ion population is lost due to poor trajectories or by charge exchange with the cold neutrals before they transfer their energy to the plasma particles. As the current and density rise, the ratio P_{NB}^{abs}/P_{NB} increases, and at $I_p > 0.2$ MA and $\bar{n} > 4 \times 10^{19}$ m^{-3} it achieves a value of about 0.9–1.

The neoclassical ion thermal diffusivity χ_i^{neo} can play a significant role in the ion energy balance at high plasma densities. In tight aspect ratio tokamaks, the toroidal field can vary over the plasma cross section by a factor of 6–8. As a result, the poloidal and toroidal fields at the outward plasma edge are comparable. This effect leads to significant corrections in χ_i^{neo} [7]. Our analysis shows that, in the collisional regime on START, the χ_i^{neo} value at the edge decreases by a factor of 25–40 in comparison with the basic Shafranov expression [8]. As a result, the calculated ion energy confinement time τ_{Ei} becomes comparable with the electron one, τ_{Ee}.

The paper is organized as follows. In Section 2, the CPTM extension to tight aspect ratio tokamaks is described. In Section 3, the approximate expressions for χ_i^{neo} are derived. The validation of the model by the simulation of OH discharges is discussed in Section 4. The results of simulations of NBI discharges are presented in Section 5. Preliminary calculations for the MAST spherical tokamak at Culham are presented in

1063-780X/00/2607-0539$20.00

Section 6. Section 7 contains the conclusions. The analytical estimates of hot-ion losses and the cold-neutral density are presented in the Appendix.

2. THE TRANSPORT MODEL

We present here the basic CPTM expressions for the L-mode, which we used in the calculations. The set of transport equations consists of the equations for the electron and ion temperatures

$$\begin{aligned}\frac{3}{2}\frac{\partial}{\partial t}(nT_e) &= -\operatorname{div} q_e + Q_e,\\ \frac{3}{2}\frac{\partial}{\partial t}(nT_i) &= -\operatorname{div} q_i + Q_i\end{aligned} \tag{1}$$

and the diffusion equation for the poloidal magnetic field [5–6]. The equilibrium is obtained by solving the Grad–Shafranov equation. We introduce the canonical profiles of the ion and electron temperatures in Kadomtsev's form [9]

$$T_{kc}(\rho)/T_{kc}(0) = (1 + \rho^2/a_j^2)^{-1}, \tag{2}$$

where $k = e, i$; ρ is the generalized radial coordinate ($0 < \rho < a$); $a_j = a(q_0/(q_s - q_0))^{1/2}$ is the current radius; q is the safety factor; and q_s is the value of q on the magnetic surface that surrounds the current I_s equal to a fixed fraction of the total plasma current, $I_s = sI_p$. We also put $T_{ec}(\rho) = T_{ic}(\rho) = T_c(\rho)$.

We assume the following form of the heat fluxes:

$$q_k = q_k^{con} + q_k^{an} + q_k^{PC} \quad (k = i, e), \tag{3}$$

where

$$q_k^{con} = 5/2\Gamma_n T_k, \tag{4}$$

$$q_k^{an} = -\kappa_k^{an}\frac{\partial T_k}{\partial \rho}, \quad \kappa_k^{an} = n\chi_k^{an}, \tag{5}$$

$$q_k^{PC} = -n\chi_k^{PC}\frac{\rho T_k}{a^2}z_{Tk} = -n\chi_k^{PC}\left(\frac{\partial T_k}{\partial \rho} - \frac{T_{kc}'}{T_{kc}}T_k\right). \tag{6}$$

Here, q_k^{con} is the convective heat flux; q_k^{an} is the part of the anomalous (or neoclassical) heat flux, which is proportional to the temperature gradient; q_k^{PC} is the part of the anomalous heat flux, which is determined by the plasma self-organization and the tendency of the plasma temperature profile to evolve into the canonical profile; Γ_n is the particle flux; $\kappa_k^{PC} = n\chi_k^{PC}$ is the "stiffness" of the canonical profile; and

$$z_{Tk} = \frac{a^2}{\rho}\frac{\partial}{\partial \rho}\ln\left(\frac{T_k}{T_{kc}}\right). \tag{7}$$

The quantities z_{Tk} are dimensionless measures of the deviations of the real profiles from the corresponding canonical profiles. We propose that the particle flux Γ_n is known from the experiment and choose the following transport coefficients:

$$\begin{aligned}\kappa_k^{PC} &= \alpha_k^{PC}(1/M)(a/R)^{0.75}q(a/2)\\ &\times q_{cyl}(a)(T_k(a/4))^{0.5}\bar{n}(3/R)^{1/4}/B = \text{const}(\rho),\end{aligned} \tag{8}$$

$$\begin{aligned}\chi_e^{an} &= \text{const}(\rho)\\ &= \tilde{\alpha}_e\frac{(T_e(a/2))^{1/2}}{n(a/2)R}f_e^{an}(q, \beta, \nu^*, a/R, k, \delta),\end{aligned} \tag{9}$$

$$f_e^{an}(q, \beta, \nu^*, a/R, k, \delta) = 9.4(4/q_{95})(a/R)^{2.5}, \tag{10}$$

$$\chi_i^{an} = \chi_i^{neo}, \quad q_{cyl} = \frac{5a^2B}{I_pR}\frac{1+k^2}{2}, \tag{11}$$

$$\alpha_e^{PC} = 3.5, \quad \alpha_i^{PC} = 5, \quad \tilde{\alpha}_e \approx 2, \quad s = 0.95. \tag{12}$$

Here, M is the atomic mass of the main plasma component and k and δ are the plasma elongation and triangularity, respectively. The transport coefficients (8)–(12) are distinguished slightly from those used for conventional tokamaks [5, 6] with the usual aspect ratio $A = R/a \sim 3$. First, we complement the stiffness coefficient κ_k^{PC} (8) by the factor $(3/R)^{1/4}$, which makes this coefficient satisfy the dimensionality constraints. This factor is not essential for conventional tokamaks but very important for a tight aspect ratio tokamak with a small major radius R. Second, we add the factor f_e^{an} in the expression for the anomalous electron thermal diffusivity χ_e^{an} (9). This factor is close to unity for conventional tokamaks, but it is large for spherical tokamaks because it includes a sharp inverse dependence on the aspect ratio $A = R/a$. Note that the heat flux q_e^{an} containing the thermal diffusivity χ_e^{an} (9) is responsible for the improvement of the energy confinement as the plasma density increases. Expression (10) is supported by the analysis of START discharges in the Ohmic heating regime (see Section 4). The modified expression for q_{95} is discussed in the next section. We use here the following units: T in keV, B in T, a and R in m, n in 10^{19} m^{-3}, χ_k in m^2 s^{-1}, and κ_k in 10^{19} m^{-1} s^{-1}. The full neoclassical conductivity σ is used throughout.

3. ION THERMAL DIFFUSIVITY

We consider carefully the neoclassical part of the ion thermal diffusivity χ_i^{neo}, because it is important under START conditions (see also [7]). In the shots under study, the dimensionless ion collision frequency ν_i^* is rather large: $\nu_i^* \approx 1$ at $\rho/a \approx 0.5$, and $\nu_i^* \approx 10$ near the center and at the edge. Thus, we can find all

three neoclassical regions: banana, plateau, and Pfirsch–Schluter regions in different zones of the plasma cross section. However, in tokamaks with a small aspect ratio $A = R/a < 2$, the standard neoclassical expressions for the thermal diffusivity χ_i^{neo} require revision.

First, we consider the Pfirsch–Schluter region. The heat flux here depends on the length of the magnetic field line along which the Pfirsch–Schluter currents are closed. This length L_{PS} is proportional to the ratio

$$L_{PS} \propto \frac{\rho B}{RB_p}. \tag{13}$$

In standard tokamaks ($A \approx 3$–4), this ratio is proportional to q. However, for $A \approx 1.5$, the pitch of the helical magnetic field line at the outer part of the torus exceeds the helical pitch at the inner part by many times. Correspondingly, the Pfirsch–Schluter currents are closed mainly near the outer part, where the length of the magnetic field line between the top and bottom of the plasma column is several times shorter than in standard tokamaks with the same plasma cross section and the same values of the current and magnetic field. Therefore, instead of q, which is determined by the equilibrium of a tight torus and which is large at the edge, we should use the quantity q^{eff} in the transport coefficients. Approximately, q^{eff} is determined as follows:

$$q^{\text{eff}}(a) = q_a^{\text{eff}} = \left(\frac{\rho B}{RB_p}\right)_{\text{out}} \cong \frac{A}{A+1} q_{cyl}. \tag{14}$$

Here, the index "out" stands for the outer part of the torus. We use a parabolic approximation for q^{eff}:

$$q^{\text{eff}} = q^{\text{eff}}(\rho) = q_0 + (q_a^{\text{eff}} - q_0)(\rho/a)^2, \tag{15}$$

where $q_0 = q(0)$.

Thus, the expression for χ_i^{neo} in the Pfirsch–Schluter region has the form [8]

$$\chi_i^{neo} = \rho_i^2 \nu_{ii}(1 + 1.6(q^{\text{eff}})^2), \quad \nu_i^* > (\rho/R)^{-3/2}, \tag{16}$$

where ρ_i is the Larmor radius of ions and ν_{ii} is the frequency of ion–ion collisions. For START, we have $q_{95} = 10$–15 and $q_a^{\text{eff}} \approx q_{95}(1/5$–$1/6)$; therefore, the substitution of q^{eff} for q decreases χ_i^{neo} at the edge by a factor of 25–36.

The trapped particles are located in the outer part of the torus; therefore, we should also substitute q^{eff} for q in expressions for χ_i^{neo} in the plateau and banana regions. In the plateau region, we have $\chi_i^{neo} \propto q$; this region is located in the vicinity of the point $\rho/a \approx 0.5$. Therefore, the replacement of q by q^{eff} actually decreases χ_i^{neo} in the plateau by a factor of 3–4. Near the plasma center, where $R/\rho \gg 1$ and $q^{\text{eff}} \approx q \approx 1$, such a replacement is not necessary.

Of course, formula (16) is approximate and should be refined. However, for a sperical tokamak, χ_i^{neo} is expected to be much less than the thermal diffusivity given by the Shafranov expression. As a result, in the most part of the START cross section, the heat flux $q_i^{neo} = -\chi_i^{neo}\frac{\partial T_i}{\partial r}$ will be much less than q_k^{PC}.

4. THE VALIDATION OF THE MODEL BY OHMIC SHOTS

The transport model described in Section 2 has been previously benchmarked for conventional aspect ratio tokamaks at $R/a \sim 2.5$, $q_{95} \sim 4$, and $f_e^{an} \sim 1$ [5–6]. Our goal now is to justify the choice of f_e^{an} in the form (10). We choose a set of 21 START shots in the OH regime (nos. 32863–35517) with maximum plasma currents in the range $0.1 < I_p < 0.186$ MA and chord-averaged densities in the range $2.2 \times 10^{19} < \bar{n} < 6 \times 10^{19}$ m^{-3}. The time behavior of the plasma current I_p, density n, toroidal magnetic field B, and geometrical parameters (minor radius a, major radius R, plasma elongation k, and triangularity δ) were taken from the experiment. The profiles of the electron temperature $T_e(\rho)$ and density $n(\rho)$ were measured by Thomson scattering diagnostics one time per discharge at the moment $t = t_{TS}$. The value of t_{TS} could change from shot to shot. In calculations, we kept the density profile unchanged in time but calibrated it by the interferometry measurements of the chord-averaged density. We also put $Z_{\text{eff}} = 2$ for all shots. The dependence of the final results on the choice of Z_{eff} will be discussed later.

For each shot, we generate the time-history of the discharge up to the instant $t = t_{TS}$ by means of the CPTM and calculate the functionals (deviations)

$$dT_1 = \frac{\sum(T_e^{exp} - T_e)}{\sum T_e^{exp}} \tag{17}$$

or

$$dT_2 = \sqrt{\frac{\sum(T_e^{exp} - T_e)^2}{\sum(T_e^{exp})^2}} \tag{18}$$

at this instant. The separate terms in sums (17) and (18) correspond to the measured values of the electron temperature along the major radius. Then, we introduce the mean deviations for the chosen set of the shots,

$$\langle dT_1 \rangle = \sum dT_1/N, \quad \langle dT_2 \rangle = \sum dT_2/N, \tag{19}$$

where $N = 21$ is the number of shots in the chosen set. The fitting of the CPTM is performed by choosing the

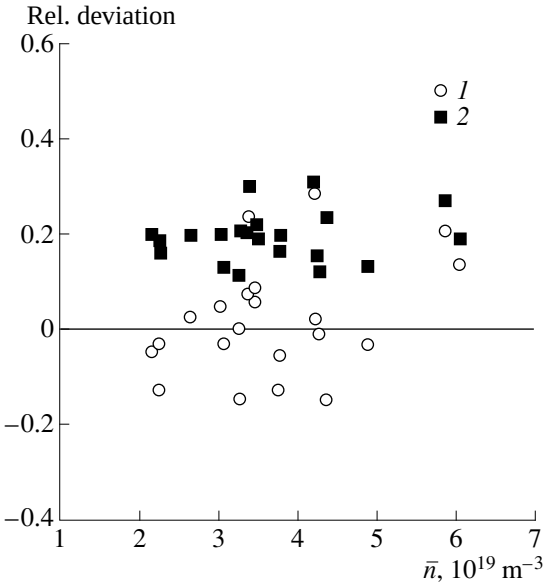

Fig. 1. Average deviations dT_1 (open circles) and dT_2 (closed squares) of the calculated electron temperature from the experimental vs. the chord-averaged density $\bar{n}$ for the set of 21 Ohmic START shots.

form of the anomalous factor f_e^{an} and its permanent multiplier by minimizing the functionals $\langle dT_1\rangle$ or $\langle dT_2\rangle$. The scatter in the experimental points in the Thomson scattering data makes the quantities (17) and (18) (and, consequently, $\langle dT_1\rangle$ and $\langle dT_2\rangle$) nonequivalent. The mean deviation $\langle dT_2\rangle$ describes not only the uncertainty of the model but also the dispersion of the experimental points; therefore, we prefer to use the mean deviation $\langle dT_1\rangle$ in the minimization procedure.

To take sawtooth oscillations into account, we increase the electron heat diffusivity χ_e in the region

$$0 < \rho < \rho_{mix} \sim \rho_s\ (q(\rho_s) = 1)$$

by a value $\delta\chi_e$, which is also determined by the minimization procedure. As a result, we obtain expression (10) for the anomalous factor f_e^{an} and the value of $\delta\chi_e$. Simultaneously, the profiles of $T_e(\rho)$ and $T_i(\rho)$, the energy confinement time τ_E, and the heat fluxes are also found.

The values of the deviations dT_1 (open circles) and dT_2 (closed squares) for the set of 21 Ohmic shots are shown in Fig. 1. The mean value of dT_1 for this set is approximately zero ($\langle dT_1\rangle \sim 0$), but the scattering of points is fairly large: $\max|dT_1| \sim 20\%$. To clarify the reason for such a large scatter, let us consider the behavior of dT_2 in Fig. 1. It is seen that the dT_2 points are scattered around the mean value of $\langle dT_2\rangle \sim 20\%$, which describes the average spread of the experimental points along the electron temperature profile. However, the value of dT_1 is very sensitive to the details of the scattering in the experimental points, which determines the large scattering in the dT_1 points in Fig. 1. The typical experimental and calculated electron temperature profiles, $T_e^{exp}(R)$ and $T_e(R)$, as functions of the major radius R for shot no. 33854 are shown in Fig. 2. In this case, $dT_1 = -5\%$ and $dT_2 = 19\%$. In spite of the large spread of the experimental points (the apparent "hollow" profile), the value of dT_1 is low due to the mutual compensation of different terms in equation (17) for dT_1.

The calculations show a very weak dependence of the deviations on Z_{eff}. In Fig. 3, the dependence of dT_1 and dT_2 on Z_{eff} is shown for shot no. 35127. The increase in Z_{eff} from 1 to 5 leads to a decrease in dT_1 from +11% to –13% confirming our choice of $Z_{eff} = 2$. The change in dT_2 in this case is very small.

5. THE SIMULATION OF NBI SHOTS

5.1. General Considerations

The total neutral beam power P_{NB} can be represented as a sum of several terms describing the different channels of losses:

$$P_{NB} = P_{NB}^S + P_{NB}^{pt} + P_{NB}^{capt}, \quad (20)$$

$$P_{NB}^{capt} = P_{NB}^{cx} + P_{NB}^{abs}, \quad P_{NB}^{abs} = (1 - \alpha_{cx})P_{NB}^{capt}, \quad (21)$$

where P_{NB}^S is the power carried away by the shine-through particles (the particles that pass through the plasma), P_{NB}^{pt} is the power related to the particles that were captured on poor trajectories and then leave the plasma without energy exchange, P_{NB}^{capt} is the power related to the hot ions captured on good trajectories, P_{NB}^{cx} is the power that is lost due to charge exchange of the captured hot ions with cold neutrals, P_{NB}^{abs} is the power absorbed by thermal plasma particles, and α_{cx} is the fraction of the captured power that is lost due to charge exchange. Only the term P_{NB}^{abs} is useful for plasma heating. Semiquantitative estimates of P_{NB}^S, P_{NB}^{cx}, the total cold-neutral density n_n, and parameter α_{cx} are presented in the Appendix. One is required to perform massive calculations to find the value of P_{NB}^{pt} [10]. The multiplicity of loss channels for the beam particles and the uncertainty of many parameters determining these losses make direct calculations of the absorbed beam power P_{NB}^{abs} rather unreliable. Therefore, other methods allowing us to find this power have to be developed. One of these methods is considered in this section.

Since the absorbed beam power P_{NB}^{abs} has the same order of magnitude as the Ohmic power P_{OH}, we suppose that the model for electron energy balance that we verified for the OH shots is also valid for NBI shots. The unknown values of P_{NB}^{abs} are to be determined during the simulation using a minimization procedure very similar to the case of Ohmic heating. Thus, the average temperature deviations dT_1 and dT_2 described by (17) and (18) in the case of auxiliary heating have to be minimized by a choice of the value of the unknown absorbed power P_{NB}^{abs}.

5.2. The Dependence of the Absorbed Power on Density and Current

Figure 4 shows the value of P_{NB}^{abs} for the set of 37 shots versus the plasma density at the instant $t = t_{TS}$. These shots with very different parameters were chosen from the START 1996–1998 database. Closed squares correspond to the shots with a plasma current in the range $0.18 < I_p < 0.25$ MA, and the open circles show the shots in the range $0.165 < I_p < 0.18$ MA. We see that, at low plasma densities $\bar{n} < 3 \times 10^{19}$ m^{-3}, the absorbed power P_{NB}^{abs} is small. In the range of medium plasma densities $3.3 \times 10^{19} < \bar{n} < 5.5 \times 10^{19}$ m^{-3}, P_{NB}^{abs} increases with the plasma density and reaches a maximum at $\bar{n} \sim 6 \times 10^{19}$ m^{-3}. Within this range, one can see the difference in P_{NB}^{abs} for high and low plasma currents: the energy absorption is higher for higher plasma currents. For densities higher than $\bar{n} \sim 6 \times 10^{19}$ m^{-3}, the absorbed power P_{NB}^{abs} decreases sharply.

The following effects can explain the peculiarities of the absorbed NBI power shown in Fig. 4 (also see the Appendix). The shine-through fraction of the beam P_{NB}^{S} decreases with increasing the plasma density. Therefore, the captured power P_{NB}^{capt} increases, which leads to an increase in the absorbed power P_{NB}^{abs}. The optical thickness of the plasma with respect to cold neutrals increases as the plasma density rises. Thus, the cold neutral density in the plasma core decreases exponentially and the charge-exchange losses P_{NB}^{cx} of captured hot particles decreases sharply. At low currents, the deviations of hot-ion trajectories from magnetic surfaces become large and poor-orbit losses P_{NB}^{pt} increase. An increase in the current leads to an improvement of hot-ion confinement on "fat" banana trajectories. At very high plasma densities ($\bar{n} > 6 \times 10^{19}$ m^{-3}), most of the beam particles are captured near the plasma edge on poor trajectories. Therefore, these particles leave the plasma instantaneously and P_{NB}^{capt} (and, consequently, P_{NB}^{abs}) decreases.

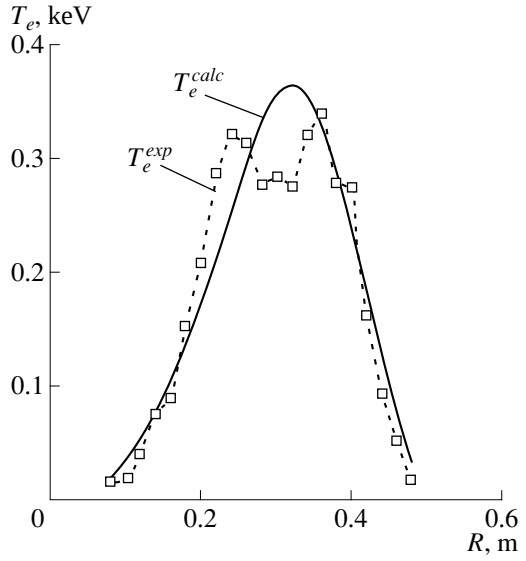

Fig. 2. The profiles of the experimental and calculated electron temperatures for shot no. 33854 at $t = 38$ ms. The measured points are marked by squares. $dT_1 = -5\%$, $dT_2 = 19\%$.

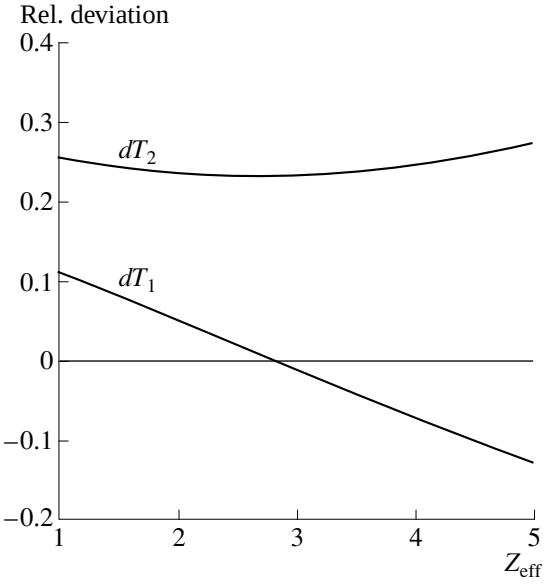

Fig. 3. Deviations dT_1 and dT_2 vs. Z_{eff} for the parameters of shot no. 35127.

5.3. Modeling the Evolution of NBI Shots

We describe here the simulation of the evolution of two sets of shots (A and B). Set A includes seven shots

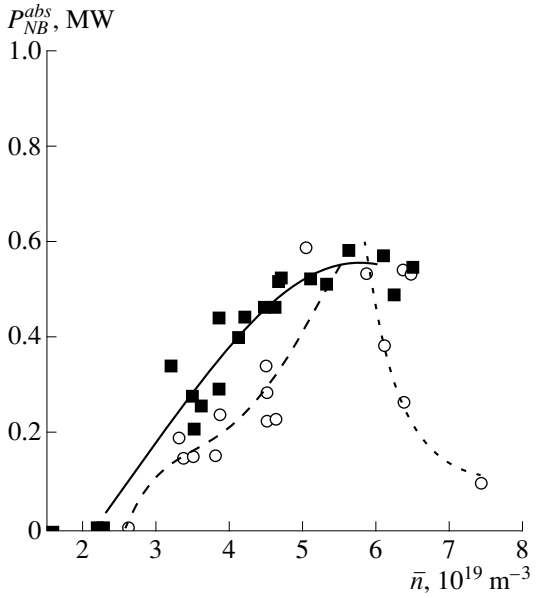

Fig. 4. The calculated absorbed neutral beam power P_{NB}^{abs} vs. the chord-averaged density $\bar{n}$ for the two sets of NBI START shots. Closed squares correspond to the shots with currents in the range $0.18 < I_p < 0.25$ MA, and the open circles show the shots with currents in the range $0.165 < I_p < 0.18$ MA. The smooth fitting of the points underlines the increase in the absorbed power P_{NB}^{abs} with increasing the density at $\bar{n} < 5.5 \times 10^{19}$ m^{-3}.

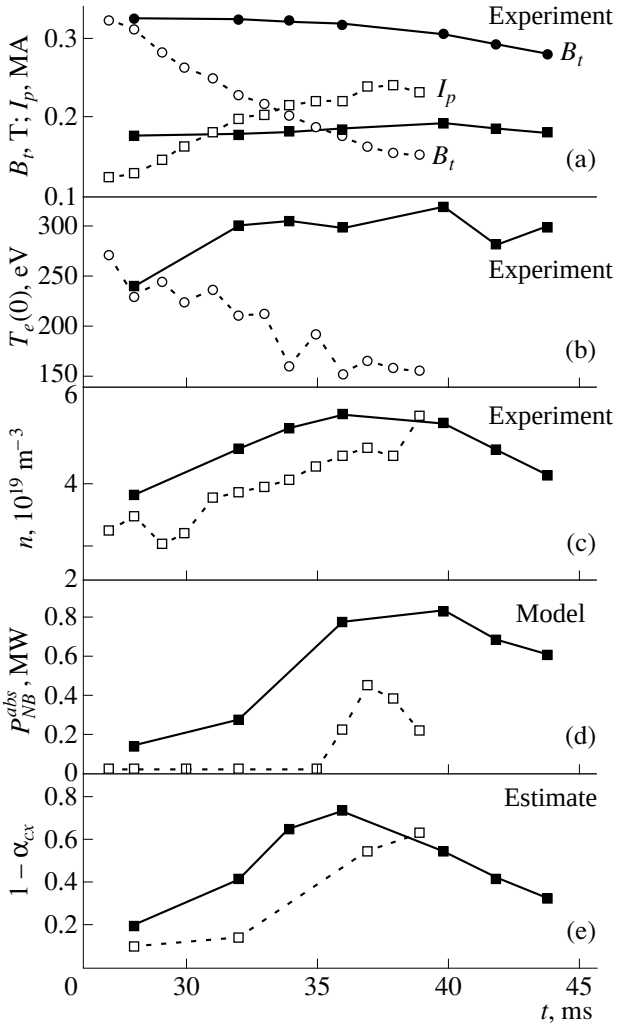

Fig. 5. Time evolution of the several experimental and calculated plasma parameters for the two sets of START shots (A and B): (a) the total plasma current I_p (squares) and toroidal magnetic field B (circles), (b) the experimental central electron temperature, (c) chord-averaged density $\bar{n}$, (d) the absorbed power calculated by the CPTM, and (e) the fraction of the absorbed power calculated by approximate expressions (A.3). Each point in the figure corresponds to a particular shot. The points for sets A and B are joined by solid and dashed lines, respectively.

(nos. 34034–34040) with a relatively quiet evolution of the plasma parameters. Set B includes 13 shots (nos. 35578–35592) with a large decrease in the toroidal magnetic field to the end of the discharge. This set relates to the experiments with a high value of β_t. Inside each set, all discharges were approximately similar, but the Thomson scattering diagnostics was switched on at different times $t = t_{TS}$ for different shots. Due to irreproducibility, the spread of the plasma parameters in the same set for different discharges attains ±10% in the plasma current and ±15% in the energy content.

Thus, for simulations, we have seven (for set A) or thirteen (for set B) slightly different experimental scenarios for the plasma current $I_p(t)$, toroidal magnetic field $B(t)$, plasma density $n(t)$, major and minor plasma radii $R(t)$ and $a(t)$, elongation $k(t)$, triangularity $\delta(t)$, and the corresponding values of the electron temperature and density profiles $T_e(R)$ and $n(R)$. As in the previous section, we only simulate the ion and electron temperatures, the other parameters being taken from the experiment.

The simulation procedure is as follows. We evolve each chosen shot separately up to the instant $t = t_{TS}$, attempting to minimize the deviation dT_1 at this moment by the iteration procedure changing P_{NB}^{abs}. We finish the iterations usually when $|dT_1|$ reaches a value of 1–3%. As a result, we obtain the value of the absorbed power P_{NB}^{abs} for the chosen shot at $t = t_{TS}$. Then, we repeat the minimization procedure for the other shots with different t_{TS} for both sets A and B.

The results of calculations and some experimental data are shown in Fig. 5 by points. Solid and dashed lines join the points corresponding to the sets A and B, respectively. Note that each point for all of the plasma parameters in this figure corresponds to some particular

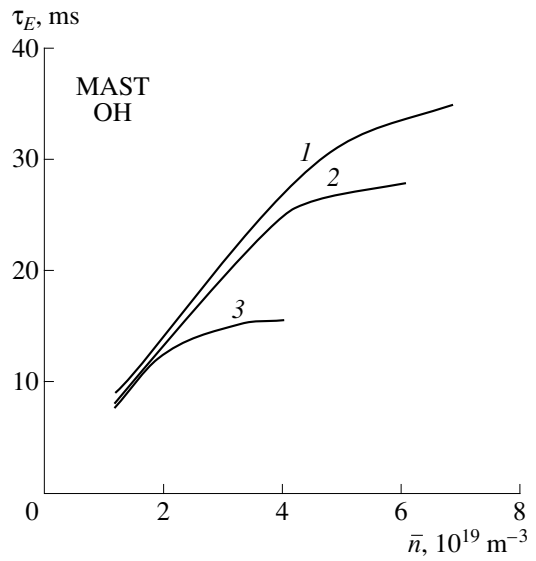

Fig. 6. The energy confinement time τ_E vs. chord-averaged density $\bar{n}$ for different currents I_p in MAST (OH regime) for (*1*) I_p = 1.5 MA and B = 0.6 T, (*2*) I_p = 1. MA and B = 0.6 T, and (*3*) I_p = 0.5 MA and B = 0.3 T.

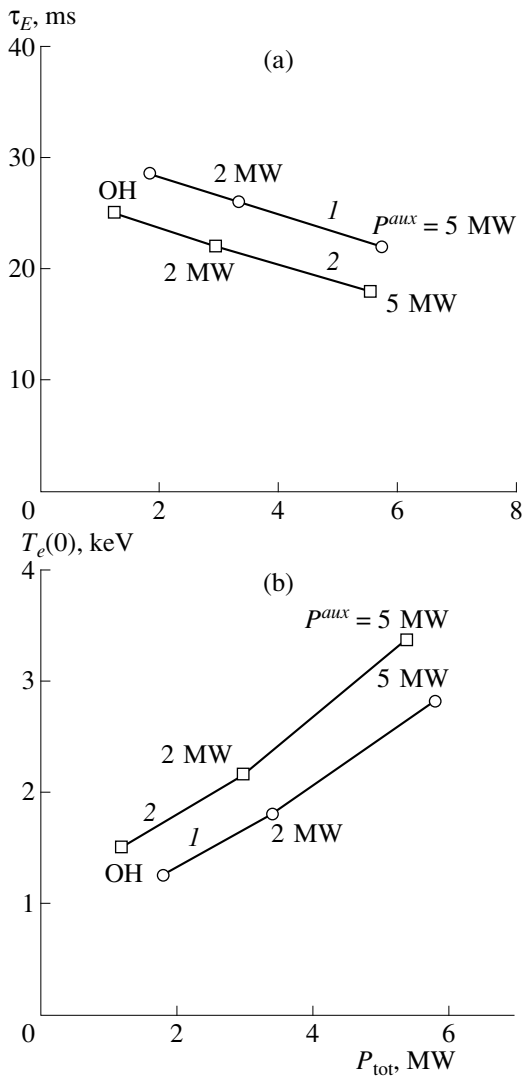

Fig. 7. (a) The energy confinement time τ_E and (b) central electron temperature T_e vs. the total heating power for different plasma densities in MAST with I_p = 1 MA and B = 0.6 T for n = (*1*) 6×10^{19} and (*2*) 4×10^{19} m^{-3}.

shot at the time $t = t_{TS}$. This is the reason why the lines connecting the different points are not smooth. However, for simplicity, we will call these lines "the evolution" of the plasma parameters. Figure 5e shows the evolution of the parameter $1 - \alpha_{cx}$ (the ratio between the absorbed and captured powers; see the Appendix), which does not include the poor-orbit losses P_{NB}^{pt}.

Let us now compare the plasma time behavior in different sets. Set A is characterized by a quiet evolution of I_p, B, $\bar{n}$, and $T_e(0)$. As a result, the calculated behavior of P_{NB}^{abs} is also quiet. The absorbed power P_{NB}^{abs} is low in the initial phase of the discharges, when the plasma density is low. Then, P_{NB}^{abs} increases and reaches its maximum at the moment when the plasma current and density are maximum ($I_p \sim 0.19$ MA and $\bar{n} \sim 5 \times 10^{19}$ m^{-3}; see also Fig. 4). At $t \sim 40$ ms, the absorbed power $P_{NB}^{abs} \sim 0.8$ MW is close to the injected beam power.

In contrast, set B is characterized by rapid time changes of several plasma parameters. In the initial phase of the discharge, both the plasma current and plasma density are low. This determines the very low level of the absorbed power P_{NB}^{abs} (on the order of tens of kW). The evolution of the toroidal field B is quite different from set A: it decreases by a factor of two reaching the very small value of $B \sim 0.15$ T at the end of the discharge. The Larmor radius r_L of 25-keV ions at such a small B is very large ($r_L \sim 16$ cm) and is comparable with the plasma radius $a \sim 20$–25 cm. This also leads to a high value of P_{NB}^{pt}. As a result, the maximum absorbed power $P_{NB}^{abs} \sim 0.4$ MW is low in spite of the large current $I_p \sim 0.22$ MA and optimal density $\bar{n} \sim 5 \times 10^{19}$ m^{-3} (see Fig. 5d). The low value of P_{NB}^{abs} correlates with a low electron temperature measured in the shots from set B. The time behavior of the fraction of the absorbed power $1 - \alpha_{cx}$ calculated by the analytical expressions presented in the Appendix is shown in Fig. 5e. It is seen that, at the time t = 38–39 ms, the values of $1 - \alpha_c$ are the same for both sets A and B but the absolute values of P_{NB}^{abs} differ by a factor of 2–2.5. It also confirms the important role of the losses due to

poor trajectories for set B with a low magnetic field at the end of the discharge.

6. MODELING OF MAST DISCHARGES

The MAST tokamak typically has the following parameters: $R = 0.7$ m, $a = 0.5$ m, $B = 0.6$ T, and $k = 1.8$. First, we simulate the time evolution of the Ohmic discharges. We ramp up the plasma current to $I_p = 1.5$ MA with the rate $dI_p/dt = 10$ MA s^{-1}. Calculations show that the typical current diffusion time is large (0.3–0.5 s) and approximately equals the typical duration time of the discharge. The central electron and ion temperatures attain the values of $T_e(0) \approx 1.0$–1.4 keV and $T_i(0) \approx 0.5$–0.6 keV and the self-inductance is on the level of $l_i \approx 0.8$. The monotonic profile of the current density (evidence of the absence of the skin effect) is a result of some favorable factors: the neoclassical resistivity and relatively low temperatures at the density $\bar{n} \approx 6 \times 10^{19}$ m^{-3}. However, towards the end of the discharge, $q(0) < 1$ so that sawtooth oscillations can appear.

Next, we discuss the scalings of the plasma parameters. Figure 6 shows the dependence of the energy confinement time τ_E on the density at different currents. At low densities, τ_E increases with density; at high densities, this dependence saturates. The higher the current, the higher the density at which the saturation occurs. The expected maximum τ_E value at a maximum current is 30–35 ms. The energy losses through electrons and ions are comparable; therefore, the saturation of the $\tau_E(\bar{n})$ dependence in MAST is similar to that in conventional tokamaks.

Figure 7 presents the dependences of τ_E and $T_e(0)$ on the total power P_{tot} in the regimes with auxiliary NBI heating, when 60% of the deposited power P_{aux} is absorbed by electrons and 40% is absorbed by ions. A very weak degradation of confinement with increasing the power is seen for these conditions. With the auxiliary power $P_{aux} \approx 5$ MW, the electron temperature increases to $T_e \approx 3$–3.5 keV.

7. CONCLUSION

In this paper, the CPTM is extended to the description of discharges in tight-aspect-ratio tokamaks (so-called "spherical tokamaks"). The analysis of OH discharges from START allowed us to specify the behavior of the anomalous thermal diffusivity of electrons. As a rule, in such discharges, the role of the ion channel in the thermal diffusivity is small. The analysis of NBI START discharges required us to reconsider the expressions for the neoclassical ion thermal diffusivity χ_i^{neo}. As a result, the value of χ_i^{neo} at the plasma periphery was substantially reduced in comparison with the usual Shafranov expression. The detailed modeling of 37 NBI START shots showed a low efficiency of NBI plasma heating at low plasma densities, $\bar{n} < 2 \times 10^{19}$ m^{-3}. At moderate densities, $2 \times 10^{19} < \bar{n} < 4.5 \times 10^{19}$ m^{-3}, and currents of $I_p > 200$ kA, the heating efficiency increases to 80–100% and the energy confinement time τ_E increases to $\tau_E \sim 3$–3.2 ms. At the highest density, $\bar{n} > 5 \times 10^{19}$ m^{-3}, the absorbed power P_{NB}^{abs} decreases again due to peripheral trapping of the beam particles. The energy confinement times for electrons and ions (τ_{Ee} and τ_{Ei}) are close to each other at the moderate plasma density, $\bar{n} \sim 4 \times 10^{19}$ m^{-3}: $\tau_{Ee} \approx \tau_{Ei} \sim 2$ ms. The value of τ_{Ee} increases and τ_{Ei} slightly decreases with increasing the plasma density. Note that the proximity of ion and electron temperatures at high densities, $\bar{n} > 3.5 \times 10^{19}$ m^{-3}, makes it difficult to distinguish experimentally between the ion and electron energy transfer channels and determine τ_{Ee} and τ_{Ei}.

The simulation of shots with different currents shows that the absorbed power increases with increasing the current. It corresponds to the decrease in the deviations of hot-ion trajectories from the magnetic surfaces as the current increases.

The modeling of the set of shots confirms the low value of the absorbed power during a significant phase of the discharge. This is due to the combined effect of the low plasma density, low current, and high density of cold neutrals. The absorption becomes noticeable if the following conditions are satisfied simultaneously: $\bar{n} > 3.5 \times 10^{19}$ m^{-3} and $I_p > 200$ kA.

The modified CPTM is then applied to preliminary calculations of the energy balance in MAST. The main dependences of the plasma parameters on the plasma density in the OH regime are found. The values of the central temperature and τ_E are determined in the case of auxiliary heating with a power up to 5 MW. Conventional tokamaks with a moderate aspect ratio $R/a \sim 3$ and the same minor radius show the same plasma temperature but at a much larger toroidal magnetic field.

It should be noted that the influence of some factors on the discharge and their description in the model remain uncertain. For example, the applicability of the neoclassical conductivity to spherical tokamaks is still unclear. A model for the anomalous ion thermal diffusivity is also not completed, because this requires the creation of a sufficiently large and reliable database for ion temperature profiles. We hope that the new data from MAST, which will begin operating in 2000, will help to solve this problem.

ACKNOWLEDGMENTS

We would like to acknowledge A. Sykes and C.M. Roach for useful discussions. This work was supported in part by the UK Department of Trade and

Industry and Euratom (UKAEA Consultancy Agreement no. GQ13158).

APPENDIX

Estimation of Hot-Ion Losses due to Charge Exchange

First, we estimate *the power related to the shine-through part of the neutral beam.* We assume that the beam particles are trapped by charge exchange and electron ionization and neglect other atomic processes. The e-folding length of the beam trapping is

$$L_{tr} = \frac{1}{\bar{n}\sigma}, \quad \sigma = \sigma_{cx} + \frac{\langle \sigma_i v_e \rangle}{v_0}, \tag{A.1}$$

where σ_{cx} and σ_i are the charge-exchange and electron ionization cross sections, $\bar{n}$ is the line averaged plasma density, and v_0 is the velocity of the beam particles. For a beam energy of $E_0 = 25$ keV and $T_e = 0.2$ keV, we have $\sigma_{cx} = 7.5 \times 10^{-20}$ m^2, $v_0 = 2.15 \times 10^6$ m/s, and $\langle \sigma_i v_e \rangle / v_0 = 1.4 \times 10^{-20}$ m^2; as a result, we obtain $L_{tr} = 1.13/\bar{n}$ m ($\bar{n}$ is in units of 10^{19} m^{-3}). We designate the length of the beam path in the plasma as L, the dimensionless "optical" thickness of the plasma with respect to the beam as $\eta = L/L_{tr}$, and the fraction of the shine-through particles as $\alpha^S = \exp(-\eta)$. In notations of expression (20), we have $P^S_{NB} = \alpha^S P_{NB}$. For START, we have $L \approx 1.0$ m; hence, for $\bar{n} = 2$ (in units of 10^{19} m^{-3}), we obtain $L_{tr} = 0.56$ m, $\eta = 1.8$, and $\alpha^S = 0.16$ and, for $\bar{n} = 4$, we obtain $L_{tr} = 0.28$ m, $\eta = 3.6$, and $\alpha^S = 0.025$. For real plasmas with impurities, the values of α^S should become less due to the excitation of the beam particles and the increase in the charge-exchange and ionization cross sections. For other beam components with energies $E_0/2$ and $E_0/3$, the values of α^S are very small. Thus, for the plasma densities $\bar{n} > 3 \times 10^{19}$ m^{-3}, most of the beam particles are ionized or charge-exchanged in the plasma.

Now, we estimate the role of *hot-ion losses* [the value of α_{cx} in (21)] determined by charge exchange with neutrals. The characteristic charge-exchange time equals $\tau_{cx} = 1/(\sigma_{cx} v_0 n_n)$ s, where n_n is the total neutral density. For $E_0 = 25$ keV, we have $\tau_{cx} = 1/(1.5 n_{n0})$ ms, where n_{n0} is the neutral density (in units of 10^{16} m^{-3}).

The characteristic time of energy transfer from hot ions to electrons is

$$\tau_{E_{0e}} = \frac{3}{8(2\pi)^{1/2}} \frac{T_e^{3/2}}{n e^4 (m_e)^{1/2} \lambda} = 63 \frac{(T_e \text{ keV})^{3/2}}{n(10^{19} \text{ m}^{-3})} \text{ (ms)}. \tag{A.2}$$

Here, $\lambda = 15$ is the Coulomb logarithm.

The fraction α_{cx} of the hot-ion losses due to charge exchange is determined as

$$\alpha_{cx} = \frac{\tau_{E_{0e}}}{\tau_{E_{0e}} + \tau_{cx}} = \frac{\xi}{1+\xi}, \quad \text{where } \xi = \tau_{E_{0e}}/\tau_{cx} = 10^2 \frac{n_{n0} T_e^{3/2} \text{ (keV)}}{n(10^{19} \text{ м}^{-3})}. \tag{A.3}$$

The total neutral density averaged along the plasma torus consists of four components: $n_n = n_b + n_{bs} + n_w + n_h$, where n_b is the beam neutral density, n_{bs} is the density of secondary hot neutrals, n_w is the density of cold wall neutrals, and n_h is the "halo" neutral density of warm particles.

We first estimate *the averaged beam neutral density* n_b. The effective length of the beam trajectory in the plasma is determined by equation (A.1). For a tangential trajectory, the average value of the beam neutral density along the magnetic axis is equal to $n_b = n_b^0 (1 - 1/e) L_{tr}/(2\pi R) = n_b^0 0.6L/(2\pi\eta R)$, where n_b^0 is the beam neutral density at the input of the beam into the plasma: $n_b^0 = P_{NB}/(E_0 v_0 S)$. Here, P_{NB} is the total beam power and S is the beam cross-section area. For START conditions ($P_{NB} = 0.5$ MW, $R = 0.3$ m, and $S = 0.02$ m^2), we obtain $n_b^0 = 3 \times 10^{15}$ m^{-3}. For a tight-aspect-ratio tokamak, we have $L \sim 2\sqrt{3} R$, so that $n_b = n_b^0/(2\sqrt{3}\eta)$. For START at $\bar{n} = 2$, we obtain $\eta = 1.8$ and $n_b = n_b^0/6 = 0.05 \times 10^{16}$ m^{-3} and, at $\bar{n} = 4$, we obtain $\eta = 3.6$ and $n_b = n_b^0/12 \sim 0.025 \times 10^{16}$ m^{-3}.

The density of the secondary hot neutrals n_{bs} is low as compared to the other components, and we do not consider it further.

Next, we consider *the density of cold wall neutrals*, n_w. In the 1D diffusion approximation, taking into account multiple charge exchange with the plasma ions and electron ionization, the e-folding length of relaxation of this density, L_c, has the form [11]

$$L_c = \frac{v_i}{(3\nu\nu_3)^{1/2}}, \text{ where } v_i \text{ is the ion thermal velocity,} \quad \nu = \nu_1 + \nu_3, \quad \nu_1 = \sigma_{cx} v_i n, \quad \nu_3 = \langle \sigma_i v_e \rangle n. \tag{A.4}$$

For $T_e \sim T_i \sim 0.2$ keV, we have $\sigma_{cx} = 3 \times 10^{-19}$ m^2, $v_i = 2 \times 10^5$ m/s, $\langle \sigma_i v_e \rangle = 3 \times 10^{-14}$ m^3 s^{-1}, $\nu_3 = 0.52\nu_1$, $\nu = \nu_1 + \nu_3 = 1.5\nu_1$. From here, we obtain $L_c = 0.22/\bar{n}$ m ($\bar{n}$ is in units of 10^{19} m^{-3}) and $\lambda = a/L_c = a\bar{n}/0.22$, where λ is the optical thickness of the plasma with respect to cold neutrals. For $\bar{n} = 2$ and $a = 0.25$ m, we have $\lambda = 2.28$ and, for $\bar{n} = 4$, we have $\lambda = 4.56$. In the latter case, the cold neutral density in the center is a fac-

Estimates of the densities of the different neutral components in the plasma core for $n_w = 2 \times 10^{17}$ m^{-3} (at the edge), $P_{NB} = 0.5$ MW, and $T_e = 0.25$ keV

$\bar{n}$, 10^{19} m^{-3}	n_b, 10^{16} m^{-3}	n_w, 10^{16} m^{-3}	n_h, 10^{16} m^{-3}	n_n, 10^{16} m^{-3}	$1 - \alpha_{cx}$
2	0.05	6	0.3	6.35	0.025
4	0.025	0.6	0.15	0.78	0.28
6	0.016	0.06	0.08	0.14	0.75

tor of ten less than in the former. In real plasma geometry, the cold neutral density in the center, $n_w(0)$, is several times greater than that following from the solution to the plane problem for a semi-infinite plasma. Approximately, we can write $n_w(0) = gn_w(a)\exp(-\lambda)$, where $g \approx 2$–3 is a geometrical factor describing the transformation from plane geometry to the real plasma with an elongated cross section. We set the cold neutral density at the edge as $n_w(a) = 2 \times 10^{17}$ m^{-3} [10]. For $\bar{n} = 2$, assuming $g = 3$, we obtain $n_w(0) = 0.6 \times 10^{17}$ m^{-3}; for $\bar{n} = 4$, we have $n_w(0) = 0.06 \times 10^{17}$ m^{-3}.

Finally, we discuss *the halo neutral density*, n_h. In the 1D plane geometry and in the diffusive approximation, the equation for n_h is as follows [11]:

$$d^2n_h/dx^2 - (3\nu\nu_3/v_i^2)n_h = -(3\nu/v_i^2)S_h, \quad 0 < x < a, \tag{A.5}$$

where S_h [m^{-3} s^{-1}] is the source of warm neutrals due to charge exchange of beam neutral particles with the plasma ions. Hence, we have $S_h = q_{cx}/V$, where q_{cx} is the total number of charge-exchanged beam particles per second, V is an effective volume, $q_{cx} = (\nu_1/\nu)q_{NB}$, and

$$q_{NB}[\mathrm{s}^{-1}] = P_{NB}/E_0 = P_{NB}[\mathrm{MW}]/E_0[\mathrm{keV}] \times 10^{22}. \tag{A.6}$$

At the medium plasma density, $\bar{n} \sim 3 \times 10^{19}$ m^{-3}, the source q_{NB} is localized in a torus T_Δ with the major radius R and minor radius $\Delta \ll a$, where Δ is the effective radius of the beam. The effective volume of this torus is $V = 2\pi R\pi\Delta^2$. The halo neutral density is only interesting inside this torus because, outside it, the density of the wall neutrals is much higher than the halo neutral density. We solve (A.5) with the boundary condition $dn_h/dx = 0$ at $x = 0$ and require that n_h decreases with increasing x. For a solution that is smooth at $x = \Delta$, we obtain

$$n_h = (S_h\Delta/v_i)(3\nu/\nu_3)^{1/2}\exp((\Delta - x)(3\nu\nu_3/v_i^2)^{1/2}).$$

Thus, in the plasma core (inside the torus T_Δ), for $\nu/\nu_3 \approx 3$ and $T_e \sim T_i \sim 0.2$ keV ($x \le \Delta$), we obtain $n_h = (S_h\Delta/v_i)(3\nu/\nu_3)^{1/2} \approx 3(S_h\Delta/v_i)$. For START, we have $\Delta \approx 0.1$ m and $\nu_1/\nu = 0.8$. Thus, $q_{NB} = 1.3 \times 10^{20}$ s^{-1} and $S_h\Delta = q_{cx}\Delta/V = 2 \times 10^{20}$ m^{-2} s^{-1}. Hence, in the plasma core at the medium plasma density, we obtain $n_h \sim 0.3 \times 10^{16}$ m^{-3}. At large plasma densities ($\bar{n} > 3 \times 10^{19}$ m^{-3}), the neutral beam is partially damped before it reaches the torus T_Δ. In this case, we have to replace P_{NB} in (A.6) with $P_{NB}^d = P_{NB}\exp(-d/L_{tr}) \approx P_{NB}\exp(-0.2n_p)$, where $d \sim 0.2$ m is the distance between the plasma boundary and the torus T_Δ along the beam trajectory and n_p is the average plasma density outside the torus T_Δ. As a result, we obtain $n_h \sim 0.3\exp(-0.2n_p) \times 10^{16}$ m^{-3}.

To estimate *the absolute value of the wall neutral density*, we first find the influx of cold neutrals, P_n, that is needed to supply the very large experimental value of $dN/dt \sim 2 \times 10^{21}$ s^{-1} for shot nos. 35574–35592 (see Section 5.3). Here, N is the total number of particles in the plasma. The equation of particle balance is as follows: $dN/dt = P - N/\tau_p$, where $P = (1 - \alpha)P_n$ is the total source of charged particles, P_n is the total influx of neutrals, α is the plasma albedo with respect to cold neutrals, and τ_p is the particle confinement time. It is natural to choose $\alpha = 0.5$ and $\tau_p = 2\tau_E = 4$ ms, where $\tau_E = 2$ ms is a reasonable estimate of the energy confinement time. As a result, we obtain $P_n = (dN/dt + N/\tau_p)/(1 - \alpha)$ and $Q_n = P_n/S$, where Q_n is the specific influx of cold neutrals. Setting $N = nV_p = 2.5 \times 10^{19}$ (where $n = 5 \times 10^{19}$ m^{-3} is the volume-averaged plasma density, $V_p = 0.5$ m^3 is the plasma volume, $dN/dt = 2 \times 10^{21}$ s^{-1}, and $S = 3.5$ m^2), we obtain $P_n \cong 1.5 \times 10^{22}$ s^{-1} and $Q_n = 4.5 \times 10^{21}$ m^{-2} s^{-1}.

For START, the ratio V_p/V_c (where V_c is the volume of the vacuum chamber) is very small. As a result, the density of neutrals near the wall is very high and the average energy of cold neutrals at the plasma edge is low, $T_n(a) \sim 2$ eV. Using the expressions $Q_n = n_n v_T$ for the neutral density at the plasma edge, we obtain $n_n = 2 \times 10^{17}$ m^{-3}. This is consistent with the estimates for START in [10] but is one order of magnitude larger than the neutral density in conventional tokamaks.

The table presents the neutral densities of each component in the plasma core at different plasma densities. The total neutral density n_n is also included. The last column shows the value of $1 - \alpha_{cx}$ (the fraction of the captured NBI power, P_{NB}^{capt}). At the low plasma density,

$\bar{n} = 2$, only 2% of P_{NB}^{capt} is absorbed. For the high plasma density, $\bar{n} = 6$, this fraction increases to 75%.

REFERENCES

1. D. C. Robinson, Plasma Phys. Controlled Fusion **41**, A143 (1999).
2. A. Sykes, Phys. Plasmas **4**, 1665 (1997).
3. M. Gryaznevich, R. Akers, P. G. Carolan, *et al.*, Phys. Rev. Lett. **80**, 3972 (1998).
4. A. Sykes, A. Akers, L. Appel, *et al.*, Plasma Phys. Controlled Fusion **39**, Suppl. 12B, B247 (1997).
5. Yu. N. Dnestrovskij, E. L. Berezovskiĭ, S. E. Lysenko, *et al.*, Nucl. Fusion **31**, 1877 (1991).
6. Yu. N. Dnestrovskij, S. E. Lysenko, and K. N. Tarasyan, Nucl. Fusion **35**, 1047 (1995).
7. C. M. Roach, Plasma Phys. Controlled Fusion **38**, 2187 (1996).
8. V. D. Shafranov, At. Énerg. **19**, 120 (1965).
9. B. B. Kadomtsev, Fiz. Plazmy **13**, 251 (1987) [Sov. J. Plasma Phys. **13**, 443 (1987)].
10. R. J. Akers, P. G. Carolan, N. J. Conway, *et al.*, *Proceedings of 25th European Conference on Controlled Fusion and Plasma Physics, Prague, 1998* [ECA **22C**, 2014 (1998)].
11. Yu. N. Dnestrovskij and D. P. Kostomarov, *Numerical Simulation of Plasmas* (Nauka, Moscow, 1993; Springer-Verlag, New York, 1986).

Translated by the authors

Plasma Physics Reports, Vol. 26, No. 7, 2000, pp. 550–559. Translated from Fizika Plazmy, Vol. 26, No. 7, 2000, pp. 590–599.

MAGNETIC CONFINEMENT SYSTEMS

Pseudosymmetry Near a Magnetic Surface in a Plasma Confinement System

A. A. Skovoroda

Institute of Nuclear Fusion, Russian Research Centre Kurchatov Institute, pl. Kurchatova 1, Moscow, 123182 Russia

Received September 23, 1999; in final form, December 23, 1999

Abstract—The possibility is demonstrated of finding vacuum equilibrium magnetic configurations with an exactly pseudosymmetric nonparaxial boundary magnetic surface in the vicinity of which the pseudosymmetry condition is satisfied approximately. Equations are derived for calculating the boundary surface from a prescribed particular dependence of the magnetic field strength in special magnetic flux coordinates. In calculations, magnetic coordinates serve as ordinary angular coordinates, while their "magnetic" character is specified by additional integral conditions. As an example, a "tubular" orthogonal magnetic surface is calculated analytically. *© 2000 MAIK "Nauka/Interperiodica".*

1. INTRODUCTION

The search for the optimum magnetic configurations from the standpoint of steady-state confinement of hot high-pressure fusion plasmas is largely based on the analysis of the topography of the magnetic field strength B on an equilibrium magnetic surface [1–6]. The magnetic field strength should satisfy certain necessary conditions, which can be written most simply in *special* magnetic flux coordinates. As an example, we can mention the familiar Boozer [1, 2] and Mikhaĭlov [3] conditions under which there are no "superbanana" losses in stellarators. The Boozer condition for quasisymmetric stellarators has the form $B = B(\Phi, \theta_B)$, where Φ is the toroidal magnetic flux and θ_B is the Boozer poloidal angle coordinate. The Mikhaĭlov condition for pseudosymmetric stellarators is $B = B(\Phi, \theta)$, where θ is the poloidal angle in any flux coordinates with straightened field lines (SFL). The Mikhaĭlov condition is less restrictive because the Boozer coordinates are a particular case of coordinate systems with SFL.

The general pseudosymmetry condition is represented as [5]

$$\frac{[\mathbf{B}\nabla\rho]\nabla B}{\mathbf{B}\nabla B} = f, \tag{1}$$

where f is a bounded function of the flux coordinates, $\mathbf{B}$ is the magnetic field vector, and ρ is an arbitrary magnetic surface label. Depending on the choice of f, we can formulate different requirements (in addition to the above two requirements for stellarators) for the magnetic field geometry, which would improve to a greater or lesser extent plasma confinement. The requirement $f = 0$ (known as the isodynamic or orthogonality condition, since it implies that $B = B(\rho)$ or that the magnetic field lines are orthogonal to the B = const contours on a magnetic surface [7, 8]) makes the configuration an ideal geometry for confining plasmas, because the drift surfaces of charged particles coincide with the magnetic surfaces. Unfortunately, this requirement, which completely eliminates neoclassical transverse transport and secondary longitudinal plasma currents, limiting the maximum possible β values consistent with equilibrium, can only be achieved in the vicinity of a straight magnetic axis in open systems or in tokamaks with "exotic" current distributions. The requirement $f = f(\rho)$ (known as the quasisymmetry condition for closed confinement systems with irrational rotational transforms, because it ensures, as in the symmetric case, the existence of the integral of drift motion in a certain spatial region [9, 10]) indicates a tokamak-like confinement and is characteristic of a new generation of stellarators. Confinement systems with closed magnetic field lines provide a wider choice: $f = f(\rho, \lambda)$; i.e., the function f can depend not only on the magnetic surface label ρ but also on the magnetic field line label λ (this generalization is a consequence of the isometric character of a magnetic confinement system [6]). The pseudosymmetry condition implies merely that the function f should be bounded, in which case superbanana drift orbits are eliminated, although the integral of motion is absent [3].

By an appropriate choice of the special magnetic flux coordinates, we can reduce the general condition (1) to a restriction on the behavior of the magnetic field strength on a magnetic surface. This is easily seen from the two familiar representations of the magnetic field in arbitrary flux coordinates [11],

$$\begin{aligned} 2\pi\mathbf{B} &= [\nabla\Phi\nabla\theta] + [\nabla\Psi\nabla\zeta] + [\nabla\rho\nabla\eta], \\ 2\pi\mathbf{B} &= J\nabla\theta + F\nabla\zeta - \nu\nabla\rho + \nabla\tilde{\varphi}. \end{aligned} \tag{2}$$

1063-780X/00/2607-0550$20.00

Here, we use the standard notation adopted in the literature: $J(\rho)$ is the toroidal current; $\Phi(\rho)$ is the toroidal magnetic flux; $F(\rho)$ is the *external* poloidal current; $\Psi(\rho)$ is the *external* poloidal magnetic flux; and $\tilde{\varphi}$, η, and ν are periodic equilibrium coordinate-dependent functions of the arbitrary angular variables θ and ζ. For simplicity, we consider vacuum ($\nu = 0$ and $F = \text{const}$) magnetic fields in the absence of toroidal currents ($J = 0$). We choose the *special* coordinates θ_B and ζ_B on the magnetic surfaces so as to drive to zero the periodic functions $\tilde{\varphi}$ and η (this choice corresponds to magnetic coordinates with SFL or to Boozer coordinates). As a result, we obtain

$$\begin{aligned} 2\pi\mathbf{B} &= [\nabla\Phi\nabla\theta_B] - \mu[\nabla\Phi\nabla\zeta_B], \\ 2\pi\mathbf{B} &= F\nabla\zeta_B, \end{aligned} \tag{3}$$

where $\mu(\rho) = -\psi'/\Phi'$ is the rotational transform and the prime denotes the derivative with respect to ρ. To simplify the presentation, it is convenient to switch to a new flux coordinate system:[1] Φ, $\theta = \theta_B - \mu\zeta_B$ and $\zeta = \zeta_B$. In the new coordinates, the divergence and curl of the vacuum magnetic field $\mathbf{B}$ expressed simultaneously in the two forms,

$$\begin{aligned} 2\pi\mathbf{B} &= [\nabla\Phi\nabla\theta], \\ 2\pi\mathbf{B} &= F\nabla\zeta, \end{aligned} \tag{4}$$

are both identically zero. Taking the denominator and numerator in (1) with the first and second representations of the field in (4), respectively, and accounting for the redefinition of the function f puts the pseudosymmetry condition (1) in the form

$$\hat{L}B = 0, \tag{5}$$

where $\hat{L} = \dfrac{\partial}{\partial\theta} + f\dfrac{\partial}{\partial\zeta}$ is the surface operator.

Since the pseudosymmetry condition (1) refers to a magnetic surface, it is possible to optimize the magnetic configuration layer by layer. Actually, in order for a plasma to be well confined in a closed magnetic system, it is necessary to satisfy condition (1) over a fairly narrow boundary layer inside of which the local low transverse transport plays the role of a barrier that acts to reduce the losses from the central plasma regions. The possibility of such a "layer-by-layer" optimization is especially important for three-dimensional magnetic confinement systems, because the isometry (orthogonality and quasisymmetry) conditions [6] can be satisfied only asymptotically in a local region around a certain magnetic surface in the plasma column.

However, the question arises of how to use the pseudosymmetry condition (1) in the search for good confinement systems. It seems that the most straightforward way is to specify the magnetic field strength $B = B(\theta, \zeta)$ so as to satisfy condition (5) and to calculate the magnetic surface in the inverted variables $\mathbf{r} = \mathbf{r}(\theta, \zeta)$. This problem is the inverse of the familiar problem of unambiguously determining the magnetic field from a prescribed closed vacuum magnetic surface (see, e.g., [12]). Here, we examine the possibility of studying this reverse problem, in which the special magnetic coordinates θ and ζ serve in calculations as ordinary angular coordinates varying from 0 to 2π. We consider only vacuum magnetic configurations. Our paper is organized as follows. In Section 2, we analyze specific features of the description of magnetic configurations in the inverted variables, in which case the formulation of the boundary conditions requires separate consideration. Taking as an example the familiar orthogonal system with a straight magnetic axis, we demonstrate how the reverse problem can be solved in the paraxial approximation by using the special magnetic coordinates as conventional coordinates. In Section 3, we formulate the reverse problem of calculating an exactly pseudosymmetric boundary magnetic surface and satisfying the pseudosymmetry condition approximately in its immediate vicinity. As an example, in Section 4, we apply the equations derived to calculate a possible periodic tubular orthogonal magnetic surface.

2. SPECIFIC FEATURES OF THE DESCRIPTION OF MAGNETIC CONFIGURATIONS IN THE INVERTED VARIABLES

We are interested in three-dimensional steady-state vacuum magnetic configurations with a zero toroidal plasma current J. In order for the plasma to be confined as a whole, it is necessary for there to be a closed (periodic) equilibrium boundary magnetic surface. On the other hand, we do not require the existence of magnetic surfaces over the entire confinement region, because the problem under discussion implies that the special magnetic flux coordinates can be introduced only near the boundary surface. This possibility allows us to solve the reverse problem, i.e., to calculate the boundary surface from a prescribed dependence of the magnetic field strength on the magnetic variables. Then, the magnetic field in the region enclosed by the boundary surface can be calculated by solving a direct problem without introducing flux coordinates.

To do this, we turn to (4) to derive the inverted magnetic equations for Cartesian coordinates $\mathbf{r} = \mathbf{r}(\Phi, \theta, \zeta)$. Using the definitions of the basis vectors,

$$\mathbf{e}_1 = \frac{\partial\mathbf{r}}{\partial\Phi} = \sqrt{g}[\nabla\theta\nabla\zeta], \quad \mathbf{e}_2 = \frac{\partial\mathbf{r}}{\partial\theta} = \sqrt{g}[\nabla\zeta\nabla\Phi],$$

[1] For simplicity, this coordinate system is not distinguished by an additional index; here and below (unless otherwise stated), all coordinates without indices refer to this special coordinate system.

$$\mathbf{e}_3 = \frac{\partial \mathbf{r}}{\partial \boldsymbol{\zeta}} = \sqrt{g}[\nabla\Phi\nabla\theta],$$
$$\mathbf{e}^1 = \nabla\Phi = \frac{[\mathbf{e}_2\mathbf{e}_3]}{\sqrt{g}}, \quad \mathbf{e}^2 = \nabla\theta = \frac{[\mathbf{e}_3\mathbf{e}_1]}{\sqrt{g}}, \tag{6}$$
$$\mathbf{e}^3 = \nabla\zeta = \frac{[\mathbf{e}_1\mathbf{e}_2]}{\sqrt{g}}, \quad \sqrt{g} = \frac{\partial \mathbf{r}}{\partial\Phi}\left[\frac{\partial \mathbf{r}}{\partial\theta}\frac{\partial \mathbf{r}}{\partial\zeta}\right],$$

we obtain the inverted analogues of (4):

$$2\pi\mathbf{B} = \frac{1}{\sqrt{g}}\frac{\partial \mathbf{r}}{\partial \boldsymbol{\zeta}}, \quad 2\pi\mathbf{B} = \frac{F}{\sqrt{g}}\left[\frac{\partial \mathbf{r}}{\partial\boldsymbol{\Phi}}\frac{\partial \mathbf{r}}{\partial\boldsymbol{\theta}}\right]. \tag{7}$$

We equate the field representations (7) to arrive at the fundamental vector magnetic relation

$$\mathbf{r}_\zeta = F[\mathbf{r}_\Phi\mathbf{r}_\theta]. \tag{8}$$

Here and below, the subscripts refer to the corresponding partial derivatives. For further analysis, we need some relationships between the metric tensor elements $g_{ik} = \mathbf{e}_i\mathbf{e}_k$, which can be easily obtained by taking the scalar product of (8) with different basis vectors:

$$g_{23} = g^{23} = g_{13} = g^{13} = 0,$$
$$g_{33} = \frac{1}{g^{33}}, \quad g_{22} = \frac{1}{g^{22}}, \quad \frac{g_{33}}{F} = \sqrt{g}. \tag{9}$$

The magnetic field strength can be found by taking the scalar product of the two representations in (7):

$$B^2 = \frac{F}{4\pi^2\sqrt{g}} = \frac{F^2}{4\pi^2 g_{33}}. \tag{10}$$

Equations (8) can also be represented as

$$z_\Phi = -\frac{1}{F}\frac{x_\Phi x_\zeta + y_\Phi y_\zeta}{x_\Phi y_\theta - x_\theta y_\Phi},$$
$$z_\theta = -\frac{1}{F}\frac{x_\theta x_\zeta + y_\theta y_\zeta}{x_\Phi y_\theta - x_\theta y_\Phi}, \tag{11}$$
$$z_\zeta = -F(x_\theta y_\Phi - x_\Phi y_\theta).$$

Equating the second derivatives of z found by differentiating different pairs of the set (11) yields the consistency conditions for this set in the form of elliptic equations:

$$\frac{1}{F^2}\frac{\partial^2 x}{\partial\zeta^2} + \frac{\partial}{\partial\Phi}\left(g_{22}\frac{\partial x}{\partial\Phi} - g_{12}\frac{\partial x}{\partial\theta}\right)$$
$$+ \frac{\partial}{\partial\theta}\left(g_{11}\frac{\partial x}{\partial\theta} - g_{12}\frac{\partial x}{\partial\Phi}\right) = 0,$$
$$\frac{1}{F^2}\frac{\partial^2 y}{\partial\zeta^2} + \frac{\partial}{\partial\Phi}\left(g_{22}\frac{\partial y}{\partial\Phi} - g_{12}\frac{\partial y}{\partial\theta}\right) \tag{12}$$
$$+ \frac{\partial}{\partial\theta}\left(g_{11}\frac{\partial y}{\partial\theta} - g_{12}\frac{\partial y}{\partial\Phi}\right) = 0.$$

The same equation can also be obtained for the z-coordinate.[2]

In order to demonstrate an important aspect of the solution of problems associated with magnetic configurations by using the inverted equations (12), we consider a straight axisymmetric magnetic confinement system. The cylindrical symmetry of the problem allows us to seek a solution in the form $x = r(\Phi, \zeta)\cos\theta$, $y = r(\Phi, \zeta)\sin\theta$, and $z = z(\Phi, \zeta)$, in which case the metric coefficients are found to be $g_{12} = 0$, $g_{22} = r^2$, and $g_{11} = r_\Phi^2 + \frac{1}{F^2}\frac{r_\zeta^2}{r^2}$. In determining g_{11}, we used the first equation in (11). Equations (12) can be transformed to

$$\frac{\partial}{\partial\Phi}r\frac{\partial r}{\partial\Phi} + \frac{1}{F^2}\frac{\partial}{\partial\zeta}\frac{1}{r}\frac{\partial r}{\partial\zeta} = 0,$$
$$\frac{\partial}{\partial\Phi}r^2\frac{\partial z}{\partial\Phi} + \frac{1}{F^2}\frac{\partial^2 z}{\partial\zeta^2} = 0, \tag{13}$$

which coincide with the equations derived in [13, 14]. It is noteworthy that the first equation in (13) contains the only unknown function r. An important feature of these equations is associated with the procedure for imposing the boundary conditions, i.e., the specification of the boundary magnetic surface in special magnetic flux coordinates. However, since these coordinates still remain unknown, the procedure for imposing the boundary conditions requires separate consideration. This problem is the main subject of our study. In contrast to the direct magnetic problem, which is based on a single equation for the magnetic potential and in which it is a simple matter to impose the boundary conditions, the reverse magnetic problem is much more complicated because of the larger number of equations and the difficulties in formulating the boundary conditions.

One way of choosing the boundary conditions is to use the paraxial approximation. Note that any closed curve can be a magnetic field line along which a periodic dependence of the magnetic field strength B_0 can be specified in an arbitrary fashion. Consequently, assuming that this curve is a magnetic axis ($\Phi = 0$), we can specify the axis itself and the magnetic field strength along the axis in special magnetic coordinates,

[2] Note that equations (12) can also be derived in a simpler way, namely, by writing the trivial (in Cartesian coordinates) relationships $\Delta x \equiv 0$, $\Delta y \equiv 0$, and $\Delta z \equiv 0$ in the above special magnetic flux coordinates with the help of the familiar formula for transforming the Laplace operator $\Delta = \frac{1}{\sqrt{g}}\frac{\partial}{\partial x^i}\left(\sqrt{g}g^{ik}\frac{\partial}{\partial x^k}\right)$. Analogously, the inverted expressions (7) for the magnetic fields can be obtained from the identities $\mathbf{B} \equiv (\mathbf{B}\nabla)\mathbf{r}$ and $\mathbf{B} \equiv -1/2[[\mathbf{B}\nabla]\mathbf{r}]$, while relationship (8) can be found from the equations $\frac{dx}{B_x} = \frac{dy}{B_y} = \frac{dz}{B_z} = \frac{dl}{B}$ for the magnetic field lines.

just as in ordinary angular coordinates. For example, for a straight magnetic axis, we have $x = y = 0$, $z = z(\zeta)$, and $B_0 = B_0(\zeta)$. Then, equations (11) are solved by expanding the Cartesian coordinates in powers of the magnetic flux $\Phi \ll 1$ under different *a priori* assumptions regarding the symmetry and periodicity conditions written in special magnetic coordinates. For magnetic configurations with closed field lines (i.e., configurations with a rational rotational transform $\mu = n/m$), writing the periodicity condition in the special magnetic coordinates (θ, ζ) presents no difficulties because ζ changes along the field lines and θ serves to label them. Magnetic configurations in which the magnetic field lines do not close on themselves (i.e., configurations with an irrational rotational transform μ) should be described in Boozer coordinates (θ_B, ζ_B), which are well suited for writing the periodicity conditions. In the above equations, the transition from one coordinate system to another is described by the simple relationships

$$\frac{\partial}{\partial\theta} = \frac{\partial}{\partial\theta_B}, \quad \frac{\partial}{\partial\zeta} = \frac{\partial}{\partial\zeta_B} + \mu\frac{\partial}{\partial\theta_B},$$
$$g_{22} = g_{22}^B, \quad g_{23} = g_{23}^B + \mu g_{22}^B = 0, \tag{14}$$
$$g_{33} = g_{33}^B + 2\mu g_{23}^B + \mu^2 g_{22}^B = g_{33}^B - \mu^2 g_{22}^B.$$

For example, in Boozer coordinates, equations (11) become

$$z_\Phi = -\frac{1}{F}\left[\frac{x_\Phi x_{\zeta_B} + y_\Phi y_{\zeta_B}}{x_\Phi y_{\theta_B} - x_{\theta_B} y_\Phi} + \mu\frac{x_\Phi x_{\theta_B} + y_\Phi y_{\theta_B}}{x_\Phi y_{\theta_B} - x_{\theta_B} y_\Phi}\right],$$

$$z_\theta = -\frac{1}{F}\left[\frac{x_{\theta_B} x_{\zeta_B} + y_{\theta_B} y_{\zeta_B}}{x_\Phi y_{\theta_B} - x_{\theta_B} y_\Phi} + \mu\frac{x_{\theta_B}^2 + y_{\theta_B}^2}{x_\Phi y_{\theta_B} - x_{\theta_B} y_\Phi}\right], \tag{15}$$
$$z_{\zeta_B} = -F(x_{\theta_B} y_\Phi - x_\Phi y_{\theta_B})$$
$$+ \frac{\mu}{F}\left[\frac{x_{\theta_B} x_{\zeta_B} + y_{\theta_B} y_{\zeta_B}}{x_\Phi y_{\theta_B} - x_{\theta_B} y_\Phi} + \mu\frac{x_{\theta_B}^2 + y_{\theta_B}^2}{x_\Phi y_{\theta_B} - x_{\theta_B} y_\Phi}\right],$$

and the operator $\hat{L}$ in the pseudosymmetry condition (5) has the form $\hat{L} = (1 + \mu f)\frac{\partial}{\partial\theta_B} + f\frac{\partial}{\partial\zeta_B}$.

Let us derive, as an example, the *orthogonality* equation ($f = 0$) in the vicinity of a straight magnetic axis. Intuitively, from the geometric viewpoint, we can seek the desired solution (15) in the form

$$x = \sqrt{\Phi}(a(\zeta_B)\cos\delta(\zeta_B)\cos(\theta_B + \alpha(\zeta_B))$$
$$+ b(\zeta_B)\sin\delta(\zeta_B)\sin(\theta_B + \alpha(\zeta_B))),$$
$$y = \sqrt{\Phi}(b(\zeta_B)\cos\delta(\zeta_B)\sin(\theta_B + \alpha(\zeta_B)) \tag{16}$$
$$- a(\zeta_B)\sin\delta(\zeta_B)\cos(\theta_B + \alpha(\zeta_B))),$$

which implies that the cross sections of the magnetic surfaces are ellipses with a ratio of a/b of the semiaxes that are rotating at a rate δ around the magnetic axis. The angle α reflects the fact that a magnetic field line and an ellipse rotate at different rates. Substituting (16) into (15) yields

$$z_\Phi = -\frac{1}{Fab}\left[aa_{\zeta_B}\cos^2(\theta_B + \alpha) + bb_{\zeta_B}\sin^2(\theta_B + \alpha)\right.$$
$$\left. + \frac{1}{2}(b^2 - a^2)(\alpha_{\zeta_B} + \mu)\sin 2(\theta_B + \alpha)\right],$$
$$z_{\theta_B} = -\frac{2\Phi}{Fab}\left[\frac{1}{2}(bb_{\zeta_B} - aa_{\zeta_B})\sin 2(\theta_B + \alpha)\right. \tag{17}$$
$$+ (b^2 - a^2)(\alpha_{\zeta_B} + \mu)\cos^2(\theta_B + \alpha)$$
$$\left. + (b^2 + a^2)(\alpha_{\zeta_B} + \mu) - ab\delta_{\zeta_B}\right],$$
$$z_{\zeta_B} = \frac{F}{2}ab + O(\Phi).$$

The requirement for the second expression in (17) to be periodic in θ_B yields the relationship $(b^2 + a^2)(\alpha_{\zeta_B} + \mu) - ab\delta_{\zeta_B} = 0$, and formula (10) taken with $\Phi = 0$ gives the magnetic field at the axis, $B_0 = \frac{1}{\pi ab}$. In the desired order of smallness, solution (17) can be represented as

$$z = \frac{F}{2}\int abd\zeta_B - \frac{\Phi}{Fab}[aa_{\zeta_B}\cos^2(\theta_B + \alpha)$$
$$+ bb_{\zeta_B}\sin^2(\theta_B + \alpha) \tag{18}$$
$$\left. + \frac{1}{2}(b^2 - a^2)(\alpha_{\zeta_B} + \mu)\sin 2(\theta_B + \alpha)\right].$$

Expressions (16) and (18) make it possible to investigate the possibility of satisfying the orthogonality condition (5). Taking into account (10) and (14), we can rewrite (5) in the form $(g_{33}^B - \mu^2 g_{22}^B)_{\theta_B} = 0$. At the axis, where $\Phi = 0$, this condition is identically satisfied. We present the requirements for the magnetic configuration under which the orthogonality condition is satisfied near the magnetic axis through first order in $\Phi \ll 1$. We must drive to zero the coefficients in front of the sine and cosine functions in the orthogonality condition taken with (16) and (18). As a result, we arrive at the relationships

$$\delta_{\zeta_B} = \text{const} \times \frac{ab(a^2 + b^2)}{(a^2 - b^2)^2},$$
$$a_{\zeta_B}^2 - b_{\zeta_B}^2 - ab\left(\frac{aa_{\zeta_B} - bb_{\zeta_B}}{ab}\right)_{\zeta_B} \tag{19}$$
$$+ \frac{(a^2 - b^2)\delta_{\zeta_B}^2(a^4 + 6a^2b^2 + b^4)}{(a^2 + b^2)^2}.$$

We simplify (19) by switching from ζ_B to a new coordinate, $z_0 = \frac{F}{2}\int ab\, d\zeta_B$, along the magnetic axis. Let the derivative with respect to z_0 be denoted by the prime. Then, relationships (19) take the form

$$\delta' = \text{const} \times \frac{a^2 + b^2}{(a^2 - b^2)^2},$$
$$aa'' - bb'' - C^2\frac{a^4 + 6a^2b^2 + b^4}{(a^2 - b^2)^3} = 0, \quad (20)$$

where the constants C and F are determined from the periodicity conditions $\int_0^L \delta' dz_0 = \pi$ and $\frac{F}{2}\int_0^{2\pi} ab\, d\zeta_B = L$ with L the period of the confinement system along the magnetic axis. Note that, for $C \neq 0$, relationships (20) coincide with the similar relationships derived by Lortz and Nührenberg [15]. Setting $C = 0$ gives the familiar orthogonality condition for open systems with a zero rotational transform [16, 17]. Specific periodic solutions to equations (20) for magnetic systems with both zero and nonzero rotational transforms are known.

The example analyzed above reveals two important aspects. First, from the standpoint of calculations, the special angular magnetic coordinates introduced here do not differ from ordinary angular coordinates. Second, we choose an exactly pseudosymmetric magnetic axis ($\Phi = 0$) and satisfy the pseudosymmetry condition (5) asymptotically in its vicinity ($\Phi \ll 1$). In the next section, we extend this approach to magnetic surfaces; specifically, we calculate an exactly pseudosymmetric magnetic surface $\Phi = \Phi_0$ and satisfy the pseudosymmetry condition (5) asymptotically in its vicinity (for $\Phi - \Phi_0 = d\Phi \ll 1$).

3. PSEUDOSYMMETRY NEAR A MAGNETIC SURFACE

In contrast to the paraxial approximation, we cannot specify a magnetic surface in the form $\mathbf{r} = \mathbf{r}(\theta, \zeta)$ independently of the magnetic field strength $B = B(\theta, \zeta)$ on it. This can be seen, e.g., from the first field representation in (7), which, with allowance for (9), unambiguously determines the magnetic field from the magnetic surface specified in the form $\mathbf{r} = \mathbf{r}(\theta, \zeta)$. However, it is also necessary to satisfy the second field representation in (7). An important point here is that the representation $\mathbf{r} = \mathbf{r}(\theta, \zeta)$ of a magnetic surface differs fundamentally from other possible representations in that, if we solved a direct problem, then the contours of the magnetic field strength on a magnetic surface would coincide with the ζ = const contours of the angular coordinate. Since the magnetic field is not known *a priori* (i.e., the magnetic coordinates remain unknown), we are trying to perform calculations so that, in working with magnetic coordinates, this characteristic feature is taken into account automatically, as is the case with ordinary angular coordinates.

A magnetic surface close to the surface $\mathbf{r} = \mathbf{r}(\Phi_0, \theta, \zeta)$ can be represented as

$$\mathbf{r}^{d\Phi} = \mathbf{r}(\Phi_0, \theta, \zeta) + \mathbf{r}_\Phi d\Phi. \quad (21)$$

The expression for $\mathbf{r}_\Phi$ can be found by taking the vector product of the fundamental magnetic relation (8) with $\mathbf{r}_\theta$:

$$\mathbf{r}_\Phi = \frac{[\mathbf{r}_\theta \mathbf{r}_\zeta]}{F g_{22}} + \mathbf{r}_\theta \frac{g_{12}}{g_{22}}. \quad (22)$$

To determine the metric tensor element g_{12} on the magnetic surface $\Phi = \Phi_0$, we consider the derivative

$$\left(\frac{g_{12}}{g_{22}}\right)_\zeta \equiv \frac{g_{22}(\mathbf{r}_\theta \mathbf{r}_{\zeta\Phi}) + g_{22}(\mathbf{r}_\Phi \mathbf{r}_{\zeta\theta}) - 2(\mathbf{r}_\theta \mathbf{r}_\Phi)(\mathbf{r}_\zeta \mathbf{r}_{\zeta\theta})}{g_{22}^2}. \quad (23)$$

Substituting (22) into the right-hand side of this identity and using the relationship $\mathbf{r}_\Phi \mathbf{r}_{\zeta\theta} = \mathbf{r}_\theta \mathbf{r}_{\Phi\zeta}$, which follows from the equality $g_{13\theta} - g_{23\Phi} = 0$ [see (9)], we transform (23) to

$$\left(\frac{g_{12}}{g_{22}}\right)_\zeta = \frac{2k_{23}}{F g_{22}}\sqrt{\frac{g_{33}}{g_{22}}}, \quad (24)$$

where $k_{23} = \frac{\mathbf{r}_{\theta\zeta}[\mathbf{r}_\theta \mathbf{r}_\zeta]}{\sqrt{g_{22}g_{33} - g_{23}^2}}$ is one of the elements of the second quadratic form of the magnetic surface [18, 19]. Consequently, the quantities g_{12} and $\mathbf{r}_\Phi$ and, accordingly, the shape of a neighboring magnetic surface $\mathbf{r}^{d\Phi}$ are governed by the shape of the surface $\mathbf{r} = \mathbf{r}(\Phi = \Phi_0, \theta, \zeta)$. We emphasize that this relation between the surfaces is nonlocal in character.

The first magnetic field representation in (4) makes it possible to write the derivative along a magnetic field line as $\frac{\partial}{\partial \zeta} = 2\pi\sqrt{g}\,\mathbf{B}\nabla$, which reduces (24) to the standard magnetic differential equation [20, 21]

$$\mathbf{B}\nabla\frac{g_{12}}{g_{22}} = \frac{k_{23}}{\pi g_{22}^{3/2}\sqrt{g_{33}}}. \quad (25)$$

The requirement that the solution to (25) be single-valued imposes certain constraints on the right-hand side of (25). The first constraint (see [20]) reduces to the condition that the integral of the right-hand side over the volume between the neighboring magnetic surfaces be vanishing. For systems with closed magnetic field lines, this condition has the form

$$\int_0^{2\pi}\int_0^{2\pi} \frac{k_{23}}{g_{22}}\sqrt{\frac{g_{33}}{g_{22}}}\, d\theta d\zeta = 0. \quad (26)$$

For systems with irrational rotational transforms, condition (26) should be written in Boozer coordinates

according to prescriptions (14). Systems with closed magnetic field lines should also satisfy a more severe constraint [21]:

$$\int_0^{2\pi} \frac{k_{23}}{g_{22}}\sqrt{\frac{g_{33}}{g_{22}}}d\zeta = 0. \tag{27}$$

Consequently, the specific character of magnetic coordinates results in two additional integral constraints, (26) and (27), at the magnetic surface.

The fundamental theorem in the theory of magnetic surfaces implies that, in order for the surface to be determined unambiguously (correct to its orientation in space), it is necessary to specify the first and second quadratic forms [18, 19]. In other words, to determine the surface requires knowledge of six functions of two surface angular variables: three metric tensor elements—g_{22}, g_{23}, and g_{33} (the first form)—and three curvature tensor elements—k_{22}, k_{23}, and k_{33} (the second form).

From the magnetic equations (7) and (8), we can find two functions for the first quadratic form defined by (10) with (9):

$$g_{23} = 0, \qquad g_{33} = \frac{F^2}{4\pi^2 B^2}. \tag{28}$$

Recall that we specify the magnetic field strength distribution B on a magnetic surface. Three of the remaining four functions can be deduced from the Gauss–Weinharten equations, which describe how the basis vectors $\mathbf{e}_2$, $\mathbf{e}_3$, and $\mathbf{n} = \dfrac{[\mathbf{r}_\theta \mathbf{r}_\zeta]}{|[\mathbf{r}_\theta \mathbf{r}_\zeta]|}$ change along the coordinate lines on a magnetic surface [18, 19]. Taking into account the relationship $g_{23} = 0$, for $\theta = \text{const}$ (i.e., along a field line on a magnetic surface), we obtain

$$\begin{aligned}
\mathbf{e}_{2\zeta} &= \mathbf{e}_2\frac{g_{22\zeta}}{2g_{22}} + \mathbf{e}_3\frac{g_{33\theta}}{2g_{33}} + \mathbf{n}k_{23},\\
\mathbf{e}_{3\zeta} &= -\mathbf{e}_2\frac{g_{33\theta}}{2g_{22}} + \mathbf{e}_3\frac{g_{33\zeta}}{2g_{33}} + \mathbf{n}k_{33},\\
\mathbf{n}_\zeta &= -\mathbf{e}_2\frac{k_{23}}{g_{22}} - \mathbf{e}_3\frac{k_{33}}{g_{33}}.
\end{aligned} \tag{29}$$

Analogously, for $\zeta = \text{const}$, we have

$$\begin{aligned}
\mathbf{e}_{2\theta} &= \mathbf{e}_2\frac{g_{22\theta}}{2g_{22}} - \mathbf{e}_3\frac{g_{22\zeta}}{2g_{33}} + \mathbf{n}k_{22},\\
\mathbf{e}_{3\theta} &= \mathbf{e}_2\frac{g_{22\zeta}}{2g_{22}} + \mathbf{e}_3\frac{g_{33\theta}}{2g_{33}} + \mathbf{n}k_{23},\\
\mathbf{n}_\theta &= -\mathbf{e}_2\frac{k_{22}}{g_{22}} - \mathbf{e}_3\frac{k_{23}}{g_{33}}.
\end{aligned} \tag{29'}$$

The consistency conditions for (29) and (29') yield three familiar equations (the Gauss Egregium Theorem and the Peterson–Mainardi–Kodacci equations), which relate the elements of the metric and curvature tensors [18, 19]:

$$\begin{aligned}
k_{22}k_{33} - k_{23}^2 &= g_{22}g_{33}K = -\frac{1}{2}(g_{22\zeta\zeta} + g_{33\theta\theta})\\
&\quad + \frac{1}{4}\left(\frac{g_{22\zeta}^2}{g_{22}} + \frac{g_{33\theta}^2}{g_{33}} + \frac{g_{22\theta}g_{33\theta}}{g_{22}} + \frac{g_{22\zeta}g_{33\zeta}}{g_{33}}\right),\\
k_{22\zeta} - \frac{g_{22\zeta}}{2g_{22}}k_{22} - \frac{g_{33\theta}}{2g_{33}}k_{23} &= k_{23\theta} - \frac{g_{22\theta}}{2g_{22}}k_{23} + \frac{g_{22\zeta}}{2g_{33}}k_{33},\\
k_{23\zeta} + \frac{g_{33\theta}}{2g_{22}}k_{22} - \frac{g_{33\zeta}}{2g_{33}}k_{23} &= k_{33\theta} - \frac{g_{22\zeta}}{2g_{22}}k_{23} - \frac{g_{33\theta}}{2g_{33}}k_{33},
\end{aligned} \tag{30}$$

where K is the total (Gaussian) curvature.

Hence, equations (28) and (30) constitute the set of five equations for the six functions entering the first and second quadratic forms for a magnetic surface. These equations should be supplemented with the integral conditions (26) and (27). A certain freedom in choosing the last (sixth) function reflects the circumstance that the magnetic surface cannot be unambiguously determined from the distribution of the magnetic field strength. We can use this freedom to obtain pseudosymmetry near a magnetic surface.

On the surface $\Phi = \Phi_0$, the pseudosymmetry condition (5) can be satisfied by appropriately choosing the dependence of the magnetic field strength B in the second equation in (28), in which case no new additional equations appear. The requirement that the pseudosymmetry condition (5) be satisfied through first order in $d\Phi \ll 1$ gives

$$(\hat{L}g_{33})_\Phi = 0, \tag{31}$$

which can also be written as

$$\hat{L}(\mathbf{r}_\zeta \mathbf{r}_{\zeta\Phi}) + \frac{1}{2}g_{33\zeta}f_\Phi = 0. \tag{32}$$

In deriving these formulas, we took into account relationship (10). The scalar product to which the operator $\hat{L}$ is applied can be represented as

$$\mathbf{r}_\zeta \mathbf{r}_{\zeta\Phi} = -\frac{k_{33}}{F}\sqrt{\frac{g_{33}}{g_{22}}} + \frac{g_{12}}{g_{22}}(\mathbf{r}_\zeta \mathbf{r}_{\zeta\theta}), \tag{33}$$

where $k_{33} = \dfrac{\mathbf{r}_{\zeta\zeta}[\mathbf{r}_\theta \mathbf{r}_\zeta]}{\sqrt{g_{22}g_{33} - g_{23}^2}}$ is one of the elements of the second quadratic form of a magnetic surface [18, 19]. Expression (33) was derived by differentiating (8) with respect to ζ and by taking the vector and scalar products

of the resulting relation with $\mathbf{r}_\zeta$ and $\mathbf{r}_\theta$, respectively. Now, we can write condition (31) in the final form:

$$\hat{L}\left(k_{33}\sqrt{\frac{g_{33}}{g_{22}}} - g_{33\theta}\int\frac{k_{23}}{g_{22}}\sqrt{\frac{g_{33}}{g_{22}}}d\zeta\right) = \frac{F}{2}g_{33\zeta}f_\Phi. \quad (34)$$

We can see that all of the quantities in (34) are determined exclusively by the shape of the magnetic surface $\Phi = \Phi_0$. Consequently, supplementing equations (28) and (30) with equation (34) provides a closed set of equations for calculating a pseudosymmetric magnetic surface $\Phi = \Phi_0$ and for satisfying the pseudosymmetry condition approximately in its vicinity.

For orthogonal magnetic systems ($f = 0$), condition (34) takes the simplest form:

$$\left(k_{33}\sqrt{\frac{g_{33}}{g_{22}}}\right)_\theta = 0. \quad (35)$$

Note that the quasisymmetry condition (34) for magnetic systems with an unclosed field line geometry contains the shear of the magnetic field lines. As we have already mentioned, the periodicity condition for magnetic systems with irrational rotational transforms necessitates the transition to Boozer coordinates according to prescriptions (14). In Boozer coordinates, the quasisymmetry condition (5) with $f = f(\Phi)$ reduces to $B = B(\Phi, \theta_B - \frac{(1+\mu f)}{f}\zeta_B)$. The condition for the magnetic field strength to be periodic in θ_B and ζ_B gives $\frac{1+\mu f}{f} = \frac{N}{M}$, where N and M are integers. The topology of the membranes $\theta_B = \text{const}$ and $\zeta_B = \text{const}$ can always be chosen so that $N = 0$; therefore, for $f = -1/\mu$, we arrive at the Boozer quasisymmetry condition $B = B(\Phi, \theta_B)$. Thus, to calculate a quasisymmetric magnetic surface and to achieve quasisymmetry in its vicinity, we must specify in advance not only the magnetic field strength but also the rotational transform μ and shear μ_Φ on this surface.

The equations derived should be supplemented with the condition for the magnetic field to be finite (i.e., the condition that there be no current-carrying windings) inside a closed magnetic surface. To derive this condition, we turn to the Laplace equation $\Delta\zeta = 0$, which follows from the second magnetic field representation in (4), and to the requirement that the curl of the vacuum magnetic field be zero inside a closed magnetic surface. The main integral Green's formula [22] enables us to write

$$\oiint\zeta\mathbf{n}\nabla\frac{1}{|\mathbf{R}|}dS - \oiint\frac{1}{|\mathbf{R}|}\mathbf{n}\nabla\zeta dS + 2\pi\zeta_0 = 0, \quad (36)$$

where $\mathbf{R} = \mathbf{r} - \mathbf{r}_0$ and the zero subscript indicates an arbitrary point with the coordinates (θ_0, ζ_0) on the surface. We introduce the unit vector $\mathbf{I} = \frac{\mathbf{R}}{|\mathbf{R}|}$ and take into account the relationships $\mathbf{n}\nabla\zeta = 0$ and $\nabla\frac{1}{|\mathbf{R}|} = -\frac{\mathbf{R}}{|\mathbf{R}|^3}$ to rewrite (36) as

$$\oiint\zeta\mathbf{I}[\mathbf{I}_\theta\mathbf{I}_\zeta]d\theta d\zeta = 2\pi\zeta_0. \quad (37)$$

As a result of the mapping of the surface S onto a unit sphere, we have $\mathbf{I} \parallel [\mathbf{I}_\theta\mathbf{I}_\zeta]$ and $\oiint\mathbf{I}[\mathbf{I}_\theta\mathbf{I}_\zeta]d\theta d\zeta = 2\pi$, which finally lead to the condition

$$\oiint\zeta\sqrt{\mathbf{I}_\theta^2\mathbf{I}_\zeta^2 - (\mathbf{I}_\theta\mathbf{I}_\zeta)^2}d\theta d\zeta = 2\pi\zeta_0 \quad (38)$$

or

$$\oiint(\zeta - \zeta_0)\sqrt{\mathbf{I}_\theta^2\mathbf{I}_\zeta^2 - (\mathbf{I}_\theta\mathbf{I}_\zeta)^2}d\theta d\zeta = 0. \quad (38')$$

Calculating a pseudosymmetric surface with irrational μ, we naturally obtain an equilibrium magnetic surface. Calculating an isometric surface with rational μ (corresponding to closed magnetic field lines), we again immediately arrive at an equilibrium magnetic surface with $\oint\frac{dl}{B} = \text{const}$, which is a consequence of (5). A pseudosymmetric surface with rational μ should be calculated under the additional assumption that the magnetic surface is equilibrium; i.e., $\oint\frac{dl}{B} = \text{const}$.

Note that, in solving the above closed set of equations (26)–(28), (30), (34), and (38) for the functions determining the first and second quadratic forms, we used the special magnetic coordinates as ordinary angular coordinates. Various *a priori* conditions for the solutions to be symmetric, periodic, finite, etc., are formulated in magnetic coordinates. The integral conditions (26), (27), and (38) ensure that the angular coordinates on a surface are magnetic in character.

4. TUBULAR ORTHOGONAL MAGNETIC SURFACE

As the simplest example of how to implement the approach described in Section 3, we calculate a tubular orthogonal surface with a zero rotational transform ($\mu = 0$) in Boozer coordinates $\theta = \theta_B$ and $\zeta = \zeta_B$. By the tubular surface, we mean a magnetic surface of a magnetic field that is periodic along the Z-axis. The transverse coordinates x and y of a tubular surface are periodic functions of θ and ζ.

The orthogonality condition written in the form of (28), $g_{33} = \left(\frac{F}{2\pi B(\zeta)}\right)^2$, allows us to switch from ζ to the new coordinate ω defined as

$$\zeta = \frac{2\pi}{F}\int B(\omega)d\omega. \tag{39}$$

In the new coordinates, we have $g_{33} = 1$ and $g_{23} = 0$, which substantially simplifies relationships (29), (30), and (35). The curvature tensor elements k_{22}, k_{23}, and k_{33} and the metric tensor element g_{22} are determined from the following equations, which do not explicitly contain the magnetic field strength:

$$\begin{gathered}\frac{k_{22}}{\sqrt{g_{22}}}\frac{k_{33}}{\sqrt{g_{22}}} - \left(\frac{k_{23}}{\sqrt{g_{22}}}\right)^2 = -\frac{(\sqrt{g_{22}})_{\omega\omega}}{\sqrt{g_{22}}} = K,\\ \left(\frac{k_{23}}{\sqrt{g_{22}}}\right)_\theta = \left(\frac{k_{22}}{\sqrt{g_{22}}}\right)_\omega - k_{33}(\sqrt{g_{22}})_\omega,\\ \sqrt{g_{22}}k_{33\theta} = (\sqrt{g_{22}}k_{23})_\omega,\\ \left(\frac{k_{33}}{\sqrt{g_{22}}}\right)_\theta = 0.\end{gathered} \tag{40}$$

Since we are interested in tubular magnetic surfaces for which the curvature in the transverse direction is much larger than the curvature in the longitudinal direction, we consider the approximation $k_{22}/g_{22} \gg k_{33}$ and neglect the second term on the right-hand side of the second equation in (40). Below, we will specify the range of validity of this approximation and analyze its close relation to the paraxial approximation.

It is straightforward to show that one of the possible solutions to equations (40) is

$$\begin{gathered}g_{22} = f_1^2(\omega)\sin^2\theta + f_2^2(\omega)\cos^2\theta,\\ k_{33} = \frac{f_1'' f_2 - f_1 f_2''}{f_1^2 - f_2^2}\sqrt{g_{22}},\\ k_{23} = \frac{f_1' f_2 - f_1 f_2'}{2\sqrt{g_{22}}}\sin 2\theta,\\ k_{22} = \frac{f_1 f_2}{\sqrt{g_{22}}},\end{gathered} \tag{41}$$

where the prime denotes the derivative with respect to ω and f_1 and f_2 are positive periodic functions that depend only on the argument ω and satisfy the equation

$$f_1 f_1'' = f_2 f_2''. \tag{42}$$

Without going into the details of the derivation of equations (41) and (42), note only that we sought tubular surfaces with convex cross sections (corresponding to a positive transverse element of the curvature tensor, $k_{22} > 0$); we also adopted the simplest angular dependence of the positive definite function g_{22} in order to ensure the existence of two symmetry planes: $\theta = 0$ and $\theta = \pi/2$. The expressions obtained are valid in the approximation $\left(\frac{f_1}{f_2}\right)^2 f_1 f_1'' \ll 1$.

Knowing the first and second quadratic forms described by the tensor elements in (28) and (41), we can calculate the magnetic surface $\mathbf{r} = \mathbf{r}(\theta, \zeta)$. To do this, we can employ, e.g., the linear equations (29) and transform them to the new coordinates:

$$\begin{gathered}\mathbf{e}_{2\omega} = \mathbf{e}_2\frac{g_{22\omega}}{2g_{22}} + \mathbf{n}k_{23},\\ \mathbf{e}_{3\omega} = \mathbf{n}k_{33},\\ \mathbf{n}_\omega = -\mathbf{e}_2\frac{k_{23}}{g_{22}} - \mathbf{e}_3 k_{33}.\end{gathered} \tag{43}$$

Taking into account that, in (43), $\theta = \text{const}$, we introduce the new variable Ω,

$$\frac{d\Omega}{d\omega} = \frac{k_{23}}{\sqrt{g_{22}}} \tag{44}$$

and the new vector $\mathbf{e}_2^* = \mathbf{e}_2/\sqrt{g_{22}}$ in order to simplify equations (43) to

$$\begin{gathered}\mathbf{e}_{2\Omega}^* = \mathbf{n},\\ \mathbf{e}_{3\Omega} = \varepsilon\mathbf{n},\\ \mathbf{n}_\Omega = -\mathbf{e}_2^* - \varepsilon\mathbf{e}_3,\end{gathered} \tag{45}$$

where $\varepsilon = k_{33}\sqrt{g_{22}}/k_{23} \ll 1$. To zero order in ε, the general solution to (45) is

$$\begin{gathered}\mathbf{n} = \mathbf{C}_1\sin\Omega + \mathbf{C}_2\cos\Omega,\\ \mathbf{e}_2^* = -\mathbf{C}_1\cos\Omega + \mathbf{C}_2\sin\Omega,\\ \mathbf{e}_3 = \mathbf{C}_3,\end{gathered} \tag{46}$$

where $\mathbf{C}_{1,2,3}$ are constant vectors. Using (41) and (44), we find $\Omega = \arctan\left(\frac{f_1}{f_2}\tan\theta\right)$, so that solution (46) can be rewritten as

$$\begin{gathered}\mathbf{n} = \mathbf{C}_1\frac{f_1\sin\theta}{\sqrt{g_{22}}} + \mathbf{C}_2\frac{f_2\cos\theta}{\sqrt{g_{22}}},\\ \mathbf{e}_2 = -\mathbf{C}_1 f_2\cos\theta + \mathbf{C}_2 f_1\sin\theta,\\ \mathbf{e}_3 = \mathbf{C}_3.\end{gathered} \tag{47}$$

From the conditions

$$g_{33} = \mathbf{e}_3\mathbf{e}_3 = 1, \quad g_{23} = \mathbf{e}_2\mathbf{e}_3 = 0,$$
$$g_{22} = \mathbf{e}_2\mathbf{e}_2 = f_1^2\sin^2\theta + f_2^2\cos^2\theta, \tag{48}$$

we can see that $\mathbf{C}_{1,2,3}$ are triply orthogonal unit vectors, which indicates that they are the basis vectors of the Cartesian coordinate system. To zero order in ε, from (47) we obtain the position vector $\mathbf{r}$ of the magnetic surface in Cartesian coordinates (x, y, z): $\mathbf{r} = (f_1\cos\theta, f_2\sin\theta, \omega)$. Treating the terms with ε in (45) as small perturbations, we can obtain the position vector $\mathbf{r}$ satisfying conditions (48) to first order in ε:

$$\mathbf{r} = \left(f_1\cos\theta;\ f_2\sin\theta;\ \omega + \frac{1}{2}\int f_1 f_1''\,d\omega - \frac{1}{2}f_1 f_1'\cos^2\theta - \frac{1}{2}f_2 f_2'\sin^2\theta\right). \tag{49}$$

The expressions derived do not explicitly contain the magnetic field strength, which appears explicitly only in the integral conditions (26), (27), and (38). We consider condition (27), which takes the following form in the coordinates introduced in this section:

$$\oint \frac{k_{23}}{g_{22}^{3/2}B(\omega)}\,d\omega = 0. \tag{50}$$

Using solution (41), we can reduce (50) to

$$\oint \frac{d\left(\frac{f_1}{f_2}\right)}{Bf_2^2\left(\cos^2\theta + \sin^2\theta\left(\frac{f_1}{f_2}\right)^2\right)^2} = 0. \tag{51}$$

For periodic functions $f_{1,2}$, equality (51) should hold at any θ; this is indeed possible if the magnetic field strength obeys the functional dependence

$$B = \text{const}\frac{w\left(\frac{f_1}{f_2}\right)}{f_2^2}, \tag{52}$$

where an arbitrary function w of the argument f_1/f_2 should be of fixed sign. We can easily verify that condition (26) holds for the magnetic field strength in the form (52). The function w is found from condition (38'). Introducing the function $W(\omega) = \int_0^\omega\left(1 - \frac{w/f_2^2}{\langle w/f_2^2\rangle}\right)d\omega$, we can reduce (38') to a linear integral equation of the first kind [23]:

$$\int_{-\infty}^{\infty}\int_0^{2\pi} K(\omega, \omega_0, \theta, \theta_0)W(\omega)\,d\omega\,d\theta = f(\omega_0, \theta_0), \tag{53}$$

where $K = \sqrt{\mathbf{I}_\theta^2\mathbf{I}_\zeta^2 - (\mathbf{I}_\theta\mathbf{I}_\zeta)^2}$ is the kernel, $f = \int_{-\infty}^{\infty}\int_0^{2\pi}\omega\,K\,d\omega\,d\theta$, and the angular brackets stand for averaging over the magnetic field period. Equations (42) and (53) can be solved only numerically.

Analytically, the tubular surface approximation is closely related to the paraxial approximation. Note, in particular, that, for $C = 0$, condition (42) and the orthogonality condition in (20) are identical. Formally, to pass over from the tubular surface approximation to the paraxial approximation, we must adopt $\mathbf{r}^{d\Phi}$ in (21) as the prescribed coordinates of the magnetic axis. This indicates that, in the example at hand, we must set $x^{d\Phi} = y^{d\Phi} = 0$, thereby determining the function $w = f_2/f_1$ in (52), so that $B = \text{const}/(f_1 f_2)$.

5. CONCLUSION

Our analysis shows that it is possible in principle to find a vacuum equilibrium magnetic configuration with an exactly pseudosymmetric nonparaxial boundary magnetic surface in the vicinity of which the pseudosymmetry condition is satisfied approximately. To do this, the special magnetic flux coordinates can be used as ordinary angular coordinates on a magnetic surface; the magnetic character of the flux coordinates is given by the additional integral constraints (26), (27), and (38). In this case, all *a priori* conditions for the solutions to be pseudosymmetric, symmetric, periodic, finite, etc., should be formulated in magnetic coordinates.

The calculation of a nonparaxial vacuum boundary magnetic surface with prescribed properties is the first step in calculating the equilibrium and stability of the plasma inside the boundary surface. This calculation is especially important for searching for closed compact systems with strongly rippled magnetic fields, such as DRAKON [24]. Present-day numerical schemes [25] are practically inapplicable to such systems because of the very large number of spatial magnetic-field harmonics.

In order to improve the global plasma confinement in a device by creating an edge barrier (i.e., a boundary region with low transverse transport), it is necessary to satisfy one of the most restrictive versions of the pseudosymmetry condition (e.g., the orthogonality, quasisymmetry, or isometry condition) at the boundary surface, while the pseudosymmetry condition, which is less constrained by itself, can be satisfied over the entire region where the charged particles are confined. Therefore, it seems worthwhile to search for "mixed" configurations that are, e.g., pseudosymmetric over the entire plasma column with a quasisymmetric edge region. Whether it is possible to achieve pseudosymmetry over the entire plasma column by enforcing quasisymmetry near the plasma boundary remains an open question.

ACKNOWLEDGMENTS

I am grateful to V.V. Arsenin, A.V. Zvonkov, and A.Yu. Kuyanov for fruitful discussions. This work was supported in part by the Russian Foundation for Basic Research, project no. 97-02-17695.

REFERENCES

1. A. Boozer, Phys. Fluids **24**, 1999 (1981); **26**, 496 (1983).
2. A. Boozer, Fiz. Plazmy **23**, 483 (1997) [Plasma Phys. Rep. **23**, 449 (1997)].
3. M. I. Mikhaĭlov, V. D. Shafranov, and D. Sünder, Fiz. Plazmy **24**, 706 (1998) [Plasma Phys. Rep. **24**, 653 (1998)].
4. J. R. Cary and S. G. Shasharina, Fiz. Plazmy **23**, 152 (1997) [Plasma Phys. Rep. **23**, 509 (1997)].
5. A. A. Skovoroda, Fiz. Plazmy **24**, 1059 (1998) [Plasma Phys. Rep. **24**, 989 (1998)].
6. A. A. Skovoroda and V. D. Shafranov, Fiz. Plazmy **21**, 937 (1995) [Plasma Phys. Rep. **21**, 886 (1995)].
7. D. Palumbo, Nuovo Cimento B **53**, 507 (1968).
8. D. A. Panov, Fiz. Plazmy **9**, 184 (1983) [Sov. J. Plasma Phys. **9**, 112 (1983)].
9. M. Yu. Isaev, M. I. Mikhaĭlov, and V. D. Shafranov, Fiz. Plazmy **20**, 357 (1994) [Plasma Phys. Rep. **20**, 319 (1994)].
10. D. Garren and A. Boozer, Phys. Fluids B **3,** 2805 (1991); **3**, 2822 (1991).
11. V. D. Pustovitov and V. D. Shafranov, in *Reviews of Plasma Physics*, Ed. by B. B. Kadomtsev (Énergoizdat, Moscow, 1987; Consultants Bureau, New York, 1990), Vol. 15.
12. P. Merkel, J. Comput. Phys. **66**, 83 (1986).
13. M. N. Rosenbluth and R. K. Varma, Nucl. Fusion **7**, 33 (1967).
14. V. V. Arsenin and A. Yu. Kuyanov, Fiz. Plazmy **20**, 262 (1994) [Plasma Phys. Rep. **20**, 237 (1994)].
15. D. Lortz and J. Nuhrenberg, in *Proceedings of Annual Controlled Fusion Theory Meeting, Sherwood, 1981*, Paper 3B48.
16. P. J. Catto and R. D. Hazeltine, Phys. Fluids **24**, 1663 (1981).
17. D. D. Ryutov and G. V. Stupakov, in *Reviews of Plasma Physics*, Ed. by B. B. Kadomtsev (Énergoizdat, Moscow, 1984; Consultants Bureau, New York, 1987), Vol. 13.
18. P. K. Rashevskiĭ, *Cours of Differential Geometry* (Gostekhizdat, Moscow, 1950).
19. G. A. Korn and T. M. Korn, *Mathematical Handbook for Scientists and Engineers* (McGraw-Hill, New York, 1961; Nauka, Moscow, 1972).
20. M. D. Kruskal and R. M. Kulsrud, Phys. Fluids **1**, 265 (1958).
21. W. Newcomb, Phys. Fluids **2**, 362 (1959).
22. A. N. Tikhonov and A. A. Samarskii, *Equations of Mathematical Physics* (Nauka, Moscow, 1972, Pergamon, Oxford, 1964).
23. A. F. Verlan' and V. S. Sizikov, *Methods and Computer Codes for Solving Integral Equations* (Naukova Dumka, Kiev, 1986).
24. V. M. Glagolev, B. B. Kadomtsev, B. A. Trubnikov, and V. D. Shafranov, in *Proceedings of 10th EPS Conference, Moscow, 1980*, Vol. 1, p. E-8.
25. S. P. Hirshman, W. I. van Rij, and P. Merkel, Comput. Phys. Commun. **43**, 143 (1986).

Translated by I. Kalabalyk

Plasma Physics Reports, Vol. 26, No. 7, 2000, pp. 560–574. Translated from Fizika Plazmy, Vol. 26, No. 7, 2000, pp. 600–614.

PLASMA DYNAMICS

Formation of Current Sheets in Structurally Stable and Structurally Unstable Magnetic Configurations with Two Null Lines

S. V. Bulanov*, E. Yu. Echkina, I. N. Inovenkov**, F. Pegoraro***, and V. V. Pichushkin****

**Institute of General Physics, Russian Academy of Sciences, ul. Vavilova 38, Moscow, 117942 Russia*

***Moscow State University, Vorob'evy gory, Moscow, 119899 Russia*

****University of Pisa and National Institute for Physics of Matter, Pisa, Italy*

Received September 6, 1999; in final form, November 17, 1999

Abstract—The nonlinear dynamics of magnetoacoustic and Alfvén MHD perturbations in structurally unstable magnetic configurations with two null lines (X-lines) is studied both analytically and numerically. It is shown that these perturbations cause the electric current to evolve nonlinearly in such a manner that a structurally unstable configuration of the magnetic field transforms into a structurally stable configuration. Such a transformation is forbidden in ideal magnetohydrodynamics but can occur in the process of magnetic field line reconnection. The final magnetic configuration to which the system evolves is shown to contain no separatrices connecting the null lines. © *2000 MAIK "Nauka/Interperiodica".*

1. INTRODUCTION

In space plasmas, magnetic fields play a governing role in the formation of structures that are bursty in character. Such phenomena are often attributed to rapid dissipation of the magnetic energy in highly conducting plasmas. The magnetic reconnection, which is usually regarded as the primary dissipation mechanism, occurs mainly near the magnetic field lines in the vicinity of which the current sheets (i.e., thin regions with high current densities) form.

Magnetic reconnection generally occurs in converging plasma flows in which two different field lines become so close to one another that the finite plasma conductivity comes into play and may cause them to reconnect, thereby changing both the local and global structures of the magnetic field.

It should be noted that, even when the magnetic reconnection occurs inside relatively small spatial regions, the related changes in the magnetic field topology can substantially affect the evolution and dynamics of the entire system. Magnetic reconnection has been studied in detail in many papers aimed at investigating various aspects of this important physical phenomenon (see [1–3] and the literature cited therein).

The magnetic reconnection problem is closely related to the problem of the structural stability of vector fields. The mathematical aspects of the latter problem were discussed by Arnold [4], who defined a structurally stable dynamic system as a system whose state remains topologically equivalent to the initial (unperturbed) state for any sufficiently small perturbation of the vector field. Since the magnetic field topology changes during both spontaneous and induced magnetic reconnection, it is natural to expect that the magnetic field should evolve from a structurally unstable into structurally stable configuration. Note that, in this case, the phenomenon under analysis is more complicated because, during magnetic reconnection in a highly conducting plasma, we deal with the nonlinear interaction between two vector fields: the magnetic field and the field of the plasma velocities. This circumstance significantly complicates the problem in comparison with the case of one vector field.

The simplest example of a structurally unstable solenoidal vector field is a magnetic field with a third-order null line. Such a magnetic configuration can be described by the vector potential $\mathbf{A}_0 = A_0(x, y)\mathbf{e}_z$ such that

$$A_0(x, y) = \frac{B_0}{3s^2}(x^3 - 3xy^2), \tag{1}$$

where B_0 is the magnetic field at the boundary of a region with a characteristic dimension s.

The magnetic configuration described by the vector potential (1) is structurally unstable because the critical point ($x = 0$, $y = 0$) of the vector field $\mathbf{B} = \nabla A_0 \times \mathbf{e}_z$ is degenerate. This stems from the fact that the eigenvalues of the dynamic system $\dot{\mathbf{x}} = \mathbf{B}$ linearized in the vicinity of zero are equal to zero. Small perturbations of the magnetic field described by the vector potential (1) cause the degenerate singular point to bifurcate or disappear, in which case the perturbed magnetic field can

1063-780X/00/2607-0560$20.00 © 2000 MAIK "Nauka/Interperiodica"

be expressed in terms of the perturbed vector potential

$$A_0 = \frac{B_0}{3s^2}(x^3 - 3xy^2) + \beta x^2 + \gamma y^2 + \delta xy + \varepsilon x + \mu y, \quad (2)$$

where the parameters β, γ, δ, ε, and μ are assumed to be small. Bifurcations in similar configurations with varying parameters were thoroughly discussed in a monograph by Poston and Stewart [5].

By choosing the appropriate parameters, one can make the magnetic configuration (2) physically stable but structurally unstable (in the MHD description, this is equivalent to choosing the condition $\Delta A_0 = 0$ for a plasma with a uniform density and temperature). Consequently, this configuration is suitable for analyzing magnetic reconnection in structurally unstable systems. Note that the classical problem of the tearing instability of an infinite current sheet [6] applies to configurations that are both physically and structurally unstable. In order to analyze the structural instability, we investigate magnetic configurations that are physically stable against resistive modes. In formulating the problem, we assume that the magnetic field topology changes under the action of the perturbations excited at the boundary of the region under consideration. In other words, we consider the regime of driven magnetic reconnection.

Our work is a continuation of papers [7–9], which initiated the studies on magnetic reconnection in structurally unstable magnetic configurations. The evolution of a third-order magnetic null line in the presence of magnetoacoustic perturbations was analyzed by Bulanov *et al.* [7, 8], who showed that, depending on the form of the initial magnetic configuration and the type of symmetry of the initially perturbed magnetic field, the seed magnetic perturbations result in the formation of either a current-carrying region bounded by magnetic separatrices or current sheets and shock waves localized at the separatrices. The problem of global redistribution of the electric current carried by magnetoacoustic and Alfvén modes in a magnetic configuration with two null lines was studied in [9].

Our main purpose here is to investigate the formation of current sheets in two-dimensional (2D) magnetic configurations with two null lines of the X-type (in particular, in configurations with zero net electric current) both analytically and numerically under the boundary conditions describing the excitation of azimuthally asymmetric nonlinear magnetoacoustic and Alfvén waves. We consider a structurally unstable configuration in which the X-lines are connected by a separatrix (the X–X separatrix). Note that such a configuration can be described by the vector potential (2) adjusted in a desired fashion by the proper choice of parameters. We expect that the variations in the magnetic topology that are either associated with a special choice of the initial magnetic configuration or induced by magnetoacoustic perturbations, which force the electric current to accumulate in local regions near the X-lines, will change the positions of the magnetic separatrices and cause a redistribution of the electric current driven by Alfvén perturbations. As was shown in [10, 11], the current driven by Alfvén perturbations flows along the separatrices in their vicinities. Consequently, in numerical experiments, we can expect a global redistribution of the electric current over the entire computation region.

We will solve the problems in the 2D approximation in which all of the desired functions depend only on time and the two spatial coordinates, x and y, but all three components of the plasma velocity and magnetic field are nonzero. It is well known that, in the linear approximation, the Alfvén and magnetoacoustic modes in a cold plasma in a 2D magnetic field become decoupled, so that we can study the current sheets associated with both types of modes separately. However, in three-dimensional (3D) configurations, finite-amplitude Alfvén and magnetoacoustic modes will interact nonlinearity. Solving the problem in the 3D formulation is the first step in providing a better insight into a more complicated 3D magnetic reconnection, in which case the Alfvén and magnetoacoustic modes remain coupled in the linear approximation [11–13]. In particular, the X–X separatrix is a 2D analogue of the limiting magnetic field line (which is also known as a separator) in Sweet's model of the magnetic configuration of a solar active region [14, 15]. We emphasize that a magnetic configuration with a limiting magnetic field line connecting two null points is structurally unstable. Hence, the phenomenon of global redistribution of the electric current may be of interest from the standpoint of the theory of solar flares.

2. MAGNETIC FIELD STRUCTURE

We assume that, in a magnetic configuration with two null lines, the magnetic field at the initial instant is z-independent. Such a field can be described by the vector potential $\mathbf{A}_0 = A_0(x, y)\mathbf{e}_z$ having a single z-component $A_0(x, y)$:

$$A_0(x, y) = \frac{g}{3}(x^3 - 3xy^2) + \varepsilon_1 x, \quad (3)$$

where $g = B_0/s^2$ and ε_1 is a small parameter. In the configuration defined by the vector potential (3) with $\varepsilon_1 g > 0$, the separatrix connects two saddle X-lines with the coordinates $x = 0$ and $y = \pm\sqrt{\varepsilon_1 g}$. The configuration with such a separatrix (referred to as an X–X separatrix) is structurally unstable (see Fig. 1a). A structurally stable configuration like that illustrated in Fig. 1b is described by the vector potential

$$A_0(x, y) = \frac{g}{3}(x^3 - 3xy^2) + \varepsilon_1 x + \varepsilon_2 y, \quad (4)$$

where ε_2 is a small parameter. In this configuration, there is no separatrix between two saddle points.

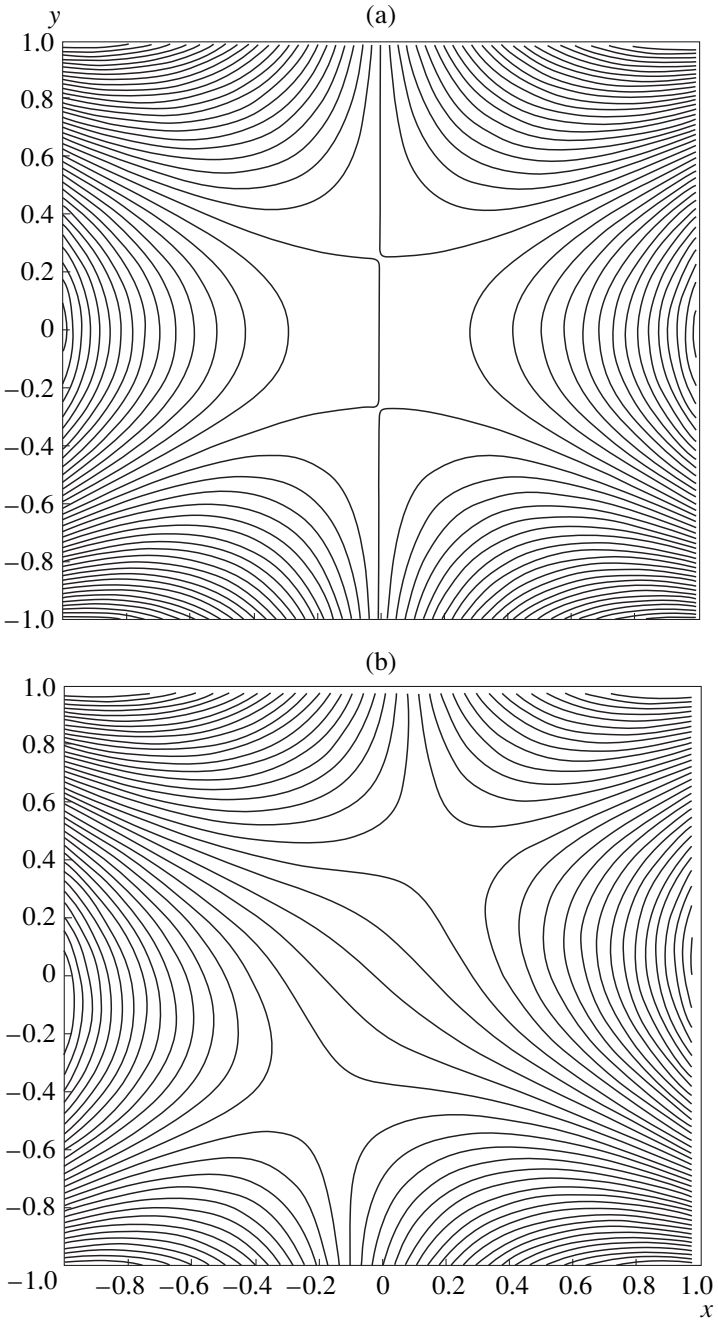

Fig. 1. Contours of the *z*-component of the vector potential for magnetic configurations with two X-lines: (a) structurally unstable configuration with the X–X separatrix and (b) structurally stable configuration.

3. BASIC EQUATIONS AND BOUNDARY CONDITIONS

We solved the set of MHD equations numerically in a square computation region ($-1 \le x \le 1, -1 \le y \le 1$). At the initial instant, the plasma in the magnetic field described by the vector potential (1) is assumed to be immobile. The coordinates, time, plasma density, plasma velocity, plasma temperature, and magnetic field are expressed in terms of the dimensionless variables

$$\frac{r}{s}, \quad \frac{gst}{(4\pi\rho_0)^{\frac{1}{2}}}, \quad \frac{\rho}{\rho_0}, \quad \frac{v(4\pi\rho_0)^{1/2}}{gs^2}, \quad \frac{T}{T_0}, \quad \frac{B}{gs^2}, \quad (5)$$

where ρ_0 and T_0 are the initial density and temperature, s is the dimension of the computation region, g is pro-

portional to the characteristic quantity $\partial^2 B_i/\partial x_j \partial x_k$, and $B_0 = gs^2$ is the magnetic field magnitude at the boundary. The dimensionless MHD equations can be written as [9]

$$\frac{\partial \rho}{\partial t} + \nabla(\rho \mathbf{v}_\perp) = 0, \tag{6}$$

$$\frac{\partial \mathbf{v}_\perp}{\partial t} + (\mathbf{v}_\perp \nabla)\mathbf{v}_\perp = -\frac{\tilde{\beta}}{2\rho}\nabla p - \frac{1}{\rho}\nabla A \Delta A - \frac{1}{2\rho}\nabla(B_\parallel^2), \tag{7}$$

$$\frac{\partial v_\parallel}{\partial t} + (\mathbf{v}_\perp \nabla) v_\parallel = -\frac{1}{\rho}(\mathbf{B}_\perp \nabla) B_\parallel, \tag{8}$$

$$\frac{\rho}{\gamma - 1}\left(\frac{\partial T}{\partial t} + (\mathbf{v}_\perp \nabla) T\right) + p \nabla \mathbf{v}_\perp = \tilde{k}\Delta T + \frac{2\tilde{\nu}_m}{\tilde{\beta}}[(\Delta A)^2 + (\nabla B_\parallel)^2], \tag{9}$$

$$p = \rho T, \tag{10}$$

$$\frac{\partial A}{\partial t} + (\mathbf{v}_\perp \nabla) A = \tilde{\nu}_m \Delta A, \tag{11}$$

$$\frac{\partial B_\parallel}{\partial t} + (\mathbf{v}_\perp \nabla) B_\parallel = (\mathbf{B}_\perp \nabla) v_\parallel - B_\parallel \nabla \mathbf{v}_\perp + \tilde{\nu}_m \Delta B_\parallel, \tag{12}$$

where the operator ∇ is

$$\nabla = \frac{\partial}{\partial x}\mathbf{e}_x + \frac{\partial}{\partial y}\mathbf{e}_y \tag{13}$$

and the plasma velocity has the form

$$\mathbf{v} = \mathbf{v}_\perp + v_\parallel \mathbf{e}_z = v_x \mathbf{e}_x + v_y \mathbf{e}_y + v_z \mathbf{e}_z. \tag{14}$$

The magnetic field **B** is characterized by three components:

$$\mathbf{B} = \frac{\partial A}{\partial y}\mathbf{e}_x - \frac{\partial A}{\partial x}\mathbf{e}_y + B_\parallel \mathbf{e}_z, \tag{15}$$

where ($\mathbf{e}_x$, $\mathbf{e}_y$, $\mathbf{e}_z$) are unit vectors of Cartesian coordinates. The adiabatic index is set to be

$$\gamma = \frac{c_p}{c_v} = \frac{5}{3}. \tag{16}$$

The dimensionless parameter β (the ratio of the plasma pressure to the magnetic field pressure at the boundary) is defined as

$$\tilde{\beta} = \frac{8\pi p_0}{B_0^2} = \frac{8\pi p_0}{g^2 s^4}, \tag{17}$$

where p_0 is the initial plasma pressure. The dimensionless magnetic diffusivity (the inverse Lundqvist number) has the form

$$\tilde{\nu}_m = \frac{c^2}{4\pi\sigma v_a s} = \frac{c^2 (4\pi\rho_0)^{1/2}}{4\pi\sigma g s^3}, \tag{18}$$

and the dimensionless thermal conductivity is

$$\tilde{k} = \frac{k}{v_a s \rho_0} = \frac{k(4\pi\rho_0)^{1/2}}{g s^3 \rho_0} = \frac{c_p}{\mathrm{Pe}}, \tag{19}$$

where $v_a = B_0/\sqrt{4\pi\rho_0}$ is the Alfvén velocity. The Péclet number $\mathrm{Pe} = k/(c_p \rho_0 v_a)$ can be assumed to be constant. The electric current density can be expressed as

$$\mathbf{j} = \nabla \times \mathbf{B} = \left(\frac{\partial B_\parallel}{\partial y}, -\frac{\partial B_\parallel}{\partial x}, -\Delta A\right). \tag{20}$$

When imposing the boundary conditions, we assumed that the perturbation is weak and that its effect at the boundary can be described in the linear approximation (see above).

A magnetoacoustic wave excited at the boundaries of the computation region, $x = \pm 1$ and $y = \pm 1$, is modeled by the vector potential

$$A(x, y, t) = A_0(x, y) + \sin\phi f(t - 1/r + 1), \tag{21}$$

where $A_0(x, y)$ is defined by (3) and (r, ϕ) are conventional polar coordinates.

A gradual rise of the electric current can be modeled by choosing the function $f(\xi)$ in the form

$$f(\xi) = \begin{cases} -\tilde{E}(\xi - 1)^2/\xi & \text{for} \quad \xi > 1, \\ 0 \quad \text{for} \quad \xi < 1, \end{cases} \tag{22}$$

where the dimensionless electric field $\tilde{E}$ is specified as

$$\tilde{E} = \frac{cE(4\pi\rho_0)^{1/2}}{(gs^2)^2}. \tag{23}$$

The excitation of Alfvén waves is modeled by the following boundary conditions for the z-component of the magnetic field:

$$B_\parallel(x = \mp 1, y, t) = \pm B_1 \min(1, t/t_{sw}). \tag{24}$$

This time dependence can also be used to describe the gradual switching-on of an external magnetic field on the characteristic time scale t_{sw}. In simulations, the amplitude B_1 of the z-component of the magnetic field was set to be 0.1. The boundary conditions for the remaining quantities were imposed in accordance with MHD equations. At the boundary regions through which the plasma enters the calculation domain, we specified the plasma density and pressure: $\rho = 1$ and $p = 1$. At the remaining boundary regions, the boundary conditions assumed a free plasma outflow out of the calculation domain.

All numerical results presented below were obtained for the magnetic diffusivity $\tilde{\nu}_m = 0.006$ and a pressure corresponding to $\tilde{\beta} = 0.012$. The dimensionless thermal conductivity and dimensionless electric field were chosen to be $\tilde{k} = 0.01$ and $\tilde{E} = 0.03$. We

imposed two types of boundary conditions on the initial configuration of the vector potential. In the first case, we used the boundary conditions (21) for magnetoacoustic perturbations, assuming that at the initial instant no Alfvén waves were excited; i.e., we set $B_1 = 0$ in the boundary condition (24). In the second case, we assumed that only Alfvén modes described by the boundary conditions (24) perturbations were excited and set $\tilde{E} = 0$ in (21).

4. RESULTS OF MHD MODELING

4.1. Magnetic Reconnection in a Structurally Unstable Configuration with Two Null Lines

The simulations were carried out for the initial vector potential (1) with $\varepsilon_1 \neq 0$. At the initial instant, the relevant magnetic configuration is structurally unstable.

Figure 2 shows the results of numerical modeling of the evolution of a magnetoacoustic perturbation: (a) the

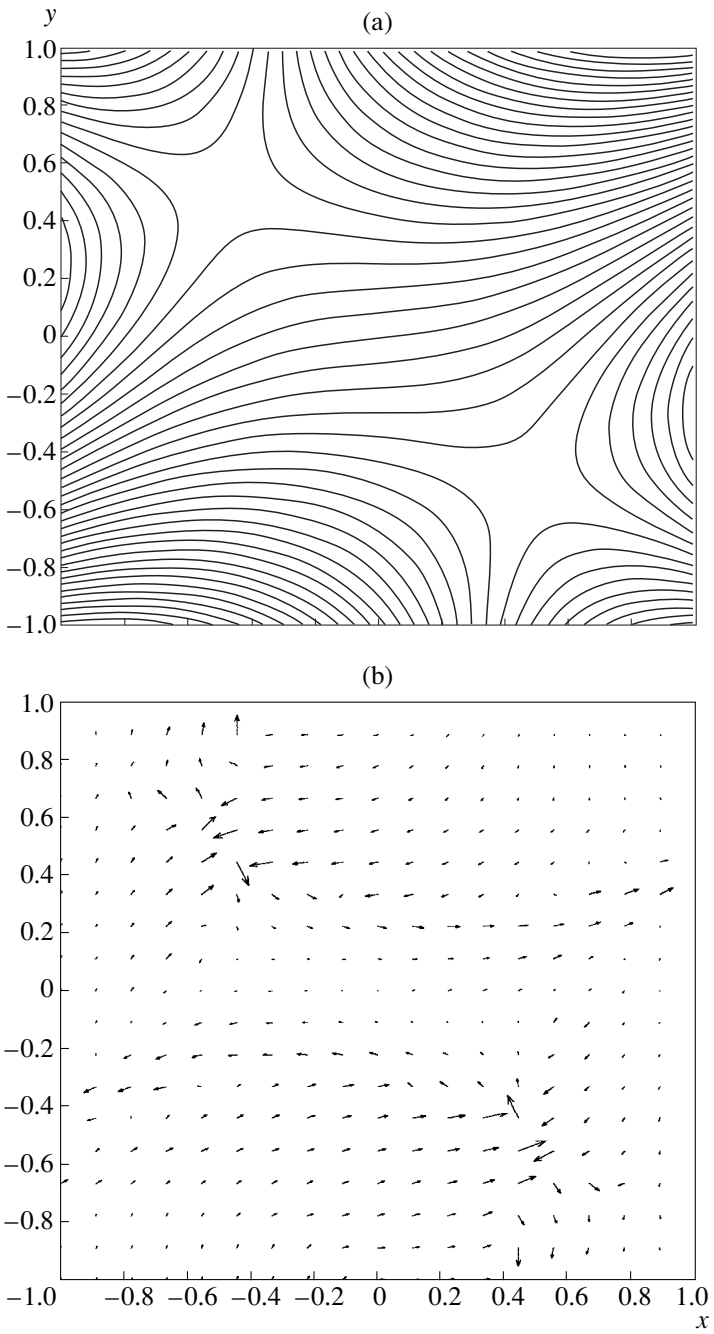

Fig. 2. Magnetoacoustic perturbations in a configuration with the X–X separatrix: (a) the contours of the z-component of the vector potential, (b) the velocity field $\mathbf{v}_\perp = v_x\mathbf{e}_x + v_y\mathbf{e}_y$, (c) the plasma density distribution, and (d) the distribution of the z-component of the electric current density at the time $t = 10$.

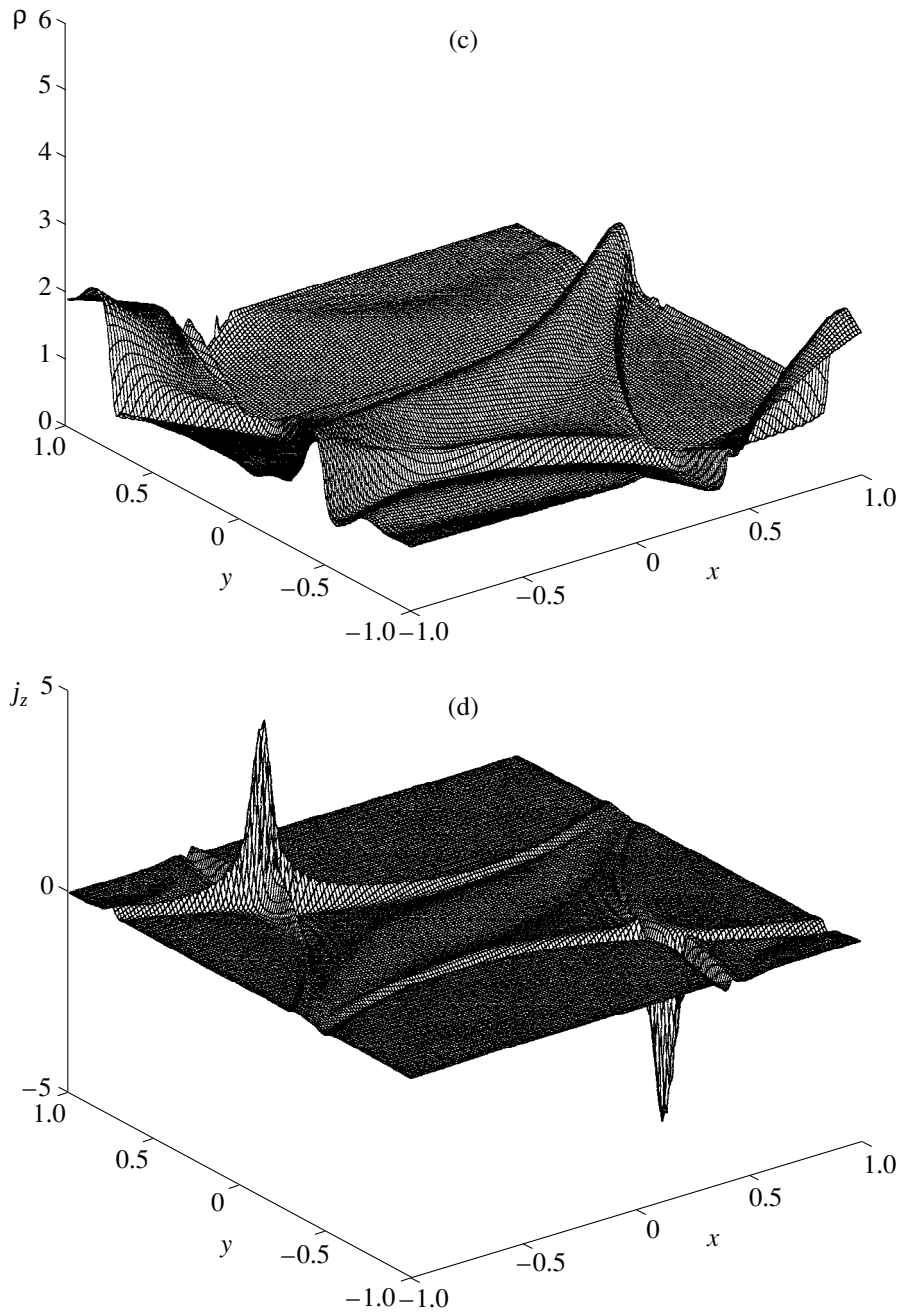

Fig. 2. (Contd.)

contours of the *z*-component of the vector potential, (b) the velocity field $\mathbf{v}_\perp = v_x\mathbf{e}_x + v_y\mathbf{e}_y$, (c) the plasma density distribution, and (d) the electric current density distribution. These results were obtained at the time $t = 10$ (recall that the time is expressed in units of Alfvén time). From Fig. 2a, we can see that the separatrix between the two null points disappears and two antisymmetric current sheets form in the vicinity of the X-lines. The structurally unstable configuration becomes structurally stable, because magnetoacoustic perturbations break the symmetry of the initial magnetic configurations. The density perturbations are localized in the vicinity of the separatrices.

Figure 3 illustrates the numerical results for the case when only an Alfvén wave is excited at the boundary of the computation region. In this case, in the 2D approximation, the magnetic field topology does not change.

Figure 3 shows (a) the contours of the *z*-component of the vector potential, (b) the velocity field, (c) the contours of the *z*-component of the velocity, (d) the

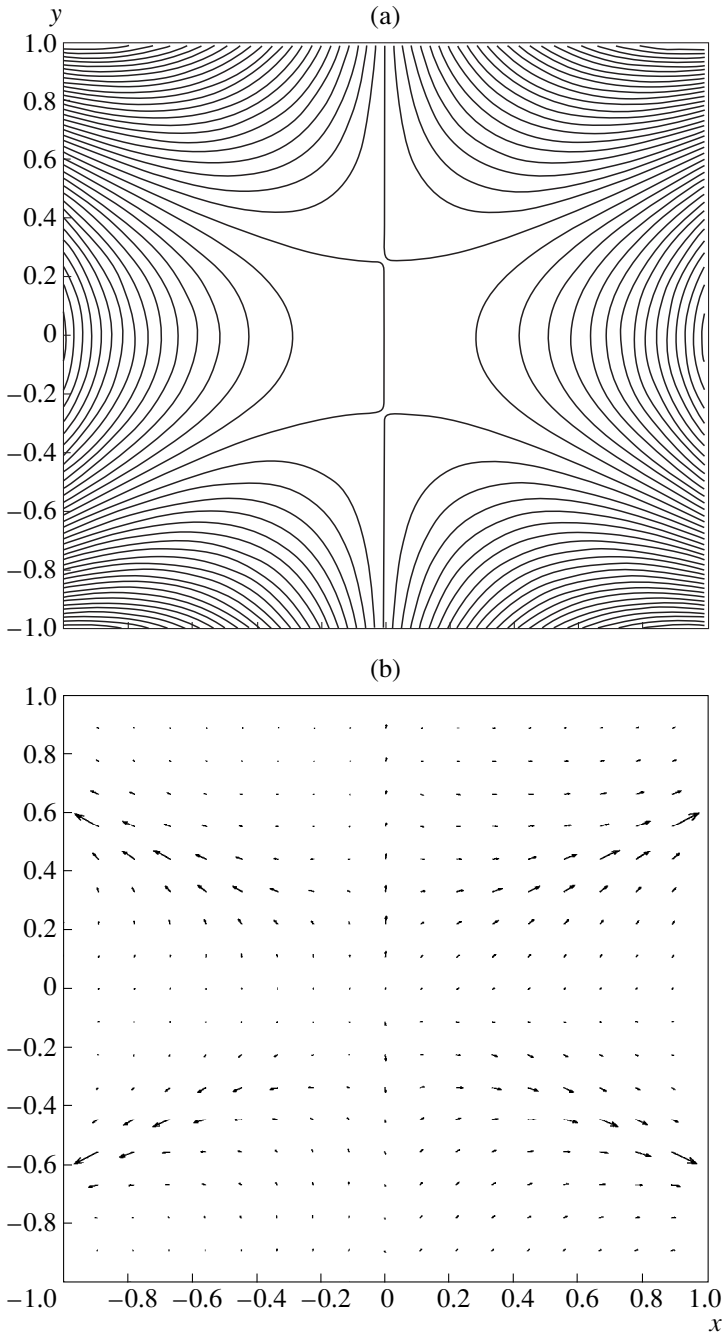

Fig. 3. (a) Contours of the *z*-component of the vector potential, (b) the velocity field, (c) the contours of the *z*-component of the velocity, (d) the plasma density distribution, and the distributions of the (e) transverse and (f) longitudinal components of the electric current density at the time $t = 10$ for Alfvén perturbations (24).

plasma density distribution, and the distributions of the (e) transverse and (f) longitudinal components of the electric current density. These results were obtained at the time $t = 10$ for an Alfvén perturbation excited at the boundaries $x = \pm 1$. By the "transverse" and "longitudinal" components of the electric current density we mean the poloidal component of the projection **j** of the current density onto the *xy* plane and the *z*-component of the electric current density.

The bulk of the transverse current flows in the vicinity of the separatrix that connects two null lines of the X-type. Recall that the topology of the initial magnetic field does not change; this circumstance characterizes exclusively Alfvén-type perturbations.

From Fig. 3e, we can also see that the nonlinear Alfvén wave generates the *z*-component of the electric current, which is dipole in nature near the separatrices.

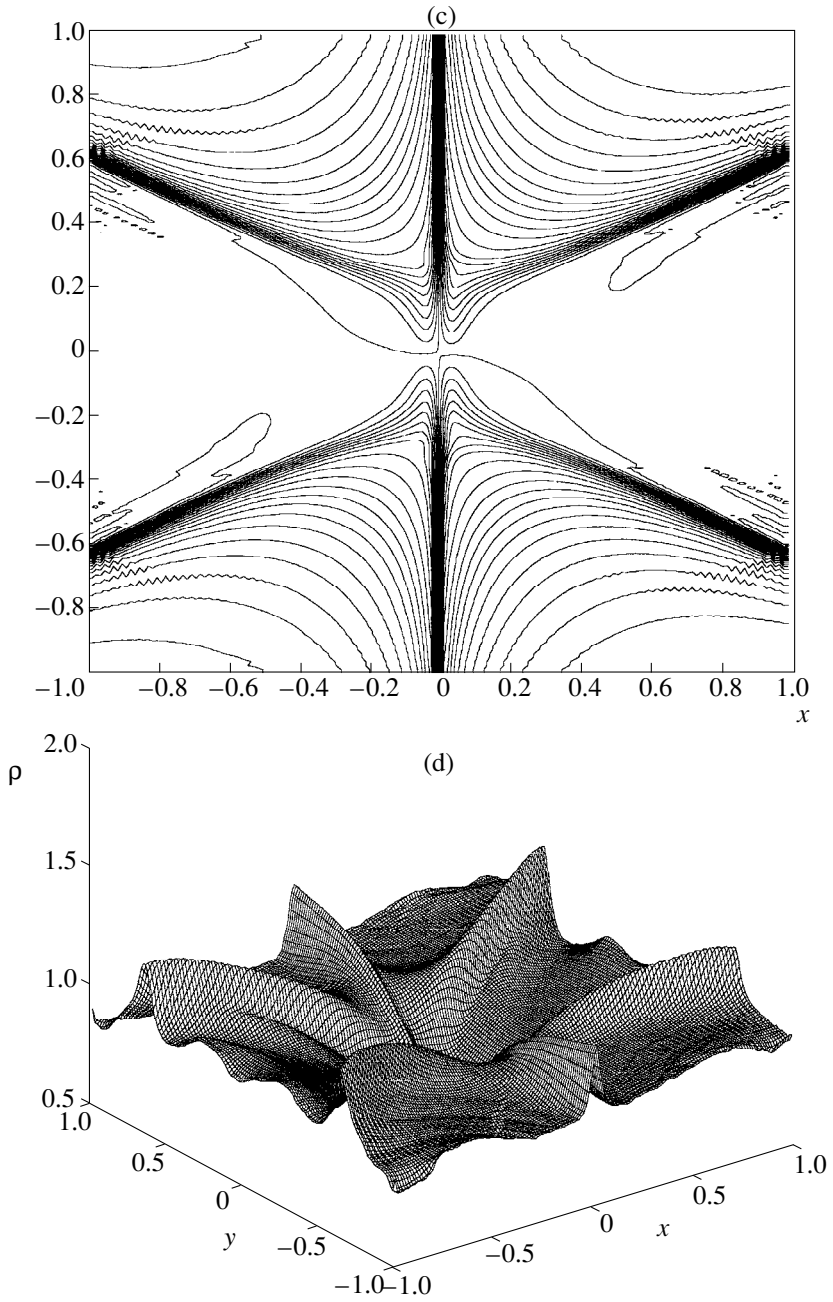

Fig. 3. (Contd.)

4.2 Evolution of the Plasma Density, Plasma Pressure, and Electric Current Density

In Figs. 2 and 3, we illustrate the plasma state in a magnetic field in the vicinity of magnetic separatrices in the quasi-steady stage (at $t = 10$). It is also very interesting to investigate how the plasma parameters evolve in the current sheet. In Fig. 4, we plot time evolutions of the plasma density, plasma pressure, and electric current density in a configuration with two magnetic null lines connected by the X–X separatrix. All of the parameters are computed at the point at which the electric current density in the current sheet is the highest; the numerals next to the curves show the maximum values of the parameters. Figure 4a corresponds to the case in Fig. 2, i.e., to the perturbations of the initial equilibrium state by magnetoacoustic waves excited at the boundary of the computation region. During the time interval $0 < t < 5.6$, the plasma density is seen to be unperturbed. After the time $t = 5.6$, the physical plasma parameters decrease only slightly.

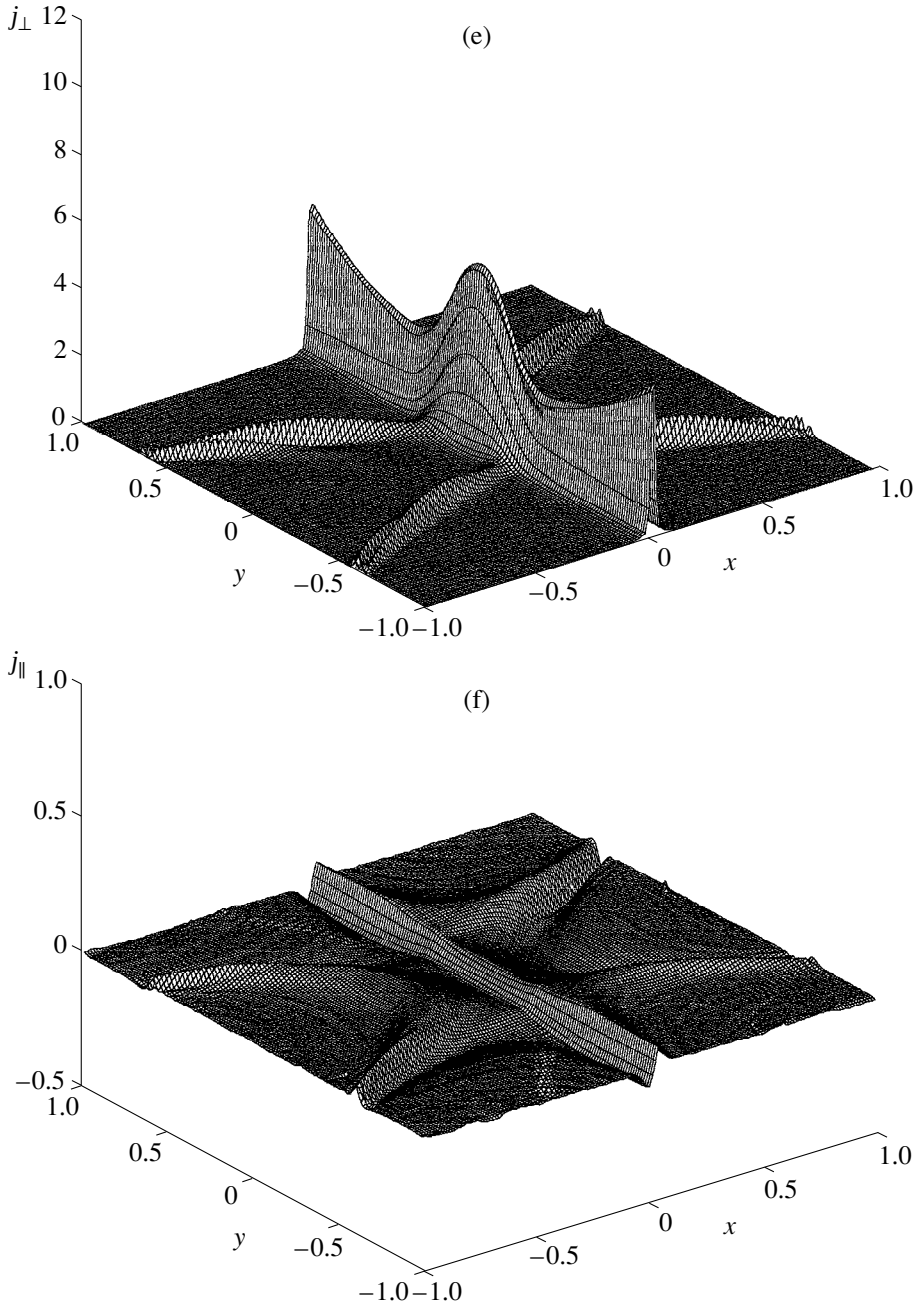

Fig. 3. (Contd.)

Figure 4b refers to the case in Fig. 3, when the current sheet forms as a result of the excitation of an Alfvén wave. In this scenario, the plasma density remains essentially unchanged and, after a transient process, the system reaches a thermodynamically equilibrium state.

In order to compare the above magnetic configurations with two X-lines and one X-line, we carried out MHD simulations of plasma dynamics in the vicinity of an isolated X-line. Note that this problem has been discussed in detail in many papers (see, e.g., [1, 10, 11]). Here, we are interested in the temporal evolution of the plasma and magnetic field.

We consider an initial magnetic field defined by the vector potential

$$A_0(x, y) = \frac{x^2 - y^2}{2}. \tag{25}$$

The related magnetic configuration has a hyperbolic null line of the X-type, which is the intersection of the two separatrix surfaces (see Fig. 5). We describe the

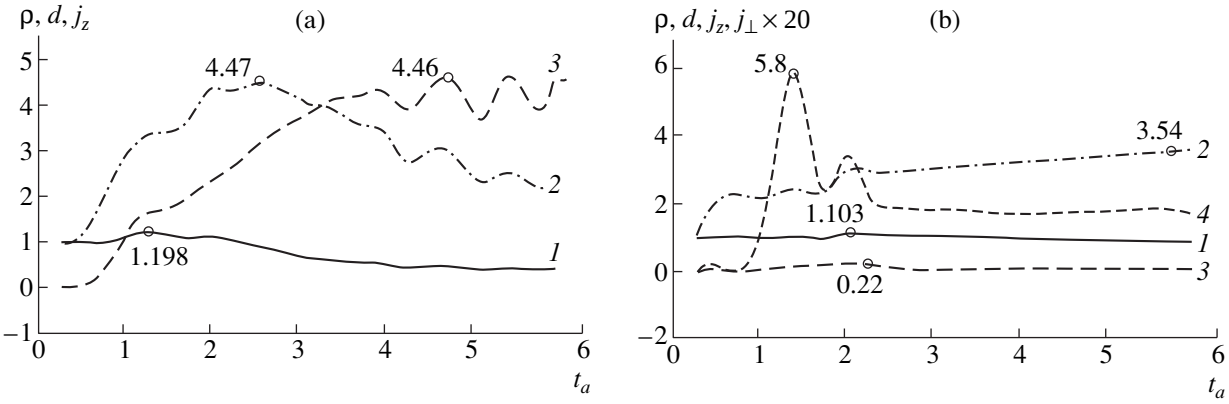

Fig. 4. Time evolutions of (*1*) the plasma density, (*2*) the plasma pressure, (*3*) the *z*-component of the electric current density, and (*4*) the perpendicular component $j_\perp$ of the electric current density in a magnetic configuration with two magnetic null lines connected by the X–X separatrix for (a) a magnetoacoustic wave and (b) an Alfvén wave excited at the boundary of the computation region. At each instant, all of the quantities are taken at the point at which the component j_z is the highest. The maximum values of the parameters are shown by numerals. The $j_\perp$ curve is scaled-up by a factor of 20.

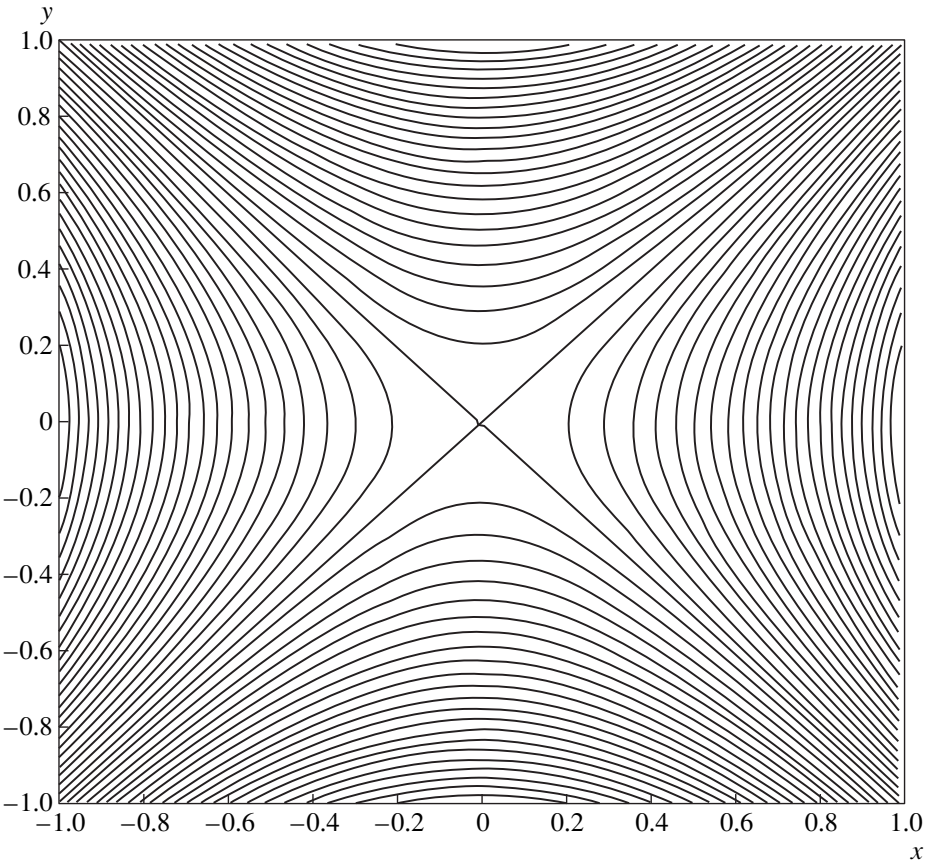

Fig. 5. Contours of the *z*-component of the vector potential for a magnetic configuration with one X-line.

magnetic configuration by the dimensionless parameters normalized as follows:

$$\frac{\rho}{\rho_0},\quad \frac{T}{T_0},\quad \frac{p}{\rho_0 T_0},\quad \frac{v(4\pi\rho_0)^{1/2}}{hl},\quad \frac{B}{hl},\quad \frac{r}{l},\quad \frac{th}{(4\pi\rho_0)^{1/2}},\quad \frac{cE(4\pi\rho_0)^{1/2}}{h^2 l^2}, \tag{26}$$

where the last expression characterizes the electric field magnitude.

The *z*-component of the electric current is carried by a magnetoacoustic wave that is excited at the boundary of the computation region and propagates toward its center. At the boundaries ($x = 1$, $-1 < y < 1$) and ($-1 < x < 1$, $y = 1$), the component j_z is expressed through the

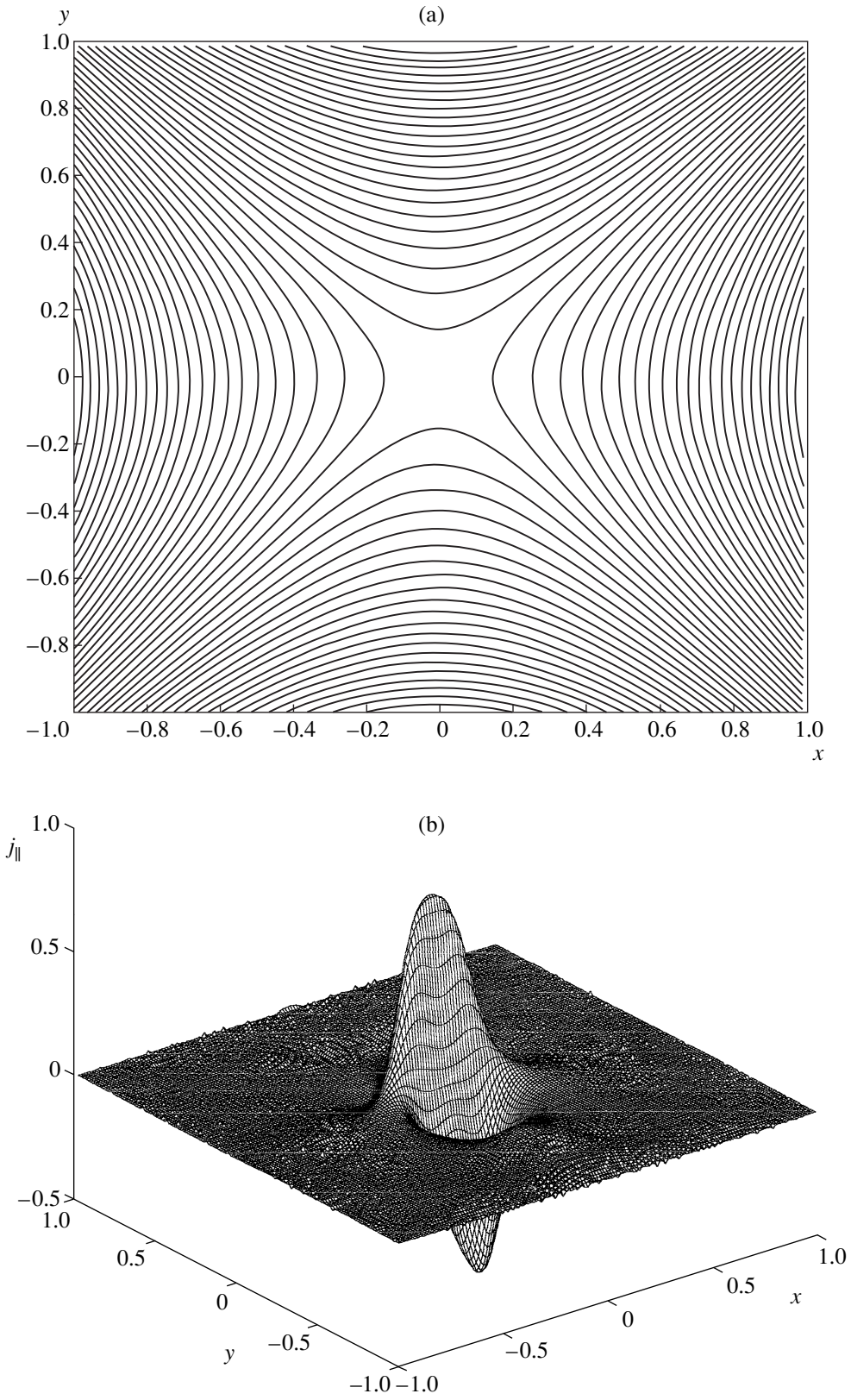

Fig. 6. Magnetoacoustic perturbations in a magnetic configuration with one X-line: (a) the contours of the z-component of the vector potential and (b) the distribution of the longitudinal component of the electric current density at the time $t = 1$.

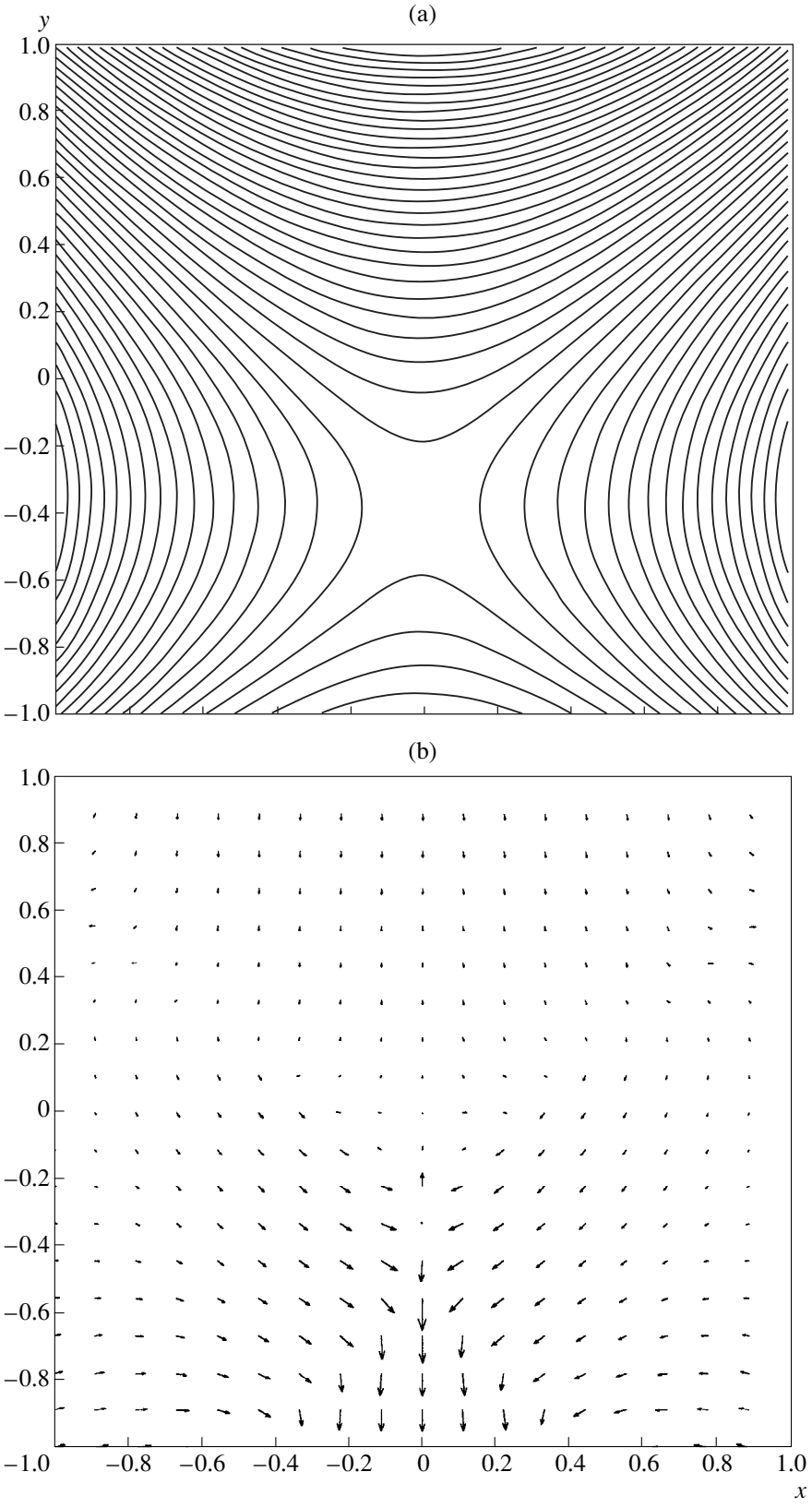

Fig. 7. (a) Contours of the *z*-component of the vector potential, (b) the velocity field, (c) the plasma density distribution, and (d) the distribution of the longitudinal component of the electric current density at the time $t = 10$ for a magnetoacoustic perturbation.

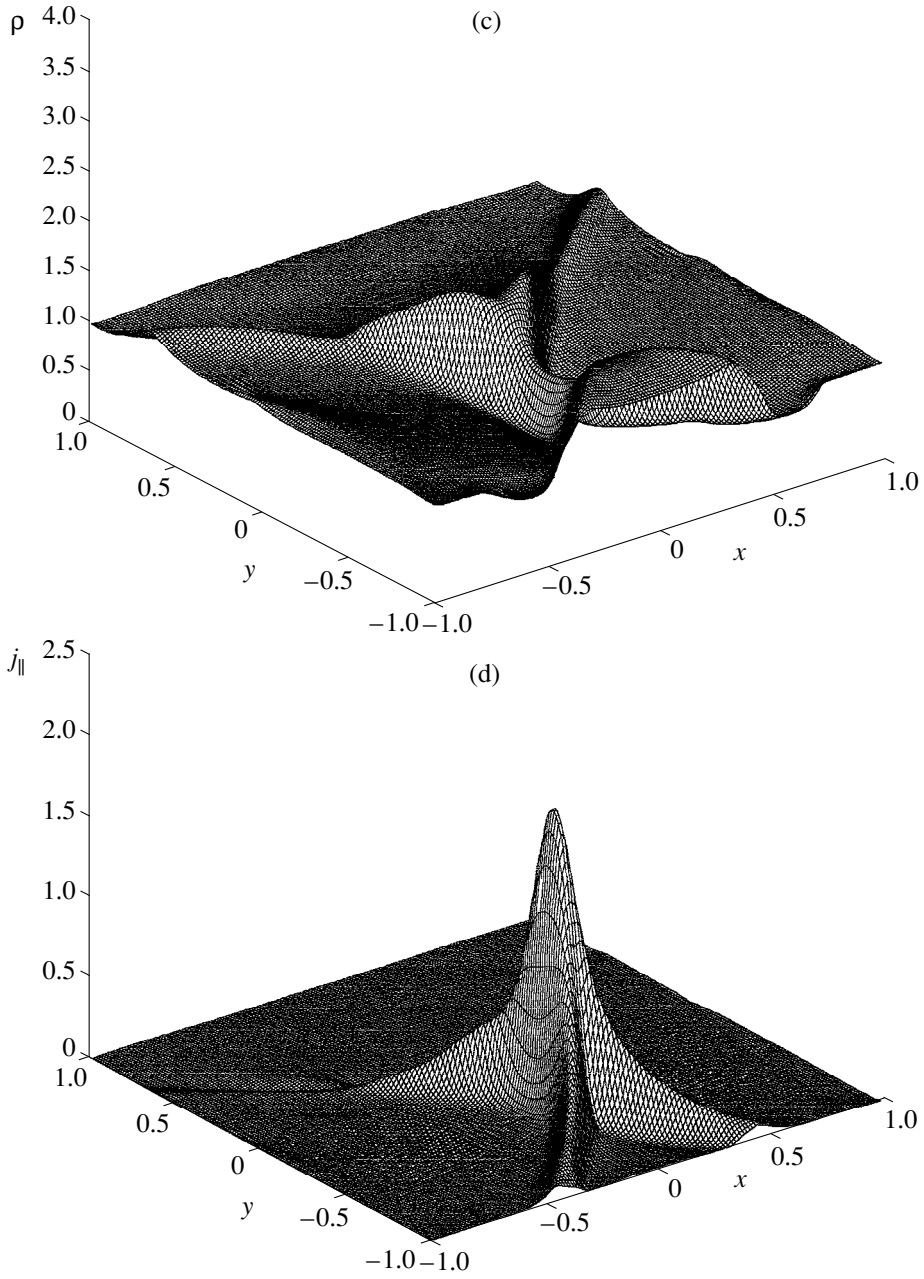

Fig. 7. (Contd.)

z-component of the vector potential as

$$A(x, y, t) = A_0(x, y) + \sin\phi f(t + \ln r), \qquad (27)$$

where $r = \sqrt{x^2 + y^2}$ and ϕ are ordinary polar coordinates and the function $f(\xi)$ is defined by (22).

As in the case of modeling a system with two X-lines, we imposed conventional gas-dynamic boundary conditions on the plasma density and plasma pressure: at the boundary regions through which the plasma enters the calculation domain, we set $\rho = 1$ and $p = 1$, and at the remaining boundary regions (where the plasma freely flows out of the domain) the derivatives of the plasma density and plasma pressure along the characteristics were set to be equal to zero.

As in the case of numerical modeling described above, the magnetic diffusivity was equal to $\tilde{\nu}_m = 0.006$ and the plasma pressure corresponded to $\tilde{\beta} = 0.012$. The dimensionless thermal conductivity and dimensionless electric field were again chosen to be $\tilde{k} = 0.01$ and $\tilde{E} = 0.03$. We treated only the boundary conditions (27) with $B_1 = 0$ in (24), which refer to mag-

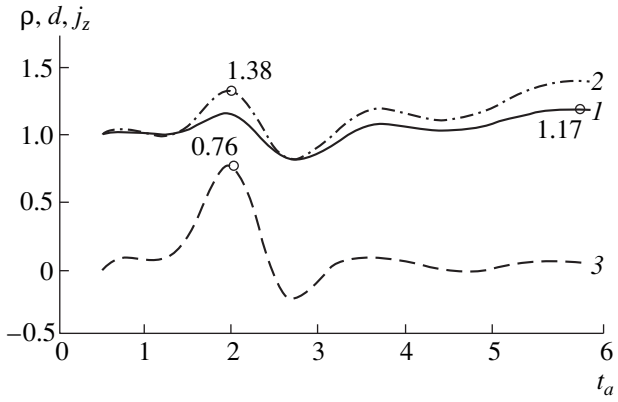

Fig. 8. Time evolutions of (*1*) the plasma density, (*2*) plasma pressure, and (*3*) electric current density in a magnetic configuration with one magnetic null line. At each instant, all of the quantities are taken at the point at which the component j_z is the highest. The maximum values of the parameters are shown by numerals.

netoacoustic perturbations. The boundary conditions corresponding to the excitation of an Alfvén wave at the boundary of the computation region were analyzed in detail in [11].

Figure 6 presents the results of simulation of a magnetoacoustic perturbation in configuration (27): (a) the contours of the *z*-component of the vector potential and (b) the electric current density distribution at $t = 1$ in the linear stage. The antisymmetric magnetoacoustic perturbations illustrated in Fig. 6b are seen to converge.

Figure 7 displays simulation results obtained with boundary conditions analogous to those in Fig. 6: (a) the contours of the *z*-component of the vector potential, (b) the velocity field $\mathbf{v}_\perp = v_x\mathbf{e}_x + v_y\mathbf{e}_y$, (c) the plasma density distribution, and (d) the electric current density distribution. These results were computed at the time $t = 10$. In the vicinity of a null line, one can observe the formation of a current sheet, which is similar to that studied in [1, 10, 11]. From Fig. 7d, we can see that, in the nonlinear stage, the magnetoacoustic perturbation breaks the symmetry of the initial magnetic configuration and a current sheet forms in which the current does not reverse direction. To make the picture more illustrative, in Fig. 7d, the electric current is plotted with the opposite sign, because the plasma flows toward the half-plane where the perturbation amplitude is negative.

Figure 8 shows time evolutions of the plasma density, plasma pressure, and electric current density in a configuration with one magnetic null line, all computed at the point at which the electric current density in the sheet is the highest. The maximum values of the parameters are also plotted.

We can see that, by the time $t = 10$, the system has already reached a thermodynamically equilibrium state.

5. CONCLUSION

We have studied the transformation of structurally unstable magnetic configurations into structurally stable configurations. In particular, we have considered the transformation of configurations in which the finite-amplitude net plasma electric current driven by the perturbations excited at the boundary of the computation region is equal to zero. We have shown that, although transformations to magnetic configurations that are not topologically equivalent to the initial configurations are forbidden in ideal magnetohydrodynamics, they can nonetheless occur during magnetic reconnection.

Analyzing a structurally unstable magnetic configuration with the X–X separatrix, we have revealed that the final configuration has no separatrices between two null lines and is far less symmetric in comparison with the initial configuration. The plasma parameters and magnetic field evolve in a fairly complicated manner. A very interesting result is that the plasma density falls off on a time scale of about several Alfvén times. A decrease in the density can be explained by the fact (which was established in [16]) that, in the vicinity of a current sheet, the plasma density behaves as $t^{-\sqrt{2}/2}$.

A nonlinear Alfvén wave gives rise to the formation of both poloidal current sheets along the separatrices and dipole toroidal current sheets. An investigation of the evolution of dipole magnetoacoustic perturbations near the magnetic X-line demonstrates the breakdown of symmetry in the nonlinear stage when the magnetic configuration is displaced by a finite distance and a current sheet forms in which the current does not reverse direction.

ACKNOWLEDGMENTS

We are grateful to V.I. Il'gisonis for valuable remarks. We thank I. Lisi and Scuole Normale Superiore in Pisa (Italy). This work was supported in part by the Russian Foundation for Basic Research, project nos. 96-15-96205 and 99-01-01167.

REFERENCES

1. D. Biskamp, *Nonlinear Magnetohydrodynamics* (Cambridge Univ. Press, Cambridge, 1993).
2. B. B. Kadomtsev, Fiz. Plazmy **1**, 710 (1975) [Sov. J. Plasma Phys. **1**, 389 (1975)].
3. E. R. Priest, *Solar Flare Magnetohydrodynamics* (Gordon and Breach, New York, 1981).
4. V. I. Arnold, *Geometrical Methods in the Theory of Ordinary Differential Equations*, (Nauka, Moscow, 1978; Springer-Verlag, Berlin, 1988).
5. T. Poston and I. Stewart, *Catastrophe Theory and Its Applications* (Pitman, London, 1978; Mir, Moscow, 1980).

6. H. P. Furth, J. K. Killer, and M. N. Rosenbluth, Phys. Fluids **6**, 459 (1963).
7. S. V. Bulanov, V. V. Pichushkin, and K. Schindler, Fiz. Plazmy **22**, 979 (1996) [Plasma Phys. Rep. **22**, 885 (1996)].
8. S. V. Bulanov, V. V. Pichushkin, and K. Schindler, in *Proceedings of International Conference on Plasma Physics, Nagoya, Japan, 1996*, p. 486.
9. S. V. Bulanov, E. Yu. Echkina, I. N. Inovenkov, *et al.*, Phys. Plasmas **6**, 802 (1999).
10. S. V. Bulanov, G. I. Dudnikova, V. P. Zhukov, *et al.*, Phys. Lett. **203**, 219 (1995).
11. S. V. Bulanov, G. I. Dudnikova, T. Zh. Esirkeptov, *et al.*, Fiz. Plazmy **22**, 867 (1996) [Plasma Phys. Rep. **22**, 783 (1996)].
12. S. V. Bulanov and M. A. Ol'shanetskiĭ, Fiz. Plazmy **11**, 727 (1985) [Sov. J. Plasma Phys. **11**, 425 (1985)].
13. J. M. Green, Phys. Fluids A **5**, 2355 (1993).
14. P. A. Sweet, Ann. Rev. Astron. Astrophys. **7**, 149 (1969).
15. J.-I. Sakai and C. de Jager, Space Sci. Rev. **77**, 1 (1996).
16. S. I. Syrovatskii, Ann. Rev. Astron. Astrophys. **19**, 163 (1981).

Translated by G. Shepekina

Plasma Physics Reports, Vol. 26, No. 7, 2000, pp. 575–585. Translated from Fizika Plazmy, Vol. 26, No. 7, 2000, pp. 615–625.

PLASMA TURBULENCE

Parametric Turbulence–Sustained Gas Discharges

A. I. Akhiezer*†, V. S. Mikhaĭlenko, V. V. Ol'shansky*, and K. N. Stepanov***

**Kharkov Institute of Physics and Technology, National Science Center, Akademicheskaya ul. 1, Kharkov, 61108 Ukraine*
***Kharkov State University, pl. Svobody 4, Kharkov, 61077 Ukraine*
Received March 12, 1999; in final form, December 6, 1999

Abstract—A brief review is given of papers on the RF production of a plasma whose electrons are heated due to the parametric turbulence driven by an alternating electric pump field and maintain the discharge by ionizing the working gas atoms. Results are summarized from studies of low-frequency parametric turbulence, specifically, ion-acoustic plasma turbulence in a magnetic field, ion-cyclotron turbulence associated with the excitation of ion Bernstein modes, and lower hybrid turbulence in a plasma with ions of one or two species. The turbulence level and the rate of turbulent heating of the electrons and ions are presented, and the results of modeling of these phenomena are described. Attention is focused on experiments in which low-frequency parametric turbulence may be observed. © *2000 MAIK "Nauka/Interperiodica".*

1. INTRODUCTION

Electron beam propagation through a plasma is accompanied by the excitation of space charge waves and electric fields, i.e., by the onset of the beam–plasma instability, which was discovered as early as 1949 by A.I. Akhiezer, Ya.B. Faĭnberg, D. Bohm, and E. Gross. An electron beam propagating through a neutral gas ionizes neutral particles and, when the electron density reaches a certain critical level, triggers the beam–plasma instability, which in turn gives rise to fluctuating fields and heating of the plasma electrons. In this stage, the gas is ionized by electrons that acquire energy in the interaction with the fluctuating turbulent fields. The discharges of this type, which were discovered in 1959–1960 by Ya.B. Faĭnberg and his colleagues, are called beam–plasma discharges (BPD) and have various applications (see, e.g., [1, 2]).

A plasma in a magnetic field and an alternating electric field with a sufficiently large amplitude is subject to numerous parametric instabilities. If an alternating electric field is switched on at the time $t = 0$ and if its component in the magnetic field direction is sufficiently strong, then the energy gained by the electrons accelerated in such a field is high enough to ionize a neutral gas and thus give rise to an electron avalanche (the transverse electron velocity is assumed to be low, which happens when the magnetic field is not too weak). If the pump field frequency is low, then, as the plasma density increases, the pump field is weakened because of the high plasma permittivity and the screening of the longitudinal electric field. As a result, the avalanche mechanism ceases to produce plasma even when the plasma density is very low, in which case, however, a parametric instability may occur, giving rise to fluctuating electric fields and turbulent heating of the plasma electrons, which continue to ionize the neutral gas. Discharges of this type are naturally called parametric turbulence–sustained discharges.

A plasma in a magnetic field is subject to numerous types of low-frequency oscillations. Many of these can be excited by an external pump field. The frequencies of these oscillations depend on the plasma density. Higher density plasmas are characterized by the onset of parametric instabilities on different oscillation branches, thereby resembling the so-called "relay-race of oscillation branches" (see, e.g., [3]).

In helicon sources, in which the plasma is created by low-frequency electromagnetic waves—whistlers (or helicons), whose frequencies are in the range between the electron-cyclotron and ion-cyclotron frequency—ion-acoustic and/or lower hybrid parametric instabilities can develop and drive the plasma into turbulent motion (see, e.g., [4]). The excitation of Alfvén waves with frequencies below the ion-cyclotron frequency (observed in experiments in the Uragan-3M torsatron [5]) can be accompanied by the parametric excitation of "kinetic" Alfvén modes, electron-acoustic modes, and ion-cyclotron (Bernstein) modes. The development of fast magnetoacoustic waves with frequencies above the ion-cyclotron frequency can also be accompanied by the onset of parametric instabilities on the branches corresponding to these modes and on the lower hybrid branch of oscillations. Parametric phenomena could also be observed in the Uragan-3M [5] and Uragan-3 [6] stellarators in experiments on creating low-temperature plasmas by whistlers in order to clean metal surfaces of the vacuum chamber, stellarator coils, and RF antennas, as well as in the TEXTOR [7, 8], TORE SUPRA [9], and other tokamaks in experiments on RF plasma production by fast magnetoacoustic waves with $\omega \sim \omega_{ci}$ with the purpose of cleaning surfaces.

† Deceased.

1063-780X/00/2607-0575$20.00 © 2000 MAIK "Nauka/Interperiodica"

Here, we briefly review the theory and particle-in-cell (PIC) modeling of ion-acoustic, ion-cyclotron, and lower hybrid parametric instabilities; the turbulence driven by these instabilities; and the related turbulent heating of plasma electrons and ions.

2. ION-ACOUSTIC KINETIC PARAMETRIC TURBULENCE OF A PLASMA IN A MAGNETIC FIELD

If an elliptically polarized low-frequency ($\omega_{ci} \ll \omega_0 \ll \omega_{ce}$) wave propagates in a plasma and if the electron oscillatory velocity $u_\perp = c(E_{0\perp}/B_0)$ in this wave is higher than the ion-acoustic speed $v_s = \sqrt{T_e/m_i}$, then the resonant interaction among the electrons moving along the external magnetic field $\mathbf{B}_0$ with a velocity $v_\parallel$ equal to the phase velocity $v_\parallel = (\omega_s - p\omega_0)/(k_\parallel - pk_{\parallel 0})$ (where $p = 0, \pm 1, \pm 2, \ldots$) of a plasma wave driven by the beatings of the pump wave and ion-acoustic oscillations gives rise to an ion-acoustic instability with the growth rate $\gamma = \gamma_e - \gamma_i - \gamma_\nu$. Here, $\gamma_e = \sum_p \gamma_p$, with γ_p the electron contribution to the growth rate (p is the number of the beat mode); γ_i is the damping rate caused by the interaction of unmagnetized ions with ion-acoustic waves; γ_ν is the rate of collisional damping due to ion viscosity; $\omega_{ci(e)}$ is the ion (electron) gyrofrequency; $\omega_s = kv_s$ is the ion-acoustic frequency; $\mathbf{E}_0$ and ω_0 are the amplitude and frequency of the electric field of the pump wave; and $k_{\parallel 0}$ is the longitudinal wavenumber. If $\gamma \approx \gamma_e \gg \gamma_{i,\nu}$, which is valid for $T_e \gg T_i$ and if the ion temperature is not too low, then, in the case of an elliptically polarized pump wave such that $E_{0x} > E_{0y}$ and

$$k_y \left| \frac{E_{0x}}{E_{0y}} \right| \geq k_x \sim \frac{\omega_0}{v_s} \geq k_y \sim 2\frac{\omega_0}{u_\perp}, \tag{1}$$

the main contribution to the growth rate comes from the $p = 1$ beat mode, so that the maximum growth rate can be estimated as [10]

$$\gamma_e \approx 0.05\sqrt{\omega_{ce}\omega_{ci}}. \tag{2}$$

For short-wavelength ion-acoustic waves, this estimate is valid at $\omega_{pe} \gg \omega_{ce}$ provided that $k_\perp \rho_e \gg 1$, $k_\perp \rho_i \gg 1$, and $k\rho_D \ll 1$ and also under the conditions $2\pi\gamma \gg \omega_{ci}$ and $k_z v_{Te} \ll \omega_{ce}$. Here, $\rho_\alpha = v_{T\alpha}/\omega_{c\alpha}$ are the gyroradii of the electrons ($\alpha = e$) and ions ($\alpha = i$) with the thermal velocities $v_{T\alpha} = \sqrt{T_\alpha/m_\alpha}$ and $\rho_D = v_{Te}/\omega_{pe}$ is the screening length. Under all of the above conditions, the magnetic field has a negligible impact on the ion motion over the time during which the ion-acoustic waves arise but strongly affects the electron motion. In the case of a uniform pump field ($k_{\parallel 0} = 0$), the expressions for γ_e were derived in [11, 12] and, in [10, 13], they were generalized to the case $k_{\parallel 0} \neq 0$.

The saturation of the ion-acoustic instability can be attributed to the induced scattering by ions [14–17]. Since the growth rate under consideration is high ($\gamma \gg \omega_{ci}$), we can neglect the magnetic field effects in calculating the nonlinear damping rate γ_{NL} caused by induced scattering by ions. Equating γ_{NL} to the linear growth rate (2), we can estimate the intensity of the ion-acoustic waves, $W = \int d\mathbf{k}\, W(\mathbf{k})$ with $W(\mathbf{k}) \approx |\varphi_\mathbf{k}|^2/(2\pi v_s^2)$, as [10, 18]

$$\frac{W}{n_0 T_e} \approx \frac{0.05}{\pi\alpha}\frac{T_e}{T_i}\frac{v_s}{u}\frac{\sqrt{\omega_{ce}\omega_{ci}}}{\omega_s}, \tag{3}$$

where the numerical factor α depends on the angular distribution of the spectral intensity in the plane orthogonal to the magnetic field (for an isotropic distribution, we have $\alpha = 1/8$).

Using estimate (3) and the generalized quasilinear kinetic equation for the averaged electron distribution function (specifically, the kinetic equation generalized to the case of finite electron displacements $a_E = (c/\omega_0 B_0)(k_y^2 E_{0x}^2 + k_x^2 E_{0y}^2)^{1/2} \geq 1$ in the pump field [19]), we arrive at the following expression for the rate of turbulent heating of the electrons, $1/\tau_h = |d\ln T_{e\parallel}/dt|$ [10]:

$$\frac{1}{\tau_h} \sim \frac{2.5 \times 10^{-3}}{\pi\alpha}\frac{\omega_{ce}\omega_{ci}}{\omega_0}\frac{T_e}{T_i}. \tag{4}$$

With the help of the energy balance relation

$$2\nu_{\text{eff}}\frac{k_0^2 c^2}{\omega_{pe}^2} W_0 \sim n_0 \frac{dT_{e\parallel}}{dt} = \frac{n_0 T_{e\parallel}}{\tau_h}, \tag{5}$$

where $k_0 = \dfrac{\omega_{pe}^2 \omega_0}{\omega_{ce} k_{0\parallel} c^2}$ is the helicon wavenumber, $k_{\parallel 0}$ is the projection of the helicon wave vector onto the magnetic field direction, ω_0 is the helicon frequency, and $W_0 \approx |\mathbf{B}^\sim|^2/16\pi \approx (1/2)(m_e n_0 u_\perp^2)(\omega_{ce}/\omega_0)(k_{0\parallel}/k_0)$ is the helicon energy density, we can write the effective damping rate of the helicons in the form [10]

$$\nu_{\text{eff}} \sim \gamma_e \frac{T_e}{2\pi\alpha T_i}\frac{\gamma}{\omega_s}\frac{v_{Te}^2}{u_\perp^2}. \tag{6}$$

This relation allows us to estimate the distance over which the helicons are damped along the magnetic field as $l_{\text{turb}} \sim \omega_{ce}/k_0\nu_{\text{eff}}$.

Formulas (2)–(5) provide a comparison with the results of experiments with helicon sources described in [20, 21], which present data on the parameters of the sources and helicons.

Typical parameter values of a helicon source are as follows: the working gas is argon at a pressure of 15 mtorr, the plasma radius is 2.5 cm, the source length is 160 cm, the longitudinal magnetic field is 800 G, the

antenna device of length 15 cm excites modes with the azimuthal numbers $m = 0$ and ± 1, the generator frequency is $\omega_0 = 1.7 \times 10^8$ s^{-1}, the input power is P = 1–2 kW, and the plasma density is about $\sim 10^{13}$ cm^{-3}. The central plasma temperature increases along the discharge axis (the z-axis) from 3 eV in the antenna region ($|z| \le 7$ cm) to the maximum value (4.5 eV) at a distance $\Delta z \simeq 15$ cm from the antenna edge and, farther out, it decreases monotonically down to 2 eV at a distance $\Delta z = 80$ cm from the antenna. The amplitude of the helicon magnetic field is maximum near the antenna, $|\tilde{B_z}| = 7$ G, and decreases gradually along the discharge axis in such a way that $|\tilde{B_z}| = 4$ G at $\Delta z = 15$ cm and $|\tilde{B_z}| = 3$ G at $\Delta z = 45$ cm. A helicon resembles a standing wave, which is a superposition of different modes, the $m = -1$ mode amplitude being the maximum. The typical values of the wavenumbers are $k_{\|0} \sim \pi/L_\| \sim 0.3$ cm^{-1} and $k_{0r} \sim 1.6$ cm^{-1}. In this case, the amplitudes of the components of the helicon electric field are $E_{0r} = E_{0x} \approx 24$ V/cm, $E_{0\varphi} = E_{0y} \sim 6$ V/cm, and $E_{0z} \sim 0.03$ V/cm, which indicates that the elliptic polarization of a helicon is highly pronounced.

Since, under these conditions, the transverse velocity of a helicon, $u_y = c(E_{0x}/B_0) \sim 3 \times 10^6$ cm/s, is one order of magnitude higher than the ion-acoustic speed $v_s = 3.1 \times 10^5$ cm/s ($T_e = 4$ eV), a short-wavelength ion-acoustic parametric instability can arise with the parameters $\omega_s \sim 0.7\omega_0 \sim 1.2 \times 10^8$ s^{-1}, $k_x \sim \omega_s/v_s \sim 400$ cm^{-1}, $k_y \sim 1.8\omega_0/u_\perp \sim 50$ cm^{-1}, and $k_\| \sim 0.6$ cm^{-1}. Unfortunately, the data on the ion temperature T_i were not given in [20, 21]. If we assume that $T_e/T_i = 20$ (i.e., $T_i = 2200$ K), then we obtain $\gamma_i = 3 \times 10^5$ s^{-1}, $\gamma_\nu = 1.6 \times 10^5$ s^{-1}, and $\gamma_e = 2.3 \times 10^6$ s^{-1}, so that $\gamma = \gamma_e - \gamma_i - \gamma_\nu = 1.8 \times 10^6$ s^{-1}.

At a distance of 25 cm from the antenna and farther out, the electron temperature does not exceed 3 eV and the ion-acoustic turbulence is suppressed by intense Landau damping by ions. The electron temperature reaches its maximum value $T_e = 4.5$ eV at a distance $\Delta z = 15$ cm from the antenna edge. This is the region where both the rate at which Ar atoms are ionized and the emission intensity of Ar^+ atoms are the highest. The ions from the region $\Delta z > 0$ propagate toward the antenna at the ion-acoustic speed (the working gas is admitted at $\Delta z \sim 40$ cm). The energy acquired by the ions in transit ($\Delta t \sim \Delta z/v_s \sim 5 \times 10^{-5}$ s) through the region where the ionization rate is the highest ($\Delta z \sim 15$ cm) is $\Delta t_i/T_e \sim \Delta t/\tau_\varepsilon$, where $\tau_\varepsilon = m_i/(2m_e\nu_{ei}) = 10^{-3}$ s is the time scale on which the energy is exchanged between the electrons and ions and $\nu_{ei} = 3.8 \times 10^7$ s^{-1} is the electron–ion (e–i) collision frequency at $T_e = 4$ eV. This indicates that $T_e/\Delta T_i \sim 20$; thus, in order of magnitude, we have $\Delta T_i \approx T_i$, which agrees with the above assumption $T_e/T_i = 20$. In calculating T_i as a function of T_e with allowance for the increment in T_i due to e–i collisions and energy losses due to charge exchange, Chen [22] found that, at $T_e = 4$ eV, the electron to ion temperature ratio is $T_e/T_i \approx 17$, which is also close to the estimate adopted here. Hence, under the experimental conditions of [20, 21], the ion-acoustic turbulence can occur only in the region near the antenna, $\Delta z \lesssim 20$ cm.

Using estimates (3)–(5) for the energy W of the ion-acoustic waves, the heating rate $1/\tau_h$, and the frequency ν_{eff}, we obtain (for $T_e = 4$ eV) $W/n_0T_e \sim 0.8$, $\nu_{\text{eff}} \sim 4 \times 10^8$ s^{-1}, and $l_{\text{turb}} \sim \omega_{ce}/k_0\nu_{\text{eff}} \sim 20$ cm. The last estimate agrees with the measurement results of [20, 21]. The effective collision frequency is one order of magnitude higher than the frequency of binary collisions (for $T_e = 4$ eV, the length scale for the collisional damping of a helicon is $l_{\text{coll}} \sim \omega_{ce}/k_0\nu_{ei} \sim 2$ m).

The proposed turbulent mechanism for heating the electrons and sustaining a helicon discharge is also supported by the analysis performed by Chen [21], who found that the electron temperature is a decreasing function of z because of the collisional electron heat transfer along the magnetic field. Chen's calculations showed that the $T_e(z)$ profiles obtained with and without allowance for the collisional absorption of a helicon essentially coincide with one another and with the experimental profiles. This indicates that the heat is transferred from the "hot" region (near the origin of the z-coordinate), where the electron temperature is the highest, along the z-axis via classical heat conduction. The region $\Delta z \le 20$ cm near the antenna is characterized by turbulent electron heating. Using estimate (5), we find that the helicon power absorbed in this region is $P \sim (n_0T_e/\tau_h)\pi r^2\Delta z \sim 1$, which agrees with the experimental data of [20, 21].

If the pump field frequency ω_0 is below the lower hybrid frequency $\sqrt{\omega_{ce}\omega_{ci}}$, then long-wavelength ($k_x\rho_{Le} < 1$) ion-acoustic waves can be excited whose frequency and growth rate are equal in order of magnitude to

$$\omega \sim k v_s, \tag{7}$$

$$\frac{\gamma}{\omega_s} \sim -\frac{\sqrt{\pi}}{2} J_1^2(a_E) z_1 e^{-z_1^2} \sim 0.4 J_1^2(a_E), \tag{8}$$

where $z_1 = (\omega - \omega_0)/\sqrt{2}\,|k_\| - k_{\|0}|v_{Te} = -1/\sqrt{2}$. In this case, the frequency and growth rate should be determined from the dispersion relation in the form of an infinite-order determinant, which cannot be solved by equating its diagonal elements to zero (as is done in the range $k\rho_{Le} \gg 1$) and requires a numerical treatment.

When $\omega_0 \le \sqrt{\omega_{ce}\omega_{ci}}$, which is typical of experiments on the RF production of low-temperature plasmas in the Uragan-3M [5] and Uragan-3 [6] stellarators, the TEXTOR tokamak [7, 8], and the TORE SUPRA tokamak with superconducting windings [9],

we may expect the onset of lower hybrid parametric instabilities.

3. ION-CYCLOTRON PARAMETRIC INSTABILITY

If the pump frequency is on the order of the ion-cyclotron frequency ($\omega_0 \sim \omega_{ci}$), then ion-cyclotron waves (ion Bernstein modes) can be excited parametrically. The situation in which the relative oscillatory velocity $u_\perp$ of the electrons with respect to the ions is below the ion thermal velocity ($u < v_{Ti}$) is characterized by the coherent excitation of short-wavelength ($k_\perp \rho_{Li} \gg 1$, where ρ_{Li} is the ion gyroradius) cyclotron waves under the resonance conditions $\omega^{(n)} - \omega^{(l)} \approx N\omega_0$, where $\omega^{(n)}$ and $\omega^{(l)}$ are the frequencies of the ion-cyclotron modes and N is an integer. In this case, the resonant particles affect the dispersion of unstable waves only slightly if $z_e = |\omega^{(n)} + m\omega_0|/\sqrt{2}\, k_\parallel v_{Te} \gg 1$ or $|z_e| \ll 1$ and $z_s = |\omega^{(n)} - s\omega_{ci} + m\omega_0|/\sqrt{2}\, k_\parallel v_{Ti} \gg 1$ ($m = 0, \pm 1, \ldots$), so that we can speak of a hydrodynamic instability. If the magnetic field–aligned velocity of the resonant electrons, which is equal to the phase velocity $(\omega^{(n)} + m\omega_0)/k_\parallel$ of the beat wave, is on the order of their thermal velocity ($|z_e| \sim 1$) but $|z_s| \gg 1$, then the resonant electrons can give rise to ion-cyclotron waves under the condition $\omega^{(n)} \approx (N/2)\omega_0$, where the integers N are even. (Different possible mechanisms for the parametric excitation of hydrodynamic [23] and kinetic [24] ion-cyclotron instabilities were examined by Kitsenko *et al.*)

In the range $k_\perp \rho_{Li} \gg 1$, the frequencies $\omega^{(n)}$ and growth rates of the ion-cyclotron parametric instabilities at $T_e \sim T_i$ have the form [24]

$$\omega^{(n)} = n\omega_{ci} + \delta\omega, \quad \frac{\delta\omega}{n\omega_{ci}} \simeq \frac{1}{\sqrt{2\pi} k_\perp \rho_{Li}}, \tag{9}$$

$$\frac{\gamma}{\omega_{ci}} \sim \frac{0.1}{k\rho_{Li}}. \tag{10}$$

These instabilities are saturated in the highly nonlinear stage, in which the nonlinear broadening of cyclotron resonances becomes important and the growth rate vanishes when the oscillation level is equal to [19, 25]

$$\frac{W}{nT} \sim \left(\frac{u_\perp}{v_{Ti}}\right)^4 \quad (T_e \sim T_i). \tag{11}$$

In this case, the rates at which the longitudinal electron temperature $T_{\parallel e}$ and the transverse ion temperature $T_{\perp i}$ grow are equal in order of magnitude to [19]

$$\frac{1}{\tau_h} \equiv \frac{d\ln T}{dt} \sim \left(\frac{u_\perp}{v_{Ti}}\right)^5 \omega_{ci}. \tag{12}$$

PIC simulations of this instability confirmed that these estimates are valid for plasmas with a single ion species [26–28] (see Figs. 1, 2) and with two ion species [29]. The frequency spectra of the largest–amplitude spatial Fourier harmonics analyzed on a time scale including the time interval over which the waves become strongly nonlinear were found to be consistent with the spectra evaluated using linear theory by solving the dispersion relation (in the form of an infinite-order determinant) with allowance for the deformation

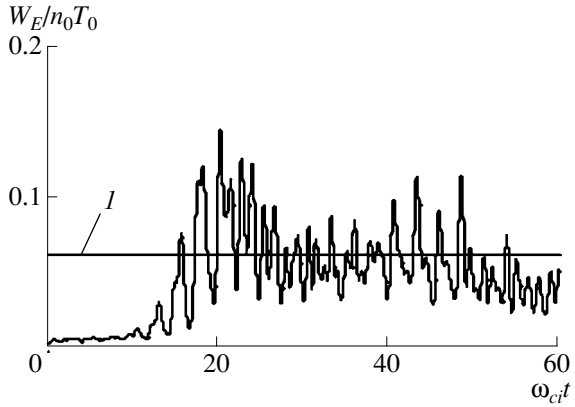

Fig. 1. Time evolutions of the energy density of the electric field of ion-cyclotron waves and electron-acoustic modes. Curve *1* illustrates the theoretical level of oscillations estimated from equation (11) for the pump frequency $\omega_0 = 1.2\omega_{ci}$ and the relative oscillatory velocity $u = 0.9v_{Ti}(0)$ of the electrons with respect to ions at $\omega_{pe}/\omega_{ce} = 0.25$ and $m_i = 100m_e$.

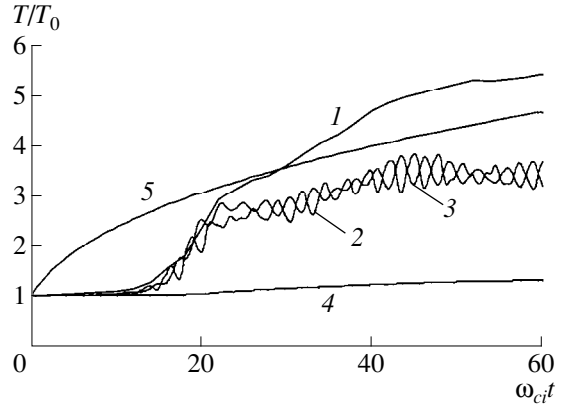

Fig. 2. Time evolutions of (*1*) the longitudinal electron temperature $T_{\parallel e}$, transverse ion temperatures, (*2*) T_{xi} and (*3*) T_{yi}, and (*4*) longitudinal ion temperature $T_{\parallel i}$ for the same parameters as in Fig. 1. Curve *5* illustrates the theoretical evolutions $T_{\parallel e}(t)$ and $T_{\perp i}(t)$ traced using equation (12).

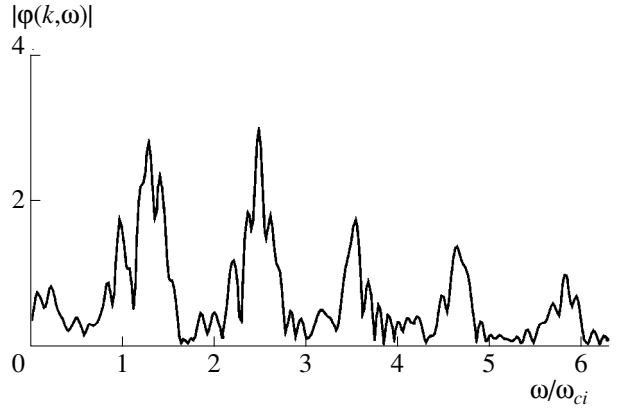

Fig. 3. Frequency spectrum of the most unstable mode for $\omega_0 = 1.2\omega_{ci}$, $k_\perp\rho_{Li} = 1$, $k_\parallel\rho_{Li} = 0.05$, $u = 0.9v_{Ti}(0)$, $\omega_{pe}/\omega_{ce} = 0.25$, and $m_i = 100m_e$.

of the spectrum shape by the pump field. Figure 3 shows the frequency spectrum of the fastest growing mode ($k_\perp\rho_i = 1$ and $k_\parallel\rho_i = 0.05$) over the interval $\omega_{ci}t = 60$, and Fig. 4 presents the frequencies (Fig. 4a) and growth rates (Fig. 4b) obtained by solving the linear dispersion relation. The solutions to the dispersion relation in Fig. 4a correspond to the spectral peaks in Fig. 3.

The development of the parametric instability is accompanied by the onset of dynamic chaos in the particle motion and in the evolution of the self-consistent field. Figure 5 shows the maximum Lyapunov exponential index as a function of the initial longitudinal electron velocity normalized to the initial electron thermal speed. The Lyapunov exponential index is equal in order of magnitude to the linear growth rate. Figure 6 illustrates the autocorrelation function for the self-consistent field. We can see that the decorrelation time is about several periods of the pump field (or several inverse growth rates).

The development of dynamic chaos is also evidenced by the fact that the phase volume is not conserved as time elapses. Figure 7 illustrates the time evolution of a volume element in the electron phase plane $(z, v_\parallel)$. At the initial instant $t = 0$, the volume element is a unit circle in the coordinate plane $(z/\rho_i, v_\parallel/v_{Ti})$. At the time $\omega_{ci}t = 20$, the circle is displaced to the right by the distances $\Delta z \approx 4\rho_i$ and $v_\parallel \approx 0.1v_{Te}$ along the corresponding axes and its shape is distorted. At the time $\omega_{ci}t = 40$ (when nonlinear effects are more pronounced), the circle becomes very narrow and resembles a boomerang. At the time $\omega_{ci}t = 60$, the circle evolves into two closely spaced, long, thin filaments. At the time $\omega_{ci}t = 100$, the filaments become thinner and break up into several parts, some of which experience a complicated motion. Numerical modeling shows that, in the range $u/v_{Ti}(0) < 0.9$, the wave intensity and heating rate decrease sharply with u, in accordance with (11) and (12).

Based on the investigations described above, Besedin *et al.* [30] simulated the particle and energy balance in experiments on the RF production and heating of plasmas in the Uragan-3M torsatron. Those experiments were carried out with an unshielded loop antenna, which created both the longitudinal field required for RF breakdown and the generation of a slow (electrostatic) oscillation branch in the stage of excitation of electromagnetic waves in the plasma and the transverse field required for the generation of an electromagnetic Alfvén wave. The excitation of waves under the conditions $\omega_0/\omega_{ci} = 0.8$ and $B_0 = 0.45$ T (the absorbed power being $P_{RF} \le 200$ kW) made it possible to produce a plasma with the density $\bar{n}_e = 2 \times 10^{12}$ cm^{-3} and to carry out measurements in a decaying plasma

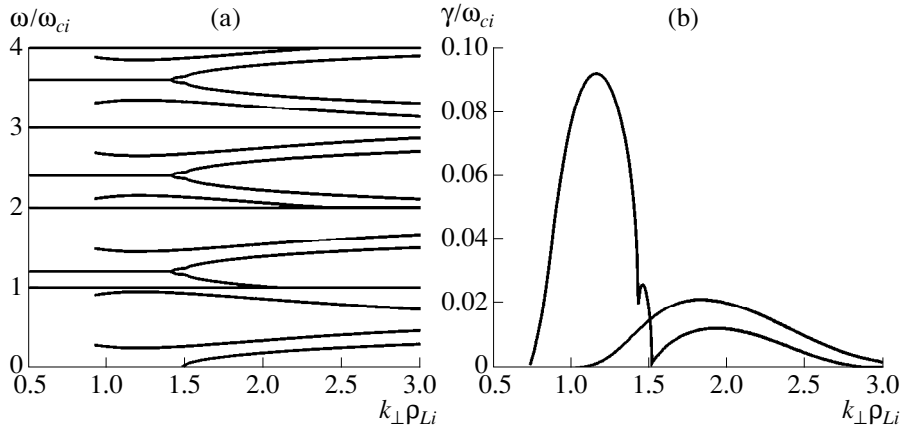

Fig. 4. Solution to the linear dispersion relation for the same parameters as in Fig. 3: (a) oscillation frequency and (b) growth rate.

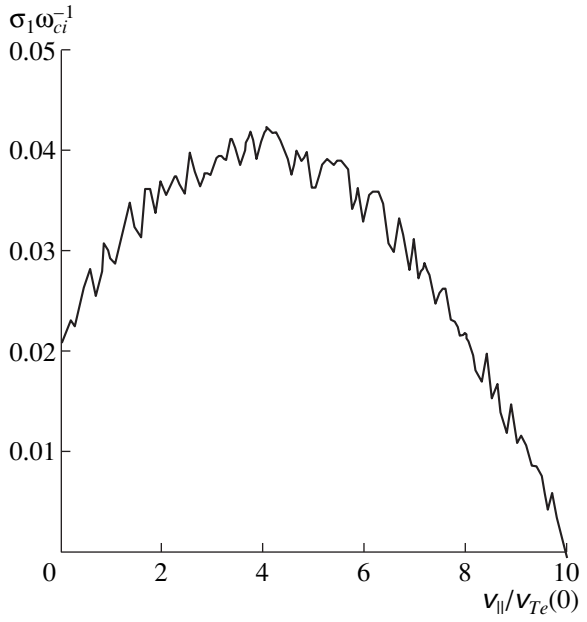

Fig. 5. Maximum Lyapunov exponential index vs. the initial longitudinal electron velocity for the same parameters as in Fig. 3.

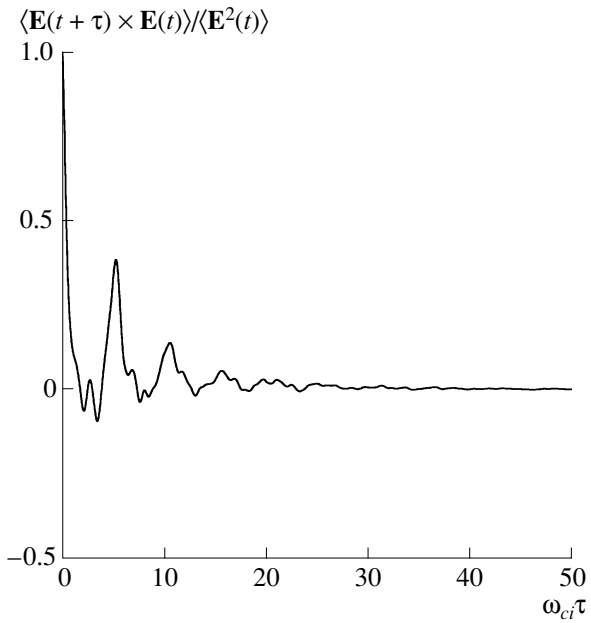

Fig. 6. Autocorrelation function for the electric field of unstable waves for the same parameters as in Fig. 3.

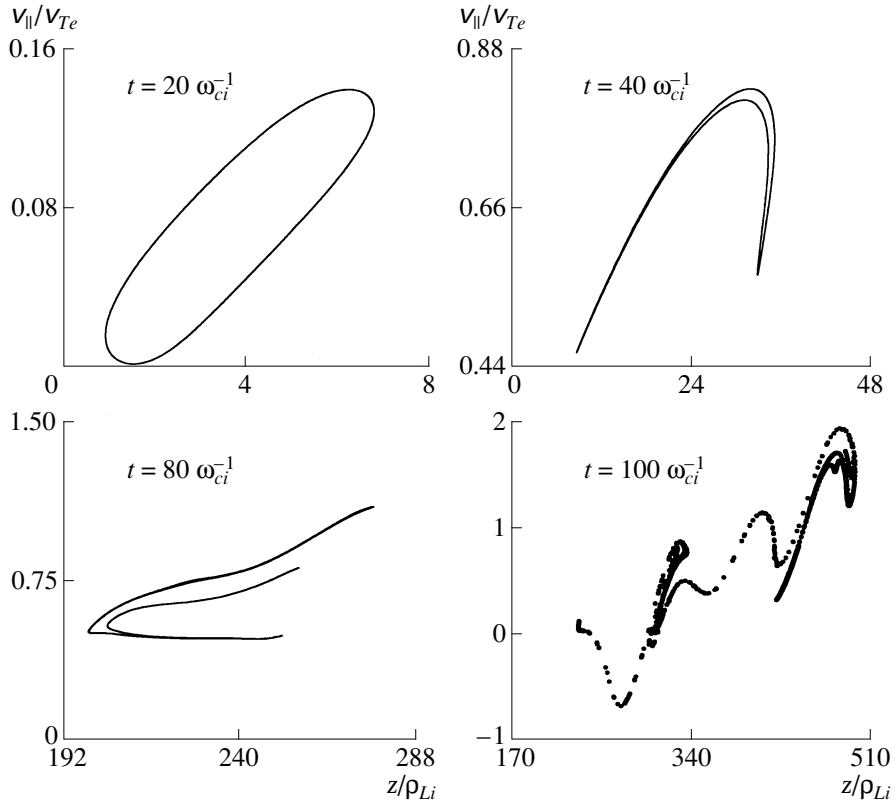

Fig. 7. Time evolution of a volume element in the electron phase plane (z, v_z). At $t = 0$, the volume element is a unit circle in the coordinate plane (z/ρ_{Li}, v_z/v_{Ti}).

(after the RF pulse was switched off). The linear absorption mechanisms (collisional and collisionless cyclotron damping) failed to explain the heating of the ion plasma component (hydrogen). Using the model of an inhomogeneous plasma cylinder and a realistic model of the antenna, Besedin *et al.* [31] calculated the distribution of the electromagnetic field generated by the antenna in order to determine the turbulent heating rate for plasma electrons and ions, $1/\tau_h$ in (12), assuming the current J_A in the antenna is prescribed. However, this plasma model accounts solely for the radial plasma inhomogeneity and may thus lead to significant errors in determining the field distribution in the local Alfvén resonance region, where the plasma density and magnetic field can be highly nonuniform in three dimensions. Consequently, the power deposition profile calculated in [31] can yield only order-of-magnitude estimates. The turbulent heating rate $1/\tau_h$, which turns out to be equal to 3×10^4 s^{-1} in the main plasma ($r/r_p \le 0.8$), increases sharply to 2.5×10^5 s^{-1} at the plasma boundary $r = r_p$ (where r_p is the plasma radius) and, in a tenuous plasma outside the antenna, it becomes as high as 3×10^5 s^{-1}. The antenna current J_A was adjusted to achieve the best agreement between the calculated and experimentally measured fractions of the plasma-deposited RF power, taking into account the turbulent absorption of RF power by the ions and electrons and the electron Cherenkov absorption. In addition, the flow of a neutral gas admitted into the working volume of the plasma (the neutral pressure) was assumed to be prescribed and account was taken of such processes as neutral gas ionization, inelastic electron–electron collisions, neoclassical diffusion and neoclassical heat conduction (which are important in the main plasma, $r/r_p \le 0.8$), and anomalous diffusion and anomalous heat conduction (which are important in the plasma edge region, $r/r_p \ge 0.8$).

The results of this modeling can be summarized as follows:

(i) the mechanisms for both ion heating (the central ion temperature is close to the experimentally measured temperature) and the generation of hot ions, which accumulate in the edge region, are established;

(ii) the calculated central electron temperature $T_e(0)$ and the calculated electron temperature profile $T_e(r)$ agree well with those measured in experiments;

(iii) the calculated electron density profile $n_e(r)$ coincides with the experimental profile;

(iv) in accordance with the experiment [5], the ambipolar field calculated from the condition that the electron and ion fluxes are equal to each other is positive at the plasma edge;

(v) the calculated neutral density coincides with the measured one (see also [32]).

The agreement between the results from this transport model for Uragan-3M and the experimental data allows us to conclude that the model is capable of qualitatively (and even quantitatively) describing the real situation, in particular, the mechanism for plasma heating.

In the ion-cyclotron frequency range, parametric phenomena were observed in straight systems [33–37]; in the toroidal ATC device (with a zero rotational transform) [38–41]; in the ASDEX [42, 43], TEXTOR [44, 45], JET [46], JT-60 [47], and D-IIID [48] tokamaks; and in the Uragan-3M torsatron [49, 50].

4. LOWER HYBRID PARAMETRIC INSTABILITY

A sufficiently strong pump wave ($v_{Ti} \ll u \ll v_{Te}$) with a frequency close to the lower hybrid frequency $\omega_{lh} = \omega_{pi}(1 + \omega_{pe}^2/\omega_{ce}^2)^{-1/2}$ ($\omega_0 \sim \omega_{lh}$) can give rise to electrostatic hydrodynamic waves ($\omega > k_\parallel v_{Te}$). In the absence of the pump field, the frequencies of these waves are equal to

$$\omega(\mathbf{k}) = \omega_{lh}(1 + q)^{1/2}, \quad q = (m_i/m_e)(k_\parallel^2/k^2). \quad (13)$$

In the range $q \gg 1$, for $\omega_0 \approx n\omega(\mathbf{k})$, the growth rate has the form

$$\gamma \sim \gamma_{\max} = \left(\frac{1}{2q} J_n^2(a_E)\right)^{1/3} \omega. \quad (14)$$

In the range $q \ll 1$, for $\omega_0 \approx n\omega_{lh}$, we have

$$\gamma \sim \gamma_{\max} = \left(\frac{1}{2} q J_n^2(a_E)\right)^{1/3} \omega_{lh}. \quad (15)$$

In the case of small displacements, $a_E \sim (ku)/\omega_0 \ll 1$, the wave frequency is described by formula (13) and the growth rate is equal to

$$\gamma \sim \gamma_{\max} = 1/2(q_1 a_E^2)^{1/3} \omega, \quad q_1 = q/(1 + q)^2. \quad (16)$$

In both ranges $q \gg 1$ and $q \ll 1$, expression (16) coincides with (14) and (15) taken in the limit $a_E \ll 1$.

If $q \sim 1$, then, for $a_E \approx 1$, the wave frequency differs from the frequency (13) because of the presence of the pump field. However, in order of magnitude, the wave frequency remains equal to (13), so that we have

$$\omega_0 \sim \omega(\mathbf{k}) \sim \omega_{lh} \sim \gamma \sim ku \ (q \sim 1). \quad (17)$$

The above expressions for the growth rate in the ranges $q \gg 1$ and $q \ll 1$ (for $a_E \sim 1$) and in the range $q \sim 1$ (for $a_E \ll 1$) were derived in [11, 51, 52]. Formula (14) was obtained earlier by Aliev *et al.* [53], and formula (15) was obtained by Porkolab [54] in the limit $a_E \ll 1$. The dispersion relation for parametrically unstable lower hybrid waves was analyzed numerically in a recent paper by Baĭtin and Ivanov [55].

We can expect that, when the lower hybrid parametric instability saturates, the nonlinear terms in the equations of motion and the electron continuity equation will become comparable in order of magnitude to the

linear terms. Then, we can use estimates (17) to obtain that, in the range $q \sim 1$, the electric field amplitude $\tilde{E}$ of the lower hybrid waves, the electron oscillatory velocity $\tilde{v}_e$, the electron displacement $\tilde{\xi}$, the deviation $\tilde{n}_e$ of the electron density from its equilibrium value, and the energy density W of the lower hybrid waves are equal in order of magnitude to

$$\tilde{E} \sim (u/c)B_0, \tag{18}$$

$$\tilde{v}_e \sim (c/B_0^2)|\tilde{\mathbf{E}} \times \tilde{\mathbf{B}}_0| \sim u, \tag{19}$$

$$k\tilde{\xi} \sim 1 \ (\tilde{\xi} \sim \tilde{v}_e/\omega_0), \tag{20}$$

$$|\tilde{n}_e|/n_0 \sim \omega_{lh}/\omega_{ce}, \tag{21}$$

$$\frac{W}{n_0 T_e} \sim \left(\frac{u}{v_{Te}}\right)^2 \left(1 + \frac{\omega_{ce}^2}{\omega_{pe}^2}\right). \tag{22}$$

The rates at which the longitudinal electron temperature and transverse ion temperature grow under the action of stochastic turbulent oscillations can be estimated as

$$\frac{dT_{\perp i}}{dt} \sim \frac{\omega_{ci}^2}{\omega_{lh}} \frac{m_i u^2}{2}, \quad \frac{dT_{\parallel e}}{dt} \sim \frac{\omega_{ci}^2}{\omega_{lh}} \frac{m_i u^2}{2} \frac{u}{v_s}. \tag{23}$$

Estimates (18)–(23) for the lower hybrid beam instability of a plasma with a transverse current were derived in [56–63] under the condition $\omega_0 \ll \omega_{lh}$. In those papers, one can also find analogous estimates obtained at $u < v_{Ti}$ and $T_i \gg T_e$ for the electron-acoustic instability, which develops under the same conditions and is closely related to the lower hybrid instability. In order to describe the electron-acoustic instability, we can use the adiabatic approximation and assume that the velocity u is constant, i.e., that it does not change during the instability. The frequency $\omega(\mathbf{k})$, growth rate $\gamma(\mathbf{k})$, and wave vector $\mathbf{k}$ of this instability are equal in order of magnitude to those in relationship (17) for the lower hybrid parametric instability. We can therefore expect [11] that the electron-acoustic instability will possess the same nonlinear properties as those described by estimates (18)–(23) for the lower hybrid beam instability in a plasma with a transverse current.

The nonlinear damping rate, which, according to the theory of weak turbulence, lowers the growth rate, is proportional to $|\mathbf{k} \times \mathbf{k}'|_z^2$. In other words, unstable waves that are saturated at the level described by estimates (18)–(22) are essentially three-dimensional: the inequality $|\mathbf{k} \times \mathbf{k}'|_z^2 \neq 0$ holds only for $k_x \neq 0$ and $k_y \neq 0$, while the growing waves are those with $k_z \neq 0$. Modeling of these instabilities for the case of two-dimensional waves with ($k_x \neq 0$, $k_y = 0$, $k_z \neq 0$) showed that the instabilities saturate from a trapping of the electrons in the electric field of the waves at a level significantly above that described by (18).

Kitsenko *et al.* [64] modeled the lower hybrid instability in a plasma containing two ion species with masses m_1 and m_2. The frequency and growth rate of the lower hybrid parametric instability occurring in such a plasma in the range $u \gg v_{Ti}$ ($i = 1, 2$) have the form

$$\omega_0 \sim \omega(\mathbf{k}) \sim \gamma \sim ku \sim \omega_{lh}, \quad k_\parallel/k \ll \sqrt{m_e/m_i}, \tag{24}$$

where

$$\omega_{lh} = \left(\frac{\omega_{p1}^2 + \omega_{p2}^2}{1 + \omega_{pe}^2/\omega_{ce}^2}\right)^{1/2}. \tag{25}$$

Two-dimensional PIC simulations of this instability in the ranges $\omega_0 > \omega_{lk}$ and $\omega_0 < \omega_{lh}$ (for $k_z = 0$ and $\omega_{pe}^2 \ll \omega_{ce}^2$) [64] showed the excitation of waves with frequencies and wavenumbers described by (24). The development of the lower hybrid instability is accompanied by effective heating of the ions of both species. The instability saturates when the ion thermal velocity becomes comparable with the relative velocity of the ions of one species with respect to the ions of another species, $v_{Ti} \sim u$, in which case the ion motion becomes highly nonlinear. The nonlinear terms in the equations of electron motion can be neglected when $\omega_{pe}^2 \ll \omega_{ce}^2$. In reality, it is likely that the lower hybrid parametric instability also occurs in the range $u < v_{Ti}$, in which decay processes involving ion-cyclotron waves are possible in principle. In this case, the turbulent heating rate is lower and the established temperature is governed by heat losses, as is the case with other heating mechanisms.

If the pump frequency is on the order of the ion-cyclotron frequency, $\omega_0 \sim \omega_{ci}$, then, in a plasma with two ion species, ion-cyclotron waves can be excited parametrically. Kasilov *et al.* [65] carried out PIC simulations of this instability (at $\omega_{p1}/\omega_{c1} = 5$, $\omega_{pe}^2/\omega_{ce}^2 \ll 1$, $m_2 = 2m_1$, $n_{01} = n_{02}$, $m_1 = 100m_e$) in the case of two-dimensional inhomogeneous unstable waves and sufficiently strong ($u/v_{T1}(0) = 8.2$, 4.1, and 3.2) pump fields and under the ion–ion hybrid resonance condition $\omega_0 = \omega_{ii}$, where

$$\omega_{ii} = \left(\frac{\omega_{c1}^2\omega_{p2}^2 + \omega_{c2}^2\omega_{p1}^2}{\omega_{p1}^2 + \omega_{p2}^2}\right)^{1/2}. \tag{26}$$

Kasilov *et al.* inferred the excitation of long-wavelength ($k_2\rho_{Li} \ll 1$) waves and found that the ion temperature increased significantly (by a factor of 20.5, and 2.5, respectively). For $u/v_{T1}(0) = 2.1$, the ion temperature was found to increase by 10% (Fig. 8). The most unstable modes are those with $k_x\rho_i \sim k_y\rho_i \leq 0.1$. In accordance with linear theory, the frequency spectra

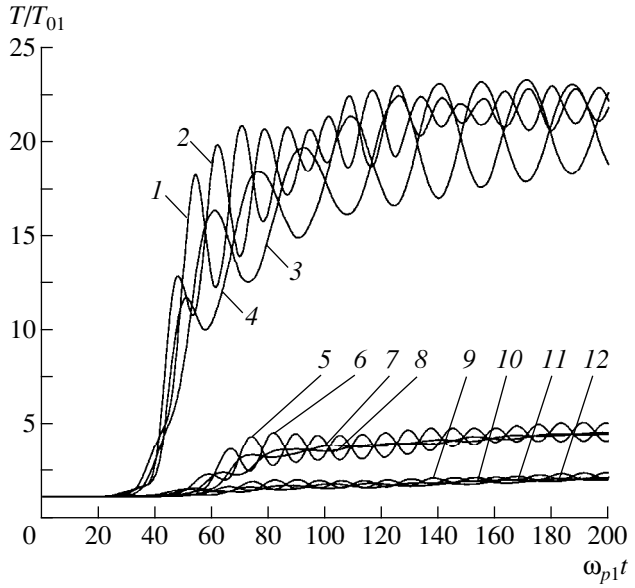

Fig. 8. Time evolutions of the transverse temperatures of the ions of two species, (T_{1x}, T_{1y}) and (T_{2x}, T_{2y}), at $\omega_0 = \omega_{ii} = 0.14\omega_{p1}$ for different pump field amplitudes: curves *1–4* correspond to $u/v_{T1}(0) = 8.2$, curves *5–8* correspond to $u/v_{T1}(0) = 4.1$, and curves *9–12* correspond to $u/v_{T1}(0) = 3.1$. The remaining parameters are $m_2 = 2m_i$, $n_{01} = n_{02}$, $T_1(0) = T_2(0)$, $\omega_{p1}^2/\omega_{c1}^2 = 25$, and $m_i = 100m_e$.

$|\varphi_{\mathbf{k}}(t)|$ of the most unstable modes (with $k_x\rho_i = 0.05$ and $k_y = 0$) are peaked at the frequencies $\omega = \omega_{ci} + n\omega_0$ ($n = 1$, 2, and 3). There is also a peak corresponding to the lower hybrid resonance frequency $(\omega_{p1}^2 + \omega_{p2}^2)^{1/2}$ (with allowance for the corrections introduced by thermal dispersion). Presumably, this peak reflects the adiabatic excitation of a beam instability in the nonlinear regime. The instability under consideration also is not affected by the electron nonlinearity. The instability saturation can be attributed to ion heating: as the ion temperature rises, the effect of the heated ions on the dispersion of ion–ion hybrid waves may become strong enough to destroy the parametric resonance $\omega(\mathbf{k}) \approx \omega_0$ for the mode with the wave vector $\mathbf{k}$, so that this mode becomes stable.

The transverse ion temperatures T_{ix} and T_{iy} are approximately the same, while the temperature of the light ions is somewhat lower than the temperature of the heavy ions. The time evolutions of the temperatures $T_{1x,y}$ and $T_{2x,y}$ are oscillatory with frequencies $2\omega_{c1}$ and $2\omega_{c2}$, respectively. The oscillatory nature of the evolutions stems from the fact that, in the nonlinear stage, the ion distribution functions become asymmetric because of the acceleration of the ions that are in the tails of the distribution functions. In this stage, the ions obey a double-humped v_x distribution (with two slight peaks). In the later stage, the ion distribution function broadens and resembles a Maxwellian function. In this stage, short-wavelength waves are damped and only waves with the longest wavelengths ($k_x\rho_i = 0.05$) persist. A similar effect of redistributing oscillations from the short-wavelength to long-wavelength spectral range during the lower hybrid parametric instability in a plasma with one ion species was pointed out by Musher *et al.* [66]. In the nonlinear stage, these oscillations form streams in the space of the wavenumbers; the wave vectors corresponding to the streams are governed by Landau damping. Shapiro *et al.* [67] showed that, in a plasma with two ion species, the parametric excitation of lower hybrid waves can also give rise to the formation of nonlinear coherent structures (solitons).

5. CONCLUSION

The above analysis allows us to draw the following conclusions:

(i) Discharges sustained by low-frequency parametric turbulence have found widespread use in laboratory experiments, plasma technology, and fusion devices.

(ii) Low-frequency parametric turbulence often appears to be well developed, so that the results of turbulence studies described above can be used only for estimates.

(iii) PIC simulations of the low-frequency parametric turbulence revealed important turbulence properties that are difficult to investigate experimentally. In a number of cases, one- and two-dimensional simulations fail to reveal the qualitative features of turbulence; i.e., a full three-dimensional analysis is required.

(iv) Since the published experimental results on low-frequency parametric turbulence are insufficient to make a definitive comparison with analytical and numerical calculations, it becomes desirable to obtain further experimental data and to carry out the relevant two- and three-dimensional simulations.

ACKNOWLEDGMENTS

This work was supported in part by the Ukrainian Foundation for Fundamental Research (project no. 2.5.2/34) and the Center for Science and Technology of Ukraine (project no. 253).

REFERENCES

1. E. A. Kornilov, O. F. Kovpik, Ya. B. Faĭnberg, and I. F. Kharchenko, Zh. Tekh. Fiz. **35**, 1372 (1965) [Sov. Phys. Tech. Phys. **10**, 1064 (1965)].
2. E. A. Kornilov, O. F. Kovpik, Ya. B. Faĭnberg, *et al.*, Zh. Tekh. Fiz. **35**, 1378 (1965) [Sov. Phys. Tech. Phys. **10**, 1069 (1965)].
3. O. M. Shvets, A. G. Dikij, I. A. Dikij, *et al.*, in *Proceedings of 4th International Symposium on Heating of Toroidal Plasmas, Rome, 1984*, Vol. 1, p. 513.
4. K. N. Stepanov, Plasma Phys. Controlled Fusion **38** (12A), A13 (1996).

5. E. D. Volkov, I. Yu. Adamov, A. V. Arsenev, *et al.*, Plasma Phys. Controlled Nucl. Fusion Res. **2**, 679 (1993).
6. N. I. Nazarov, V. V. Plyusnin, T. Yu. Ranyuk, *et al.*, Fiz. Plazmy **13**, 1511 (1987) [Sov. J. Plasma Phys. **13**, 871 (1987)].
7. A. I. Lyssoivan, B. Giesen, R. Koch, *et al.*, in *Proceedings of 22rd EPS Conference on Controlled Fusion and Plasma Physics, Bournemouth, 1995* [ECA **19** C(II), 341 (1995)].
8. A. I. Lyssoivan, H. G. Esser, R. Koch, *et al.*, in *Proceedings of 23rd EPS Conference on Controlled Fusion and Plasma Physics, Kiev, 1996* [ECA **20** C(II), 879 (1996)].
9. E. De la Cal and E. Gauthier, Plasma Phys. Controlled Fusion **39**, 1013 (1997).
10. A. I. Akhiezer, V. S. Mikhaĭlenko, and K. N. Stepanov, Phys. Lett. **245**, 117 (1998).
11. A. B. Kitsenko, V. I. Panchenko, K. N. Stepanov, and V. F. Tarasenko, Nucl. Fusion **13**, 557 (1973).
12. A. B. Kitsenko, V. I. Panchenko, and K. N. Stepanov, Ukr. Fiz. Zh. **18**, 1591 (1973).
13. A. F. Korzh, V. S. Mikhaĭlenko, and K. N. Stepanov, Fiz. Plazmy **15**, 716 (1989) [Sov. J. Plasma Phys. **15**, 413 (1989)].
14. V. I. Petviashvili, Dokl. Akad. Nauk SSSR **153**, 1295 (1963).
15. B. B. Kadomtsev, in *Reviews of Plasma Physics*, Ed. by M. A. Leontovich (Atomizdat, Moscow, 1964; Consultants Bureau, New York, 1968), Vol. 4.
16. V. P. Silin and S. A. Uryupin, Fiz. Plazmy **22**, 790 (1996) [Plasma Phys. Rep. **22**, 714 (1996)].
17. V. N. Tsytovich, *Theory of Turbulent Plasma* (Atomizdat, Moscow, 1971; Plenum, New York, 1974).
18. O. I. Akhiezer, V. S. Mikhaĭlenko, and K. N. Stepanov, Ukr. Fiz. Zh. **42**, 990 (1997).
19. V. S. Mikhaĭlenko and K. N. Stepanov, Zh. Éksp. Teor. Fiz. **87**, 161 (1984) [Sov. Phys. JETP **60**, 92 (1984)].
20. F. F. Chen, Phys. Plasmas **3**, 1783 (1996).
21. F. F. Chen, I. D. Sudit, and M. Light, Plasma Sources Sci. Technol. **5**, 173 (1996).
22. F. F. Chen, J. Vac. Sci. Technol. A **10**, 1389 (1992).
23. A. B. Kitsenko, V. I. Panchenko, and K. N. Stepanov, Zh. Tekh. Fiz. **43**, 1426 (1973) [Sov. Phys. Tech. Phys. **18**, 905 (1973)].
24. A. B. Kitsenko, V. I. Panchenko, and K. N. Stepanov, Zh. Tekh. Fiz. **43**, 1437 (1973) [Sov. Phys. Tech. Phys. **18**, 911 (1973)].
25. V. S. Mikhaĭlenko and K. N. Stepanov, in *Proceedings of 2nd International Workshop on Nonlinear and Turbulent Processes in Physics, Kiev, 1983* (Harwood Academy, New York, 1984), Vol. 1, p. 421.
26. V. V. Ol'shansky, Dopovidi Nats. Akad. Nauk Ukr., No. 2, 95 (1999).
27. V. V. Ol'shansky, V. V. Demchenko, G. Kamelander, and K. N. Stepanov, in *Proceedings of 23rd EPS Conference on Controlled Fusion and Plasma Physics, Kiev, 1996* [ECA **20** C(II), 894 (1996)].
28. V. V. Ol'shansky and K. N. Stepanov, in *Proceedings of International Congress on Plasma Physics Combined with 25th EPS Conference on Controlled Fusion and Plasma Physics, Prague, 1998*, Abstracts of Invited and Contributed Papers, Part II, p. 846.
29. V. V. Ol'shansky and K. N. Stepanov, in *Problems of Atomic Science and Technology, Ser.: Plasma Physics* (National Science Center Kharkov Institute of Physics and Technology, Kharkov, 1999), Vols. 1–2, p. 135.
30. N. T. Besedin, S. V. Kasilov, I. M. Pankratov, *et al.*, in *A Collection of Papers Presented at the IAEA Techn. Com. Meeting VIII Stellarator Workshop, Kharkov, 1991* (IAEA, Vienna, 1991), p. 53.
31. N. T. Besedin, S. V. Kasilov, I. M. Pankratov, *et al.*, in *A Collection of Papers Presented at the IAEA Techn. Com. Meeting on Stellarators and Other Helical Confinement Systems, Garching, 1993* (IAEA, Vienna, 1993), p. 277.
32. E. D. Volkov, S. V. Kasilov, A. N. Letuchiĭ, *et al.*, Fiz. Plazmy **21**, 111 (1995) [Plasma Phys. Rep. **21**, 105 (1995)].
33. M. Ono, M. Porkolab, and R. P. H. Chang, Phys. Rev. Lett. **38**, 962 (1977).
34. M. Ono, M. Porkolab, and R. P. H. Chang, Phys. Fluids **23**, 1656 (1980).
35. M. Ono, M. Porkolab, and R. P. H. Chang, Phys. Fluids **23**, 1675 (1980).
36. K. Yatsui, M. Shimada, S. Okamoto, and M. Yokoyama, in *Proceedings of 3rd Topical Conference on Radiofrequency Plasma Heating, Pasadena, 1978*.
37. K. Yatsui and T. Imai, Phys. Rev. Lett. **35**, 1279 (1975).
38. F. Skiff, M. Ono, and K. L. I. Wong, Phys. Fluids **27**, 1051 (1984).
39. F. Skiff, K. L. I. Wong, and M. Ono, Phys. Fluids **27**, 2205 (1984).
40. K. L. Wong and M. Ono, Phys. Rev. Lett. **47**, 842 (1981).
41. F. Skiff, M. Ono, and K. L. I. Wong, in *Proceedings of 6th Topical Conference on Radiofrequency Plasma Heating, Callaway Gardens, 1985*, Ed. by D. Swanson (AIP, New York, 1985), p. 91.
42. R. van Nieuvenhoven, G. van Oost, J.-M. Noterdaeme, *et al.*, Nucl. Fusion **28**, 1603 (1988).
43. R. van Nieuvenhoven, M. Brambilla, J. Gernhardt, *et al.*, in *Proceedings of 15th European Conference on Controlled Fusion and Plasma Heating, Dubrovnik, 1988* [ECA **12** B(II), 762 (1988)].
44. R. van Nieuvenhoven, G. van Oost, and D. Bora, in *Proceedings of 17th European Conference on Controlled Fusion and Plasma Heating, Amsterdam, 1990* [ECA **14B**(III), 1068 (1990)].
45. R. van Nieuvenhoven, G. van Oost, J. Beuken, *et al.*, in *Proceedings of 15th European Conference on Controlled Fusion and Plasma Heating, Dubrovnik, 1988* [ECA **12** B(II), 778 (1988)].
46. D. F. H. Start, V. P. Bhatnagar, G. Bosia, *et al.*, in *Proceedings of 8th Topical Conference on Radiofrequency Power in Plasmas, Irving, 1989*, Ed. by R. McWilliams (AIP, New York, 1989), p. 205.
47. M. Saigusa, H. Kimura, T. Fujii, *et al.*, in *Proceedings of 8th Topical Conference on Radiofrequency Power in Plasmas, Irving, 1989*, Ed. by R. McWilliams (AIP, New York, 1989), p. 726.
48. R. I. Pinsker, M. J. Maybarry, M. Porkolab, and M. Prater, in *Proceedings of 8th Topical Conference on*

Radiofrequency Power in Plasmas, Irving, 1989, Ed. by R. McWilliams (AIP, New York, 1989), p. 314.

49. Yu. G. Zaleskiĭ, P. I. Kurilko, and N. I. Nazarov, Fiz. Plazmy **15**, 1424 (1989) [Sov. J. Plasma Phys. **15**, 827 (1989)].
50. Yu. G. Zaleskyj, N. I. Nazarov, V. V. Plusnin, and O. M. Shvets, in *Proceedings of 16th European Conference on Controlled Fusion and Plasma Physics, Venice, 1989* [ECA **13** B(III), 1073 (1989)].
51. V. F. Tarasenko, A. B. Kitsenko, V. I. Panchenko, and K. N. Stepanov, Zh. Tekh. Fiz. **42**, 1996 (1972) [Sov. Phys. Tech. Phys. **17**, 1596 (1972)].
52. A. B. Kitsenko, V. I. Panchenko, K. N. Stepanov, and V. F. Tarasenko, in *Proceedings of 5th European Conference on Controlled Fusion and Plasma Physics, Grenoble, 1972*, Vol. 1, p. 113.
53. Yu. M. Aliev, V. P. Silin, and K. Watson, Zh. Éksp. Teor. Fiz. **50**, 943 (1966) [Sov. Phys. JETP **23**, 626 (1966)].
54. M. Porkolab, Nucl. Fusion **12**, 329 (1972).
55. A. V. Baĭtin and A. A. Ivanov, Fiz. Plazmy **21**, 507 (1995) [Plasma Phys. Rep. **21**, 479 (1995)].
56. V. I. Aref'ev, I. A. Kovan, and L. I. Rudakov, Pis'ma Zh. Éksp. Teor. Fiz. **8**, 286 (1968) [JETP Lett. **8**, 176 (1968)].
57. L. I. Grigor'eva, B. I. Smerdov, K. N. Stepanov, *et al.*, Pis'ma Zh. Éksp. Teor. Fiz. **8**, 616 (1968) [JETP Lett. **8**, 379 (1968)].
58. V. I. Aref'ev, Zh. Éksp. Teor. Fiz. **55**, 679 (1968) [Sov. Phys. JETP **28**, 354 (1968)].
59. V. L. Sizonenko, K. N. Stepanov, and J. Teichmann, in *Proceedings of 2nd International Symposium on the Interaction of Electromagnetic Oscillations with Plasmas, Saclay, 1968*, Vol. I, p. 485.
60. L. I. Grigor'eva, A. V. Longinov, A. I. Pyatak, *et al.*, Plasma Phys. Controlled Nucl. Fusion Res. **3**, 573 (1971).
61. A. I. Pyatak and V. L. Sizonenko, Ukr. Fiz. Zh. **17**, 141 (1971).
62. V. L. Sizonenko, in *Proceedings of 2nd International Conference on Theory of Plasma, Kiev, 1974* (Naukova Dumka, Kiev, 1976), p. 188.
63. V. V. Demchenko, V. L. Sizonenko, and K. N. Stepanov, Nucl. Fusion **11**, 245 (1971).
64. A. B. Kitsenko, V. V. Ol'shansky, V. I. Panchenko, and K. N. Stepanov, Fiz. Plazmy **21**, 159 (1995) [Plasma Phys. Rep. **21**, 151 (1995)].
65. S. V. Kasilov, V. V. Ol'shansky, A. I. Pyatak, and K. N. Stepanov, Ukr. Fiz. Zh. **40**, 402 (1995).
66. S. L. Musher, A. M. Rubenchik, and B. I. Sturman, Plasma Phys. **20**, 1131 (1978).
67. V. D. Shapiro, G. I. Soloviev, J. M. Dawson, and R. Bingham, Phys. Plasmas **2**, 516 (1995).

Translated by I. Kalabalyk

Plasma Physics Reports, Vol. 26, No. 7, 2000, pp. 586–591. Translated from Fizika Plazmy, Vol. 26, No. 7, 2000, pp. 626–632.

DUSTY PLASMA

Analysis of the Formation of Ordered Dust-Grain Structures in a Thermal Plasma

A. A. Samarian, O. S. Vaulina, A. P. Nefedov, and O. F. Petrov

Institute for High energy Densities, Associated Institute for High Temperatures, Russian Academy of Sciences, Izhorskaya ul. 13/19, Moscow, 127412 Russia

Received August 12, 1999; in final form, September 29, 1999

Abstract—The possibility is studied of the formation of ordered dust-grain structures in a low-temperature thermal plasma consisting of electrons, ions, and micron-sized charged dust grains. The range of the required values of the coupling parameter Γ defining the degree to which the plasma is nonideal is calculated using the results of diagnostic measurements carried out in a plasma consisting of combustion products of propane in air with grains of different materials. The results obtained show that the most favorable conditions for the formation of strongly correlated grain structures (for both positively and negatively charged grains) take place at the maximum grain number density and a plasma temperature close to the minimum flame temperature (~1600 K). In this case, the optimum grain radii lie in the range 4–10 μm and the maximum value of the parameter Γ is less than 200. Since the calculated values of Γ give an upper estimate, liquidlike ordered structures are most likely to form in a thermal plasma. Based on the results of the analysis, it is stated that an increase in the parameter Γ and, accordingly, the formation of plasma-crystal structures in a thermal plasma can only occur for positively charged grains. © *2000 MAIK "Nauka/Interperiodica".*

1. INTRODUCTION

In recent years, thermal dusty plasmas have attracted considerable interest in connection with both their practical importance as a working medium in a number of engineering areas (such as energetics, rocket engineering, and film depositing) and fundamental research in the physics of nonideal plasmas. Recently, the phenomenon of self-organization of charged grains in a low-temperature plasma, which leads to the formation of ordered structures [1–3], has been revealed. The study of these structures has shown that they exhibit a number of unique properties, which makes it possible to use them as model systems in studying the fundamental properties of solids. A strong dependence of the grain structures on the parameters of the bulk plasma enables one to study phase transitions in a dusty plasma, whereas the short relaxation time of these structures to equilibrium, as well as the short-time response to external perturbations, allows the dynamical and structural properties of plasmas to be studied.

Traditionally, the models of a one-component plasma or a plasma with a screened (Debye) potential have been used to describe the interaction between the grains. (The latter model is also known as a Yukawa model.) In these models, classical quasineutral unbounded plasmas are considered for which the critical (corresponding to phase transitions) values of the Coulomb coupling parameter

$$\gamma = \frac{Z_p^2 e^2}{\langle r \rangle T_p} \tag{1}$$

are calculated numerically. Here, e is the elementary charge; Z_p is the grain charge number; $\langle r \rangle \equiv (4\pi n_p/3)^{-1/3}$ is the intergrain distance; and T_p and n_p are the temperature and number density of grains, respectively.

In the one-component model, the plasma is treated as an idealized ion system against a uniform neutralizing background, so that the system as a whole is electrically neutral. In this case, the interaction between grains is described by the Coulomb potential $U(r)$ and, for γ higher than $\gamma = 171$ [4], a three-dimensional ordered structure is formed. For low γ values ($\gamma < 4$), the plasma is in the gaseous state.

In the Debye model, it is assumed that the grain charge is screened by a charged background, which leads to the Debye–Hückel interaction potential. With allowance for the screening, whose effect is determined by the relation $\kappa = \langle r \rangle / r_D$ (where r_D is the screening radius), the relevant coupling parameter

$$\Gamma = \gamma \exp(-\langle r \rangle / r_D) \tag{2}$$

is introduced. The short-range order in such a system is established for $\Gamma > 1$ [5]. Hence, the plasma thermodynamics and, accordingly, phase-transition conditions in the Debye model are described by two parameters, namely, γ and κ.

In this paper, we consider the possibility of the formation of an ordered grain structure in a low-temperature thermal plasma consisting of electrons, ions, and micron-sized dust grains. To determine the value of Γ in such a plasma, we use the results of diagnostic mea-

1063-780X/00/2607-0586$20.00 © 2000 MAIK "Nauka/Interperiodica"

surements carried out in combustion-product plasma flows with cerium dioxide (CeO_2) and aluminum oxide (Al_2O_3) grains.

The charge composition of a thermal plasma depends substantially on the easily ionized alkali-metal (usually, Na or K) impurities, which are always present in the dust-grain material. The alkali-metal atom density n_a, the gas temperature $T \simeq T_p$, and the work function W_{te} of the thermal electrons emitted from the grain surface determine the electrophysical properties of the thermal plasma and significantly affect the magnitude and sign of the grain charge. As the plasma temperature rises, both the electron emission from the grain surface and the degree of ionization of alkali-metal atoms increase, which can change the magnitude and sign of the grain charge. In turn, the alkali-metal atom density depends on the material, number density, and size of the dispersed-phase grains. Therefore, in order to determine the parameters of the thermal dusty plasma at which the nonideality parameter Γ is maximum, it is necessary to solve a self-consistent problem using both the reference and experimental data on the emission and chemical properties of the grain material.

2. DUST-GRAIN CHARGING IN A THERMAL PLASMA

In the general case, the equilibrium potential of a dust grain embedded in a thermal plasma is established as a result of the balance between the electron–ion recombination on the grain surface and the thermoemission (electron) current from its surface:

$$I_e + I_{te} + \sum I_i = 0, \tag{3}$$

where I_{te} is the thermal electron flux and I_e and I_i are the electron and ion fluxes that arrive from the surrounding plasma and are absorbed by the grain.

The charge eZ_p of a spherical particle of radius $R \ll r_D$ is related to its surface potential φ_s with respect to the plasma potential (which is assumed to be zero) by the equation $\varphi_s = eZ_p/R$. The plasma-particle flux onto the surface of an isolated dust grain depends on the sign of the grain charge with respect to the absorbed electrons (ions). In the orbit motion limited (OML) model, in the absence of an external electric field, this flux can be represented as [6, 7]

$$I_{e(i)} = Z_{e(i)} e n_{e(i)} (8\pi T/m_{e(i)})^{1/2} R^2 (1 + e|Z_{e(i)}\varphi_s|/T), \quad Z_{e(i)}\varphi_s < 0; \tag{4a}$$

$$I_{e(i)} = Z_{e(i)} e n_{e(i)} (8\pi T/m_{e(i)})^{1/2} R^2 \exp(-e|Z_{e(i)}\varphi_s|/T), \quad Z_{e(i)}\varphi_s > 0, \tag{4b}$$

where R is the grain radius, $n_{e(i)}$ is the electron (ion) density, $m_{e(i)}$ is the electron (ion) mass, and $Z_{e(i)}$ is the charge number of the plasma electrons (ions). The electron (ion) velocity is assumed to satisfy the Maxwellian distribution with the temperature T. The electron (ion) density $n_{e(i)}$ is assumed to satisfy the plasma neutrality condition: $(n_e - Z_p n_p) = n_i$.

Note that the OML model is valid for a collisionless plasma with sufficiently small grains,

$$R \ll r_D < l,$$

where l is the electron (ion) mean free path.

For a thermal plasma at temperatures of ~2000 K and atmospheric pressure, the mean free path of electrons with respect to collisions with neutrals is ~100 μm, whereas that of ions is two orders of magnitude lower. Here, we only use the OML model because, under the conditions in question, the error in calculating the ion fluxes does not play a decisive role.

The thermal electron flux from the charged-grain surface is described by [8]

$$I_{te} = (4\pi RT)^2 m_e \exp(-W_{te}/T)/h^3, \quad Z_p < 0; \tag{5a}$$

$$I_{te} = (4\pi RT)^2 m_e (1 + e\varphi_s/T) \exp(-(W_{te} + e\varphi_s)/T)/h^3, \quad Z_p > 0. \tag{5b}$$

The thermoelectronic work function W_{te} of various materials usually ranges from 1 to 5 eV. If the system under study consists of only dust grains and electrons emitted by them ($n_e = n_p Z_p$), then the grain charge $Z_p \geq 0$ can be found from the balance between the fluxes of electrons emitted and absorbed by the grain (assuming that the emitted and absorbed electrons have the same temperature):

$$n_e = 2(2\pi T m_e/h^2)^{3/2} \exp(-(W_{te} + e\varphi_s)/T), \quad n_e \equiv n_p Z_p. \tag{6}$$

Equation (6) is similar to the Richardson–Deshman equation. Figure 1 illustrates the dependence of the

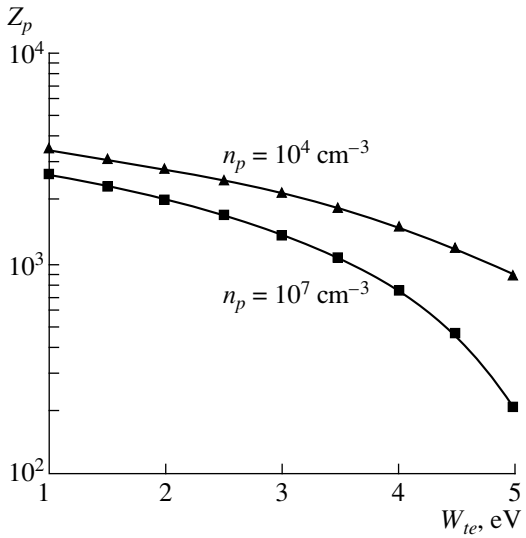

Fig. 1. Dependence of the grain charge Z_p on the work function W_{te} at a temperature of T = 2000 K.

charge number Z_p on the work function W_{te} for grains of radius $R = 1$ μm at various densities n_p and a temperature of $T = 2000$ K, which is typical of combustion-product plasmas. It is easily seen that the positive grain charges are relatively low: $Z_p < 4000\ R$ [μm]. Therefore, the presence of easily ionized alkali-metal atoms in such a plasma results in an additional electron flux onto the grain, and the grain charge can even change its sign because the thermal velocity of plasma ions is much less than the electron velocity.

3. INFLUENCE OF ALKALI-METAL IMPURITIES ON THE GRAIN CHARGE

Two processes govern the electron density in an equilibrium thermal plasma. The first process is associated with thermoelectronic emission and electron attachment to the grain surface, and the second one is associated with ionization and recombination processes in the gaseous phase. For most gases, atom and molecule ionization energies are higher than 10 eV; hence, at temperatures below 3000 K, the charged-component density depends on the content of easily ionized impurities in the heated gas.

As was mentioned above, dust grains are the main source of easily ionized impurities in a thermal plasma. The alkali-metal atom density and, accordingly, the electron and ion densities in the bulk plasma depend on the size, number density, and material of the dust grains. Hence, to choose the optimum conditions (the size, number density, and temperature of grains) such that the coupling parameter Γ is maximum, we should examine how the charge of the grains depends on their radius R, number density n_p, and temperature T taking into account the content of the alkali-metal impurity in the grain material. For grains of a given material, the density of alkali-metal atoms emitted from the grain surface may depend, in two limiting cases, either on the grain surface area or the grain volume and thus can be related to n_p in the following two ways:

$$n_a = cR^2 n_p, \tag{7a}$$

$$n_a = kR^3 n_p, \tag{7b}$$

where n_a is the alkali-metal atom density and c and k are certain constants that can be obtained from experimental measurements carried out at one or several temperatures in a plasma containing grains of the material under study.

The well-known methods for measuring the grain size and number density, as well as the alkali-metal atom density, are described in detail in [9–12].

In the case of a plasma without dust grains but with an admixture of alkali atoms [13], the electron and ion densities, n_e^* and n_i^* (in this case, $n_e^* = n_i^*$), can be found from the Saha equation for a gas with a known temperature and density:

$$n_e^* n_i^* = 2n_a \frac{g_i}{g_a}\left(\frac{2\pi m_e T}{h^2}\right)^{3/2} \exp(-I_a/T), \tag{8}$$

where I_a is the ionization energy of an atom.

To determine the electron n_e and ion n_i densities at the same alkali-metal atom density n_a in a dusty plasma, when the dust grains are the only source of easily ionized atoms, the Saha equation should be complemented by the quasineutrality condition

$$n_e = n_i + n_p Z_p. \tag{9}$$

In this case, the densities of electrons and ions arriving at the surface of a positively or negatively charged grain are determined by the relations

$$n_e = n_e^* \sqrt{1 + \left(\frac{Z_p n_p}{2n_e^*}\right)^2} + \frac{Z_p n_p}{2}, \tag{10a}$$

$$n_i = n_i^* \sqrt{1 + \left(\frac{Z_p n_p}{2n_i^*}\right)^2} - \frac{Z_p n_p}{2}. \tag{10b}$$

For positively charged grains, the charge Z_p can be found from expressions (6) and (10) with no regard for the ion flux onto the grain surface because the thermal velocity of plasma ions is much less than the electron velocity. To determine the maximum negative charge Z_p (for $Z_p < 0$, $I_{te} \simeq 0$; i.e., the thermoelectronic emission can be neglected), we can write the balance equation (3) in the form

$$\exp(-e|\varphi_s|/T) n_e = n_i (m_e/m_i)^{1/2} (1 + e|\varphi_s|/T). \tag{11}$$

This allows us to perform a more general analysis of the maximum value of the coupling parameter Γ without invoking additional unknown data on the grain material.

4. ANALYSIS OF THE PARAMETERS OF A DUST STRUCTURE IN A COMBUSTION-PRODUCT PLASMA

All of the above equations are rather general and independent of the method for producing a thermal plasma. Here, we restrict ourselves to the analysis of a plasma consisting of the products of combustion of propane in air at pressures near atmospheric pressure. It is this plasma in which liquidlike plasma–dust structures have been revealed for the first time [3]. The temperature range typical of propane–air flames is 1600–2000 K. When determining the coupling parameter Γ in the plasma of combustion products, we take into account the limitation on the maximum grain number density:

$$n_p \le n_p^{\lim}\ [\mathrm{cm}^{-3}] = 8 \times 10^7/(\pi R^2\ [\mu\mathrm{m}^2]). \tag{12}$$

This condition was obtained experimentally for grains of various materials from measurements of the limiting optical depth τ for grains at which flame inhibition (quenching) occurs. The dependence of the maximum number density $n_p^{\lim}$ on the grain radius R is shown in Fig. 2. The restriction on the maximum grain radius ($R < R^{\lim} = 20$ μm) is determined by the dynamic viscosity and velocity of the propane–air flow, i.e., its ability to drag the grain in the Earth's gravity field.

Let us examine the conditions for the formation of ordered structures by using the results of measurements carried out in a plasma with CeO_2 grains when the content of alkali-metal impurities is relatively low. The results of observations of the formation of CeO_2 ordered structures in a plasma of combustion products at temperatures of 1700–1800 K are presented in [14, 15]. The mean diameter of grains was 1.5–2 μm, the typical distance between grains was $\langle r \rangle = 15$–50 μm (which corresponded to $n_p = 10^6$–10^7 cm^{-3}), and the electron density was $n_e = (5$–$8) \times 10^9$ cm^{-3}. The main contribution to the electron and ion densities came from the alkali-metal impurities—sodium ($I_a = 5.12$ eV) and potassium ($I_a = 4.34$ eV), which had nearly the same densities. However, by virtue of the lower ionization energy of potassium, its ion density in the gaseous phase was one order of magnitude higher.

Figure 2 shows the dependence $n_a(R)$ for two types of the functional dependence of the density of emitted alkali-metal atoms on the grain parameters [relations (7a) and (7b)] in the case of the limiting grain number density $n_p^{\lim}$. Curves are drawn for different values of the coefficients $c = (3.4$–$5.4) \times 10^{13}$ cm^{-2} and $k \equiv c/R^* = (3.4$–$5.4) \times 10^{17}$ cm^{-3} obtained from the experimental measurements [16]. Here, $R^* \simeq 1$ μm is the mean radius of CeO_2 grains for which the test measurements of n_p and n_a were performed.

The above intervals of the c and k values were determined taking into account the contribution from experimental errors in determining the grain radius R, optical depth of the grain layer $\tau \sim R^2 n_p$, and potassium atom density n_a. The grain charge Z_p was determined from expressions (6) and (10) and the reference data on the CeO_2 electronic work function: $W_{te} = 2.6$ eV [17]. The results of calculations of the parameter Γ for various radii, number densities, and temperatures of grains are presented in Figs. 3 and 4.

The analysis of the temperature dependence of the parameter Γ for different particle radii and number densities shows that, for both cases corresponding to relations (7a) and (7b), the value of Γ is maximum for the maximum grain number density; in this case, functional dependence (7a) for the density of the emitted alkali-metal atoms gives the maximum values of the parameter Γ that belong to the temperature range under consideration (see Fig. 3). The lower values of the cou-

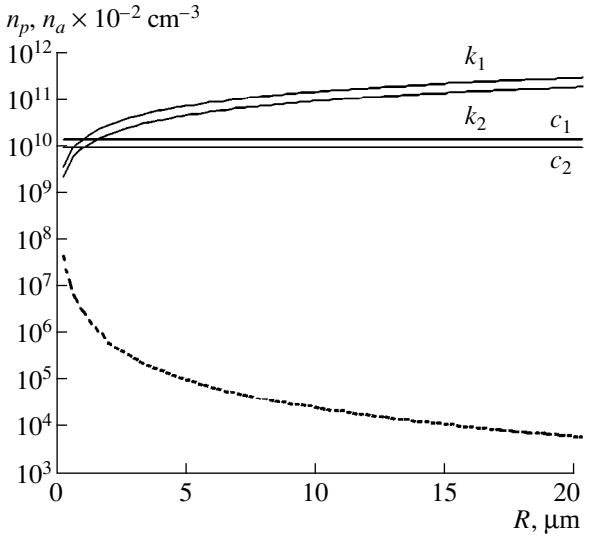

Fig. 2. Limiting grain number density $n_p^{\lim}$ (dashed curve) and alkali-metal atom density n_a (solid curve) as functions of the particle radius R for the limiting grain number density for the cases corresponding to relations (7a) and (7b) and different values of the coefficients: $c_1 = 5.4 \times 10^{13}$ cm^{-2}, $c_2 = 3.4 \times 10^{13}$ cm^{-2}; $k_1 = 5.4 \times 10^{17}$ cm^{-3}, and $k_2 = 3.4 \times 10^{17}$ cm^{-3}.

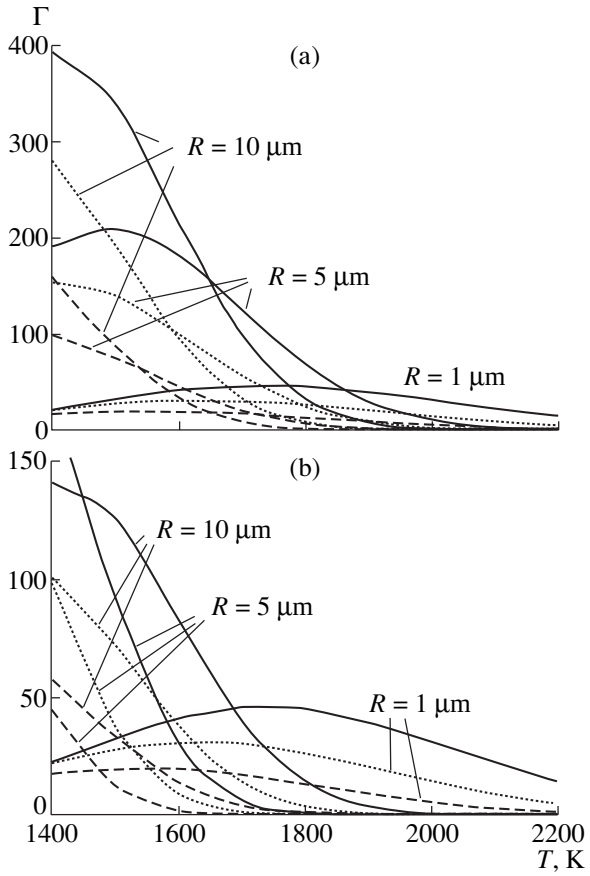

Fig. 3. Temperature dependence of the parameter Γ for different grain radii at the limiting grain number density $n_p^{\lim}$ (solid curves) and the grain number density decreased by a factor of 10 (dotted lines) and 100 (dashed lines) in the cases corresponding to relations (a) (7a) and (b) (7b).

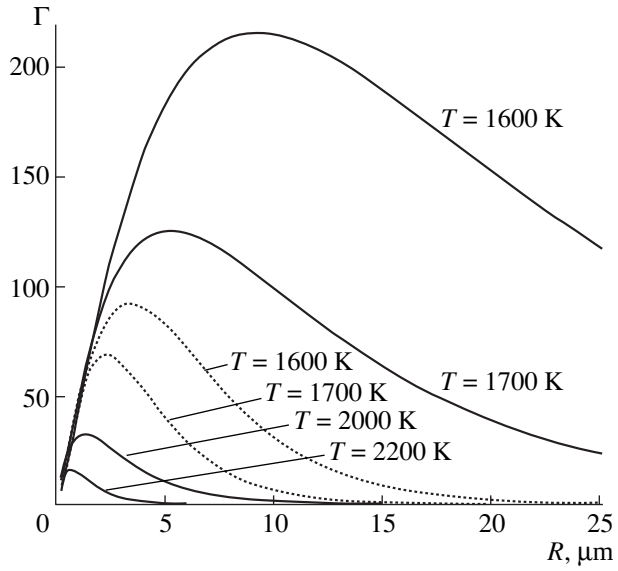

Fig. 4. Dependence of the parameter Γ on the radius R for various temperatures T in the case of a positive grain charge; solid curves correspond to relation (7a), and dashed-and-dotted curves correspond to (7b).

pling parameter in the case corresponding to relation (7b) are explained by the higher impurity emission and, accordingly, a greater electron flux onto the grain surface, which decreases both the grain charge and the Debye radius (Fig. 5).

The nonmonotonic character of the dependences $\Gamma(T)$ and $\Gamma(R)$ is governed by two competing processes: the charging of particles due to thermoelectronic emission and the screening of grains by the electron and ion components that are formed due to the ionization of alkali-metal atoms. As the electronic work function increases, the parameter Γ decreases. For $W_{te} > 3.2$–3.4 eV, in the temperature range 1600–2200 K and the alkali-metal atom density range under study (see Fig. 2), the grains are no longer charged positively.

Let us determine the coupling parameter for a thermal plasma with negatively charged dust grains. We assume that the densities of ionized atoms n_a and electrons n_e remain the same (Fig. 2). To obtain the upper estimate for the parameter Γ, we neglect the thermoelectronic emission; in this case, the grain charge is determined from (11). The results of calculations of the parameter Γ for the limiting grain number density $n_p^{\lim}$ (Fig. 3) in the case corresponding to relation (7a) are shown in Fig. 6.

In the case corresponding to relation (7b) (as in the case of a positive particle charge), the parameter Γ decreases with decreasing the grain number density ($n_p < n_p^{\lim}$). This is because the screening length of the grain charge decreases as the densities of plasma electrons and ions increase, whereas the charge Z_p itself depends weakly on n_e^*. It is easily seen that, for a negatively charged grain (at $W_{te} > 3.2$–3.4 eV), the cou-

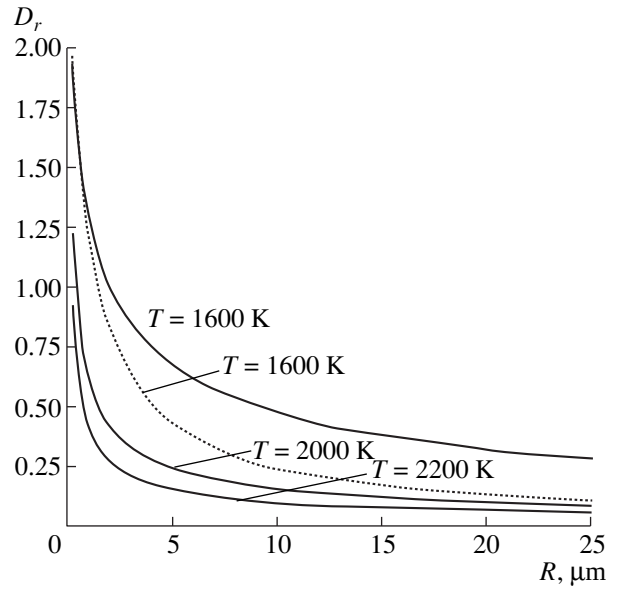

Fig. 5. Ratio $D_r = r_D/(4\pi n_p/3)^{-1/3}$ of the Debye radius to the intergrain distance as a function of radius R for different temperatures; solid curves correspond to relation (7a), and dashed-and-dotted curves correspond to (7b).

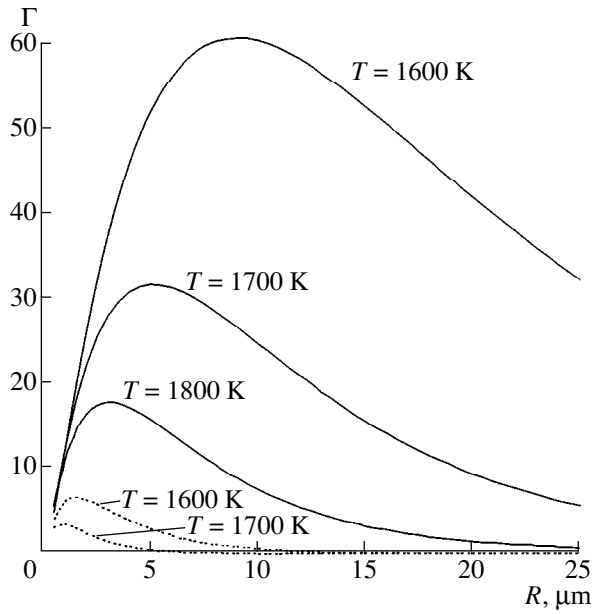

Fig. 6. Dependence of the parameter Γ on the radius R for different temperatures T in the case of a negative particle charge; solid curves correspond to $n_e = 3 \times 10^{10}$ cm^{-3}, and dashed-and-dotted curves correspond to $n_e = 3 \times 10^{11}$ cm^{-3}.

pling parameter Γ reduces by a factor of more than 3. Furthermore, the tenfold increase in the electron density n_e (which corresponds to a 100-fold increase in the alkali-metal atom density n_a) decreases the parameter Γ by almost one order of magnitude (Fig. 6).

Assuming that, on heating, all potassium compounds evaporate from the grain material and decompose in the plasma, the alkali-metal atom density in the plasma volume (~10^{12}–10^{13} cm^{-3}) corresponds to the specific mass concentration of alkaline impurities in the grain material on the order of 10^{-4}–10^{-5}. This value is typical of the alkaline-metal impurity concentration for grains of various materials if they are not specially purified.

5. CONCLUSION

An analysis of the numerical results shows that the most favorable conditions for the formation of strongly correlated grain structures (for both positively and negatively charged grains) take place at the maximum grain number density and a plasma temperature close to the minimum flame temperature (~1600 K). The optimum particle radii lie in the range 4–10 μm (Figs. 4, 6), and the maximum value of the coupling parameter Γ is less than 200. Since the obtained values of Γ give an upper estimate, liquidlike structures are most likely to form in a thermal plasma, in contrast to crystal structures observed in gas discharges in which the parameter Γ attains a value of 10^3–10^4.

This result agrees with the available experimental data on dust-grain structures in a thermal plasma. Indeed, when studying an ensemble of dust grains in a combustion-product plasma flow, it was found that the maximum value of the parameter Γ was 40–50 and the liquidlike structures were formed at grain number densities of $n_p > 10^6$ cm^{-3} and plasma temperatures less than 1900 K [14, 15]. The formation of a cloud of dust grains was observed in a thermal plasma produced by exploding a metal wire in air, the parameter Γ being estimated as ~100 [18]. In the plasma of the combustion products of propellants, in the boundary sheath of the condensation region, where liquidlike plasma–dusty structures were observed, the value of the parameter Γ varied from 3 to 40 [19].

Based on the above analysis, we can state that, in a dust-grain system in a thermal plasma, the parameter Γ can only be increased for positively charged grains with a minimal content of easily ionized impurities. In the limiting case of perfectly pure grains, we obtain a plasma consisting of grains and electrons emitted by them; it is this plasma in which a Coulomb plasma crystal can be formed.

ACKNOWLEDGMENTS

This work was supported in part by the Russian Foundation for Basic Research, project no. 98-02-16825.

REFERENCES

1. J. Chu and I. Lin, Phys. Rev. Lett. **72**, 4009 (1994).
2. H. Thomas, G. E. Morfill, V. Demmel, *et al.*, Phys. Rev. Lett. **73**, 652 (1994).
3. V. E. Fortov, A. P. Nefedov, O. F. Petrov, *et al.*, Pis'ma Zh. Éksp. Teor. Fiz. **63**, 176 (1996) [JETP Lett. **63**, 187 (1996)]; V. E. Fortov, A. P. Nefedov, O. F. Petrov, *et al.*, Phys. Rev. E **54**, R2236 (1996); V. E. Fortov, A. P. Nefedov, O. F. Petrov, *et al.*, Phys. Lett. A **219**, 89 (1996).
4. S. Ichimaru, Rev. Mod. Phys. **54**, 1017 (1982).
5. H. Ikezi, Phys. Fluids **29**, 1764 (1986).
6. J. E. Allen, Phys. Scr. **45**, 497 (1992).
7. V. N. Tsytovich, Usp. Fiz. Nauk **167**, 57 (1997) [Phys. Usp. **40**, 53 (1997)].
8. M. S. Sodha and S. Guha, Adv. Plasma Phys. A **4**, 219 (1971).
9. A. P. Nefedov, O. F. Petrov, and O. S. Vaulina, Appl. Opt. **36**, 1357 (1997).
10. A. P. Nefedov, O. F. Petrov, and O. S. Vaulina, J. Quant. Spectrosc. Radiat. Transf. **54**, 435 (1995).
11. S. É. Frish, in *Spectroscopy of Gas-Discharge Plasma*, Ed. by S. É. Frish (Nauka, Leningrad, 1970), p. 7.
12. A. A. Samarian, A. V. Chernyshev, A. P. Nefedov, and O. F. Petrov, Fiz. Plazmy **25**, 988 (1999) [Plasma Phys. Rep. **25**, 912 (1999)].
13. V. I. Molotkov, A. P. Nefedov, and V. F. Kosov, Teplofiz. Vys. Temp. **29**, 633 (1991).
14. V. E. Fortov, A. P. Nefedov, O. F. Petrov, *et al.*, Zh. Éksp. Teor. Fiz. **111**, 467 (1997) [JETP **84**, 256 (1997)].
15. V. E. Fortov, V. S. Filinov, A. P. Nefedov, *et al.*, Zh. Éksp. Teor. Fiz. **111**, 889 (1997) [JETP **84**, 489 (1997)].
16. A. V. Chernyshev, *Charge Composition of a Dusty Plasma*, Preprint No. 3-411, IVTAN (Associated Institute of High Temperatures, Russian Academy of Sciences, Moscow, 1997).
17. V. S. Fomenko, in *Emission Properties of Materials* (Naukova Dumka, Kiev, 1981), p. 164.
18. A. M. Ignatov, V. N. Kunin, V. S. Pleshivtsev, and A. A. Rukhadze, in *Proceedings of 2nd International Conference on Physics of Dusty Plasmas, Hakone, Japan, 1999*, p. 117.
19. V. E. Fortov, A. A. Samarian, A. V. Chernyschev, *et al.*, in *Proceedings of 2nd International Conference on Physics of Dusty Plasmas, Hakone, Japan, 1999*, p. 101.

Translated by N. Larionova

Plasma Physics Reports, Vol. 26, No. 7, 2000, pp. 592–597. Translated from Fizika Plazmy, Vol. 26, No. 7, 2000, pp. 633–638.

PLASMA ELECTRONICS

Tunable Plasma Relativistic Microwave Amplifier

A. V. Ponomarev, P. S. Strelkov, and A. G. Shkvarunets

Institute of General Physics, Russian Academy of Sciences, ul. Vavilova 38, Moscow, 117942 Russia

Received February 11, 2000

Abstract—A stable regime of the amplification of a slow plasma wave in a plasma waveguide during the injection of a high-current relativistic electron beam is obtained. For an input-signal frequency of 9.1 GHz, there exists a range of plasma densities in which the spectrum of the output microwave radiation lies in a 0.5-GHz-wide band. For a 40-kW input power at a frequency of 9.1 GHz, the maximum output power is 8 MW. It is shown experimentally for the first time that the beam–plasma amplifier can operate at frequencies of 9.1 GHz and 12.9 GHz. The range of plasma densities in which the regime of amplification is observed agrees with the results of calculations based on linear theory. *© 2000 MAIK "Nauka/Interperiodica".*

1. INTRODUCTION

A cylindrical coaxial plasma waveguide, whose central electrode is a column of magnetized plasma with a sharp boundary, is a slow-wave electrodynamic structure. In such a waveguide, there exist slow (with a phase velocity lower than the speed of light) eigenmodes whose electric field has a nonzero longitudinal component (*E*-modes). The maximum phase velocity of these modes increases with increasing the plasma density n_p and approaches the speed of light as $n_p \longrightarrow \infty$. Hence, when an electron beam is injected into the plasma waveguide, the Cherenkov synchronism between the beam and a waveguide eigenmode can occur if the plasma density exceeds a certain threshold value. Theoretical research on the mechanism for the excitation of the eigenmodes of a coaxial plasma waveguide by a relativistic electron beam (REB) has been carried out since the 1970s (see review [1]).

Note that, initially, the interaction of a nonrelativistic electron beam with a plasma was studied both theoretically and experimentally. These studies can be divided into two groups. In the first group, the plasma was used to change the configuration of the electric field in vacuum microwave sources in order to improve their parameters. This made it possible to increase the efficiency of such sources and to create high-power microwave amplifiers and noise masers with a frequency tuning of ±30% and a rather high efficiency (~40%) [2, 3]. On the other hand, such use of the plasma could not significantly broaden the frequency tuning range. In the second group of investigations, the microwave power was generated through the coupling between a nonrelativistic electron beam and slow modes of a plasma waveguide. This showed promise for creating microwave devices capable of tuning the operating frequency over a wide range. However, such devices have not been created because it is impossible to provide an efficient output of such a broadband microwave radiation from the plasma.

It is important to note that the radial structure of the field of slow waves in a coaxial plasma waveguide is similar to the structure of the TEM mode of a coaxial metal waveguide with a similar geometry if their phase velocities are close to the speed of light ($v_{ph}/c \geq 0.8$). This circumstance significantly simplified the problem of the output of microwave power from the plasma waveguide and showed promise for the use of REBs for the generation and amplification of electromagnetic waves in beam–plasma systems.

The first successful experiment on microwave generation with the use of an REB exciting eigenmodes of a plasma waveguide was carried out in 1982 [4]. The experiment confirmed the main theoretical predictions about the mechanism for the beam–plasma coupling and showed that it is possible to attain a high (about 10%) efficiency of generation. The experiment also demonstrated the main features of a Cherenkov plasma maser (CPM): a broad frequency band (~40%) and the possibility of tuning the generated frequency over a wide range. As the plasma density varied from its threshold value $n_p \approx 1 \times 10^{13}$ cm^{-3} to $n_p \approx 8 \times 10^{13}$ cm^{-3}, the generated frequency varied from 10 to 20 GHz.

In subsequent experiments on the generation of microwave radiation in a relativistic beam–plasma system, the accuracy of the measurements of the absolute power and emission spectrum was increased and the parameters of the beam, plasma, and output facility were optimized [5–7]. The theory, in turn, developed nonlinear time-dependent models best suiting the experimental conditions [8, 9]. At present, a good agreement has been achieved between the theory and the experiment. It is shown that a CPM generates a broad emission spectrum with a relative width no less than 20% and that the central generated frequency can be varied sevenfold by varying the plasma density in the plasma waveguide. Attempts to make the emission spectrum width comparable with that of vacuum relativistic oscillators (~3%) have been unsuccessful.

1063-780X/00/2607-0592$20.00

In order to narrow the CPM emission spectrum, it was proposed that the signal from an external source be fed to the CPM. In this case, the beam–plasma system can operate either in the amplification or generation mode, but the central radiation frequency in both modes is governed by the frequency of the input signal.

The first successful experiment on the amplification of microwave signals in a beam–plasma system [10] demonstrated the possibility of amplifying an external signal at plasma densities within a relatively narrow interval near the threshold density. However, the amplification regime was insufficiently stable and was accompanied by spontaneous generation at frequencies other than the frequency of the input signal.

An efficient method for suppressing spontaneous generation is the use of a large-volume microwave absorber. For this reason, it is of interest to study experimentally the amplification of plasma waves by an REB in a system partially filled with a microwave absorber. This is the aim of the present paper.

2. EXPERIMENTAL LAYOUT

A schematic of the device is shown in Fig. 1. An annular plasma column (*1*) with a mean radius of 7.5 mm and thickness of 1 mm is immersed in a uniform longitudinal magnetic field $B = 1.6$ T in a cylindrical metal waveguide (*2*) of radius 22 mm. The plasma is produced in a hot-cathode discharge in xenon. The cathode potential is 600 V, the discharge current is up to 100 A, and the xenon pressure is 3.5×10^{-4} torr. The parameters of an REB (*3*) propagating along the waveguide axis are the following: the electron energy is 550 keV, the current is 1.5 kA, the pulse duration is 150 ns, the mean beam radius is 10 mm, and the beam-wall thickness is 1 mm. A microwave converter (*4*) is mounted at the entrance to the plasma waveguide. The converter excites a TEM mode, which is transformed into the fast and slow modes of the plasma waveguide. The slow plasma mode is amplified by the REB, is converted into a TEM mode of the output metal coaxial waveguide, and is emitted by a large-cross-section output coaxial horn (*5*). The length of the beam–plasma interaction is equal to 29 cm. The system design allows the installation of an annular microwave absorber (*6*) with an outer radius of 22 mm, inner radius of 11.5 mm, and length of 14 cm. The absorber is placed at a distance of 3 cm from the conical collector of the REB at the exit from the system. The microwave-power absorption coefficient was 20 dB for the TEM mode in a coaxial waveguide with an inner radius of 5 mm and outer radius of 22 mm and was equal to 50 dB for the TM_{01} mode in a hollow waveguide of radius 22 mm. Measurements were carried out at a frequency of 9.1 GHz.

As a source of input microwave signals, we used one of two pulsed magnetrons. The first magnetron had a frequency of $f_0 = 12.9$ GHz, pulse duration of 2 μs, and power of $P_{in} = 75$ kW. The corresponding parameters of the second magnetron were 9.1 GHz, 20 μs, and 40 kW, respectively.

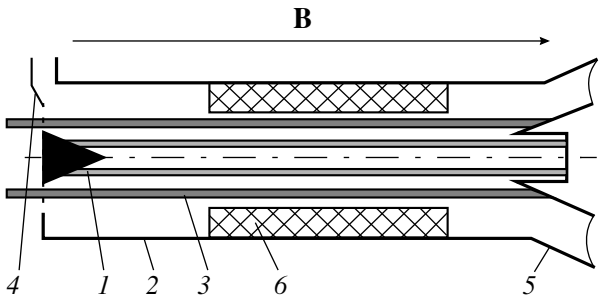

Fig. 1. Schematic of the plasma relativistic microwave amplifier: (*1*) plasma, (*2*) metal waveguide, (*3*) REB, (*4*) entrance of the amplifier, (*5*) coaxial conical emitting horn, and (*6*) microwave absorber.

The output microwave power and radiation spectrum were recorded by two detectors placed in a 23×10 mm^2 receiver waveguide. The first detector (a broadband receiver) measured the total microwave power entering the receiver waveguide. At the input of the second detector (a narrowband receiver), one of two narrowband microwave filters (with a passband $\Delta f = 0.29$ GHz for $f_0 = 12.9$ GHz or $\Delta f = 0.51$ GHz for $f_0 = 9.1$ GHz) tuned to the magnetron frequency was installed. Both receivers had nearly the same power sensitivity. For this reason, when the radiation spectrum at the receiver entrance was narrower than the passband of the microwave filter, the narrowband-to-broadband signal ratio was equal to unity. When the radiation spectrum at the receiver entrance was broader than the passband of the microwave filter, this ratio was lower. Hence, it was possible to estimate the width of the spectrum of output microwave radiation.

To carry out absolute measurements of the output microwave power, we used a broadband wide-aperture microwave calorimeter [11]. The calorimeter measured the total energy of the output microwave pulse, and the envelope of the microwave pulse was recorded by the detector. This allowed us to determine the output microwave power.

3. EXPERIMENTAL RESULTS

Figure 2a shows the output energy of spontaneous microwave radiation on the plasma density (crosses) in the absence of an absorber. It is seen from the figure that self-excitation occurs if $n_p \geq 4 \times 10^{12}$ cm^{-3}. When an external 40-kW microwave signal at a frequency of $f_0 = 9.1$ GHz is fed to the input of the beam–plasma system, the density range in which the generation is observed expands toward lower plasma densities. The corresponding experimental data are shown by circles in Fig. 2a. Hence, there exists a range of plasma densities, $2.5 \times 10^{12} < n_p < 4 \times 10^{12}$ cm^{-3}, in which the output

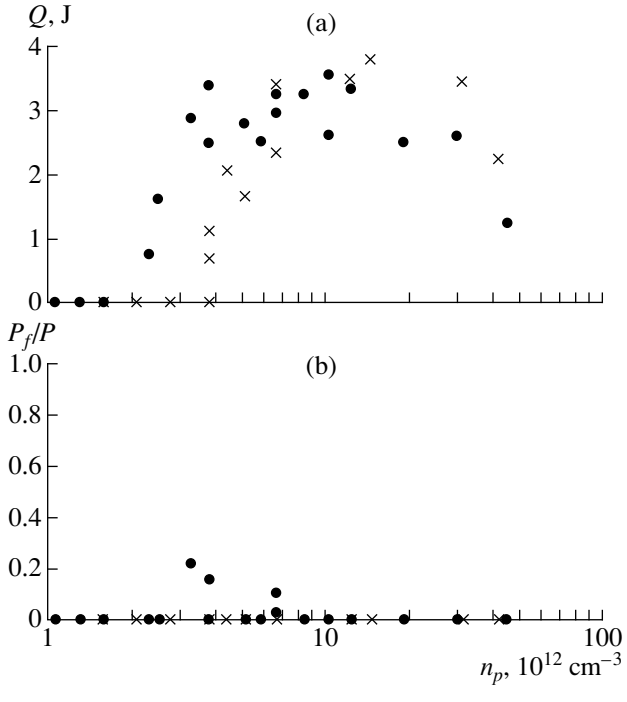

Fig. 2. (a) The output microwave radiation energy measured by the calorimeter as a function of the plasma density and (b) the ratio between the power measured by the narrowband and broadband receivers vs. the plasma density at t = 75 ns after applying the voltage pulse to the diode in the case when a 40-kW signal at a frequency of 9.1 GHz is fed to the entrance of the system (circles) and without an input signal (crosses); the microwave absorber is absent.

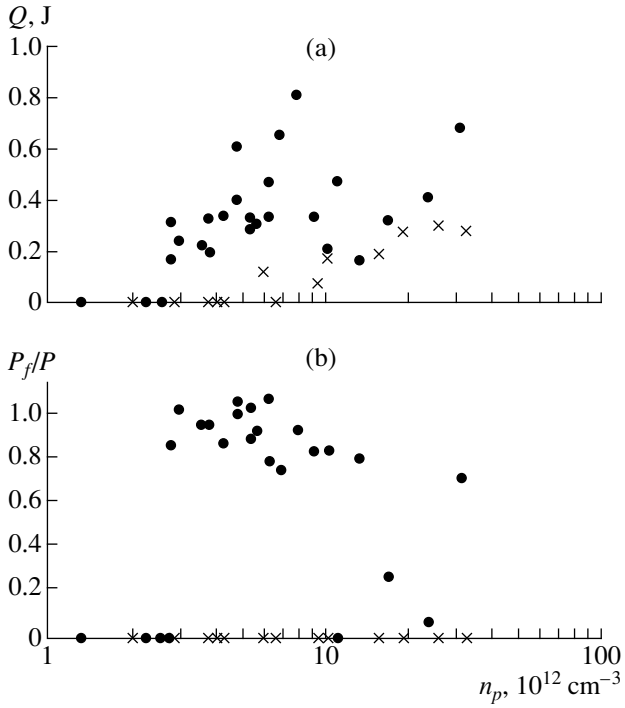

Fig. 3. (a) The output microwave radiation energy measured by the calorimeter as a function of the plasma density and (b) the ratio between the power measured by the narrowband and broadband receivers vs. the plasma density at t = 75 ns after applying the voltage pulse to the diode in the case when a 40-kW signal at a frequency of 9.1 GHz is fed to the entrance of the system (circles) and without an input signal (crosses); the microwave absorber is present.

signal is detected only if the input signal is fed; this may be interpreted as signal amplification. The output power in this operation mode attains 60 MW.

As was mentioned above, in order to estimate the width of the emission spectrum, the output radiation was measured by two (broadband and narrowband) microwave receivers that had the same sensitivity. Figure 2b shows the ratio between the powers detected by the narrowband and broadband receivers as a function of the plasma density. This ratio was calculated at the time t = 75 ns after applying the voltage pulse to the diode. The circles correspond to the presence of a signal at the entrance to the beam–plasma system. It is seen from the figure that the power ratio is no higher than 0.3; this means that only about 35% of the radiation power falls into the sensitivity band of the narrowband receiver.

The data presented in Fig. 2 allow us to conclude that, at $n_p > 4 \times 10^{12}$ cm^{-3}, the beam–plasma system under study operates in the regime of spontaneous generation. At $2.5 \times 10^{12} < n_p < 4 \times 10^{12}$ cm^{-3}, it operates in a mixed mode. In the regime of spontaneous generation, the output signal is unaffected by the input signal and, in most of the pulses, the ratio between the signals from the narrowband and broadband receivers is no higher than 0.05. In the mixed mode, a substantial (about 35%) fraction of the emission power lies within a 0.5-GHz-wide band and the output signal is detected only in the presence of the input signal.

To suppress spontaneous generation, we used a large-volume microwave absorber (Fig. 1, position *6*). Figure 3a shows the output radiation energy as a function of the plasma density in the absence (crosses) and presence (circles) of a 40-kW input signal at a frequency of f_0 = 9.1 GHz. It is seen from Fig. 3a that, with an absorber, the energy of spontaneous emission generated in the range of plasma densities $2 \times 10^{12} < n_p < 1.7 \times 10^{13}$ cm^{-3} is lower by a factor more than 15 than without an absorber. At the same time, the energy of the amplified signal decreases only by a factor of 5, which is evidence of the positive effect of the absorber. Figure 3a demonstrates that, in the range of plasma densities $3 \times 10^{12} < n_p < 3 \times 10^{13}$ cm^{-3}, the amplified radiation dominates over the spontaneous emission. In this case, the maximum power of the amplified signal is 8 MW, whereas the maximum power of spontaneous emission is 1 MW.

Figure 3b shows the ratio between the signals from the narrowband and broadband receivers in the presence of an absorber at t = 75 ns after applying the voltage pulse to the diode. It is seen that, in the range of

plasma densities $3 \times 10^{12} < n_p < 1.2 \times 10^{13}$ cm^{-3}, the output signal from the beam–plasma system always lies within the sensitivity band of the narrowband receiver (the power ratio is close to unity). This property fundamentally distinguishes this system from the above system without an absorber as well as from the system described in [10]. Note that the value of P_f/P was measured accurate to within 15%. That is why, for some shots in Fig. 3b, we have $P_f/P > 1$.

Figure 4a shows the waveforms of the signals from the broadband (*1*) and narrowband (*2*) receivers and the voltage pulse at the diode (*3*) for a plasma density of 5×10^{12} cm^{-3}. As was noted above, the receivers have the same sensitivity; consequently, the fact that the first waveform is identical to the second one shows that the spectrum of the output radiation lies within the passband of the narrowband microwave filter throughout the entire voltage pulse. We note that, for $9 \times 10^{12} < n_p < 1.5 \times 10^{13}$ cm^{-3}, spontaneous generation occurs by the end of the voltage pulse and the spectrum of the output radiation broadens. This is illustrated by Fig. 4b, which corresponds to a plasma density of 10^{13} cm^{-3}. It is seen that, during a time of ~80 ns from the beginning of the voltage pulse, the signals from the narrowband and broadband receivers are identical; later, they show a different behavior. This indicates that the radiation spectrum is wider than the passband of the microwave filter.

Figure 5 shows the theoretical frequency dependence of the linear single-pass wave-power amplification coefficient for different plasma densities. (The plots in Figs. 5 and 6c were calculated with the help of a numerical code developed by M. A. Krasil'nikov.) It follows from Fig. 5 that it is possible, first, to realize the amplification regime (within a frequency band of about 40%) for a given plasma density and, second, to tune the amplified frequency from 8 ± 1.5 to 35 ± 4 GHz by varying the plasma density from 8×10^{12} to 7×10^{13} cm^{-3}. To verify these theoretical predictions, we carried out experiments on the amplification of a signal at a frequency of 12.9 GHz. A 75-kW signal was fed to the input of the beam–plasma system with a microwave absorber. Figure 6a shows the output radiation energy as a function of the plasma density in the absence (crosses) and presence (circles) of the input signal. It is seen from Fig. 6a that, in the range of plasma densities $10^{13} < n_p < 1.6 \times 10^{13}$ cm^{-3}, spontaneous generation is absent but there is an amplified signal with a power of up to 4 MW. Figure 6b (similar to Figs. 2b and 3b) illustrates the ratio between the signals from the narrowband and broadband receivers at $t = 75$ ns after applying the voltage pulse to the diode. A comparison of Figs. 3b and 6b shows that the operation of the system at a frequency of $f_0 = 12.9$ GHz is less stable and the P_f/P ratio lies within the range 0.2–0.9 for the plasma density in the range $10^{13} < n_p < 3 \times 10^{13}$ cm^{-3}. Nevertheless, we can conclude that the amplification also takes place at a frequency of 12.9 GHz.

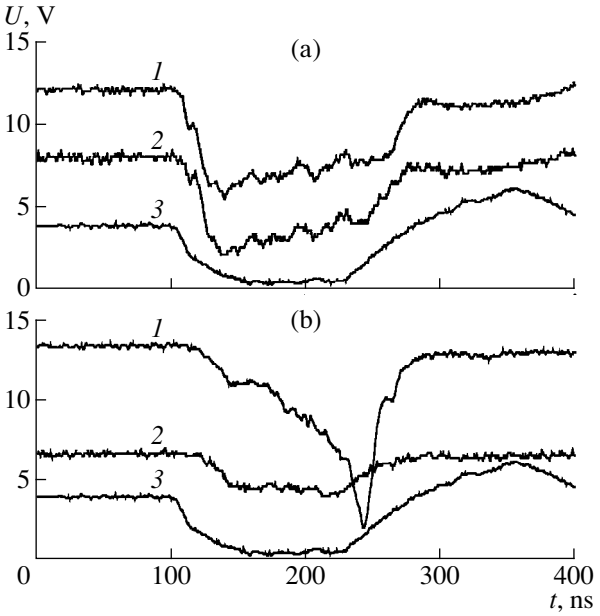

Fig. 4. Waveforms of the signals from (*1*) the broadband and (*2*) narrowband receivers and (*3*) the voltage pulse at the diode for $f_0 = 9.1$ GHz, $P_{in} = 40$ kW, and $n_p =$ (a) 5×10^{12} and (b) 10^{13} cm^{-3}; the microwave absorber is present.

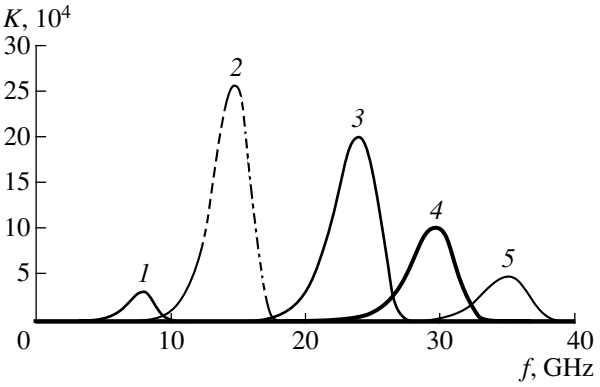

Fig. 5. Frequency dependences of the single-pass wave-power amplification coefficient calculated using linear theory for the parameters of the beam–plasma system presented in Section 2 at the plasma densities of $n_p =$ (*1*) 8×10^{12}, (*2*) 2×10^{13}, (*3*) 4×10^{13}, (*4*) 5.5×10^{13}, and (*5*) 7×10^{13} cm^{-3}.

Figure 6c shows the theoretical dependence of the linear single-pass wave-power amplification coefficient on the plasma density for two input-signal frequencies: 9.1 GHz (curve *1*) and 12.9 GHz (curve *2*). A comparison of Figs. 3b, 6b, and 6c shows that the experimental results are in good agreement with the results of theoretical calculations. For both signal frequencies, the experimentally observed ranges of plasma densities in

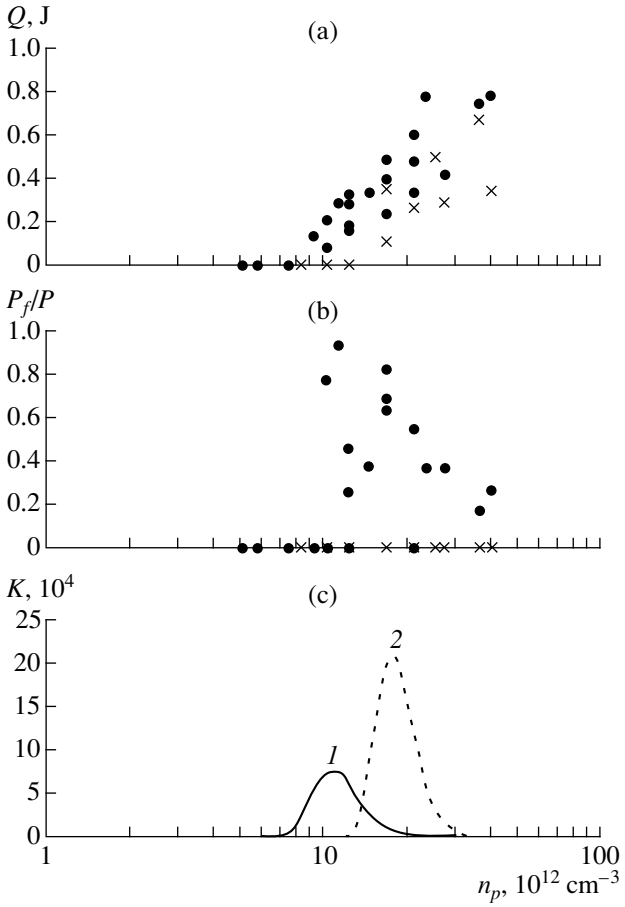

Fig. 6. (a) The output microwave radiation energy measured by the calorimeter as a function of the plasma density and (b) the ratio between the power measured by the narrowband and broadband receivers vs. the plasma density at t = 75 ns after applying the voltage pulse to the diode in the case when a 75-kW signal at a frequency of 12.9 GHz is fed to the entrance of the system (circles) and without an input signal (crosses); the microwave absorber is present. (c) Dependence of the linear single-pass wave-power amplification coefficient on the plasma density at f_0 = (*1*) 9.1 and (*2*) 12.9 GHz.

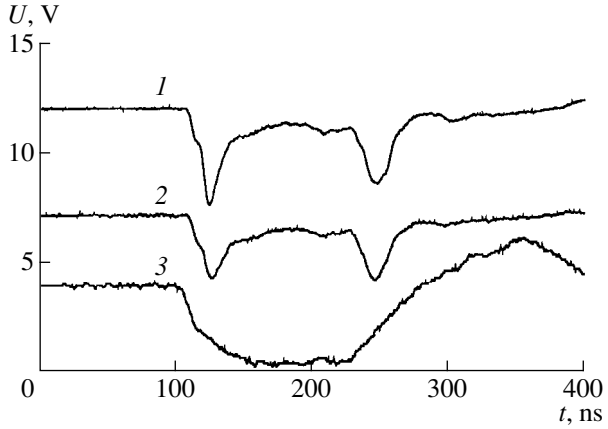

Fig. 7. Waveforms of the signals from (*1*) the broadband and (*2*) narrowband receivers and (*3*) the voltage pulse at the diode for f_0 = 9.1 GHz, P_{in} = 40 kW, and $n_p = 3 \times 10^{12}$ cm^{-3}; the microwave absorber is present.

which the system operates as an amplifier are in agreement with theoretical predictions. However, the theoretical and experimental threshold values of the density at which the system passes over to the amplification regime are different. This discrepancy can be explained by the inaccuracy of the measurements of the absolute values of the plasma density. We also note that it makes no sense to compare the experimental and calculated values of the amplification coefficient, because the presence of the microwave absorber in the system was ignored in calculations. It also follows from Fig. 6c that, according to the theory, there exists a range of plasma densities in which the amplification can take place for both frequencies of the input signal. In the experiment, at a plasma density of $n_p = 1.2 \times 10^{13}$ cm^{-3}, the beam–plasma system amplified the signal at frequencies of both 9.1 and 12.9 GHz.

It is also of interest to compare the experimental and theoretical dependences of the parameters of the amplification regime on the energy of REB electrons. According to the theory, for a given frequency of the input signal, the electron energy at which the amplification occurs increases with increasing the plasma density. Figure 7 shows the waveforms of the signals from the broadband (*1*) and narrowband (*2*) receivers and the voltage pulse at the diode (*3*). The figure corresponds to a plasma density of $n_p = 3 \times 10^{12}$ cm^{-3} and an input-signal frequency of f_0 = 9.1 GHz. It is seen from the figure that the amplification coefficient is maximum at the leading and trailing edges of the voltage pulse when the energy of the REB electrons is lower than the maximum energy. As the plasma density increases, the maximum value of the amplification coefficient shifts to the top of the voltage pulse, where the energy of REB electrons is maximum (Fig. 4a).

It is seen from Fig. 7 that, although the system operates in the amplification regime, the ratio between the signals from the narrowband and broadband receivers is below unity at the leading edge of the voltage pulse. It looks as if the spectrum of the output radiation is broader than 0.5 MHz. However, we believe that this effect may be attributed to an insufficiently fast response of the narrowband receiver, which cannot trace fast signals lasting several nanoseconds. The Q-factor of the microwave filter of the narrowband receiver is on the order of 20; consequently, the characteristic rise time of the signal is $t_0 = Q/f_0 \approx 2$ ns. In Fig. 7, the rise time of the first signal from the broadband receiver is ~5 ns, which is comparable with t_0. If the signal duration is much longer than 2 ns (as, e.g., in Fig. 4), then the narrowband receiver correctly reproduces the signal shape.

4. CONCLUSION

(i) A stable regime of amplification of a slow plasma wave in a beam–plasma system has been obtained for the first time. For a 9.1-GHz input signal, there exists a

range of plasma densities in which the spectrum of the output microwave radiation lies in a 0.5-GHz-wide band throughout the entire voltage pulse at the diode. The output power of the amplified signal attains 8 MW, and the power amplification coefficient is on the order of 200. The experimentally measured range of plasma densities in which the amplification of a 9.1-GHz signal takes place agrees well with the results of calculations using linear theory.

(ii) It has been shown experimentally for the first time that the beam–plasma amplifier can operate at frequencies of 9.1 and 12.9 GHz. The range of plasma densities in which the amplification is observed agrees with the theoretical results. Moreover, the experiment confirms the theoretical prediction that there is a value of the plasma density at which the beam–plasma system can amplify signals at both frequencies.

(iii) The influence of the energy of REB electrons on the amplification band has been observed experimentally. The results obtained agree with theoretical predictions.

ACKNOWLEDGMENTS

We thank A.A. Rukhadze and O.T. Loza for fruitful discussions of the results obtained and I.L. Bogdankevich for help in calculations. This work was performed with the Plasma Relativistic Maser device (registration no. 01-04) and was supported in part by the Russian State Committee on Science and Technology and the Russian Foundation for Basic Research (project no. 97-02-16948).

REFERENCES

1. L. S. Bogdankevich, M. V. Kuzelev, and A. A. Rukhadze, Usp. Fiz. Nauk **133** (1), 3 (1981) [Sov. Phys. Usp. **24**, 1 (1981)].
2. A. N. Antonov, Yu. P. Bliokh, Yu. A. Degtyar', *et al.*, Fiz. Plazmy **20**, 777 (1994) [Plasma Phys. Rep. **20**, 699 (1994)].
3. L. A. Mitin, V. I. Perevodchikov, M. A. Zav'yalov, *et al.*, Fiz. Plazmy **20**, 733 (1994) [Plasma Phys. Rep. **20**, 662 (1994)].
4. M. V. Kuzelev, F. Kh. Mukhametzyanov, M. S. Rabinovich, *et al.*, Zh. Éksp. Teor. Fiz. **83**, 1358 (1982) [Sov. Phys. JETP **56**, 780 (1982)]; Dokl. Akad. Nauk SSSR **267**, 829 (1982) [Sov. Phys. Dokl. **27**, 1030 (1982)].
5. M. V. Kuzelev, A. A. Rukhadze, P. S. Strelkov, and A. G. Shkvarunets, Fiz. Plazmy **13**, 1370 (1987) [Sov. J. Plasma Phys. **13**, 793 (1987)].
6. A. G. Shkvarunets, A. A. Rukhadze, and P. S. Strelkov, Fiz. Plazmy **20**, 682 (1994) [Plasma Phys. Rep. **20**, 613 (1994)].
7. M. V. Kuzelev, O. T. Loza, A. V. Ponomarev, *et al.*, Zh. Éksp. Teor. Fiz. **109**, 2048 (1996) [JETP **82**, 1102 (1996)].
8. M. V. Kuzelev, V. A. Panin, A. P. Plotnikov, and A. A. Rukhadze, Zh. Éksp. Teor. Fiz. **101**, 460 (1992) [Sov. Phys. JETP **74**, 242 (1992)].
9. M. A. Krasil'nikov, M. V. Kuzelev, and A. A. Rukhadze, Zh. Éksp. Teor. Fiz. **108**, 521 (1995) [JETP **81**, 280 (1995)].
10. A. V. Ponomarev, P. S. Strelkov, and A. G. Shkvarunets, Fiz. Plazmy **24**, 53 (1998) [Plasma Phys. Rep. **24**, 48 (1998)].
11. A. G. Shkvarunets, Prib. Tekh. Éksp., No. 4, 72 (1996).

Translated by N. Larionova

Plasma Physics Reports, Vol. 26, No. 7, 2000, pp. 598–601. Translated from Fizika Plazmy, Vol. 26, No. 7, 2000, pp. 639–642.

PLASMA ELECTRONICS

Generation of Broadband Radio Pulses by a New-Type Reflex Triode with a Virtual Cathode

S. V. Bulychev, A. E. Dubinov, V. S. Zhdanov, I. L. L'vov, S. A. Sadovoy, V. D. Selemir, and V. N. Khaldeev

All-Russia Research Institute of Experimental Physics, Russian Federal Nuclear Center, Sarov, Nizhni Novgorod oblast, 607188 Russia

Received November 24, 1999

Abstract—Results are presented on the development and experimental study of a reflex triode with a new type of virtual cathode. In this device, a discharge excited along a ferroelectric surface is used as a source of electrons and loop antennas are used for emitting radiation. Generation of broadband radio pulses with a central frequency of ~300 MHz and power of ~80 W is achieved. © *2000 MAIK "Nauka/Interperiodica".*

Reflex triodes (RT), proposed in 1978 by Kapetanakus *et al.* [1], are now one of the main types of superpowerful microwave oscillators with a virtual cathode (VC). The current state of the development and study of RTs is presented in reviews [2–4]. The main features of present-day RTs are as follows: the use of an explosive-emission cathode, generation of radiation at frequencies of ~3 GHz in a gigawatt power range, horn-type microwave output, and single-pulse operation.

In connection with a number of engineering applications, the problem of designing an RT microwave oscillator with different output characteristics, specifically, a moderate-power repetitive microwave oscillator operating at a high repetition rate, arises. Clearly, it is rather difficult from an engineering standpoint to achieve such operation conditions in the relativistic range of the cathode–anode voltages (200 kV and higher). At the same time, there exist compact pulsed voltage sources generating voltage pulses with an amplitude of up to10 kV at a repetition rate of up to 1 kHz and higher (see, e.g., [5]).

However, at such voltages at a vacuum diode, explosive emission is hardly possible because of the high threshold with respect to the electric field. At voltages of about 1 kV, such emission is certainly impossible in diodes with a several-millimeter-wide gap. We note that the high threshold with respect to the applied voltage is due to the fact that, in this scheme, explosive emission is uncontrollable because the same voltage pulse creates an explosive plasma and accelerates plasma electrons.

Hence, it is necessary to search for other types of cathodes that either have a low threshold or do not have one at all.

Thus, in [6, 7], thermoemission microwave oscillators with a VC are described. However, the currents in those devices were not high enough to form a proper VC and generation was achieved due to the reflection of electrons from a magnetic mirror. Therefore, it seems that the cathode must have emission characteristics comparable to those of explosive-emission cathodes.

In [8], a scheme of extracting electrons and ions from a plasma produced in an electric explosion was proposed in which explosive emission could be controlled and had no threshold.

The basic concept of scheme [8] is that the plasma is produced and charged particles are extracted in two different voltage pulses. It is also proposed to use triple "metal–dielectric–vacuum" points as electric-field concentrators instead of the cathode micropoints that are traditionally used in schemes based on explosive emission from metallic cathodes.

It is well known that a triple point (especially in the case of a dielectric with a high permittivity) strengthens the electric field in its vicinity. This field results in an intense autoelectronic emission from the metal edge near the triple point, which leads to an electric explosion of the metal edge. The electric explosion, in turn, can initiate a discharge along the dielectric surface [9].

Therefore, according to the above scheme, the emitter should consist of two electrodes separated by an insulator. A controlling-voltage pulse applied to the electrodes initiates an electric explosion at the edge of one of the electrodes (cathode) and, then, a discharge along the dielectric surface. The surface-discharge plasma short-circuits the interelectrode gap and shunts the controlling voltage. Then, by applying a voltage pulse of a certain polarity and amplitude to an additional extraction electrode, it is possible to obtain either an electron beam or a positive-ion beam with the required particle energy.

Based on this concept, a compact high-current emitter was designed in [8]. This emitter not only has parameters competing with the well-known explosive-emission emitters but also possesses new functional capabilities, such as controllability, the absence of a

1063-780X/00/2607-0598$20.00

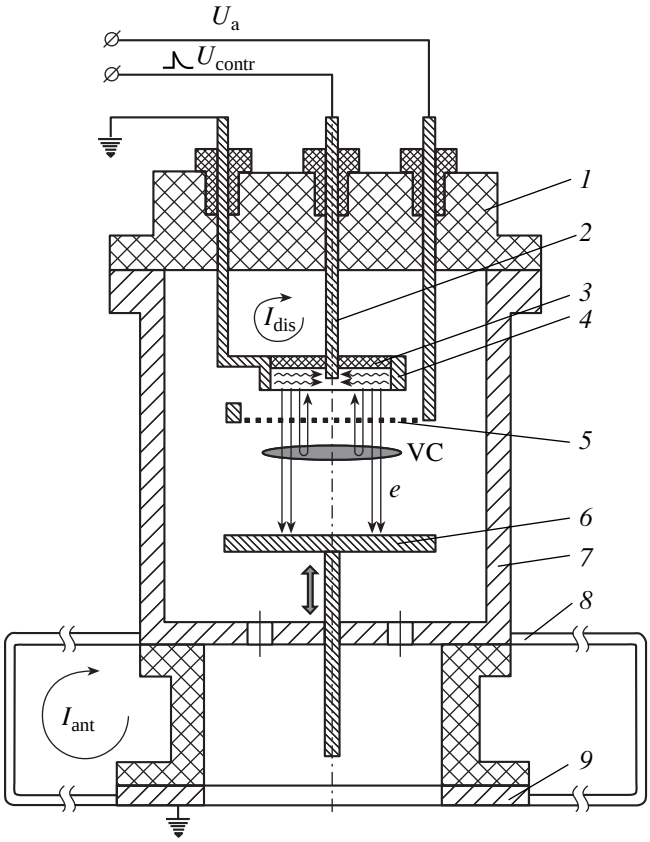

Fig. 1. Design of the RT: (*1*) insulator, (*2*) high-voltage electrode for controlling the surface discharge, (*3*) ferroelectric pellet, (*4*) grounded electrode, (*5*) anode grid, (*6*) electron collector, (*7*) vacuum chamber, (*8*) loop antenna, and (*9*) pump flange.

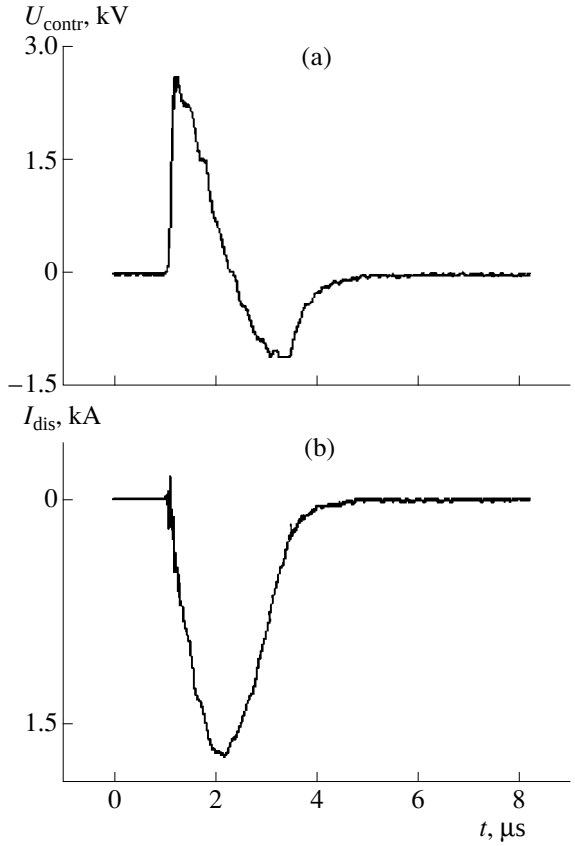

Fig. 2. Synchronized waveforms: (a) voltage pulse at the electrodes of the surface discharge and (b) discharge-current pulse.

threshold, and the possibility of producing positive-ion beams. In this paper, we describe an RT with such an emitter operating at diode voltages in the range 0.2–10 kV.

It is easy to show that the generation frequency of an RT with a diode-gap width equal, e.g., to 5 mm, would lie in the range 150–1000 MHz. Evidently, if the antenna system of an RT operating in this frequency range were made according to a conventional waveguide–horn scheme, then it would be rather cumbersome.

Specifically for VC-based generators, we also elaborated a new output system in which the RT radiation is emitted with the help of loop antennas placed between the cathode and the reflector (collector) and serving also as return-current circuits.

This kind of RT also differs substantially from the known RTs in terms of the principle of generation. Let us consider this in more detail. First of all, we note that RTs [1–4] are based on electric-dipole microwave generation; in this case, the generation occurs due to oscillations of the electric dipole VC–VC image at the cathode. It is clear that, in order to increase the generation power, it is necessary that the maximum possible fraction of the electron flux is reflected from the VC back to the injection site (i.e., to the cathode). Thereby, a maximum charge in the electric dipole can be achieved by providing the condition $I/I_{lim} \longrightarrow \infty$, where I is the RT diode current and I_{lim} is the limiting current for the region bounded by the anode and the collector; i.e., the region where the VC is formed. For this reason, in the known RTs, the volume of this region is fairly large.

In our RT, the wires of the return-current circuit are loop antennas emitting microwaves through magnetic-dipole emission. Therefore, in order to ensure the maximum power and maximum efficiency, one must try to attain the complete modulation of the current injected from the diode through the anode grid into the cavity bounded by the anode and the collector. Then, in order to obtain the maximum emission power at a given supply power, it is necessary that the condition $I/I_{lim} \approx 2$ holds, which can be easily achieved by varying the distance between the anode grid and the collector.

Note that this output system has additional advantages: it is compact; the geometry of the entire antenna system can be promptly rearranged to suit the operating

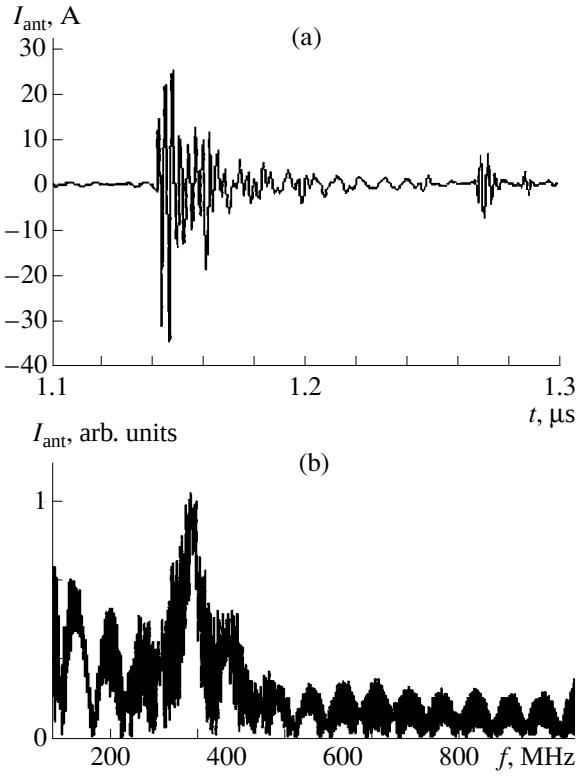

Fig. 3. Generated radio pulse: (a) waveform of the current in the loop antennas and (b) Fourier transform of the current pulse in the loop antennas.

conditions of the RT and the required directional diagram; and the emission power P can be increased according to the known value of $R \propto (L_e/\lambda)^2$, where R is the wave impedance and L_e is the effective length of the loop antenna [10]. Furthermore, loop antennas can be used in phased arrays with RTs by catenating the wires of two neighboring RTs in the form of ordinary HF transformers (e.g., Tesla transformers).

Based on the above considerations, we designed and created an RT whose scheme is shown in Fig. 1. The RT vacuum chamber is a hollow stainless-steel cylinder with an inner diameter of 50 mm and length of 70 mm. On the top, the chamber is hermetically covered by an insulator, in which three electrodes are mounted. One of the electrodes is connected to a grid anode, the second electrode holds a ferroelectric pellet, and the third is grounded. The grid anode is made from a tantalum wire 0.1 mm in diameter and has a geometrical transmittance of about 80%. The ferroelectric pellet is made from lead zirconate-titanate (TsTS-19) and is 3 mm thick and 15 mm in diameter and has a hole 2 mm in diameter; the ferroelectric permittivity is $\varepsilon = 1060$. The emitting area of the ferroelectric source of electrons is $S = 30$ mm^2, and the interelectrode gap of the surface discharge is 1.5 mm. The anode position with respect to the emitter can be varied. A movable collector—a metal disk 40 mm in diameter—is installed on the bottom of the chamber. The vacuum chamber is connected to the pumping system through holes in the chamber bottom. The collector is in electric contact with the chamber. Since the chamber should be at the collector potential when recording signals, the chamber is insulated from the grounded body of the pump on which it is mounted. The residual gas pressure in the chamber is no higher than 3×10^{-5} torr.

As a return-current circuit and, at the same time, the radiation-output facility, we used four symmetrically positioned loop antennas made from a copper wire 1 mm in diameter with a length of $L = 40$ cm. Calibrated 5-Ω resistors connected in the circuit of each loop measured the antenna currents.

To ignite a discharge along the generator surface, we used a specially designed high-voltage pulsed generator. Figure 2a shows the waveform of the voltage pulse $U_{contr}(t)$ with an amplitude of ~2.5 kV applied to the discharge gap. Figure 2b presents the waveform of the surface-discharge current $I_{dis}(t)$; the waveform is synchronized with the voltage pulse. A constant accelerating voltage of 0.2–2 kV was applied to the grid anode.

Figure 3a shows a typical waveform of the antenna current $I_{ant}(t)$; the signal was taken from calibrated resistors and processed with an HF filter cutting off the frequencies below 100 MHz. The waveform was obtained for an emitter–anode gap of 5 mm and an accelerating voltage of 1 kV. Figure 3b presents the Fourier spectrum of this signal. It is seen that the amplitude is maximum at a frequency of ≈300 MHz, whereas numerical estimates for the frequency of electron oscillations in the emitter–VC potential well yield 320 MHz. The FWHM of the central emission peak is no less than 60 MHz. At an accelerating voltage of 2 kV, the emission frequency was higher than that in Fig. 3 by a factor of 1.4. Thus, there is a good agreement between the expected and observed frequencies, which proves the generation mechanism based on the modulation of the injected current by an oscillating VC.

The peak emission power was estimated by the formulas presented in [10] for loop antennas whose length is comparable with the emission wavelength. This estimate yields the peak emission power at a level of ~80 W.

The pulse duration under various operating conditions was no higher than 100 ns. Such a short duration may be explained as follows: the magnetic pressure of the discharge current expels the plasma onto the anode grid; as a result, the cathode–anode gap of the RT is shunted and the generation of the electron beam terminates. To prolong the generation, in future experiments, it will be reasonable to employ electron sources based on an incomplete slipping discharge (see [11]).

So far, the RT has been mainly tested in a repetitive mode at a repetition rate of 1 Hz. In experiments in which the emitter operated at a repetition rate of 50 Hz, it has also demonstrated stable operation during several half-hour series [12]. We plan to carry out special resource tests of the RT at a repetition rate of 50 Hz.

REFERENCES

1. C. A. Kapetanakos, P. A. Sprangle, R. A. Mahaffey, and J. Golden, US Patent No. 4150340, H 01 J 25/74 (April 17, 1979).
2. A. N. Didenko, A. P. Arzin, A. G. Zherlitsyn, *et al.*, in *Relativistic High-Frequency Electronics* (Inst. Prikl. Fiz. Akad. Nauk SSSR, Gorki, 1984), Vol. 4, p. 104.
3. A. N. Didenko, V. P. Grigor'ev, and A. G. Zherlitsyn, in *Plasma Electronics* (Naukova Dumka, Kiev, 1989), p. 112.
4. A. E. Dubinov and V. D. Selemir, Zarubezhnaya Radioélektron., No. 4, 54 (1995).
5. E. S. Fulkerson, D. C. Norman, and R. Booth, in *Digest of Technical Papers of 11th IEEE International Pulsed Power Conference, Baltimore, 1997*, Vol. II, p. 1341.
6. W. Pingshan, H. Kesong, H. Sunren, *et al.*, Int. J. Infrared Millim. Waves **11**, 1395 (1990).
7. R. Kraft, IEEE Trans. Plasma Sci. **21**, 739 (1993).
8. A. E. Dubinov, S. A. Sadovoy, and V. D. Selemir, in *Proceedings of XXVI Zvenigorod Conference on Plasma Physics and Controlled Nuclear Fusion, Zvenigorod, 1999*, p. 170.
9. G. A. Mesyats, Dokl. Akad. Nauk SSSR **336**, 610 (1994) [Phys. Dokl. **39**, 417 (1994)].
10. M. S. Zhuk and Yu. B. Molochkov, *Designing of Lense, Scanning, and Broadband Antennas and Feeder Devices* (Énergiya, Moscow, 1973).
11. S. P. Bugaev and G. A. Mesyats, Dokl. Akad. Nauk SSSR **196**, 324 (1971) [Sov. Phys. Dokl. **16**, 41 (1971)].
12. S. V. Bulychev, A. E. Dubinov, V. S. Zhdanov, *et al.*, Prib. Tekh. Éksp., No. 3, 116 (1999).

Translated by N. Larionova

Plasma Physics Reports, Vol. 26, No. 7, 2000, pp. 602–605. Translated from Fizika Plazmy, Vol. 26, No. 7, 2000, pp. 643–646.

NONLINEAR PHENOMENA

Thomson Scattering in a Plasma Created by a Short Intense Laser Pulse

M. V. Chegotov

Institute for High Energy Densities, Associated Institute for High Temperatures, Russian Academy of Sciences, Izhorskaya ul. 13/19, Moscow, 127412 Russia

Received May 24, 1999; in final form, December 20, 1999

Abstract—Thomson scattering spectra from a plasma created through ionization of a gas consisting of multielectron atoms by a laser pulse with an intensity of about 10^{16} W/cm^2 or higher and with a duration $\tau_{imp} \le 100$ fs are studied theoretically with allowance for electron groups with different temperatures. © *2000 MAIK "Nauka/Interperiodica".*

The electron component of a plasma produced in the interaction of an ultrashort intense laser pulse with matter is studied experimentally using various diagnostic techniques such as spectroscopic and spectrometric methods (see, e.g., [1–3]) and the methods based on the scattering of laser light by a plasma (see, e.g., [4–6]). One of the main parameters measured by these diagnostics is the electron temperature of a laser-produced plasma. Theoretical investigations of electron heating during ionization are, as a rule, based on a classical paper by Corcum *et al.* [7]. Although experimental temperatures measured by the above diagnostic techniques are comparable in order of magnitude, they differ from theoretical predictions [7] and, even when recorded under similar experimental conditions, may differ from each other by several times (see, e.g., [1, 2, 4, 5]).

This discrepancy may be explained by the fact that the diagnostic data are processed without allowance for the following important features of a plasma produced in the interaction of an ultrashort intense laser pulse with matter (see [8] for details). First, the electron gas produced during the ionization of multielectron atoms by an intense laser field consists of several electron groups, differing in their temperatures on a fairly long time scale. Second, the electron velocity distribution function $f_e(\mathbf{v})$ also remains anisotropic for a long time; moreover, the anisotropy of $f_e(\mathbf{v})$ is associated with the fact that the velocity distribution of the electrons in each group is anisotropic because, during gas ionization, the electrons are ejected from each atomic level preferentially in the direction of the laser field (see, e.g., [9]). The anisotropy of the distribution function of the electrons produced during ionization of matter by an intense field of a harmonic electromagnetic wave was also pointed out by Bychenkov and Tikhonchuk [10].

The main features of Thomson scattering can be understood by considering the spectral distribution of the correlation function (correlator) of the electron density fluctuations, $\langle \delta N_e^2 \rangle_{\omega, \mathbf{k}}$, which characterizes the scattering by electron density perturbations with the wave vector $\mathbf{k}$ and frequency ω (see [11], p. 346). In CGS units, the correlator can be written as (cf. [11], p. 333)

$$\begin{aligned}\langle \delta N_e^2 \rangle_{\omega, \mathbf{k}} &= 2\pi \left| \frac{1 + \delta\varepsilon_i(\omega, \mathbf{k})}{\varepsilon(\omega, \mathbf{k})} \right|^2 \int f_e(\mathbf{v}_e) \delta(\omega - \mathbf{k}\mathbf{v}_e) d^3\mathbf{v}_e \\ &+ 2\pi \left| \frac{\delta\varepsilon_e(\omega, \mathbf{k})}{\varepsilon(\omega, \mathbf{k})} \right|^2 \sum_\alpha \int f_i^{\langle\alpha\rangle}(\mathbf{v}_i) \delta(\omega - \mathbf{k}\mathbf{v}_i) d^3\mathbf{v}_i.\end{aligned} \quad (1)$$

Here, $\delta\varepsilon_i(\omega, \mathbf{k}) = \frac{4\pi}{|\mathbf{k}|^2} \sum_\alpha \frac{e_\alpha^2}{M_\alpha} \int \frac{\mathbf{k} \partial f_i^{\langle\alpha\rangle}/\partial \mathbf{v}_i}{\omega - \mathbf{k}\mathbf{v}_i} d^3\mathbf{v}_i$, $\delta\varepsilon_e(\omega, \mathbf{k}) = \frac{4\pi e^2}{|\mathbf{k}|^2 m_e} \int \frac{\mathbf{k} \partial f_e/\partial \mathbf{v}_e}{\omega - \mathbf{k}\mathbf{v}_e} d^3\mathbf{v}_e$, $\varepsilon(\omega, \mathbf{k}) = 1 + \delta\varepsilon_e(\omega, \mathbf{k}) + \delta\varepsilon_i(\omega, \mathbf{k})$, $f_e(\mathbf{v}_e)$ is the electron distribution function, $f_i^{\langle\alpha\rangle}(\mathbf{v}_i)$ is the distribution function of the ions of species α, $n_e = \int f_e(\mathbf{v}_e) d^3\mathbf{v}_e$ is the total electron density, $n_i = \sum_\alpha \int f_i^{\langle\alpha\rangle}(\mathbf{v}_i) d^3\mathbf{v}_i \equiv \sum_\alpha n_i^{\langle\alpha\rangle}$ is the total ion density, m_e and e are the mass and charge of an electron, and M_α and e_α are the mass and charge of an ion of species α. The wave vector of the electron density perturbations $\mathbf{k}$ is related to the wave vectors of the incident and scattered light ($\mathbf{k}_i$ and $\mathbf{k}_s$) in a usual manner: $\mathbf{k} = \mathbf{k}_i - \mathbf{k}_s$.

In accordance with the investigations of Delone and Kraĭnov [9], we can expect that the velocity distribution of the electrons that are ejected from the same energy level of the gas atoms during ionization is described by an anisotropic Maxwellian function. According to [1], the groups of electrons that are ejected from atomic lev-

1063-780X/00/2607-0602$20.00

els with different ionization potentials are characterized by different temperatures. The time scales on which the temperatures of different electron groups are equalized by electron–electron (e–e) collisions and the time scales on which the velocity distributions of different electron groups become isotropic due to electron–ion (e–i) collisions differ from each other and may be very long. This enables us to describe the total electron velocity distribution as the sum of anisotropic Maxwellian velocity distribution functions of the electrons in different groups:

$$f_e(\mathbf{v}) = \frac{n_e}{Z}\left(\frac{m_e}{2\pi}\right)^{3/2}\sum_{n=1}^{Z}\frac{1}{\sqrt{T_{n,x}T_{n,y}T_{n,z}}} \times \exp\left\{-\frac{m_e}{2}\left(\frac{v_x^2}{T_{n,x}}+\frac{v_y^2}{T_{n,y}}+\frac{v_z^2}{T_{n,z}}\right)\right\}, \quad (2)$$

where Z is the degree of plasma ionization. The anisotropy of the total electron distribution is associated with gas ionization by a high-power laser pulse, which passes along the z-axis and whose electric field vector is in the xy plane (in particular, this may be an elliptically polarized laser pulse). Using spectra (1) to determine the parameters of the electron distribution function, we must treat the range of relatively high frequencies, $\omega \gg |\mathbf{k}|v_{Ti}$, where v_{Ti} is the characteristic ion thermal velocity (see [11], pp. 348, 349). In this way, we can investigate the electron distribution function $f_e(\mathbf{v}_e)$ assuming that the contribution of the ion component to the spectral distribution of the correlator of the electron density fluctuations $\langle \delta N_e^2 \rangle_{\omega,\mathbf{k}}$ is relatively small only when the characteristic electron thermal velocity v_{Te} is much higher than v_{Ti}. In a plasma created by an intense femtosecond laser pulse transmitted through a gas at a relatively low pressure, the condition $v_{Te} \gg v_{Ti}$ holds because of the difference in both the electron and ion masses and the characteristic temperatures T_e and T_i. In fact, in a plasma with a relatively low density, the efficiency of collisional ion heating in the laser field is low, since the relative velocity of electrons with respect to ions is high. After the passage of the pulse, ion heating via heat exchange with the electrons is also inefficient because of the large difference between the ion and electron masses. That T_i is lower than T_e is evidenced, in particular, by the experiments of [4]. In the frequency range $\omega \gg |\mathbf{k}|v_{Ti}$, the ion component can be assumed to be cold, $f_i^{\langle\alpha\rangle}(\mathbf{v}_i) = n_i^{\langle\alpha\rangle}\delta(\mathbf{v}_i)$, in which case we have $\delta\varepsilon_i(\omega,\mathbf{k}) = -\sum_\alpha 4\pi e_\alpha^2 n_i^{\langle\alpha\rangle}/(M_\alpha\omega^2)$. Substituting the distribution function (2) into the expression for $\delta\varepsilon_e(\omega,\mathbf{k})$ yields (see [11], p. 74)

$$\delta\varepsilon_e(\omega,\mathbf{k}) = \frac{4\pi e^2 n_e}{|\mathbf{k}|^2 Z}\sum_{n=1}^{Z}\frac{1}{T_n(\theta,\varphi)}\left[1 - J_+\left(\frac{\omega}{|\mathbf{k}|}\sqrt{\frac{m_e}{T_n(\theta,\varphi)}}\right)\right],$$

where $J_+(x) = x\exp(-x^2/2)\int_{i\infty}^{x}\exp(t^2/2)dt$. On the other hand, inserting (2) into (1) and integrating the resulting expression, we obtain

$$\langle \delta N_e^2\rangle_{\omega,\mathbf{k}} = \frac{2\pi n_e}{Z|\mathbf{k}|}\sqrt{\frac{m_e}{2\pi}}\left|\frac{1+\delta\varepsilon_i(\omega,\mathbf{k})}{\varepsilon(\omega,\mathbf{k})}\right|^2 \times \sum_{n=1}^{Z}\frac{1}{\sqrt{T_n(\theta,\varphi)}}\exp\left(-\frac{m_e\omega^2}{2|\mathbf{k}|^2 T_n(\theta,\varphi)}\right), \quad (3)$$

where

$$T_n(\theta,\varphi) = T_{n,x}\sin^2\theta\cos^2\varphi + T_{n,y}\sin^2\theta\sin^2\varphi + T_{n,z}\cos^2\theta \quad (4)$$

and the angles θ and φ determine the direction of the wave vector $\mathbf{k}$ with respect to the x-, y-, and z-axes: $\mathbf{k} = k(\sin\theta\cos\varphi, \sin\theta\sin\varphi, \cos\theta)$.

Note that, for an isotropic electron distribution ($T_{n,x} = T_{n,y} = T_{n,z}$) and when the temperatures of all of the electron groups are the same (and are equal to T), we obtain from (3) the following familiar expression for the spectral distribution of the correlator of the electron density fluctuations, $\langle \delta N_e^2\rangle_{\omega,\mathbf{k}}$:

$$\langle \delta N_e^2\rangle_{\omega,\mathbf{k}} = \frac{2\pi n_e}{|\mathbf{k}|}\sqrt{\frac{m_e}{2\pi T}} \times \left|\frac{1-\sum_\alpha \frac{4\pi e_\alpha^2 n_i^{\langle\alpha\rangle}}{M_\alpha\omega^2}}{1-\sum_\alpha \frac{4\pi e_\alpha^2 n_i^{\langle\alpha\rangle}}{M_\alpha\omega^2} + \frac{4\pi e^2 n_e}{|\mathbf{k}|^2 T}\left[1 - J_+\left(\frac{\omega}{|\mathbf{k}|}\sqrt{\frac{m_e}{T}}\right)\right]}\right|^2 \times \exp\left(-\frac{m_e\omega^2}{2|\mathbf{k}|^2 T}\right). \quad (5)$$

The asymptotics of this expression were investigated analytically in [11] (pp. 348, 349). It follows from (5) that the temperature T determined from the experimentally observed function $\langle \delta N_e^2\rangle_{\omega,\mathbf{k}}$ is independent of the direction of $\mathbf{k}$.

The situation is radically different when the electron distribution function is anisotropic. We assume that a high-power laser pulse is linearly polarized so that the electric field $\mathbf{E}$ is directed along the x-axis. Starting from the instant at which the first electron group appears (this group consists of the electrons ejected from the highest energy level of gas atoms), the electron temperatures $T_{n,y} = T_{n,z}$ are low in comparison with $T_{n,x}$ on a time scale τ shorter than the characteristic time $\tau_{ei,1}$ of collisions between the electrons of the first group and ions. Consequently, according to (4), we

have $T_n(\theta, \varphi) = T_{n,x}\sin^2\theta\cos^2\varphi$, so that the mean electron temperature T, which is determined from $\langle \delta N_e^2 \rangle_{\omega, \mathbf{k}}$, depends strongly on the angles θ and φ:

$$T \propto \sin^2\theta\cos^2\varphi. \quad (6)$$

As time elapses, e–i collisions give rise to isotropization of the distribution functions of different electron groups. On a time scale τ that is longer than the time $\tau_{ei,j}$ of collisions between the electrons from the jth group and ions but is shorter than the time $\tau_{ei,j+1}$ of collisions between the electrons from the $[j+1]$th group and ions, the expression for $\langle \delta N_e^2 \rangle_{\omega, \mathbf{k}}$ has the form

$$\langle \delta N_e^2 \rangle_{\omega, \mathbf{k}} = \frac{2\pi n_e}{Z|\mathbf{k}|}\sqrt{\frac{m_e}{2\pi}}\left|\frac{1+\delta\varepsilon_i}{\varepsilon(\omega, \mathbf{k})}\right|^2 \times\left\{\sum_{n=1}^{j}\frac{1}{\sqrt{T_n}}\exp\left(-\frac{m_e\omega^2}{2|\mathbf{k}|^2 T_n}\right) + \sum_{n=j+1}^{Z}\frac{1}{\sqrt{T_n(\theta, \varphi)}}\exp\left(-\frac{m_e\omega^2}{2|\mathbf{k}|^2 T_n(\theta, \varphi)}\right)\right\}.$$

For $\tau > \tau_{imp}$, we take into account the fact that the e–e and e–i collision times are comparable in order of magnitude, in which case the last expression for $\langle \delta N_e^2 \rangle_{\omega, \mathbf{k}}$ can be simplified to

$$\langle \delta N_e^2 \rangle_{\omega, \mathbf{k}} = \frac{\sqrt{2\pi} n_e}{Z|\mathbf{k}|}\left|\frac{1+\delta\varepsilon_i}{\varepsilon(\omega, \mathbf{k})}\right|^2 \times\left\{\frac{j\sqrt{m_e}}{\sqrt{\langle T\rangle_j}}\exp\left(-\frac{m_e\omega^2}{2|\mathbf{k}|^2\langle T\rangle_j}\right) + \sum_{n=j+1}^{Z}\frac{\sqrt{m_e}}{\sqrt{T_n(\theta, \varphi)}}\exp\left(-\frac{m_e\omega^2}{2|\mathbf{k}|^2 T_n(\theta, \varphi)}\right)\right\}, \quad (7)$$

where

$$\varepsilon(\omega, \mathbf{k}) = 1 - \sum_{\alpha}\frac{4\pi e_\alpha^2 n_i^{\langle\alpha\rangle}}{M_\alpha\omega^2} + \frac{4\pi e^2 n_e}{|\mathbf{k}|^2 Z} \times\left\{\frac{j}{\langle T\rangle_j}\left[1 - J_+\left(\frac{\omega}{|\mathbf{k}|}\sqrt{\frac{m_e}{\langle T\rangle_j}}\right)\right] + \sum_{n=1+j}^{Z}\frac{1}{T_n(\theta, \varphi)}\left[1 - J_+\left(\frac{\omega}{|\mathbf{k}|}\sqrt{\frac{m_e}{T_n(\theta, \varphi)}}\right)\right]\right\}$$

and $\langle T\rangle_j \equiv \frac{1}{j}\sum_{n=1}^{j} T_n$ is the mean temperature of the electrons from the first j groups. In the limits $\theta \longrightarrow 0$ or $\varphi \longrightarrow \pi/2$, we can see that, in contrast to (6), the experimentally measured temperature approaches $\langle T\rangle_j$ rather than zero.

In the case of a high-power laser pulse with circular polarization, we have $T_{n,x} = T_{n,y}$, so that the electron temperature recorded in experiments does not depend on the position of the polarization plane (i.e., on the angle φ):

$$T_n(\theta, \varphi) = T_{n,y}\sin^2\theta + T_{n,z}\cos^2\theta.$$

Note that the theory presented makes it possible to describe anisotropy-related effects in investigating ion acoustic waves because, for $T_e \gg T_i$, the phase velocity of these waves satisfies the condition $v_s \gg v_{Ti}$ (see [11], p. 79).

Thus, we have shown that, in applying the Thomson scattering technique to the analysis of a plasma created through ionization of a gas by a short intense laser pulse, it is necessary to take into account the features of the electron velocity distribution function. Thus, at an instant at which the plasma is probed, the electron distribution function may be highly anisotropic, moderately anisotropic, or fully isotropic, depending on the stage of the progressive isotropization and thermalization of different electron groups. As a result, the temperature measurements may incompletely reflect the contributions of electron groups with anisotropic velocity distributions to the total electron temperature because of the relatively strong dependence (6) of the mean electron temperature on the angles. This circumstance may be one of the reasons for the discrepancy between the experimental results of [3] and [5]: the contribution of the high-temperature electron group was not captured by the temperature measurements carried out in [5]. Note also that Chen *et al.* [6] pointed out the difficulty in approximating the experimental Thomson scattering spectra by the theoretical spectra under the assumptions that there are no electron groups with different temperatures in a plasma and the plasma electrons obey an isotropic velocity Maxwellian distribution.

ACKNOWLEDGMENTS

This work was supported in part by the Russian Foundation for Basic Research (project no. 98-02-16263) and INTAS (grant no. 97-10236).

REFERENCES

1. Y. Nagata, K. Midorikawa, S. Kubodera, *et al.*, Phys. Rev. A **51**, 1415 (1995).
2. U. Mohideen, M. H. Sher, H. W. K. Tom, *et al.*, Phys. Rev. Lett. **71**, 509 (1993).
3. M. Nantel, G. Ma, S. Gu, *et al.*, Phys. Rev. Lett. **80**, 4442 (1998).

4. T. E. Glover, T. D. Donnelly, E. A. Lipman, *et al.*, Phys. Rev. Lett. **73**, 78 (1994).
5. W. J. Blyth, S. G. Preston, A. A. Offenberger, *et al.*, Phys. Rev. Lett. **74**, 554 (1995).
6. S.-Y. Chen, G. S. Sarkisov, A. Maksimchuk, *et al.*, Phys. Rev. Lett. **80**, 2610 (1998).
7. P. B. Corcum, N. H. Burnett, and F. Brunel, Phys. Rev. Lett. **62**, 1259 (1989).
8. N. E. Andreev, M. V. Chegotov, M. E. Veĭsman, *et al.*, Pis'ma Zh. Éksp. Teor. Fiz. **68**, 566 (1998) [JETP Lett. **68**, 592 (1998)].
9. N. B. Delone and V. P. Kraĭnov, Usp. Fiz. Nauk **168**, 531 (1998) [Phys. Usp. **41**, 469 (1998)].
10. V. Yu. Bychenkov and V. T. Tikhonchuk, Laser Phys. **2**, 525 (1992).
11. A. F. Alexandrov, L. S. Bogdankevich, and A. A. Rukhadze, *Principles of Plasma Electrocdynamics* (Vysshaya Shkola, Moscow, 1988; Springer-Verlag, Berlin, 1984).

Translated by O. Khadin

Plasma Physics Reports, Vol. 26, No. 7, 2000, pp. 606–616. Translated from Fizika Plazmy, Vol. 26, No. 7, 2000, pp. 647–657.

LOW-TEMPERATURE PLASMA

Negative-Polarity Fast Ionization Wave in Molecular Gases: Electric Field, Electron Density, and Energy Branching

N. B. Anikin, S. M. Starikovskaia, and A. Yu. Starikovskii

Moscow Institute for Physics and Technology,
Institutskiĭ proezd 9, Dolgoprudnyĭ, Moscow oblast, 141700 Russia

Received September 23, 1999

Abstract—The charge density per unit length, the longitudinal component of the electric field, and the electron density behind the front of a fast ionization wave initiated by a nanosecond negative voltage pulse in air, N_2, and H_2 in the 1- to 24-torr pressure range are reconstructed from the experimental data. It is shown that the electron density behind the wave front depends weakly on the sort of gas used and, at relatively high pressures (8–24 torr), is $(2–3) \times 10^{12}$ cm^{-3}. The energy deposited in the internal degrees of freedom is analyzed. It is shown that, for all gases used, most of the deposited energy (40–60%) is spent on the excitation of the electron degrees of freedom. The fraction of the energy deposited in the high-energy degrees of freedom (ionization and dissociation) monotonically decreases with increasing the pressure, whereas the fraction of the energy spent on the excitation of the low-energy degrees of freedom (rotational and vibrational) monotonically increases.

1. INTRODUCTION

In recent years, considerable attention has been paid to fast ionization waves (FIWs). This type of gas discharge allows the production of a substantial (tens of liters) amount of a highly ionized nonequilibrium plasma in a time of tens of nanoseconds [1–3]. Such a discharge can be used to pump gas lasers and lamps [4], initiate plasmochemical processes [5], and create fast-operating switches [6].

From the standpoint of applications, the most important discharge characteristics are the distribution of the discharge energy over the degrees of freedom of the gas and the possibility of creating the conditions for selective excitation of certain energy levels.

However, until recently, information on both the spatiotemporal dynamics of the energy deposited in the FIW and the energy distribution over the degrees of freedom was very poor. One of the few papers in this field is [7], in which it was shown that the gas is ionized and the electron degrees of freedom are excited mainly behind the FIW front in a relatively weak (300–500 Td) electric field. In [8], the energy spent on the excitation of the electron degrees of freedom and the absolute radiation yield in the range of 200–300 nm were analyzed and it was shown that the energy distribution in a glow discharge differs markedly from that in an FIW.

In this paper, we study the development of a negative-polarity FIW and analyze how the fractions of the energy deposited in different degrees of freedom depend on the sort of gas used (N_2, air, or H_2) and the total pressure.

2. EXPERIMENT

The experimental device is described in detail in [9]. The ionization wave was excited in a molybdenum-glass tube 17.5 mm in inner diameter, 21.5 mm in outer diameter, and 600 mm long. The discharge tube was surrounded by a cylindrical metal shield 60 mm in inner diameter. Voltage pulses with an amplitude of 13.5 kV, a half-height duration of 25 ns, and a leading-edge duration of 3 ns were applied from a high-voltage generator at a 40-Hz repetition rate. The dynamics of the excess charge along the discharge tube (starting from the cathode toward the anode over the distance L = 450 mm) was measured each 3 mm by a calibrated capacitive detector. Signals from the detector were recorded by an S9-4A oscillograph. The data from a capacitive detector for air under conditions similar to the conditions of this paper are presented and discussed in detail in [9].

Figure 1 shows the dynamics of the signals from the detector for N_2 pressures of 4, 8, and 16 torr and for H_2 pressures of 8, 16, and 24 torr. The signals are presented by the contour lines in the plane "time elapsed from the instant when the pulse was applied to the electrode"–"the distance from the electrode." The signals are recalculated with the use of a known capacitance per unit length of the discharge device and are presented in units of the charge per unit length, nC/cm. From Fig. 1, it is seen that the FIW starts with a delay τ_d relative to the arrival of the high-voltage pulse at the cathode. Another specific feature of the propagation of a negative-polarity ionization wave is the presence of a precursor (the region shown by a dashed line)—an ionization wave with a relatively small amplitude that

1063-780X/00/2607-0606$20.00

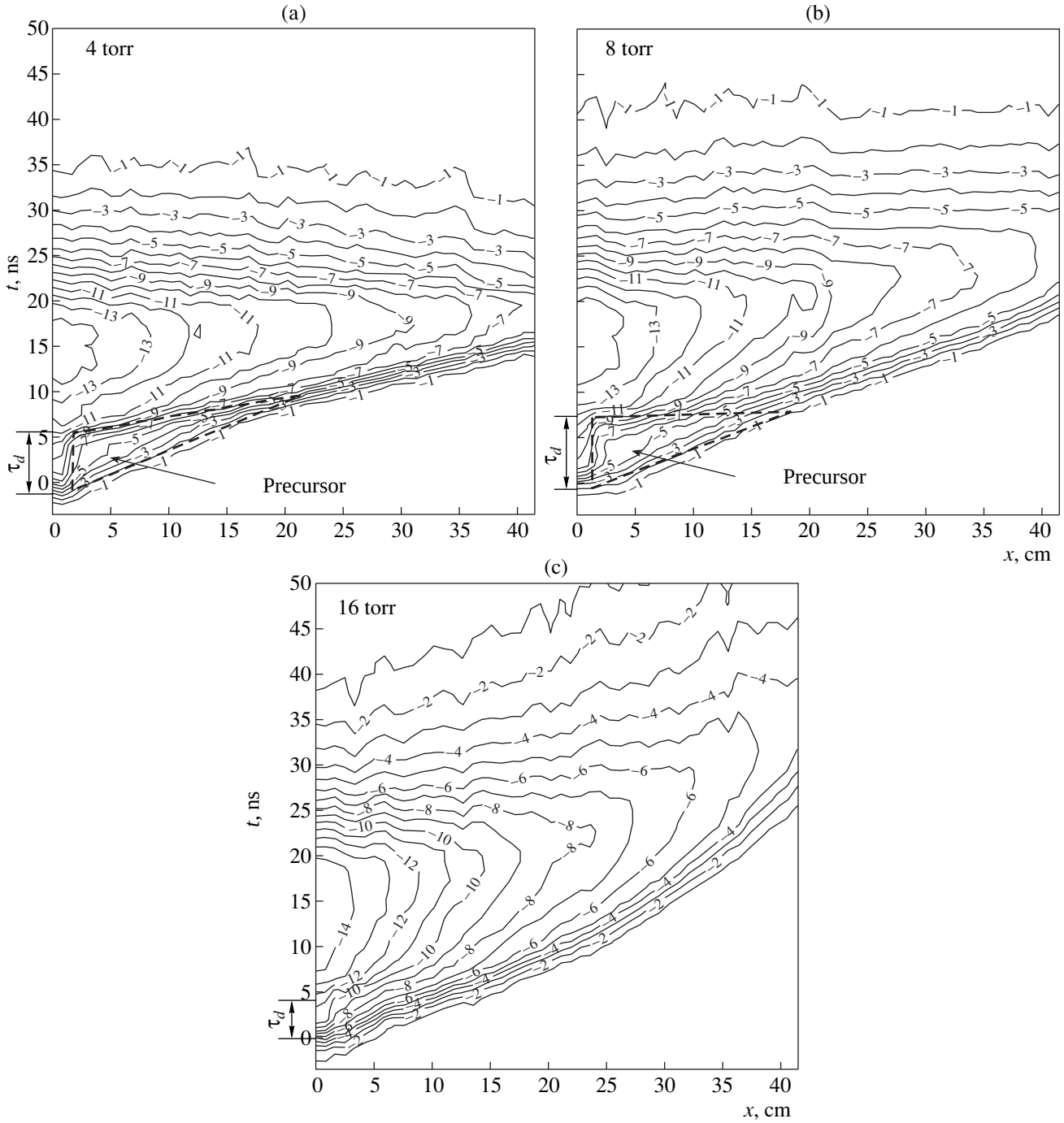

Fig. 1. Signals from the capacitive detector (in nC/cm) for N_2 at pressures of (a) 4, (b) 8, and (c) 16 torr and for H_2 at pressures of (d) 8, (e) 12, (f) 16, and (g) 24 torr. The distance between contour lines is 1 nC/cm.

develops against the background of a high voltage drop near the cathode at a low cathode current [10, 11]. The structure of the ionization wave near the cathode, where a positive uncompensated charge accumulates during the propagation of the precursor, is rather complicated [12].

The delay time of the FIW start in H_2 and N_2 was determined with the use of a capacitive detector located above the high-voltage electrode end. As the pressure increased from 1 to 16 torr, the delay time decreased from 12 to 6 ns for nitrogen and from 26 to 6 ns for hydrogen. The delay time in hydrogen could be approximated with a good accuracy by the expression τ_d [ns] = 160/(p[torr]). Thus, in hydrogen, at a pressure of less than 8 torr, the delay time of the FIW start attained the half-width of the high-voltage pulse; thus, the decrease

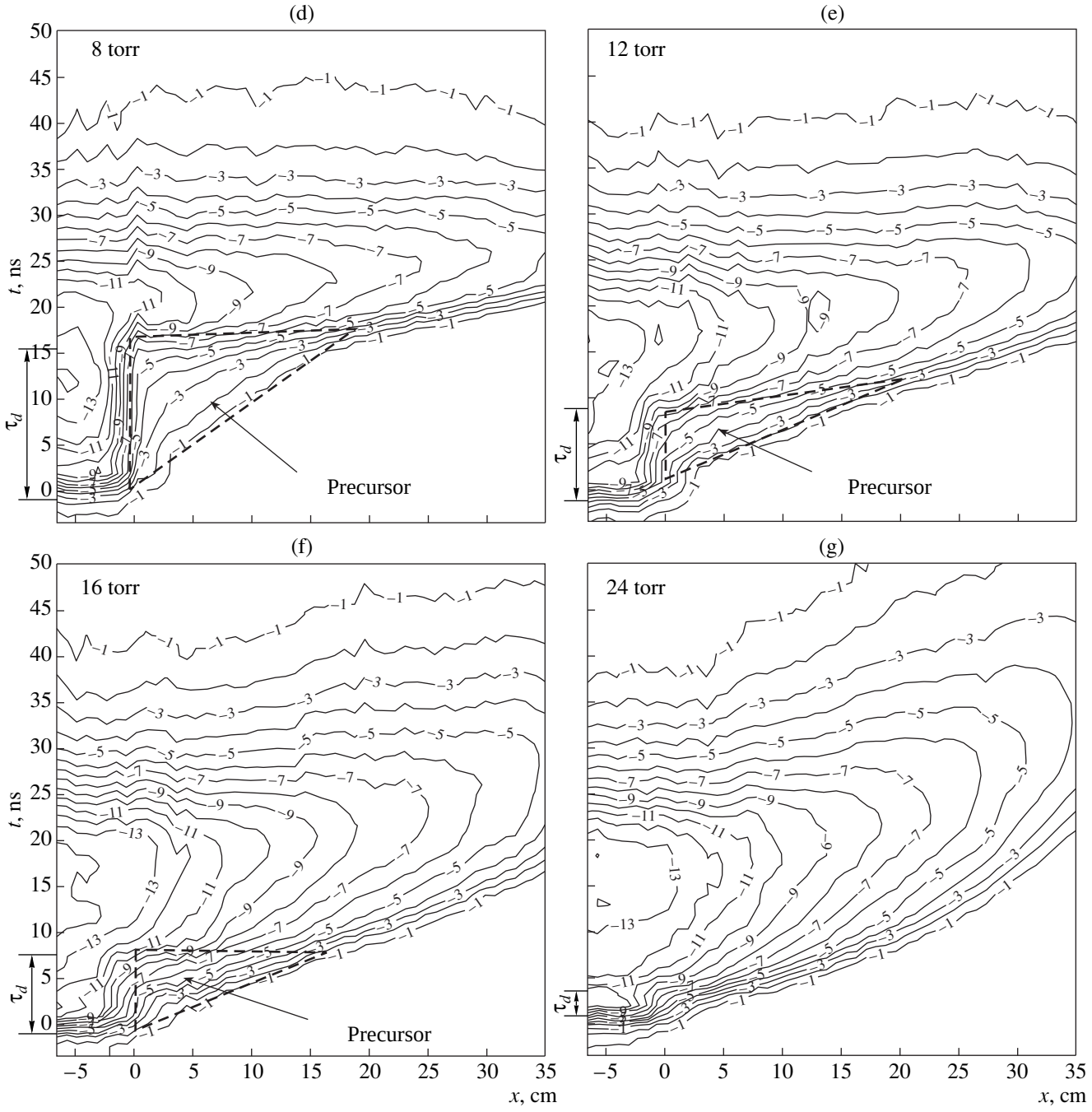

Fig. 1. (Contd.)

in the pressure resulted in a decrease in the pulse amplitude on the high-voltage electrode at the instant when the FIW started.

Figure 2 presents the velocity of the FIW front propagation as a function of pressure for the cross section located 20 cm from the cathode. The FIW front velocity at a distance of 5–40 cm from the cathode was calculated for the point at the front that corresponded to the half-height of the signal from the capacitive detector under the assumption of constant acceleration of the wave front. Note that the sharp decrease in the propagation velocity of the wave in hydrogen at pressures less than 8 torr correlates with the increase in the delay time of the FIW start. Actually, at a pressure of 7 torr, the delay time is close to the duration of the high-voltage pulse. Several nanoseconds after the FIW starts, the electrode voltage begins to decrease. Therefore, the decrease in the wave velocity $v_f(p)$ at low pressures can

be related to the increase in the delay time of the wave start.

A substantial difference of the capacitive-detector signals for air and N_2 from those for H_2 is a smaller decay of the amplitude and faster approach of the signal to its maximum value. The time needed for the signal to reach its maximum is substantially longer in H_2 than in air and N_2, which can be explained by the smaller ionization cross section for H_2.

3. RECONSTRUCTION OF THE CHARGE DENSITY PER UNIT LENGTH

In [9], it was shown that the dynamics of the charge per unit length $q(x, t)$ can be found by solving the equation

$$V_{\exp}(x_p, t) = \int_{-\infty}^{+\infty} q(x, t) f_p(x - x_p) dx, \qquad (1)$$

where x is the spatial coordinate along the discharge axis, x_p is the detector location, t is time, $V_{\exp}(x_p, t)$ is the current magnitude of the signal from the capacitive detector, and $f_p(x)$ is the spatial function of the capacitive-detector sensitivity. The method for determining the spatial function of the capacitive-detector sensitivity is described in detail in [9].

Equation (1), which is a Fredholm equation of the first kind, relates to the ill-posed problems. Therefore, this equation can be solved only with the use of *a priori* restrictions on the function $q(x, t)$ [13].

The experimental error in determining the detector signal as a function of time did not exceed ±5% in the narrow (several nanoseconds) front region and ±3% over most of the signal. At the front, the error was due to the amplitude–frequency characteristics of the detector and, in the rest of the signal, it was due to the random scatter in the data. Such an error allowed a series of different charge distributions $q(x, t)$ that satisfactorily described the same experimental data.

To solve equation (1), we used a standard method in which $q(x, t)$ was presented as a function with a certain number of inflection points (points in which the second derivative of $q(x, t)|_{t = \text{const}}$ changes its sign) [13]. In contrast to [9], we assumed that there were no oscillations at the front of the charge distribution.

It follows from this assumption that $q(x, t)$ has no more than one point of inflection at the wave front. The position of this point on the front depends on the shape of the initial signal. The lower the noise of the initial experimental data, the more accurately this position can be determined. Analysis of the tested distributions shows that, for the 3–5% measurement error on the wave front, the position of the inflection point can be determined accurate to the front width. Therefore, we further assume that the inflection point always coincides with the beginning of the charge front (point x_2).

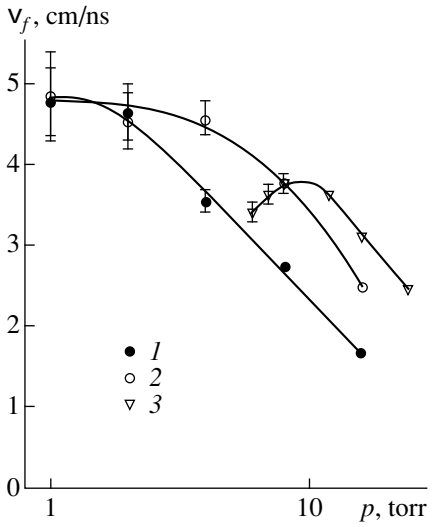

Fig. 2. FIW front velocity v_f calculated for the point corresponding to the half-height of the signal from the capacitive detector in (*1*) air, (*2*) nitrogen, and (*3*) hydrogen.

For $q(x, t)$, we chose a nonpositive function, which is convex downward with respect to the argument x in the interval $[x_1, x_2]$, i.e., from the cathode boundary of the region in which the reconstruction is performed to the zero-charge point (for $x > x_2$, we always have $q(x, t) \equiv 0$). Note that point x_1 was fixed (x_1 was independent of time, whereas x_2 changed with time). With the given set of functions, a bounded and integrable sensitivity function $f_p(x)$, and a single-valued integral operator (in our case, these conditions hold), the problem becomes well posed [13] and reduces to finding the minimum of the following functional with respect to $q(x, t)$ and $x_2(t)$ on this set of functions at any instant:

$$F(q, x_2(t))|_{t = \text{const}} = \left\| V_{\exp}(x_p, t) - \int_{x_1}^{x_2(t)} f_p(x - x_p) q(x, t) dx \right\|_{t = \text{const}}. \qquad (2)$$

From (2), it is seen that $\min_q F = \Phi(x_2)$ is a function of x_2. Thus, it is necessary first to find the position x_2 of the charge front (i.e., the minimum of the function $\Phi(x_2)$) and then, for the known x_2, solve (1) and obtain the sought distribution $q(x, t)$. For each instant, the problem of finding the minimum of $\Phi(x_2)$ was solved by the bisection method. For each fixed x_2, the minimum of functional (2) was sought with the use of a standard code described in [13].

Near the cathode, the reconstruction accuracy was low, because the *a priori* condition of convexity of the distribution of the charge per unit length along the discharge tube was violated there. This violation was related to the complex structure of the wave near the cathode. Therefore, the reconstruction was performed

in the region that began at the distance $x_1 = 5$ cm from the cathode (at a distance on the order of half-width of the sensitivity function, $\Delta f \sim 5$ cm, the contribution from the charge located on the cathode can be neglected). Near the low-voltage electrode, the data were lost because the measurement region was limited along the discharge tube. In this case, the contribution from the charges located outside the region within which the capacitive detector could be moved limits the reconstruction accuracy at the ends of this region. For these reasons, in this study, we did not consider the regions of width Δf near the electrodes.

We compared the experimental detector signals $V_{\exp}(x, t)$ with the convolution of the reconstructed charge density with the sensitivity function, $V(x, t) = \int_{-\infty}^{+\infty} f_p(x - x_p)q(x, t)dx$. Within the experimental error, $V(x, t)$ and $V_{\exp}(x, t)$ coincided.

4. RECONSTRUCTION OF THE ELECTRIC FIELD

From the reconstructed charge density per unit length of the discharge chamber, we reconstructed the longitudinal component of the electric field. The field was calculated under the assumption that the excess charge was accumulated near the glass surface. This assumption seems more reasonable for the region behind the FIW front because, after the onset of the FIW, the reconstructed charge density per unit length near the high-voltage electrode is close to the charge density per unit length on the electrode surface.

For the FIW propagating in H_2, we estimated the maximum width of the region (near the surface of the discharge tube) in which the discharge is accumulated. For this purpose, we measured the charge density per unit length on the cathode ($x = -\Delta f$) and near the cathode ($x = +\Delta f$) in the discharge tube. Knowing the difference in the charge density per unit length on the cathode and at $x = +\Delta f$, we could find the maximum difference in the capacitance per unit length $\delta C_{\max}(t)$ at $x = +\Delta f$ and on the cathode

$$\delta C_{\max}(t) = (q(-\Delta f, t) - q(+\Delta f, t))/U_c(t). \qquad (3)$$

The difference in the capacitance per unit length which is defined by (3) allows us to evaluate the minimum distance $r_{\min}$ from the axis of the discharge tube at which the charge is accumulated. By using the well-known formula for the capacitance of the capacitors connected in parallel, we obtain

$$\frac{-\delta C_{\max}}{C_0(C_0 - \delta C_{\max})} = \frac{\ln\dfrac{r_0}{r_{\min}}}{2\pi\varepsilon_0},$$

where C_0 is the capacitance per unit length of the discharge device above the electrode, ε_0 is the dielectric constant, and r_0 is the inner radius of the discharge tube.

For $r_{\min}$, we obtain

$$r_{\min} = r_0 \exp\left(\frac{-2\pi\varepsilon_0\delta C_{\max}}{C_0(C_0 - \delta C_{\max})}\right).$$

Estimates show that, at a distance of 10–15 cm from the front of an FIW propagating in H_2, the excess charge is accumulated at the distance $r_0 - r_{\min} < 2$ mm from the glass surface.

When approaching the front, the radial distribution of the charge seems to become more uniform. However, since the charge per unit length changes relatively slowly behind the front, we will assume the charge to be mainly located near the glass surface.

To find the field in the discharge tube, we numerically solved Poisson's equation taking into account the real geometry of the discharge device. We also assumed the distribution of the electric field to be axially symmetric [9] and quasi-steady (the latter is always valid for high pressures; for low pressures, it is valid up to the back front, which moves with a velocity close to the speed of light). The preliminary calculations showed that, if the charge distribution behind the FIW front varies slightly along the x-axis, the longitudinal component of the field varies insignificantly in the radial direction and the radial component is mainly concentrated near the glass surface. This allows us to consider the problem in the one-dimensional approximation.

Under the above assumptions, the longitudinal component of the electric field can be represented in the form (further, we always use the notation $E \equiv E_x$)

$$E(x, t) = \int_{-\infty}^{+\infty} q(s, t)E_0(x - s)ds,$$

where $E_0(x)$ is the electric field on the symmetry axis of a uniformly charged ring with the radius equal to the inner radius of the tube and with the unit electric charge.

Figure 3 presents the distribution of the FIW electric field at a 16-torr pressure for the gases under study. It should be noted that the assumption about the accumulation of the excess charge near the glass surface is violated at the FIW front, so that the obtained value can only be the low estimate for the electric field. At the same time, the method used in this paper for reconstructing the electric field allows a sufficiently good accuracy of determining the field in the region behind the FIW where the field is weak. Since it is this region that mainly contributes to the gas excitation [7], it is the most important for the analysis of the energy deposited in different degrees of freedom.

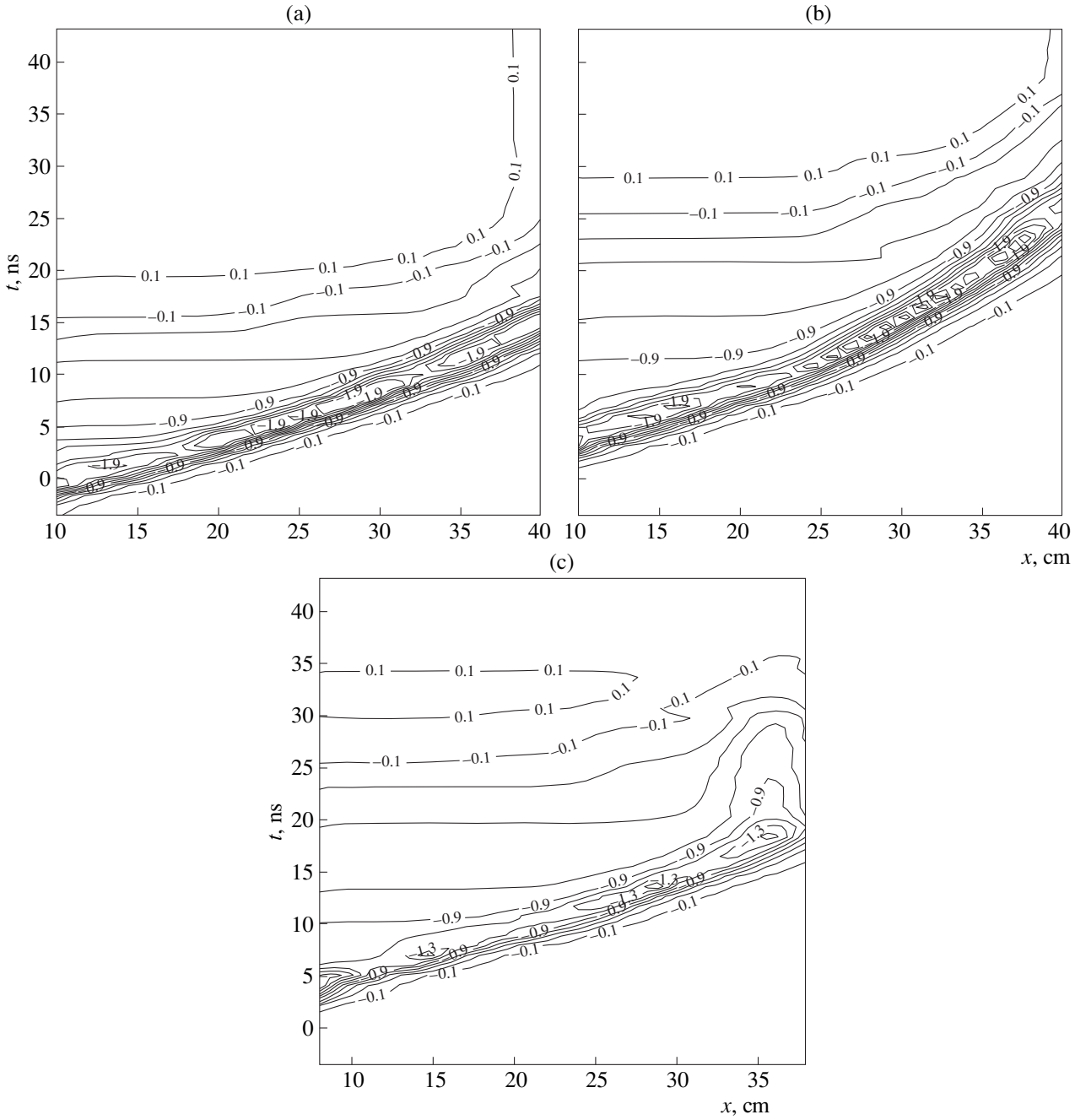

Fig. 3. Electric field (in kV/cm) as a function of time t and the distance x from the cathode for a pressure of 16 torr in (a) air, (b) N_2, and (c) H_2. The distance between contour lines is 200 V/cm.

5. ACCUMULATION OF ELECTRONS. CORRELATION WITH THE ELECTRIC-FIELD DYNAMICS

Using the data on the dynamics of the charge per unit length, we can calculate the current along the discharge gap:

$$J_x(x, t) = \frac{d}{dt}\int_0^x q(s, t)ds. \quad (4)$$

The electric field calculated above allows us to estimate the time during which the plasma space charge is neutralized:

$$\tau_n = \frac{1}{4\pi\sigma} = \frac{j_x}{4\pi E} = \frac{J_x}{4\pi SE},$$

where σ is the plasma conductivity and S is the cross-section area of the discharge tube. Starting with the point of the maximum of $E(t)$, the characteristic time of the onset of the FIW substantially exceeds the time dur-

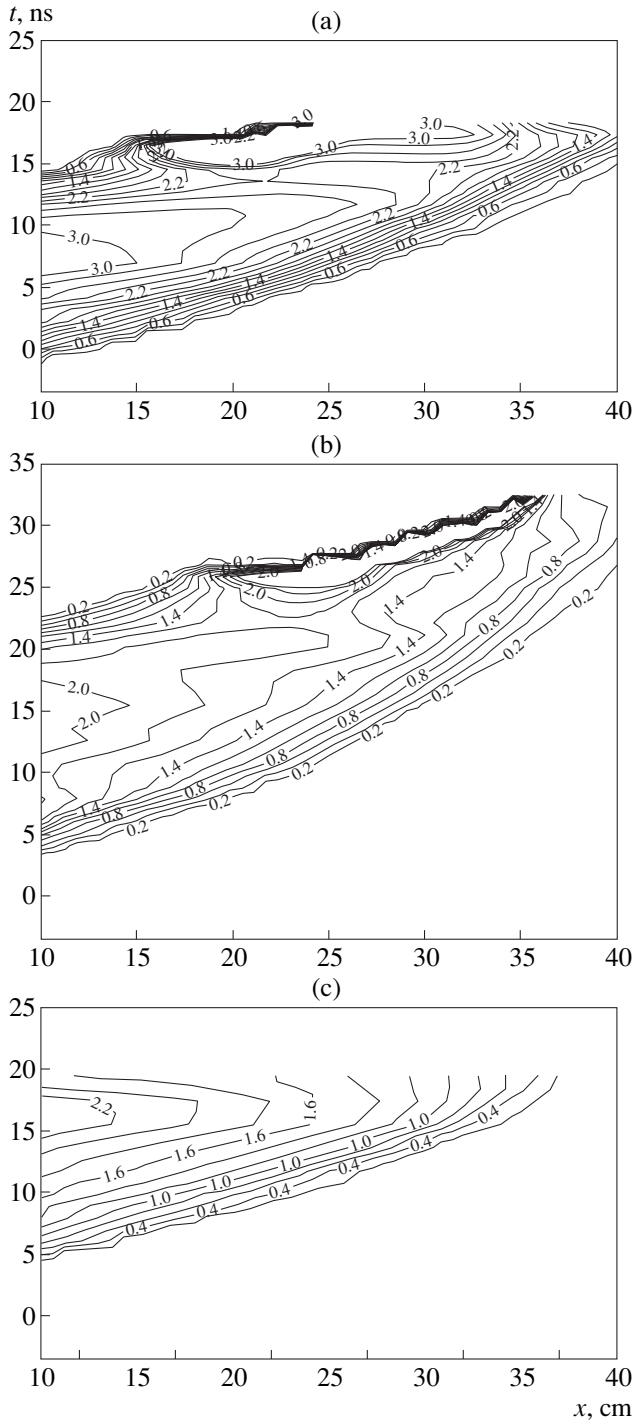

Fig. 4. Electron density (in 10^{12} cm^{-3}) as a function of time t and the distance x from the cathode for a pressure of 16 torr in (a) air, (b) N_2, and (c) H_2. The distance between contour lines is 2×10^{11} cm^{-3}.

ing which the space charge is neutralized ($\tau_n < 0.1$ ns for all pressures and gases used). This estimate confirms the validity of the assumption about the accumulation of the excess charge near the glass wall of the discharge tube.

By using the known longitudinal electric-field component $E(x, t)$ and the data on the drift velocity $v_{dr}(E/p)$ [14] and assuming the electron density to be constant over the radius, we obtain the expression describing the dynamics of the electron density behind the FIW front:

$$n_e(x, t) = \frac{j_x}{e v_{dr}} = \frac{J_x}{e v_{dr} S}. \quad (5)$$

Assuming the transport collision frequency to be fixed, the drift-velocity data from [14] were extrapolated to the region $E/p > 330$ V/(cm torr). This assumption insignificantly affects the results of this work, because the main excitation of internal degrees of freedom of the gas occurs in substantially weaker fields of $E/p \le 200$ V/(cm torr).

The electron density was calculated in the parameter ranges

$$J_x(x, t) < 0,$$
$$0.7 \min_t E(x, t) < E(x, t) < 0, \quad (6)$$
$$t < t_{\max},$$

where $t_{\max}$ is the instant the wave arrives at the last measurement point. The last limitation is due to the fact that the procedure of the current calculation is invalid for $t > t_{\max}$. The limitations on the values of $J(x, t)$ and $E(x, t)$ are related to the increase in the error in determining the current and electric field near the zero values, as well as the electric field near its peak value.

Figure 4 shows the dynamics of the electron density in an FIW in air, N_2, and H_2 at a 16-torr pressure. In nitrogen (Fig. 4b) and hydrogen (Fig. 4c), the nonzero density is recorded after 5 ns, which correlates well with the delay time of the wave start (Figs. 1c, 1d, 1f). In air, we did not measure the parameters above the electrode; in this case, the point $t = 0$ corresponded to the beginning of the voltage growth in the plasma at the distance $x = \Delta f$ from the high-voltage electrode.

In air and nitrogen, the maximum value of the electron density decays no more than one and a half times as the FIW travels from 10 to 30 cm, whereas in hydrogen the maximum electron density decays three times at the same distance. The increase in the electron density with time is substantially sharper in air and N_2 than in hydrogen. The irregular behavior of $n_e(t)$ on large time scales seems to result from the increase in the error in determining n_e on the back front due to the sharp decrease in the current and electric field.

Now, we will analyze the behavior of the field and electron density in the fixed section of the discharge tube. The values of $E(t)$ and $n_e(t)$ at a 20-cm distance from the cathode are presented in Fig. 5.

Although the proposed method for determining the electric field at the wave front (at the point where $E(t)$ is maximum) gives only the lower estimate, the obtained values of the reduced electric field can attain 1 kV/(cm torr) in nitrogen and air. This value exceeds

the threshold for the emergence of runaway electrons. The duration of the field peak does not exceed 5 ns; then, the electric field decreases to tens or hundreds of V/(cm torr), which corresponds to the intensive excitation of the internal degrees of freedom of the gas. The electric field behind the wave front increases and the reduced electric field decreases with increasing the pressure. The observed behavior of the electric field is in good agreement with the previous papers [7, 9].

In agreement with [7], the gas ionization occurs mainly behind the front of an FIW (i.e., behind the region where the electric field is maximum). The time needed for the electron density to reach its maximum value somewhat increases with increasing the pressure. It is most clearly seen in hydrogen, where this time varies from 5 to 10 ns as the pressure varies from 6 to 24 torr. The maximum value of n_e first increases with increasing the pressure (in a range of 1–2 torr for N_2 and air and 6–7 torr for hydrogen) and then remains almost unchanged (at a level of $\sim(2–3)\times 10^{12}$ cm^{-3}). In this case, the maximum density and the largest rate of its growth at the front are attained in air (Fig. 4a), which is explained by a greater ionization coefficient than in pure N_2 or H_2. The FIW propagation in hydrogen is characterized by the slowest increase in the electron density (Fig. 4c) and a wider forward front of the wave.

To check the self-consistency of the approach developed, we calculated the first Townsend ionization coefficient $\alpha(E, p)$ from the available experimental data. A comparison of the data obtained with data available in the literature allows an independent verification of the reconstructed values of n_e and E/p.

The balance equation for the electron density including ionization and drift has the form

$$\frac{\partial n_e}{\partial t} + \frac{\partial v_{dr} n_e}{\partial x} = \alpha |v_{dr}| n_e, \qquad (7)$$

from which we obtain the Townsend coefficient

$$\alpha(x, t) = \frac{1}{|v_{dr}|}\left\{\left(v_{dr}\frac{\partial}{\partial x} + \frac{\partial}{\partial t}\right)\ln|J_x| - \frac{\partial \ln|v_{dr}|}{\partial t}\right\}. \qquad (8)$$

We average the obtained ionization coefficient $\alpha(x, t)$ and electric field $E(x, t)$ over the region behind the wave front where the electric field is slowly varying along x (Fig. 3) and transform the obtained dependences $\langle\alpha(t)\rangle_x$ and $\langle E(t)\rangle_x$ into the dependence of α/p on the reduced field E/p. Figure 6 presents, as an example, the calculated ionization coefficient for N_2 as a function of the reduced field. Within a wide range of E/p, the data are in good agreement with the well-known data [1]. The scatter in the data at the lowest pressures can be related to the experimental noise, whereas the deviations at the highest pressures can be due to possible step ionization at low values of E/p. On the whole, the good agreement of the ionization coefficient with the data of other authors confirms the self-consistency of the problem and the accuracy of the reconstruction of the field and electron density behind the wave front.

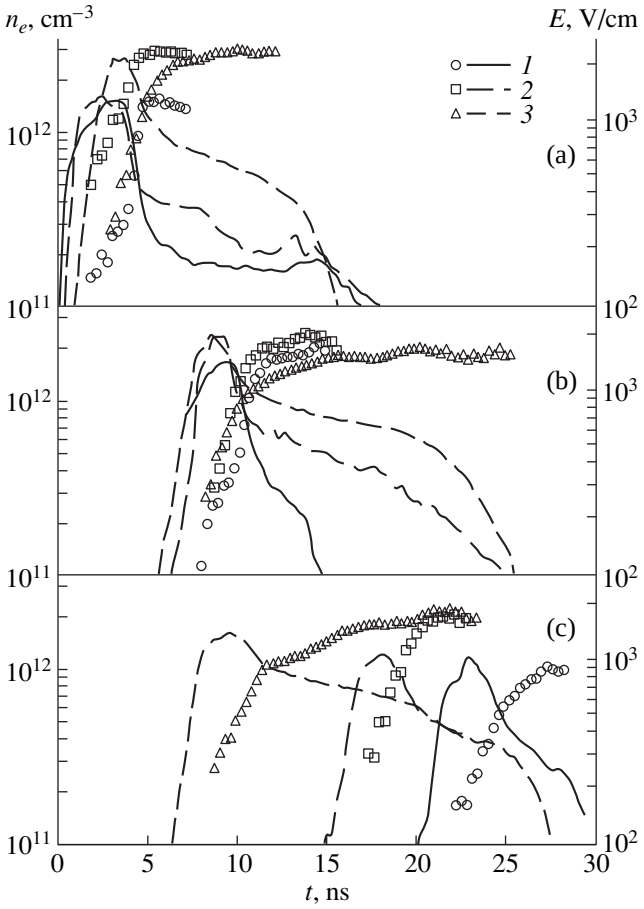

Fig. 5. Electron density (symbols) and electric field (lines) in an FIW as functions of time for (a) air at pressures of (*1*) 1, (*2*) 4, and (*3*) 16 torr; (b) N_2 at pressures of (*1*) 1, (*2*) 4, and (*3*) 16 torr; and (c) H_2 at pressures of (*1*) 6, (*2*) 8, and (*3*) 24 torr.

Note that, within this approach, we have to neglect the effects related to the nonlocal character of the electron energy distribution function (EEDF) near the FIW front. As was mentioned in [7, 15], these effects can significantly change the ionization rate constant. At the same time, the drift electron velocity behind the FIW front almost always corresponds to the local value of the electric field. A more detailed analysis of these effects will be presented in our subsequent papers. Here, we only emphasize that the comparison with the published data on α is rather qualitative, although it is very important from a methodical standpoint.

6. ENERGY DEPOSITED IN THE INTERNAL DEGREES OF FREEDOM OF A GAS

Knowing the electric field and the electron density at a fixed point x, we can calculate the energy $W_i(x)$

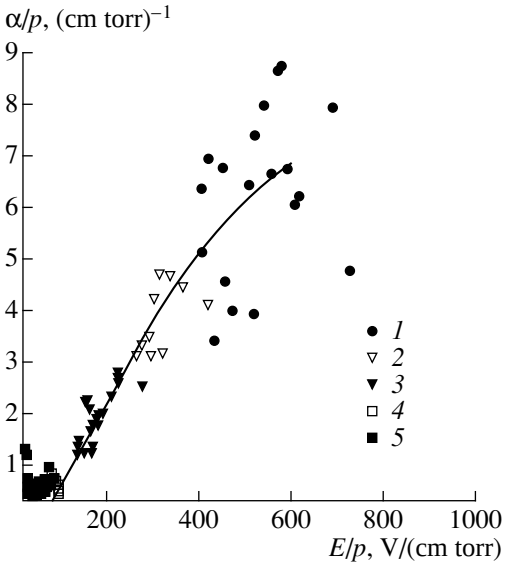

Fig. 6. Reduced Townsend ionization coefficient α/p as a function of the reduced field E/p for N_2 at pressures of (*1*) 1, (*2*) 2, (*3*) 4, (*4*) 8, and (*5*) 16 torr.

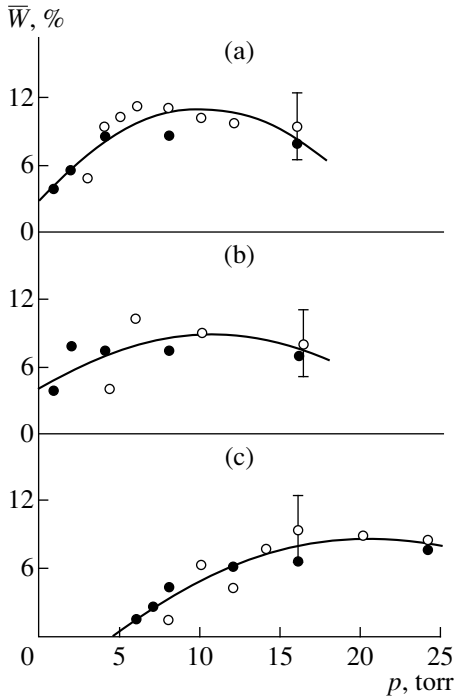

Fig. 7. Specific deposited energy per pulse (averaged over the length of the discharge tube) in (a) air, (b) N_2, and (c) H_2. Open circles show the measured deposited energy, and closed circles show the deposited energy calculated by formula (9).

deposited in different degrees of freedom during the pulse of duration T_*:

$$W_i(x) = N\sum_j\left(\Delta\varepsilon_j^i\int_0^{T_*} n_e(x,t)k_j^i(E(x,t)/p)\right)dt, \quad (9)$$

where $\Delta\varepsilon_j^i$ and $k_j^i(E/p)$ are the energy loss and the rate constant of the excitation of the jth component of the ith degree of freedom and N is the concentration of the excited component. The excitation constants $k_j^i(E/p)$ were calculated in [16–18] with the use of an EEDF obtained in the two-term approximation to the Boltzmann equation.

Since the electric field was calculated within the interval $[0; T_*]$ and the electron density in the interval $[0; t_{max}]$, where $t_{max} < T_*$ [see (6)], the value of n_e was extrapolated to the interval $[t_{max}; T_*]$ as $n_e = n_e(t_{max}) = \text{const}$. Such an extrapolation could systematically underestimate the value of the deposited energy, especially the fraction of energy spent on the excitation of the low-energy degrees of freedom. As the pressure increases, this effect becomes less important due to the increase in t_{max}. The estimates show that, for the pressure corresponding to the maximum FIW velocity, $n_e(T_*)$ exceeds $n_e(t_{max})$ by no more than 30%. In addition, t_{max} corresponds to the decrease in $J(t)$, and most of the deposited energy corresponds to the maximum current. Thus, the extrapolation of a fixed value of $n_e(t)$ to the region $t > t_{max}$ should not substantially change the energy distribution.

The ratio of deposited energy $\overline{W}$ to the total energy of the initial pulse is presented in Fig. 7 for different pressures. The deposited energy is determined from the current-shunt data as the difference between the energies of the pulse incident on the discharge gap and the reflected pulse. This method is described in more detail in [2]. The same figure shows the total deposited energy averaged over the reconstruction interval $(\Delta f, L - \Delta f)$ and calculated by the formula

$$\overline{W} = \frac{V_0}{L-2\Delta f}\sum_i\int_{\Delta f}^{L-\Delta f} W_i(x)dx, \quad (10)$$

where V_0 is the volume of the discharge tube. It is seen that, accurate to within 3% of the energy of the incident pulse, both methods for determining $\overline{W}$ give the same result.

In N_2 and air, the total deposited energy as a function of pressure has a maximum near the maximum FIW velocity; this is in qualitative agreement with [19, 20]. In hydrogen, the total deposited energy increases with the pressure. In H_2, the dependence of the delay time of the FIW start on the pressure is more sharp: τ_d varies from 26 ns for $p = 6$ torr to 6 ns for $p = 24$ torr, whereas in nitrogen, $\tau_d = 12$ ns for $p = 1$ torr and $\tau_d = 6$ ns for $p = 16$ torr. As a result, when the hydrogen pressure increases from 6 to 24 torr, the duration of the current pulse increases from approximately 20 to 90% of the duration of the current pulse in the supplying

cable. Such a sharp increase in the current duration results in a monotonic growth of the deposited energy.

The fractions of the energy deposited in different degrees of freedom and calculated by the relations similar to (10) are shown in Fig. 8. Here, the 100% value corresponds to the total energy $\overline{W}$ deposited in the gas. Both the fraction and the absolute value of the energy deposited in the low-energy degrees of freedom (vibrational and rotational) monotonically increase with increasing the pressure (Fig. 8). A fraction (up to 8%) of the total deposited energy is spent on the excitation of the rotational degrees of freedom in H_2; in air and N_2, this excitation is almost absent.

It is clearly seen that the excitation of the electron degrees of freedom is the dominant channel of the electron energy loss (40–60% of the total deposited energy) for all pressures and gases used. The energy spent on hydrogen dissociation is always larger than that spent on ionization. In air, the fractions of the energy spent on dissociation and ionization become comparable at a pressure of $p \sim 1$ torr. At the same time, in nitrogen, the curves showing the energy spent on dissociation and ionization as functions of the pressure intersect in the region where the FIW propagation velocity has a maximum with respect to the pressure. In hydrogen, similar curves are expected to intersect at lower pressures ($p <$ 6 torr). Note also that the fractions of the energy spent on dissociation and ionization are comparable; therefore, the degrees of dissociation and ionization in the FIW are of the same order.

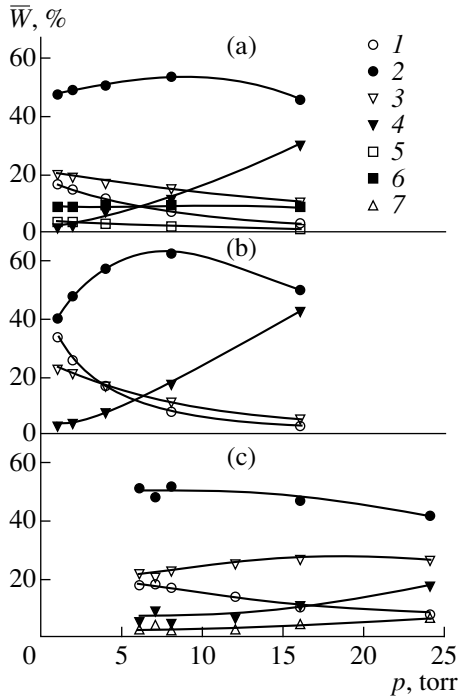

Fig. 8. The fractions of the energy (per pulse) deposited in the internal degrees of freedom [(*1*, *5*) ionization, (*2*, *6*) excitation of the electron terms, (*3*) dissociation, (*4*) excitation of the vibrational levels, and (*7*) excitation of the rotational levels] for (a) air [curves (*1*)–(*4*) correspond to N_2 and curves (*5*) and (*6*) correspond to O_2], (b) nitrogen, and (c) hydrogen.

The fraction of energy spent on ionization during the discharge does not exceed 35% of the total deposited energy for all pressures and gases used and decreases monotonically with pressure. We note that, for all gases, the absolute value of this energy as a function of pressure reaches its maximum in the pressure range corresponding to the maximum FIW velocity.

7. CONCLUSION

It is shown that the maximum electron density behind the FIW front depends weakly on the pressure and sort of gas used. In the parameter range corresponding to the gas pressures that are optimum for wave propagation, we have $n_e \sim (2–3) \times 10^{12}$ cm^{-3} for all gases used.

The obtained values of n_e correlate with the ionization coefficient in the given gas. Thus, the lowest values of the electron density are obtained for hydrogen and nitrogen, and the maximum ones are obtained for air, where the presence of O_2 leads to an appreciable increase in the ionization rate in a high electric field as compared to pure nitrogen.

A weak dependence on the sort of gas is also observed for the reduced electric field behind the FIW front, where the rate of gas excitation is maximum. In this region, the characteristic value of the reduced field is in the range of 200–500 Td. In the pressure range corresponding to the optimum conditions for the development of an FIW in hydrogen, this value is somewhat smaller than in nitrogen or air. An analysis showed that, in all of the regimes of the FIW propagation, most of the energy at the wave front is spent on gas ionization and production of runaway electrons. A sharp increase in the electron density from the background values ahead of the wave front to $n_e \sim 10^{11}$ cm^{-3} at the front in a time of 3–5 ns (for E/N on the order of several kTd) leads to an increase in the plasma conductivity and a substantial decrease in the electric field. Further ionization and excitation of the gas proceeds in a substantially weaker field behind the FIW front; the energy distribution over different degrees of freedom in the gas is determined by the processes occurring just in this region.

We have shown that, for all gases used, the main channel of the electron energy loss in an FIW is the excitation of the electron degrees of freedom (40–60% of the deposited energy). The energy spent on ionization is somewhat less (from 10 to 35%) and decreases monotonically with increasing the gas pressure. At the same time, the energy deposited in the vibrational and rotational degrees of freedom of H_2 molecules increases with increasing the pressure.

ACKNOWLEDGMENTS

This work was supported in part by the Russian Foundation for Basic Research (project no. 99-03-32237), INTAS (grant no. 96-2120), US Air Force Research Laboratory's Office of Scientific Research, the European Office of Aerospace Research and Development (grant no. SPC-99-4091), and the International Science and Technology Center (grant no. 1474).

REFERENCES

1. Yu. D. Korolev and G. A. Mesyats, in *Physics of a Pulsed Gas Discharge* (Nauka, Moscow, 1991), p. 23.
2. L. M. Vasilyak, S. V. Kostyuchenko, N. N. Kudryavtsev, *et al.*, Usp. Fiz. Nauk **164**, 263 (1994) [Phys. Usp. **37**, 247 (1994)].
3. N. B. Anikin, S. V. Pancheshnyĭ, S. M. Starikovskaia, and A. Yu. Starikovskii, J. Phys. D: Appl. Phys. **31**, 826 (1998).
4. Yu. M. Tolkunov, É. I. Asinovskiĭ, and L. M. Vasilyak, Teplofiz. Vys. Temp. **19**, 491 (1981).
5. D. V. Zatsepin, S. M. Starikovskaia, and A. Yu. Starikovskii, in *Proceedings of 27th International Symposium on Combustion, Pittsburgh, 1998*, p. 4.
6. A. Arefiev and Yu. Yudaev, in *Proceedings of 12th International Conference on Gas Discharges and Their Applications, Greifswald, 1997*, Vol. 2, p. 800.
7. S. V. Pancheshnyĭ, S. M. Starikovskaia, and A. Yu. Starikovskii, Fiz. Plazmy **25**, 362 (1999) [Plasma Phys. Rep. **25**, 326 (1999)].
8. L. M. Vasilyak, S. V. Kostyuchenko, A. V. Krasnochub, and M. E. Kuz'menko, in *Proceedings of Conference on Physics of Low-Temperature Plasma, Petrozavodsk, 1998*, Part 1, p. 462.
9. N. B. Anikin, S. M. Starikovskaia, and A. Yu. Starikovskii, Fiz. Plazmy **24**, 9 (1998) [Plasma Phys. Rep. **24**, 6 (1998)].
10. É. I. Asinovskiĭ, V. V. Markovets, D. N. Polyakov, *et al.*, Teplofiz. Vys. Temp. **23**, 606 (1985).
11. N. B. Anikin, S. M. Starikovskaia, and A. Yu. Starikovskii, Teplofiz. Vys. Temp. **36**, 992 (1998).
12. N. B. Anikin, S. M. Starikovskaia, and A. Yu. Starikovskii, in *Proceedings of Conference on Physics of Low-Temperature Plasma, Petrozavodsk, 1998*, Part 1, p. 198.
13. A. N. Tikhonov, A. V. Goncharovskiĭ, V. V. Stepanov, and A. G. Yagola, in *Numerical Methods for Solving Ill-Posed Problems* (Nauka, Moscow, 1990), p. 68.
14. V. L. Bychkov, A. V. Eletskiĭ, and B. M. Smirnov, in *Plasma Chemistry*, Ed. by B. M. Smirnov (Atomizdat, Moscow, 1983), Vol. 10, p. 146.
15. S. M. Starikovskaia and A. Yu. Starikovskii, in *Proceedings of XXIV International Conference on Phenomena in Ionized Gases, Warsaw, 1999*, Vol. 5, p. 81.
16. S. Yoshida, A. V. Phelps, and L. C. Pitchford, Phys. Rev. A **27**, 2858 (1983).
17. A. V. Phelps and L. C. Pitchford, Phys. Rev. A **31**, 2932 (1985).
18. S. J. Buckman and A. V. Phelps, J. Chem. Phys. **82**, 4999 (1985).
19. S. V. Kostyuchenko, N. N. Kudryavtsev, S. M. Starikovskaya, *et al.*, Chem. Phys. Rep. **13**, 1670 (1995).
20. S. M. Starikovskaia, Fiz. Plazmy **21**, 541 (1995) [Plasma Phys. Rep. **21**, 510 (1995)].

Translated by A. Smirnova[†]

[†] Deceased.

Plasma Physics Reports, Vol. 26, No. 7, 2000, pp. 617–620. Translated from Fizika Plazmy, Vol. 26, No. 7, 2000, pp. 658–661.

LOW-TEMPERATURE PLASMA

Continuous Optical Discharge in Crossed Laser Beams

É. B. Kulumbaev and V. M. Lelevkin

Kyrgyz–Russian Slavic University, Bishkek, 720000 Kyrgyzstan

Received August 11, 1999; in final form, January 17, 2000

Abstract—A three-dimensional radiative gas-dynamic model is applied to calculating the parameters of a continuous optical discharge in crossed CO_2 laser beams in air at atmospheric pressure. © *2000 MAIK "Nauka/Interperiodica".*

1. INTRODUCTION

For a continuous optical discharge (COD) to be implemented in practice, it is necessary to ensure the conditions under which a stable COD may exist in a gas flow. The experimental data on the parameter range in which a COD can occur in a focused CO_2 laser beam in an air flow are presented by Generalov *et al.* [1], who showed that the discharge is stable in parallel and perpendicular (with respect to the laser beam) gas flows and is unstable in a gas flowing toward the beam. As the gas flow velocity increases, the COD contracts and is displaced toward the beam waist. According to [2, 3], the conditions for a stable discharge to occur in a gas flow can be determined theoretically. Numerical simulations carried out by Surzhikov and Chentsov [2] on the basis of the radiative gas-dynamic model allowed them to determine the domain in the laser power–longitudinal flow velocity variables in which the discharge may exist; this domain agrees well with the experimental data of [1]. In [3], we applied an analogous approach to simulate a three-dimensional COD in a transverse gas flow under conditions corresponding to the experiments of [1]. The excitation of localized microwave discharges by crossed electromagnetic beams in the Earth's atmosphere was studied in [4, 5].

Our aim here is to apply the physical model developed in [2] to calculate the parameters of a COD excited in the intersection region of CO_2 laser beams in air at atmospheric pressure as functions of the gas flow velocity and the ratio between the laser powers. Our study is related to the practical implementation of a COD and is motivated by the following factors: the possibility of exciting the discharge in a desired spatial region by unfocused laser beams, the possibility of raising the total laser power in the intersection region of the electromagnetic beams using lasers of limited powers, and the possibility of exciting more stable discharges with simultaneous remote control of their shapes and dimensions.

2. MODEL

We consider a COD excited by crossed CO_2 laser beams in an air flow at atmospheric pressure (Fig. 1) under the following model assumptions [2, 3]: the flow is subsonic and laminar, the plasma is in equilibrium, the refraction of laser light and the interaction between the laser beams are both negligible, and the laser beams are Gaussian in shape. We determine the COD parameters by solving the following set of three-dimensional equations consisting of the continuity equation, the Navier–Stokes equation, the energy balance equation, the equation for selective radiation transport in the multigroup diffusion approximation, and the transport equation for laser light along the optical axes in the geometrical-optics approximation:

$$\nabla \cdot (\rho \mathbf{V}) = 0,$$

$$\rho(\mathbf{V} \cdot \nabla)\mathbf{V} = -\nabla\left(p + \frac{2}{3}\eta \nabla \cdot \mathbf{V}\right) + 2\nabla \cdot (\eta \dot{S}) + (\rho_0 - \rho)\mathbf{g},$$

$$\rho \mathbf{V} \cdot C_p \nabla T = \nabla \cdot (\lambda \nabla T) + Q_L - Q_R,$$

$$\nabla \cdot \left(\frac{1}{3\chi_k}\nabla U_k\right) = \chi_k (U_k - U_{kp}), \quad k = 1, 2, \ldots, N_k,$$

with $Q_R \approx \sum_{k=1}^{N_k} c\chi_k (U_{kp} - U_k)$ and

$$Q_L = \frac{\mu P_{L1}}{\pi R_{L1}^2} \exp\left(-\frac{x^2 + y^2}{R_{L1}^2}\right) \exp\left(-\int_{z_0}^{z} \mu dz\right) + \frac{\mu P_{L2}}{\pi R_{L2}^2} \exp\left(-\frac{x^2 + (z - z_1)^2}{R_{L2}^2}\right) \exp\left(-\int_{y_0}^{y} \mu dy\right).$$

Here, $\mathbf{V}(V_x = u, V_y = v, V_z = w)$ is the mean mass velocity; p is the deviation of the pressure from $p_0 = 10^5$ Pa; T is the temperature; $\dot{S}$ is the deformation rate tensor;

1063-780X/00/2607-0617$20.00

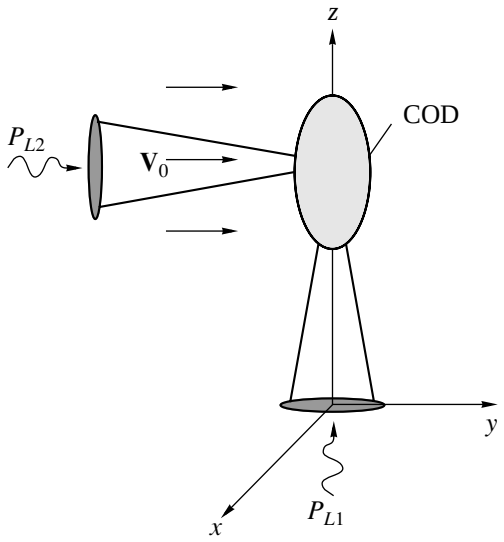

Fig. 1. Schematic of a COD in crossed laser beams in a gas flow.

ρ, C_p, η, λ, and μ are the density, heat capacity, viscosity, thermal conductivity, and the absorption coefficient of the laser light, respectively; χ_k, U_k, and U_{kp} are the group values of the absorption coefficient and of the densities of plasma and blackbody emissions averaged over each of the N_k spectral intervals; c is the speed of light; ρ_0 is the density of the cold gas; $\mathbf{g}(0, 0, g_z = -g)$ is the gravity acceleration; P_{L1} and P_{L2} are the powers of the laser beams of radii $R_{L1}(z)$ and $R_{L2}(y)$; and (x, y, z) are Cartesian coordinates. The optical axes of the laser beams are assumed to be parallel to the z- and y-axes.

2.1. Boundary Conditions

In Cartesian coordinates, the boundary conditions on the faces of the computation region in the form of a rectangular parallelepiped—$x = \{0; x_1\}$, $y = \{y_0; y_1\}$, $z = \{z_0; z_1\}$—are as follows. At the entrance ($y = y_0$) and side faces ($x = x_1$, $z = \{z_0; z_1\}$), the cold gas flow along the y-axis is uniform, the flow velocity being V_0, and no thermal radiation fluxes enter the computation region from the outside:

$$u = 0,\ v = V_0,\ w = 0,\ T = T_0,\ U_k + (2/3\chi_k)\partial U_k/\partial n = 0,$$

where the derivative is taken along the outer normal to the face. At the face $x = 0$, we impose the symmetry conditions

$$u = 0, \quad \partial v/\partial x = \partial w/\partial x = 0,$$
$$\partial p/\partial x = 0, \quad \partial T/\partial x = 0, \quad \partial U_k/\partial x = 0.$$

The length $y = y_1$ of the computation region is chosen such that the pressure changes insignificantly and the flow is essentially one-dimensional at the exit boundary:

$$u = w = 0, \quad \partial \rho v/\partial y = 0, \quad p = 0,$$
$$\partial T/\partial y = 0, \quad \partial U_k/\partial y = 0.$$

That the boundary conditions play only a minor role upstream of the exit boundary was confirmed by numerical simulations carried out with different values of y_1.

2.2. Solution Technique

We solved the above set of equations numerically using the SIMPLE finite-difference scheme [6] on a nonuniform grid of $25 \times 55 \times 55$ cells along the x-, y-, and z-axes, respectively; the grid was made finer (by reducing the grid size to about 0.1 mm) in the zones where the COD parameters changed abruptly, thereby making it possible to resolve the steepest front (from the side of the incident flow) of the discharge on spatial intervals as short as 8–10 grid sizes. *A posteriori* analysis revealed that the grid parameters affected the final numerical results only slightly.

3. RESULTS

We calculated the parameters of a COD in crossed horizontal and vertical laser beams with the same geometry (the beam radii were 0.3 cm in the cross sections $y = y_0$ and $z = z_0$ of the computation region, the focal points were at 3 cm on the related axes, and the waist radii were $R_k = 0.045$ cm) and with the same power ($P_{L1} = P_{L2} = 2.5$ kW) in a horizontal flow of a "cold" ($T_0 = 300$ K) gas (air) with the velocity $V_0 = 0.5$ and 6 m/s (Fig. 1). The boundary coordinates of the computation region were $x_1 = 2$ cm, $y_0 = -2$ cm, $y_1 = 3$ cm, $z_0 = 0$, and $z_1 = 5$ cm. For comparison, we also present the results obtained for discharges excited by a single horizontal laser beam or a single vertical beam of power 5 kW. The thermal-physics, transport, and optical ($N_k = 10$) parameters of air at atmospheric pressure were specified in accordance with the data from [7–9].

Our numerical results show that the high-temperature core of a COD is localized in the intersection region of the laser beams (Fig. 2). The overall flow pattern agrees qualitatively with the results obtained in [2, 3]. The cold gas is observed to flow at a slower rate inside the discharge front, where the pressure is elevated and the gas flows around the high-temperature core preferentially in a laminar fashion, without giving rise to vortex structures. For the burning regimes under analysis ($V_0 \geq 0.5$ m/s and $P_L = 5$ kW), the buoyancy force has an insignificant effect on the COD parameters. This result can be attributed to the small discharge dimensions (the characteristic velocity associated with the buoyancy force per square centimeter is $V_A \sim \sqrt{2gl} \approx$ 0.4 m/s) and the significant rate at which the gas is accelerated as it traverses the discharge front from the side of the incident flow [10]. Even for a COD in an air

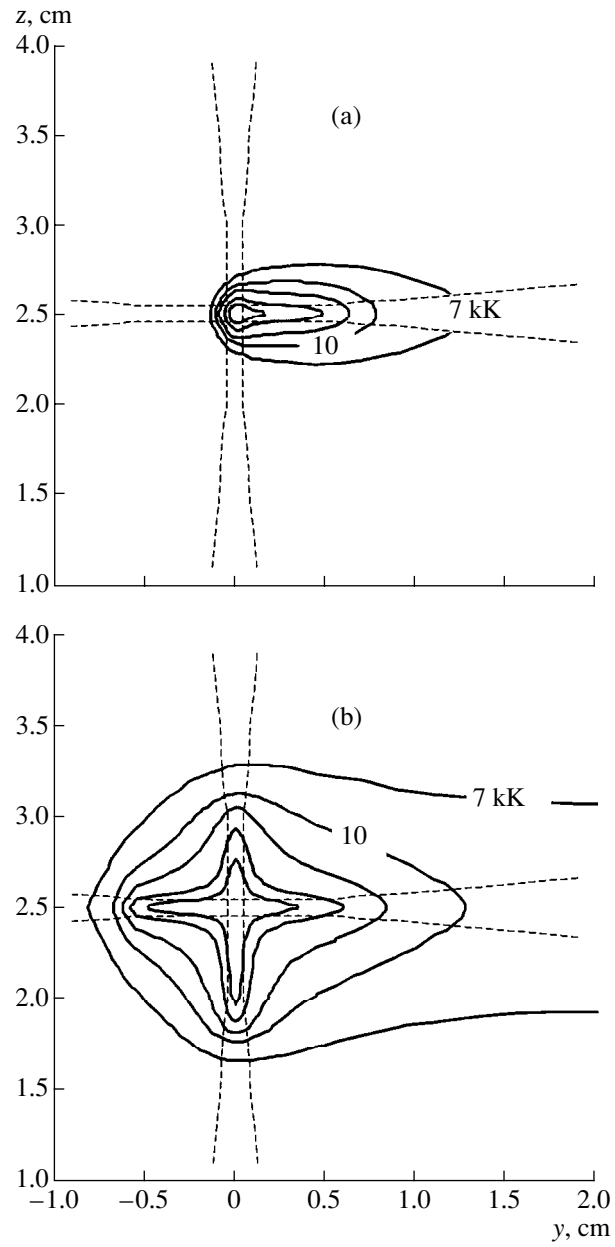

Fig. 2. Fragment of the temperature distribution (the temperature increment between adjacent isotherms is 3 kK) in the $x = 0$ plane in the case of a COD in crossed laser beams at V_0 = (a) 6 and (b) 0.5 m/s. The dashed curves correspond to the boundaries of the laser beams.

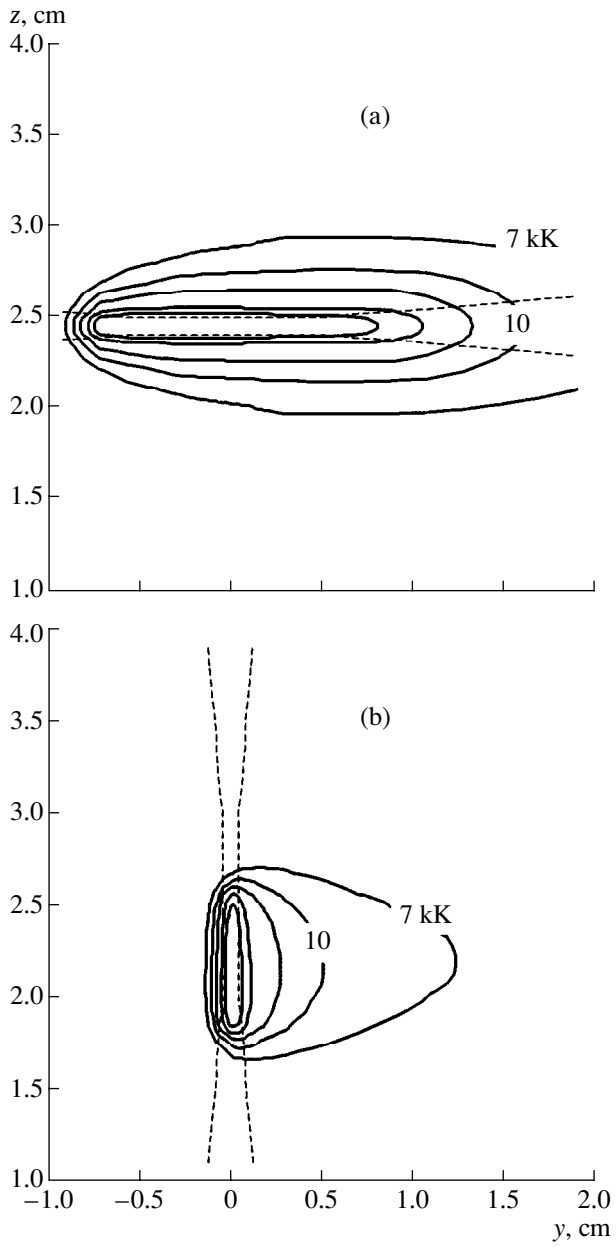

Fig. 3. Fragment of the temperature distribution (the temperature increment between adjacent isotherms is 3 kK) in the $x = 0$ plane in the case of a COD excited by (a) a horizontal and (b) vertical laser beam at V_0 = 6 m/s.

flow with the velocity $V_0 = 0.5$ m/s, the horizontal component of the flow velocity inside the core increases sharply to $V_m \approx 7.5$ m/s, thereby neutralizing the effect of the buoyancy force. The gas-dynamic model of a slowly burning COD [10] yields the estimate $V_m \approx \sqrt{\rho_0/2\rho_m}\, V_0 \approx 6.2$ m/s. Two-dimensional simulations carried out by Raĭzer and Surzhikov [11] also revealed that the vortex flow driven by the buoyancy force in a cylindrical chamber with closed ends has an insignificant effect on the thermal parameters of a COD at P_L = 6 kW.

The temperature distribution in the COD depends on the flow velocity. For $V_0 = 6$ m/s, the isotherms are teardrop-shaped in the intersection region of the beams; outside the intersection region, the isotherms are elliptic in shape and are stretched along the horizontal beam (Fig. 2). The core of the discharge in crossed beams is significantly smaller than that of the discharge excited

by one laser beam in a longitudinal or transverse gas flow (Fig. 3). The fraction of the total laser power dissipated in the discharge plasma is 1.3 kW, the fractions of the absorbed power of the vertical and horizontal beams being 0.4 and 0.9 kW, respectively. The discharge excited by a single laser beam in a longitudinal or transverse gas flow absorbs 4.1 or 2 kW of the laser power, respectively. According to the experimental data [1], the point (V_0 = 6 m/s, P_L = 2.5 kW) in the plane of the flow velocity–laser power variables lies below the domain where the COD can exist in a longitudinal or transverse gas flow; consequently, the vertical laser beam appears to fix the discharge core in space and stabilize the COD throughout the waist region where the beam is almost cylindrical in shape.

Our supplementary simulations also confirmed that a stable COD can occur in the intersection region of two unfocused beams with diameters $2R_k$. In this case, the discharge parameters were found to be almost the same as those in the case of two focused beams (Fig. 2). When the diameters of the unfocused beams were increased by a factor of two, the discharge was "blown off." We can expect that the region where a discharge in two crossed laser beams is stable will be smaller than that in the case of a COD in a single beam. This expectation is supported by the above results, according to which the discharge should become smaller in size and a lower fraction of laser power should be dissipated, as well as by the discharge blowing-off revealed in simulations at the boundaries (V_0 = 11 m/s, $P_{L1} = P_{L2}$ = 2.5 kW) and (V_0 = 6 m/s, $P_{L1} = P_{L2}$ = 1.5 kW) of the domain where a COD is stable [1]. With the existing restrictions on the laser power, the excitation of discharges in crossed beams makes it possible to increase the total laser power fed into the discharge and, accordingly, to increase the limiting flow velocity above which the discharge is unstable.

The core of a COD in an air flow with the velocity V_0 = 0.5 m/s is cross-shaped. The laser beams play essentially the same role in the formation of the discharge core. This conclusion is confirmed by the fact that the total power input into the discharge is almost equally shared between the beams (the fraction of 1.4 kW comes from the vertical beam and the fraction of 1.5 kW comes from the horizontal beam) and by the experimentally observed [1] stable COD excited by a single 2.5-kW laser beam in a longitudinal or transverse gas flow with a velocity of 0.5 m/s.

4. CONCLUSION

Our three-dimensional simulations have revealed the possibility of both obtaining a stable COD in crossed laser beams and controlling the shape of the discharge and its dimensions by varying the flow velocity, the power of the lasers, and the direction of laser beams.

REFERENCES

1. N. A. Generalov, A. M. Zakharov, V. D. Kosynkin, and M. Yu. Yakimov, Fiz. Goreniya Vzryva **22** (2), 91 (1986).
2. S. T. Surzhikov and A. A. Chentsov, Fiz. Plazmy **22**, 1054 (1996) [Plasma Phys. Rep. **22**, 957 (1996)].
3. É. B. Kulumbaev and V. M. Lelevkin, Fiz. Plazmy **25**, 568 (1999) [Plasma Phys. Rep. **25**, 517 (1999)].
4. A. L. Vikharev, V. B. Gil'denburg, O. A. Ivanov, and A. N. Stepanov, Fiz. Plazmy **10**, 165 (1984) [Sov. J. Plasma Phys. **10**, 96 (1984)].
5. V. E. Semenov, Fiz. Plazmy **10**, 562 (1984) [Sov. J. Plasma Phys. **10**, 328 (1984)].
6. S. Patankar, *Numerical Heat Transfer and Fluid Flow* (McGraw-Hill, New York, 1980; Énergoatomizdat, Moscow, 1984).
7. A. S. Predvoditelev, E. V. Stupochenko, A. S. Pleshanov, *et al.*, *Tables of Thermodynamic Functions of Air* (Vych. Tsentr Akad. Nauk SSSR, Moscow, 1959); A. S. Predvoditelev, E. V. Stupochenko, V. P. Ionov, *et al.*, *Thermodynamic Functions of Air* (Akad. Nauk SSSR, Moscow, 1960).
8. J. Bacri and S. Raffanel, Plasma Chem. Plasma Process. **9**, 133 (1989).
9. I. V. Avilova, L. M. Biberman, V. S. Vorob'ev, *et al.*, *Optical Properties of Hot Air* (Nauka, Moscow, 1970).
10. V. Ts. Gurovich, É. B. Kulumbaev, and V. M. Lelevkin, Fiz. Plazmy **24**, 1010 (1998) [Plasma Phys. Rep. **24**, 943 (1998)].
11. Yu. P. Raĭzer and S. T. Surzhikov, in *RF Discharge in Wave Fields* (Inst. Prikl. Fiz. Akad. Nauk SSSR, Gorki, 1988), p. 252; Preprint No. 344 (Inst. Prikl. Mekh. Akad. Nauk SSSR, Moscow, 1988).

Translated by G. Shepekina

Plasma Physics Reports, Vol. 26, No. 7, 2000, pp. 621–625. Translated from Fizika Plazmy, Vol. 26, No. 7, 2000, pp. 662–666.

LOW-TEMPERATURE PLASMA

Continuous Optical Discharge in a Gravitational Field

É. B. Kulumbaev and V. M. Lelevkin

Kyrgyz–Russian Slavic University, Bishkek, 720000 Kyrgyzstan

Received August 11, 1999; in final form, January 17, 2000

Abstract—A two-dimensional radiative gas-dynamic model is applied to calculating the parameters of a continuous optical discharge in a vertical focused CO_2 laser beam in air at atmospheric pressure in the Earth's gravitational field. *© 2000 MAIK "Nauka/Interperiodica".*

1. INTRODUCTION

Theoretical investigations of a continuous optical discharge (COD) in a focused CO_2 laser beam using the radiative gas-dynamic model equations [1–4] revealed the picture of discharge burning and the features of the interaction of an external cold-gas flow with the discharge. On the basis of the gas-dynamic mechanism, the authors of [5, 6] succeeded in explaining the difference between the experimentally observed velocity at which the COD front moves toward the laser source and the conventional velocity of the discharge propagation in a slowly burning regime. In [7, 8], we calculated the parameters of a COD in a focused CO_2 laser beam in air at atmospheric pressure as functions of both the rotation rate of the longitudinal (along the laser beam axis) gas flow [7] and the velocity of the transverse gas flow [8]. Numerical investigations of a COD in an external gas flow somewhat overshadowed the problem of a free convective flow in a discharge excited in a gravitational field. Raĭzer and Surzhikov [9] presented the results from calculations of the parameters of a COD excited by a 6-kW CO_2 laser beam focused into the geometric center of a cylindrical chamber with closed ends. They showed that, for certain ratios between the radius of the chamber and its height, vortex flows may form inside the discharge, which, however, have an insignificant impact on the discharge parameters.

Here, based on the physical model developed by Surzhikov and Chentsov [4], we calculate the parameters of a COD in a vertical focused CO_2 laser beam perpendicular to the Earth's surface in air at atmospheric pressure in the Earth's gravitational field, determine the discharge parameters as functions of the laser power, and reveal the peculiarities of the discharge instability at near-threshold laser powers.

2. MODEL

We consider a COD excited by a focused CO_2 laser beam in air at atmospheric pressure (Fig. 1), assuming that the discharge plasma is in equilibrium, the gas flow is subsonic and laminar, the refraction of laser light is negligible, and the laser beam is Gaussian in shape.

We determine the COD parameters by solving the following set of equations consisting of the continuity equation, the Navier–Stokes equation, the energy balance equation, the equation for the selective radiation transport in the multigroup diffusion approximation, and the transport equation for laser light in the geometrical-optics approximation:

$$\frac{1}{r}\frac{\partial}{\partial r}(r\rho v) + \frac{\partial}{\partial z}(\rho u) = 0,$$

$$\rho\left(v\frac{\partial v}{\partial r} + u\frac{\partial v}{\partial z}\right) = -\frac{\partial p}{\partial r} + \frac{2}{r}\frac{\partial}{\partial r}\left(r\eta\frac{\partial v}{\partial r}\right) - \frac{2\eta v}{r^2}$$

$$+ \frac{\partial}{\partial z}\left[\eta\left(\frac{\partial u}{\partial r} + \frac{\partial v}{\partial z}\right)\right] - \frac{\partial}{\partial r}\left[\frac{2}{3}\eta\left(\frac{1}{r}\frac{\partial rv}{\partial r} + \frac{\partial u}{\partial z}\right)\right],$$

$$\rho\left(v\frac{\partial u}{\partial r} + u\frac{\partial u}{\partial z}\right) = -\frac{\partial p}{\partial z} + 2\frac{\partial}{\partial z}\left(\eta\frac{\partial u}{\partial z}\right)$$

$$+ \frac{1}{r}\frac{\partial}{\partial r}\left[r\eta\left(\frac{\partial u}{\partial r} + \frac{\partial v}{\partial z}\right)\right]$$

$$- \frac{\partial}{\partial z}\left[\frac{2}{3}\eta\left(\frac{1}{r}\frac{\partial rv}{\partial r} + \frac{\partial u}{\partial z}\right)\right] + (\rho_0 - \rho)g,$$

$$\rho C_p\left(v\frac{\partial T}{\partial r} + u\frac{\partial T}{\partial z}\right) = \frac{1}{r}\frac{\partial}{\partial r}\left(r\lambda\frac{\partial T}{\partial r}\right)$$

$$+ \frac{\partial}{\partial z}\left(\lambda\frac{\partial T}{\partial z}\right) + Q_L - Q_R,$$

$$\frac{1}{r}\frac{\partial}{\partial r}\left(\frac{r}{3\chi_k}\frac{\partial U_k}{\partial r}\right) + \frac{\partial}{\partial z}\left(\frac{1}{3\chi_k}\frac{\partial U_k}{\partial z}\right) = \chi_k(U_k - U_{kp}),$$

$$k = 1, 2, \ldots, N_k,$$

$$Q_R \approx \sum_{k=1}^{N_k} c\chi_k(U_{kp} - U_k),$$

$$Q_L = \frac{\mu P_L}{\pi R_L^2}\exp\left(-\frac{r^2}{R_L^2}\right)\exp\left(-\int_0^z \mu dz\right).$$

1063-780X/00/2607-0621$20.00 © 2000 MAIK "Nauka/Interperiodica"

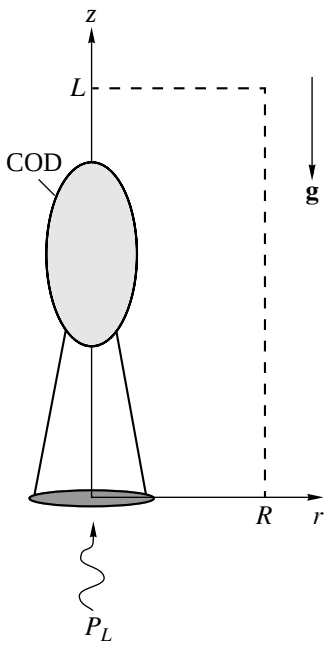

Fig. 1. Schematic of the computation region for a COD in the Earth's gravitational field.

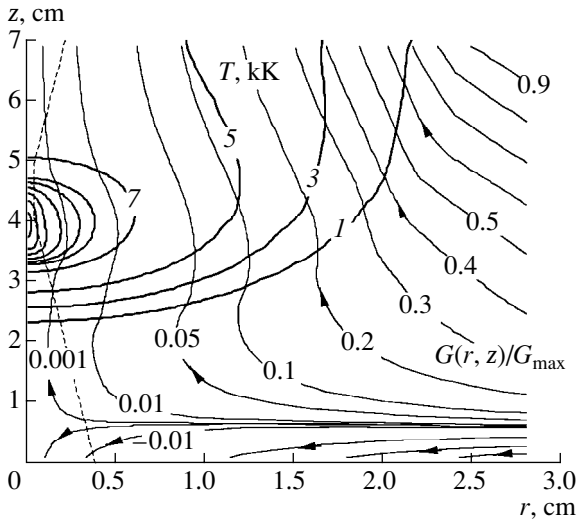

Fig. 2. Isotherms (the temperature increment between adjacent contours is 2 kK) and gas streamlines (G_{max} = 0.41 g/s) in a COD at P_L = 3 kW. The dashed curve corresponds to the laser beam boundary.

densities of plasma and blackbody emissions, averaged over each of the N_k spectral intervals; c is the speed of light; and P_L and $R_L(z)$ are the laser power and the radius of the laser beam.

2.1. Boundary Conditions

The boundary conditions at the rectangular contour around the computation region (Fig. 1) are as follows. The inflow and outflow of a cold gas at atmospheric pressure are normal to the lower (horizontal) and side boundaries, through which no thermal radiation fluxes enter the computation region from the outside:

$$\left.\begin{array}{l} z = 0, \quad 0 < r < R \\ 0 < z < L, \quad r = R \end{array}\right\} : p = p_0, \quad V_\tau = 0,$$

$$T = T_0, \quad U_k + (2/3\chi_k)\partial U_k/\partial n = 0,$$

where V_τ is the velocity component tangent to the boundary and $\partial/\partial n$ is the derivative along the outward-facing normal to the boundary.

At the axis $r = 0$, we impose the symmetry conditions

$$0 < z < L, \quad r = 0: \quad \partial u/\partial r = 0, \quad v = 0,$$
$$\partial p/\partial r = 0, \quad \partial T/\partial r = 0, \quad \partial U_k/\partial r = 0.$$

The conditions at the upper boundary correspond to a one-dimensional gas flow:

$$z = L, \quad 0 < r < R: \quad \partial \rho u/\partial z = 0, \quad v = 0,$$
$$p = p_0, \quad \partial T/\partial z = 0, \quad \partial U_k/\partial z = 0.$$

2.2. Solution Technique

As in [6–8], we solved the above set of equations in physical variables numerically using the SIMPLE finite-difference scheme [10] under conditions corresponding to air at atmospheric pressure; the data on thermal-physics, transport, and optical (N_k = 10) properties were taken from [11–13].

3. COMPUTATION RESULTS

We calculated the parameters of a COD in a vertical laser beam in the Earth's gravitational field as functions of the laser power (P_L = 2.4, 3, and 5 kW) at T_0 = 300 K and $p_0 = 10^5$ Pa. The radius of the laser beam was 0.3 cm, the focal point was at 3 cm, and the waist radius was 0.045 cm. The sizes of the computation region were chosen based on numerical experiments so as to ensure a weak effect of the boundary conditions on the COD parameters.

According to our simulation results (Fig. 2), the high-temperature core of the COD is localized in the focal region and is shifted toward the laser beam. We can see steep thermal and gas-dynamic fronts (from the

Here, v and u are the projections of the velocity vector onto the r- and z-axes; T is the temperature; p is the pressure; ρ, C_p, η, λ, and μ are the density, heat capacity at a constant pressure, viscosity, thermal conductivity, and the absorption coefficient of the laser light, respectively; ρ_0 is the density of the cold gas; $\mathbf{g}(0, 0, g_z = -g)$ is the gravitational acceleration; χ_k, U_k, and U_{kp} are the group values of the absorption coefficient and of the

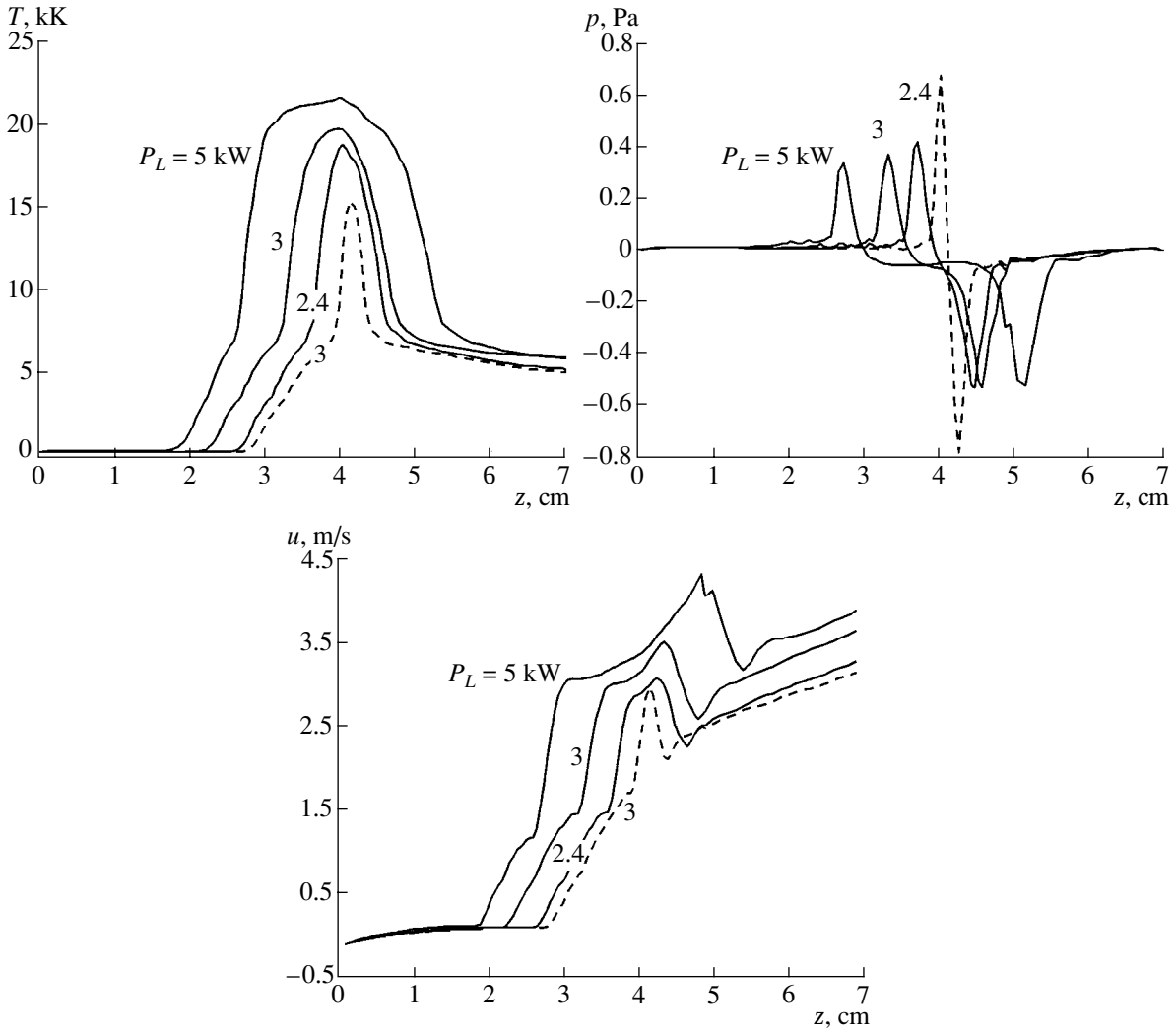

Fig. 3. Distributions of the temperature, velocity, and pressure along the COD-axis at different laser powers. The dashed curves correspond to the unstable regime.

side of the incident laser light) and trailing edges of the discharge core (Fig. 3). Ahead of the thermal front, there is a gas halo, which is heated by the thermal flux from the core due to heat transfer. In a COD in an external axial gas flow, no halo appears, because the induced convective cooling dominates over the heating due to heat transfer [1–4]. The buoyancy force acts to initiate an upward stream of the heated gas, thereby giving rise to the formation of a complicated gas-dynamic flow structure consisting of two toroidal vortices rotating in opposite directions. The gas that permanently enters the halo from the outside (because of the continuity of the flow) is heated, expands in the radial direction, and is accelerated by the buoyancy force (Figs. 2, 3). As in the case of an external axial gas flow [6], the gas is decelerated by increasing the positive pressure gradient as it traverses the front of the discharge core. In the region behind the front (where the pressure falls off sharply), the gas is rapidly accelerated and expands. Inside the discharge core, the pressure is depressed and remains essentially unchanged and the rate at which the gas is accelerated by the buoyancy force is lower. Farther along the discharge axis, the change in the discharge parameters is governed by the reverse gas motion from the discharge region where the laser power is dissipated toward the trailing edge, which is elongated due to convection and in which the gas is slowly cooled mainly via heat transfer.

For lower laser powers, the discharge is shorter in the axial direction, the core temperature is lower, and a smaller fraction of laser energy is dissipated in the discharge plasma (P_d = 4, 1.6, and 0.9 kW for P_L = 5, 3, and 2.4 kW, respectively), but the pressure gradient (the excessive pressure) at the thermal front and the velocity at which the gas flows through the front are both higher (Fig. 3). Inside the core, the pressure and mass velocity ρu remain almost unchanged. At the trailing edge, the negative pressure gradient, which ensures that the same amount of gas flows from the laser power deposition region toward the trailing part of the discharge

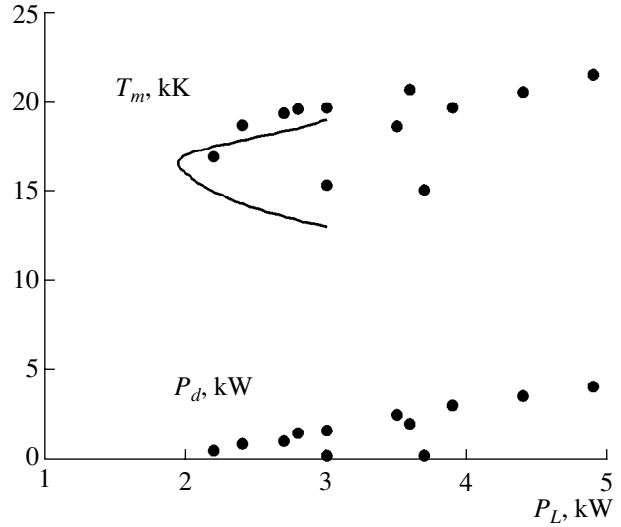

Fig. 4. Maximum temperature and the fraction of the laser power dissipated in the discharge plasma as functions of the laser power. The solid curves illustrate the results of calculations based on the model of a spherical COD [15].

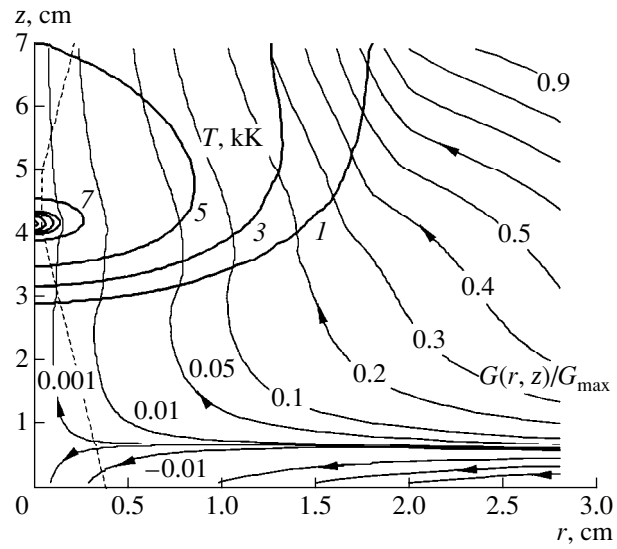

Fig. 5. Isotherms (the temperature increment between adjacent contours is 2 kK) and gas streamlines (G_{max} = 0.32 g/s) in a COD at P_L = 3 kW in the unstable regime. The dashed curve corresponds to the laser beam boundary.

(ρu = const), also does not change. The front of the core and its trailing edge propagate toward each other: at a laser power of 2.4 kW, they come together in the beam-waist cross section z = 4 cm. This laser power is the lowest (threshold) power above which the iteration procedure converges to a nontrivial solution. All of the discharges simulated iteratively at a power of 2.3 kW and lower were observed to inevitably terminate. The computed threshold turned out to be 0.4 kW higher than that obtained by Raĭzer and Silant'ev [14], who solved the equations for a COD in an immobile gas numerically by the relaxation method with allowance for the refraction of laser light.

That the discharge has a threshold in terms of the laser power is confirmed by our simulations, which also provide evidence for two different steady regimes illustrated in Fig. 4 by two (low-temperature and high-temperature) branches of the dependence $T_m(P_L)$ of the maximum temperature on the laser power. These characteristic features of discharges in electromagnetic fields were revealed by Raĭzer [15] on the basis of the model of a spherical COD. However, in performing two-dimensional simulations, Raĭzer and Silant'ev [14] found that, no matter how the discharge was seeded by the plasma, it ultimately terminated or reached the same steady regime. In that paper, the existence of two different model solutions for the same values of the external parameters was attributed to imperfections in the analytic model. In actuality, the model simulations of [14] captured only one regime because the solution with a low temperature is unstable against fluctuations (iterative approximations) of the temperature in the course of a run. Consequently, in iterations, the numerical solution always converged to a steady solution corresponding to the high-temperature branch of the dependence $T_m(P_L)$. To obtain solutions describing both branches of $T_m(P_L)$, it is necessary to specify, instead of the laser power P_L, the fraction P_d of laser power dissipated in the discharge plasma, which is uniquely related to T_m (a similar approach was applied in [16] to a low-frequency inductive transformer-type discharge and, in [17], to a spherical and a cylindrically symmetric microwave discharge). This conclusion is justified by the simulation results illustrated in Fig. 4. The parameters of a discharge in the unstable regime (P_d = 0.25 kW at P_L = 3 kW; see Figs. 3, 5) are consistent with the qualitative predictions obtained in [15].

To estimate the effect of the buoyancy force, we simulated a COD for P_L = 3 kW, taking the gravitational acceleration to be overstated by a factor of 5. We found no qualitative changes in the overall pattern of the gas flow and gas heating. Quantitatively, the pressure gradients at the front of the discharge and at its trailing edge are larger and, in the discharge core, the negative pressure is less depressed and the gas flow velocity is higher, the sizes of the region in which the laser power is dissipated being unchanged.

4. CONCLUSION

We have calculated the parameters a COD in a focused vertical (perpendicular to the Earth's surface) CO_2 laser beam in air at atmospheric pressure in the Earth's gravitational field as functions of the laser power.

We have shown that the buoyancy force gives rise to the formation of a vortex structure of the discharge. The

amount of gas flowing through the discharge is independent of the laser power and is governed by the pressure at the discharge front.

Inside the core of a COD, the pressure is depressed. At the trailing edge of the core, the pressure gradient is negative and is weakly sensitive to the laser power.

The dimensions of a COD are governed by the laser power and are independent of the gravitational acceleration. At the near-threshold laser power, the front of the discharge and its trailing edge are brought together.

REFERENCES

1. Yu. P. Raĭzer, A. Yu. Silant'ev, and S. T. Surzhikov, Teplofiz. Vys. Temp. **25**, 454 (1987).
2. S.-M. Jeng, D. R. Keefer, R. P. Welle, and C. E. Piters, AIAA J., No. 9, 1224 (1987).
3. É. B. Kulumbaev, V. M. Lelevkin, and D. K. Otorbaev, Izv. Akad. Nauk Kirg. SSR **6**, 35 (1986).
4. S. T. Surzhikov and A. A. Chentsov, Fiz. Plazmy **22**, 1054 (1996) [Plasma Phys. Rep. **22**, 957 (1996)].
5. K. G. Gus'kov, Yu. P. Raĭzer, and S. T. Surzhikov, Kvantovaya Élektron. (Moscow) **17**, 937 (1990).
6. V. Ts. Gurovich, É. B. Kulumbaev, and V. M. Lelevkin, Fiz. Plazmy **24**, 1010 (1998) [Plasma Phys. Rep. **24**, 943 (1998)].
7. É. B. Kulumbaev and V. M. Lelevkin, Fiz. Plazmy **25**, 205 (1999) [Plasma Phys. Rep. **25**, 183 (1999)].
8. É. B. Kulumbaev and V. M. Lelevkin, Fiz. Plazmy **25**, 568 (1999) [Plasma Phys. Rep. **25**, 517 (1999)].
9. Yu. P. Raĭzer and S. T. Surzhikov, in *RF Discharge in Wave Fields* (Inst. Prikl. Fiz. Akad. Nauk SSSR, Gorki, 1988), p. 252; Preprint No. 344 (Inst. Prikl. Mekh. Akad. Nauk SSSR, Moscow, 1988).
10. S. Patankar, *Numeral Heat Transfer and Fluid Flow* (McGraw-Hill, New York, 1980; Énergoatomizdat, Moscow, 1984).
11. A. S. Predvoditelev, E. V. Stupochenko, A. S. Pleshanov, *et al.*, *Tables of Thermodynamic Functions of Air* (Vych. Tsentr Akad. Nauk SSSR, Moscow, 1959); A. S. Predvoditelev, E. V. Stupochenko, V. P. Ionov, *et al.*, *Thermodynamic Functions of Air* (Akad. Nauk SSSR, Moscow, 1960).
12. J. Bacri and S. Raffanel, Plasma Chem. Plasma Process. **9**, 133 (1989).
13. I. V. Avilova, L. M. Biberman, V. S. Vorob'ev, *et al.*, *Optical Properties of Hot Air* (Nauka, Moscow, 1970).
14. Yu. P. Raĭzer and A. Yu. Silant'ev, Kvantovaya Élektron. (Moscow) **13**, 593 (1986).
15. Yu. P. Raĭzer, *Gas Discharge Physics* (Nauka, Moscow, 1987; Springer-Verlag, Berlin, 1991).
16. É. B. Kulumbaev and V. M. Lelevkin, Teplofiz. Vys. Temp. **35**, 357 (1997); **36**, 889 (1998).
17. S. V. Dresvin, A. A. Bobrov, V. M. Lelevkin, *et al.*, *RF and Microwave Plasmotrons* (Nauka, Novosibirsk, 1992), Vol. 6.

Translated by G. Shepekina

Plasma Physics Reports, Vol. 26, No. 7, 2000, pp. 626–627. Translated from Fizika Plazmy, Vol. 26, No. 7, 2000, pp. 667–668.

BRIEF COMMUNICATIONS

Ion Separation by a Curved Magnetic Field in a Multicomponent Plasma

A. V. Timofeev

Russian Research Centre Kurchatov Institute, pl. Kurchatova 1, Moscow, 123182 Russia

Received February 17, 2000

Abstract—It is shown that a curved magnetic field can be used to separate ions in a multicomponent plasma. Without selective ion preheating, the separation over one cycle is inefficient: the separated ion fractions will only be enriched with ions of the corresponding isotopes. Selective ion cyclotron resonance heating makes it possible to achieve essentially a complete separation of the ions. © *2000 MAIK "Nauka/Interperiodica".*

At present, plasma methods for processing various kinds of waste (in particular, radioactive waste) in order to extract the most harmful components are widely discussed. For this purpose, it is possible to employ the phenomenon of particle drift in curved magnetic fields. This phenomenon underlies some of the proposed schemes for direct conversion of plasma thermal energy into electrical energy [1] and for isotope separation by selective ion-cyclotron resonance (ICR) heating [2].

These schemes make use of the fact that the drift velocity of a charged particle in a curved magnetic field depends on the particle energy,

$$V_{dr} = \frac{c}{eBR}(2\varepsilon_{\parallel} + \varepsilon_{\perp}),$$

where B is the magnetic induction, R is the radius of curvature of the magnetic field lines, $\varepsilon_{\parallel}$ and $\varepsilon_{\perp}$ are the thermal ion energies in the directions parallel and perpendicular to the magnetic field, c is the speed of light in vacuum, and e is the electron charge. In such a field, charged particles with different energies are separated out automatically: when they travel a distance Δs along the magnetic field, they are displaced in the direction of the binormal to the magnetic field lines (in the z-direction) by different distances $\Delta z = V_{dr}\Delta s/v_{\parallel}$, depending on their longitudinal and transverse energies, $\varepsilon_{\parallel}$ and $\varepsilon_{\perp}$.

Note that particles with the same energy but with different masses also experience different displacements because $v_{\parallel} \propto m^{-1/2}$ so that, even in an isothermal multicomponent plasma in which all of the ions have the same mean energy, a curved magnetic field can be used to separate ions by mass. This method appears to be efficient only for separating different chemical elements, but is unlikely to be used to separate isotopes of the same element, because the difference in mass between the isotopes is too small.

The ions of different elements should be separated in a system with a curved magnetic field, and the separated ions should be collected at plates that are installed at the end of the system and have finite dimensions along the z-axis (see figure). As in [1, 2], the charge separation in the plasma can be eliminated by heated cathodes; it is convenient to arrange them at the opposite end of the system.

An accurate calculation of the fraction of ions that are extracted from the plasma requires a knowledge of the ion distribution over thermal velocities and the initial spatial distribution $f(\varepsilon, \chi, z_0)$, where χ is the pitch angle. In this case, the distribution over ε, χ, and z_1 (where z_1 is the coordinate at the exit from the system) depends on the ion mass: $f(\varepsilon, \chi, z_1 - \Delta z(\varepsilon, \chi, m_i))$, where $\Delta z = \frac{V_{dr}R\Delta\theta}{v_{\parallel}} = \sqrt{2\varepsilon m_i}\frac{c\Delta\theta}{eB}\frac{2\cos^2\chi + \sin^2\chi}{\cos\chi}$. We assume that the magnetic field lines are arcs of circles with the lengths $\Delta s = R\Delta\theta$.

Under the assumptions that the ion distribution over thermal velocities is Maxwellian and that the ion distribution over the coordinate z_0 at the entrance to the system is Gaussian with a characteristic dimension a, $f(z_0) = \frac{1}{\sqrt{\pi}a}\exp\left(-\left(\frac{z_0}{a}\right)^2\right)$, we can find the fraction of

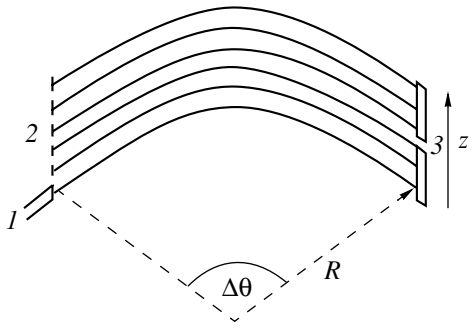

General scheme for ion separation by a curved magnetic field in a multicomponent plasma: (*1*) plasma source, (*2*) heated cathodes, and (*3*) absorbing plates. Solid curves illustrate the magnetic field lines.

1063-780X/00/2607-0626$20.00 © 2000 MAIK "Nauka/Interperiodica"

ions of species α that are deposited on a plate occupying the interval $l_1 < z < l_2$:

$$N_\alpha = \frac{4}{\pi}\int_0^{\pi/2} d\chi \sin\chi \int_0^\infty dw w^2 \exp(-w^2) \int_{\xi_{1,\alpha}}^{\xi_{2,\alpha}} d\xi \exp(-\xi^2),$$

where $\xi_{1,2;\alpha} = \left(l_{1,2} - \rho_{i,\alpha}\Delta\theta \frac{2\cos^2\chi + \sin^2\chi}{\cos\chi} w\right)\frac{1}{a}$, $\rho_{i,\alpha} = \sqrt{\frac{2T}{m_\alpha}}\frac{1}{\omega_{i,\alpha}}$, and $\omega_{i,\alpha}$ is the cyclotron frequency of the ions of species α.

In the simplest system under discussion, the displacement along the *z*-axis is determined by the magnetic field line curvature and is equal in order of magnitude to $\rho_i\Delta\theta$. The displacement can be increased by imposing a helical magnetic field, in which case, however, the separation is also far from being complete. Clearly, the degree of separation can be increased by passing the working mixture through the system several times.

An essentially complete separation over one cycle can be achieved via selective ion preheating, as is usually done in ICR-based isotope separators [3]. If it is necessary to separate out the groups of chemical elements that differ in mass (e.g., actinides and lanthanides), then the ions of the elements of one group should be ICR heated in a nonuniform magnetic field. The energy of the cyclotron gyration of the ions that have crossed the ICR heating zone increases by an amount equal to

$$\Delta\varepsilon \approx \frac{\pi}{2} m_i \left(c\frac{E}{B_0}\right)^2 \frac{L\omega_i}{v_\parallel},$$

where L is the spatial scale on which the magnetic field decreases and E is the left-polarized electric field (i.e., the electric field that rotates in the same direction as the ions). For $L = 10^2$ cm, $m_i = 10^2$ a.u., $B = 1$ kG, and $\varepsilon = 1$ eV, the RF field required to heat the ions to 10^2 eV is relatively weak: $E \approx 1$ V/cm.

Since the magnetic field in the heating system is weakened, the transverse energy gained by the ions in the ICR heating zone is partially converted into their longitudinal energy, $\cos\chi \approx \sqrt{\Delta B/B}$, where ΔB is the drop in the magnetic field across the system.

A separator based on the preheating of one of the ion species should satisfy the following two main requirements. First, hot ions should be separated out from the cold ions; i.e., they should be displaced along the *z*-axis by a distance larger than the initial transverse dimension l_0 of the plasma stream. Second, hot ions passing through the stream of cold ions should not be cooled via Coulomb collisions.

The first requirement can be represented as

$$\Delta z = V'_{dr}\frac{R\Delta\theta}{v'_\parallel} > l_0,$$

which is equivalent to the condition

$$\varepsilon' > \varepsilon\left(\frac{a_1}{\Delta\theta}\cos\chi\right)^2. \quad (1)$$

Here, the transverse dimension of the plasma stream is assumed to be several times larger than the ion Larmor radius ρ_{i0} in terms of the initial temperature: $l_0 \approx a_1\rho_{i0}$. The primed quantities refer to hot ions. Condition (1) is satisfied, provided that the ions are heated to 10^2 eV (see above) and that $a_1 = 10$ and $\Delta\theta = 3$.

Now, we turn to the second requirement—the condition for the plasma to be collisionless. Let N be the total number of particles that enter the system per unit time, so that the plasma density is $n \approx \approx \frac{N}{v_\parallel \pi a_1^2 \rho_i^2}$. For example, for $N \approx 10^{21}$ particle/s, which is equivalent to a current of 10^2 A, the plasma density is $n \approx 3\times 10^{13}$ cm^{-1}. For $R = 3\times 10^2$ cm and $\varepsilon' = 10^2$ eV, the time $T_1 = l_0/V'_{dr}$ required for hot ions to drift through the stream of cold ions is $T_1 \approx 3\times 10^{-4}$ s. The collision frequency can be estimated from the formula $\nu_i \approx \frac{n}{3\times 10^7 \varepsilon'^{3/2}} \approx 10^3$ s^{-1} (where the plasma density is in units of cm^{-3} and the energy is in eV). We can readily see that, with the parameter values adopted above, the second requirement is also satisfied.

This requirement can be written as the condition

$$\varepsilon'^{5/2} > 10^{-6}\frac{NRm_i\omega_i^2}{a_1^2\varepsilon}. \quad (2)$$

Here, the energy is again in units of eV and the remaining quantities are expressed in electrostatic units. Conditions (1) and (2) imply that the higher the energy ε', the more complete the separation.

Our estimates show that the method proposed here for ion separation can be implemented with the currently available experimental equipment.

ACKNOWLEDGMENTS

I am grateful to V.A. Zhil'tsov, A.A. Skovoroda, and V.P. Smirnov for useful discussions.

REFERENCES

1. A. V. Timofeev, Fiz. Plazmy **4**, 826 (1978) [Sov. J. Plasma Phys. **4**, 464 (1978)].
2. M. I. Belavin, A. V. Zvonkov, and A. V. Timofeev, RF Patent No. 2108141 (July 5, 1993).
3. Yu. A. Muromkin, Itogi Nauki Tekh., Ser. Fiz. Plazmy **12**, 83 (1991).

Translated by O. Khadin

Plasma Physics Reports, Vol. 26, No. 7, 2000, pp. 628–631. Translated from Fizika Plazmy, Vol. 26, No. 7, 2000, pp. 669–671.

BRIEF COMMUNICATIONS

Pair Correlation Function for a Dusty Plasma

S. A. Maĭorov

Institute of General Physics, Russian Academy of Sciences, ul. Vavilova 38, Moscow, 117942 Russia

Received October 21, 1999

Abstract—Analytic expressions for pair electron–grain and ion–grain radial distribution functions are derived under the assumption of a short-range binary interaction between mobile particles and an immobile charged grain, which is treated as a point particle. © *2000 MAIK "Nauka/Interperiodica".*

1. INTRODUCTION

In recent years, dusty plasmas have been actively studied both experimentally and theoretically [1–6]. The problem of ion and electron distributions around a dust grain is important for an adequate description of the properties of dusty plasmas. In some cases, theoretical approaches to studying ordinary plasmas fail to describe dusty plasmas [7–9]. To explain the experimentally observed evolution of micron-size dust grains into ordered structures requires knowledge of the law of electrostatic interaction between the grains. It is also important to understand the role played by the interaction between the grains and a buffer gas, because, in experiments, the degree of gas ionization is usually no higher than 10^{-2}. For example, the attracting forces between the grains can be explained in terms of the screening effect, which occurs when the molecules of a buffer gas flow freely around the grains [4].

Here, based on the solution to a dynamic problem and using the binary interaction approximation, we derive the pair correlation function of a mobile plasma particle and an immobile charged grain, which is treated below as a point particle. This approach is justified either when two particles are so close to one another that the effect of the remaining particles on their dynamics can be neglected or when the charge of one of the particles is very large (as in the case of dusty plasmas).

2. DEBYE APPROXIMATION FOR A PAIR CORRELATION FUNCTION

We consider a fully ionized plasma consisting of ions with mass M and positive charge ze and electrons with mass m and charge $-e$. Let the plasma also contain an immobile point particle of charge $Z_0e > 0$ surrounded by a spherically symmetric, charged cloud of ions and electrons. The plasma density in the cloud depends only on the distance r from the point charge. Poisson's equation for the mean electric potential $\varphi(r)$ of the point charge has the form

$$-\Delta\varphi = 4\pi e[Z_0\delta(r) + zN_i(r) - N_e(r)]. \quad (1)$$

The radial distribution of the particles of species a around the immobile point charge is usually described by a Boltzmann distribution function [7],

$$N_a(r) = N_{a0}\exp(-z_a e\varphi/T_a), \quad (2)$$

where N_{a0} is the volume-averaged particle density; T_a is the temperature; φ is the mean electrostatic potential around the immobile point charge; and $z_a = -1$ and z for the electrons and ions, respectively. In the weak interaction approximation, $z_a e\varphi/T_a \ll 1$, we can expand the exponential function in (2) in a series, in which case Poisson's equation (1) has a solution in the form of the Yukawa potential:

$$\varphi(r) = \frac{Z_0 e}{r}\exp(-r/r_D), \quad (3)$$

where the Debye radius $r_D = (4\pi\sum_a z_a^2 e^2 N_{a0}/T_a)^{1/2}$ defines the screening length for the Coulomb field of the immobile point charge [7]. In the case of potential (3), the correlation function g_{ab}, i.e., the function describing the correlation between mobile particles of species a and immobile particles of species b with charge Z_0e, has the form [7–9]

$$g_{ab}(r) = -\frac{z_a Z_0 e^2}{rT_a}\exp(-r/r_D) = -\frac{r_w}{r}\exp(-r/r_D), \quad (4)$$

where $r_w = zZ_0e^2/T$ is the classical radius of interaction (the Landau length). Expression (4) is valid under the conditions that the pair correlations be weak and that the three-particle correlations be insignificant in comparison with the pair correlations:

$$g_{ab} \ll 1, \quad g_{abc} \ll g_{ab}. \quad (5)$$

Linearizing the exponential functions in (2) and (4) also yields a physically meaningful potential of the interaction between particles on short radial scales on which conditions (5) fail to hold. Moreover, keeping terms of the second order and higher in the expansion is physically meaningless (see [9] for details).

1063-780X/00/2607-0628$20.00 © 2000 MAIK "Nauka/Interperiodica"

3. ELECTRON–GRAIN CORRELATION FUNCTION IN THE BINARY BALLISTIC APPROXIMATION

In an ideal plasma, the characteristic particle-energy and particle-momentum relaxation lengths are much longer than the mean distance $N_a^{-1/3}$ between the particles. Consequently, in the immediate vicinity of an immobile point charge, we can neglect the forces exerted by the remaining plasma particles. In a sufficiently small vicinity of an immobile point charge, the trajectories of the particles and their density are described by the equations of motion in a central field.

With allowance for electron interaction only with an immobile grain, which is treated as a point particle of charge Z_0e, we obtain the radial distribution of the electron density around the grain. Let the absolute value of the velocity of all the electrons be the same (V_0) and let the mean electron density be N_{e0}. The flux of the electrons with impact parameters in the range $(\rho, \rho + \Delta\rho)$ is equal to $2\pi\rho\Delta\rho N_{e0}V_0$. We consider a spherical layer bounded by spheres of radii r and $r + \Delta r$ around the immobile point particle; the volume of the layer is equal to $4\pi r^2\Delta r$. The radial electron velocity in the spherical layer depends only on the radius of the layer and is determined from the solution to the Kepler problem [10]:

$$V_r = V_0\left(1 + \frac{2Z_0^2e^2}{mV_0^2r} - \frac{\rho^2}{r^2}\right)^{1/2}. \tag{6}$$

Each electron that enters the spherical layer passes through it twice and stays inside the layer during the time $\Delta t = 2\Delta r/V_r$. The electron density $\Delta N_e(r, \rho, \Delta\rho)$ provided in the spherical layer by the flux $N_{e0}V_0$ of electrons with impact parameters in the range $(\rho, \rho + \Delta\rho)$ is governed by the number of electrons that enter the layer per unit time, the time required for the electrons to traverse the layer, and the layer volume: $\Delta N_e(r, \rho, \Delta\rho) = N_{e0}V_0\rho\Delta\rho/r^2V_r$. We integrate $\Delta N_e(r, \rho, \Delta\rho)$ over all possible impact parameters in the range $0 < \rho < \rho_{\max}$, where $\rho_{\max}$ is determined by the condition $V_r = 0$, to obtain

$$N_e(r, V_0) = \frac{N_{e0}}{r^2} \times \int_0^{\rho_{\max}} \rho\left(1 + \frac{2Z_0e^2}{mV_0^2r} - \frac{\rho^2}{r^2}\right)^{-1/2} d\rho = N_{e0}\left(1 + \frac{2Z_0e^2}{mV_0^2r}\right)^{1/2}. \tag{7}$$

This distribution also determines the pair correlation function for electrons with velocity V_0. If, at large distances from the immobile point particle, the electrons obey a Maxwellian velocity distribution with temperature T, then we must average (7) over the velocities. As a result, we obtain

$$N_e(r, T) = \frac{2N_{e0}}{\sqrt{\pi}}\int_0^\infty\left(x + \frac{Z_0e^2}{rT}\right)^{1/2} e^{-x}dx = N_{e0}I\left(\frac{Z_0e^2}{rT}\right). \tag{8}$$

The integral $I(x)$ in (8) is expressed through an incomplete Gamma function and has the following asymptotics: $I(x) \approx 1 + x$ for $x \ll 1$ and $I(x) \approx \sqrt{x}$ for $x \gg 1$. Since the Landau length in a collision between an electron and the immobile point particle is equal to $r_w = Z_0e^2/T$, the pair correlation function can be written as

$$g_{ab}(r) = \sqrt{r_w/r} - 1 \quad \text{for} \quad r \ll r_w, \qquad g_{ab}(r) = \frac{r_w}{r} \quad \text{for} \quad r \gg r_w. \tag{9}$$

4. ION–GRAIN CORRELATION FUNCTION

The density of the ions having the same velocity V_0 can be evaluated in an analogous manner:

$$N_i(r, V_0) = N_{i0}\left(1 - \frac{2zZ_0e^2}{MV_0^2r}\right)^{1/2}, \quad \text{for} \quad r > \frac{2zZ_0e^2}{MV_0^2},$$

$$N_i(r, V_0) = 0, \quad \text{for} \quad r < \frac{2zZ_0e^2}{MV_0^2}.$$

If the ions obey a Maxwellian velocity distribution, then their density can be expressed as

$$N_i(r, T) = \frac{4N_{i0}}{\sqrt{\pi}}\int_{x_{\min}}^\infty x\left(x^2 - \frac{zZ_0e^2}{rT}\right)^{1/2} e^{-x^2}dx = N_{i0}\exp\left(-\frac{zZ_0e^2}{rT}\right). \tag{10}$$

The domain of integration in (10) is determined from the condition for the expression under the square root to be positive. For a pair ion–grain correlation function, we have

$$g_{aa}(r) = \exp\left(-\frac{zZ_0e^2}{rT}\right) - 1 = \exp\left(-\frac{r_w}{r}\right) - 1.$$

The problem of a collision event between two mobile particles is equivalent to the problem of scattering in the central field, in which case the mass of a particle should be replaced with the reduced mass of two particles [10]. Thereby, the correlation functions derived above can be used to calculate the correlations between mobile particles.

The electron and ion density distributions around the immobile point grain, (9) and (10), and the pair correlation functions all have the Debye asymptotics on spatial scales that are longer than the radius of interaction, $r_w = zZ_0e^2/T$ (the Landau length), and shorter than the Debye radius. On spatial scales of about the Landau length and shorter, the asymptotics differ radically from the Debye asymptotics: being functions of distance, the correlations between oppositely charged particles obey the square-root law $g_{ab} \approx r_w/r$ rather than the law $g_{ab} \approx (r_w/r)^{1/2}$ in (4).

5. THE CASE OF A DUSTY PLASMA

The results obtained are of interest from the standpoint of dusty plasmas. Dust grains usually acquire a negative charge, which may be very large: $Z_0 \sim -10^6$ [1, 2]. In a dusty plasma with intense electron thermal emission, the grains may acquire a positive charge. In both cases, the region where the ion–grain correlations are strong can substantially affect the plasma parameters. However, the approach applied in some papers to describing the processes in dusty plasmas by using the Boltzmann distribution for mobile particles around the grains is unjustified.

Analyzing experiments with positively charged dust grains [3], Nefedov *et al.* [5] derived corrections to the Debye interaction potential by retaining third-order terms in the expansion of the exponential function in the Boltzmann distribution (2). Although the authors of [5] considered the potential of the interaction between the grains, such an approach can only be used to determine the mean potential around a single grain.

The corrections to the Debye interaction potential that were obtained in [5] are, as noted above, physically meaningless and even fail to give a correct answer to the question of whether the realistic screening potential is higher or lower than the Debye screening potential. The surface potential obtained in [5] is lower than the Debye potential; this corresponds to a screening stronger than the Debye screening. However, formulas (8) and (9), which were derived with allowance for particle dynamics around a grain, imply that the grain charge should be screened to a lesser extent than in the case of Debye screening. Additionally, higher order corrections may turn out to be of no less importance than the third-order corrections.

The screening potential derived in [5] merely describes the repulsion of the grains. To explain the experimentally observed formation of dust crystalline structures and dust clouds requires that there be a potential that acts to attract the grains on long spatial scales and repulse them on short scales (which should, however, be larger than the Debye radius). A more systematic approach is to solve the problem of the interaction between two grains, each surrounded by an electron cloud (i.e., to take into account the polarization of the surrounding electron clouds in the interaction between the grains).

Tkachev and Yakovlenko [6] described a dusty plasma by numerically solving Poisson's equation with a Boltzmann electron density distribution. They calculated the structures of a "Debye atom" (a positively charged grain surrounded by an electron cloud) and a "Debye quasi-molecule." This terminology was used in [6], but it seems worthwhile to use the term "Boltzmann" (rather than "Debye"). Recall that the Debye approximation, which is based on the linearization of the exponential function in the Boltzmann distribution, provides physically meaningful asymptotics on short spatial scales too. Explaining the experiments of [3], Tkachev and Yakovlenko arrived at the conclusion that the dust grains experienced exclusively attracting forces due to excessive screening and polarization of the electron clouds around the grains. Note that, in a series of papers on modeling the processes of the extraction of ions from a collisionless plasma during laser isotope separation (see the literature cited in [6]), collisional models (such as the hydrodynamic model and the model with the Boltzmann density distribution) were applied without any justification. The method for modeling a collisionless plasma in the problem of laser isotope separation was considered in more detail in my recent paper [11].

In the experiments of [3], the distribution functions of the electrons incident onto the grain surface and the thermal-emission electrons differ greatly from one another. That is why the electron distributions around a point charged grain, which were derived in this paper, may differ substantially from the real distributions. Clearly, our results are applicable to finite-size dust grains only when the distribution functions of the particles incident onto the grain surface and the particles emitted by the grain are the same. If these distribution functions are very different, then the results obtained here for a point charged grain should be refined.

ACKNOWLEDGMENTS

I am grateful to S.V. Vladimirov, A.M. Ignatov, and V.N. Tsytovich for useful discussions.

REFERENCES

1. V. N. Tsytovich, Usp. Fiz. Nauk **167**, 57 (1997) [Phys. Usp. **40**, 53 (1997)].
2. V. N. Tsytovich and J. Winter, Usp. Fiz. Nauk **168**, 899 (1998) [Phys. Usp. **41**, 815 (1998)].
3. V. E. Fortov, A. P. Nefedov, O. F. Petrov, *et al.*, Pis'ma Zh. Éksp. Teor. Fiz. **63**, 176 (1996) [JETP Lett. **63**, 187 (1996)]; Zh. Éksp. Teor. Fiz. **111**, 467 (1997) [JETP **84**, 256 (1997)]; Phys. Lett. A **219**, 89 (1996).

4. A. M. Ignatov, Fiz. Plazmy **22**, 648 (1996) [Plasma Phys. Rep. **22**, 585 (1996)]; Fiz. Plazmy **24**, 731 (1998) [Plasma Phys. Rep. **24**, 677 (1998)].
5. A. P. Nefedov, O. F. Petrov, and S. A. Khrapak, Fiz. Plazmy **24**, 1109 (1998) [Plasma Phys. Rep. **24**, 1037 (1998)].
6. A. N. Tkachev and S. I. Yakovlenko, Zh. Tekh. Fiz. **69** (1), 53 (1999) [Tech. Phys. **44**, 48 (1999)]; S. I. Yakovlenko, Pis'ma Zh. Tekh. Fiz. **25** (16), 83 (1999) [Tech. Phys. Lett. **25**, 670 (1999)].
7. L. D. Landau and E. M. Lifshitz, *Statistical Physics* (Nauka, Moscow, 1976; Pergamon, Oxford, 1980).
8. Yu. L. Klimontovich, *Statistical Physics* (Nauka, Moscow, 1982; Harwood, Chur, 1986).
9. G. Ecker, *Theory of Fully Ionized Plasmas* (McGraw-Hill, New York, 1972; Mir, Moscow, 1974).
10. L. D. Landau and E. M. Lifshitz, *Mechanics* (Nauka, Moscow, 1982; Pergamon, New York, 1988).
11. S. A. Maĭorov, Kratk. Soobshch. Fiz., No. 4, 47 (1999).

Translated by G. Shepekina

Plasma Physics Reports, Vol. 26, No. 7, 2000, p. 632. Translated from Fizika Plazmy, Vol. 26, No. 7, 2000, p. 672.

NEW BOOKS

New Textbook on Plasma Electrodynamics: A. F. Aleksandrov and A. A. Rukhadze, *Course on Electrodynamics of Plasmalike Media*

(Mosk. Gos. Univ., Moscow, 1999)

The textbook is written by prominent physicists and acknowledged experts in plasma electrodynamics. One of the authors (A.A. Rukhadze) belongs to a remarkable group of physicists who founded this field of science. The book is written in a dynamic, visual, and physically clear language. The principal points and most important problems are clearly highlighted without going into unnecessary technical details, which favorably distinguishes this textbook from others. We believe that this book will help students and experts working in the fields of plasma physics, electronics, and physics of solid plasmas. The book reads easily and with pleasure. It is evident that the authors greatly enjoy this fundamental and very complicated (but, at the same time, very important for modern technological applications) field of science. Theoretical considerations carried out at a high scientific level [however, without significant mathematics, a bias toward methodology, or a tendency for "rigorous" (often only at first sight) proofs or populist oversimplification] are appropriately supplemented and illustrated by estimates, numerical results, and quoted experimental data.

In our opinion, an obvious advantage of the book is that it presents problems with solutions on each subject. This assists not only in better understanding the subjects but also in the transfer of skills in this area. Since the problems are not "academic" in essence but are related to the new issues of present-day science and technology (as an example, we can mention free-electron lasers, whose history does not amount to even two decades), they evoke a positive response from the reader.

For future editions, we would like to suggest that the authors should supplement the list of the recommended literature with reviews and monographs recently published in Russian and English.

Also, we would like to make the following comments:

1. In our opinion, the difference between the problem formulations by A.A. Vlasov (1938) and L.D. Landau (1946) is covered insufficiently. Vlasov solved an eigenvalue problem (i.e., a Cauchy problem), and it would be a mistake if he obtained damped solutions. In contrast, Landau solved an initial problem, i.e., the problem on the relaxation of an initial perturbation. In such a problem, the damping or growth of the perturbations (e.g., the beam–plasma instability discovered by Ya. B. Faĭnberg, A.I. Akhiezer, and D. Bohm and E. Gross) is quite natural.

2. It is worthwhile to include the treatment of nonequilibrium distributions of waves and particles (see papers by V.E. Zakharov, B.B. Kadomtsev, V.I. Petviashvili, R.Z. Sagdeev, E.A. Kuznetsov, S.S. Moiseev, V.M. Kontorovich, A.V. Kats, V.I. Karas', V.E. Novikov, etc.).

Finally, note that the book of these remarkable authors is excellent and can be recommended to a wide circle of readers.

Ya. B. Faĭnberg, Academician
of the National Academy
of Sciences of Ukraine

V. I. Karas', Professor

1063-780X/00/2607-0632$20.00